The Gravitational Wave Kaleidoscope: Unveiling Strong Coupling & Topological Defects

Dissertation submitted for the award of the title
"Doctor of Natural Sciences"
to the Faculty of Physics, Mathematics and Computer Science of
Johannes Gutenberg University Mainz

Nicklas Ramberg
born in Falun, Sweden

Mainz, May 29th, 2024

JOHANNES GUTENBERG
UNIVERSITÄT MAINZ

JG|U

Date of submission: 29.05.2024
Date of defense: 22.10.2024

"The only true wisdom is in knowing you know nothing."
Socrates

"Nothing in life is to be feared, only to be understood.
Now is the time to understand more, so that we may fear less."
Marie Curie

"Sometimes it's the very people who no one imagines
anything of who do the things no one can imagine"
Christopher Morcom "The Imitation Game"

Abstract

At its core, this work delves into unraveling the early universe's particle physics by probing a stochastic gravitational wave background (SGWB) in present and future experiments. The first part of the thesis focuses on investigating the potential observation of gravitational wave (GW) signals arising from a cosmological first-order phase transition (FOPT) within a confining sector decoupled from the Standard Model (SM). Given that the sector under consideration is an SU(N) pure Yang-Mills theory (pYM), known for its strong coupling, we employ the Anti-de-Sitter/Conformal Field Theory (AdS/CFT) correspondence to maintain theoretical control. We utilize the Improved Holographic QCD model, capable of accurately describing large N_c pYM and reproducing its equilibrium thermodynamics akin to lattice QCD.

Several key conclusions emerge from this investigation. Initially, our results exhibit excellent agreement with other approaches, such as matrix models or Polyakov loop models. Furthermore, the thesis demonstrates that previous estimates of the GW signal from SU(3) YM theory may have been overestimated by as much as five orders of magnitude. This disagreement arises when incorporating a more precise formulation of the effective action and an actual estimation of the bubble wall velocity, instead of relying on phenomenological assumptions. Consequently, the prospects for future observability transition from promising to slim. Lastly, although SU(N_c) YM is not an CFT, the correspondence underscores its utility as a theoretical tool even beyond CFTs.

In the second part of the thesis, we investigate two phenomenological consequences of the initial conditions on QCD axions in the early universe. These encompass axion miniclusters due to non zero initial velocity and in a post-inflationary case to emit GWs from its associated string network large enough to reconcile data from Pulsar Timing Array (PTA) collaborations.

In the final part of the thesis, our focus shifts towards investigating the phenomenology of dark sectors mainly gravitationally coupled, particularly at energies below $T \leq 1\,\mathrm{GeV}$. In these scenarios, GWs have emerged as a prominent tool for probing such dark sectors. We introduce a novel approach by considering scalar anisotropies within the dark sector, which are damped through gravitational interactions with the photon-baryon fluid. This interaction leads to heating up the fluid, resulting in observable effects. This additional heat cause μ-distortions in the cosmic microwave background (CMB), presenting a new possibility for probing such sectors. Notably, we highlight a significant degree of observable complementarity between searches for μ-distortions arising from large dark sector fluctuations and GWs in the PTA range.

Furthermore, we delve into the potential of dark sectors with significant fluctuations for GWs emission to elucidate the recent hint of a GW background observed by PTAs such as North American Nanohertz Observatory for Gravitational Waves (NANOGrav) and International Pulsar Timing Array (IPTA). We particularly investigate the interplay between cosmological constraints and minimal BSM models to unravel promising sources of new physics capable of explaining the acclaimed signal from the recent data release of the PTA collaborations. In this context, we emphasize the substantial complementarity between constraints derived from various sources, including relativistic degrees of freedom, μ-distortions, CMB, collider experiments, and the abundance of cold dark matter (CDM).

List of Publications

The foundation of this thesis is based on the following publications and preprints. Here we outline the author's contribution to each one of them.

[1] N. Ramberg and L. Visinelli (QCD Axion & Gravitational waves NANOGrav results): All co-authors contributed to the manuscript. The content of this paper is based on the paper [2] which formed the basis of the author's master thesis. The figure for the contour plot of the spectral index and the characteristic strain amplitude were created by a collaborator and the resulting figure was verified by the author. This publication forms Chapter V with a brief added discussion on the potential implication of the most recent Pulsar Timing Array data.

[3] B. Barman, N. Bernal, N. Ramberg and L. Visinelli (QCD Axion Kinetic Misalignment without Prejudice): The author's contribution to this paper constitutes the study of the mini clusters with the press-scheckter formalism, their phenomenology, and if they could describe the OGLE/Subaru microlensing data. Furthermore, all authors contributed to the manuscript and this publication forms Chapter IV.

[4] N. Ramberg, W. Ratzinger, and P. Schwaller (one μ to rule them all CMB spectral distortions can probe domain walls, cosmic strings and low scale phase transitions): This work and manuscript was mainly worked on by a collaborator, whereas the author's contribution was partially on the manuscript, and to verify/cross-check results obtained by a collaborator. The author mainly checked the numerical implementation of this work by performing an analogous calculation alongside his collaborator, and also to verify the figures in section 6 concerning the phenomenological constraints. The study of the accuracy of the semi-analytic estimations for the acoustic sound waves against the numerical results of a toy model i.e. Section 5 of the manuscript was performed by a collaborator. In this thesis, the manuscript [4] will be presented here in Chapter VII.

[5] E. Morgante, N. Ramberg and P. Schwaller (Gravitational Waves from Dark SU(3) Yang-Mills): All co-authors contributed to the manuscript. The model calculations were made in collaboration by the author and a collaborator. The author contributed the figure showing the GW spectra for the benchmark PT points and comparing the model and the SU(3) lattice data. The publication is part of Chapter III with its main results in the appendices for a direct comparison to the refined study prepared by preprint [6].

[7] E. Madge, E. Morgante, C. Puchades-Ibanez, N. Ramberg, W.Ratzinger, S.Schenk, and P. Schwaller (Primordial gravitational waves in the nano-Hertz regime and PTA data – towards solving the GW inverse problem) All co-authors contributed to the manuscript, where the authors main contributions concerns the subsections on meta-stable topological defects. Providing with the GW templates used and aided in imposing the relevant phenomenological constraints possibly imposed on the different models. The fits to the PTA data Using Enterprice/Ceffyl with figures presented in the paper were performed by collaborators. Therefore in this a

shorthand version of that manuscript forms Chapter VI

[6] E. Morgante, N. Ramberg and P. Schwaller (The Dark Kaleidoscope: Gravitational Waves from the Colors in the Sky): All co-authors contributed to the manuscript. The refined effective action was mainly developed by a collaborator in collaboration with the author, where the author worked on an alternative approach that will be presented elsewhere and its applicability to bubble wall velocities. The author made the figures concerning the fit to lattice data and its implementation. Furthermore, the author also aided in the outcome of Figure 7 for the wall velocities. This future preprint is the foundation of Part I of the thesis i.e. Chapter III, where [5] is only a subset of this work.

Contents

Prologue

CHAPTER I

Introduction

The composition of our present universe, its past and future evolution, and its fundamental constituents have undergone revolutionary discoveries over the past century. Initially, from a theoretical standpoint, the great minds of the 20th century formulated the theories of Quantum Field Theory (QFT) and General Relativity (GR) that reshaped our understanding of everything. Subsequently, extensive experiments were conducted to validate these theories, ensuring a correct composition of our universe and the interactions among its constituents. The formulation and validation of the at present standard models in particle physics and cosmology emerged from these foundational theories and have persisted throughout the last century. Despite the remarkable successes of the previous century, we have come to realize that there persist considerable limitations inherent in these theories.

Some of these shortcomings are theoretical, such as the unification of the forces of nature and with such the corresponding theory of quantum gravity, as exemplified by String Theory and Asymptotically Safe Gravity to mention a few. On the other hand, there are more practical challenges, like the so-called Hubble tension, which signifies the discrepancy in measurements of the Hubble parameter determining the expansion rate of our universe. Additionally, significant puzzles also involve the particle constituting the majority of the universe's matter content CDM, which remains elusive both theoretically and experimentally due to limited understanding of its interactions with the standard models of particle physics and cosmology beyond gravity. The origin for the matter/antimatter asymmetry of the universe is also a missing piece of great magnitude since without it we would not be here.
One avenue of experimental achievements for uncovering the particles of the SM of particle physics has primarily been driven through particle accelerators such as the Large Electron Collider (LEP), Tevatron, and the Large Hadron Collider (LHC) at CERN in revealing the constituents of the SM of particle physics. Despite their remarkable achievements, their technology is currently reaching its utmost limits. The prospect of pushing them to even higher energies in the future may only be attainable through incremental steps. Consequently, scaling such accelerators to orders of magnitude beyond their current capacities would require an accelerator of a size approaching that of the equator, rendering it impractical for humanity.
The quote by Zeldovich, "The Universe is the poor man's particle accelerator," could not be more timely and accurate given the recent discovery of GWs originating from the merger of two black holes, an event observed using the LIGO/VIRGO Interferometers. Not only did this discovery confirm Einstein's prediction of gravitational radiation made

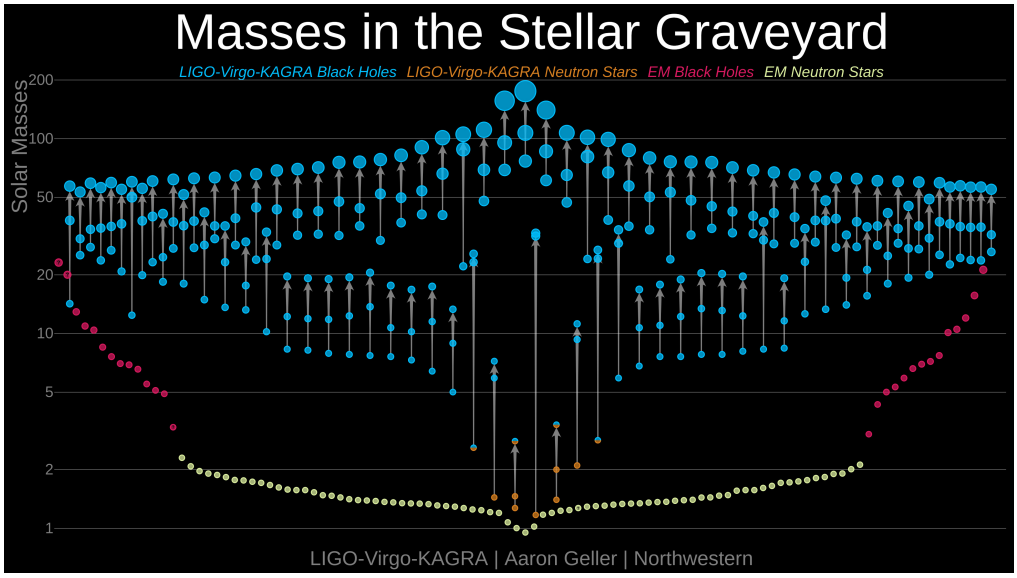

Figure I.1: Population of merger events between black holes, and neutron stars in the third observation run O(3) made by the LIGO/VIRGO/KAGRA (LVK) collaboration. The x-axis denotes the time of the event whereas the y-axis is the mass of the constituents in the merger, where they are dubbed by their colors, blue is for a black hole, orange is for neutron stars, red is for BH mergers with an electromagnetic counterpart, and finally yellow indicate a merger involving a neutron star with an EM counterpart.

almost 110 years ago now but it also unveiled the possibility of directly searching for new physics in the regime of strong gravity. Furthermore, it also posits the opportunity to increase our understanding of GR by careful extraction and reconstruction of the emitted GWs from the events. This has been an active line of research for the past 9 years and by the successful observation of more events and also events involving neutron stars an entire catalog has emerged which is dubbed as the stellar graveyard see Fig. (I.1).

Among the LVK collaboration, there exists a diverse array of present and future experiments in GW observatories, encompassing both earth-based and space-based facilities. This comprehensive suite of experiments enables the mapping of the GW background across a broad frequency spectrum ranging from $f \in [10^{-9}, 10^{3}]$, with peak sensitivities varying from $\Omega_p \sim 10^{-13} - 10^{-16}$.

The shape and magnitude of the GW power spectra offer crucial insights into the mechanisms at play during their emission. For instance, it can offer information about the nature of the source (Astrophysical or Stochastic).

GWs, being a form of radiation, propagate nearly undisturbed throughout cosmic evolution, aside from redshift effects. This characteristic makes GWs invaluable for probing the opaque plasma present in the early universe, shedding light on the physics occurring before the emission of the CMB, and potentially extending to the earliest moments of cosmic history.

Moreover, GWs are thought to play a pivotal role in probing dark sectors of the universe whose interactions are either very weak or purely gravitational to the SM plasma. This assumes that these dark sectors possess dynamics capable of emitting GWs. The imposed assumption mentioned above are essential for an interpretation of the results presented in this thesis. Therefore, we will study a set of well-motivated dark sectors that possess dynamics prone to emitting GWs over a vast range of frequencies and amplitudes with

various spectral features in their power spectra. A particular phenomenon that may have generated a GW background is a FOPT. Such FOPTs are ubiquitous in extensions of the SM, examples include warped extra-dimensions, confining SU(N) gauge theories, SM electroweak sector extensions (gauge singlets or otherwise) as well as a whole host of dark sector models.

In this thesis, we will consider a dark sector composed of a confining SU(N) gauge theory. These FOPTs source SGWBs with a unique spectra that feature arguably the most intimate connection with fundamental particle physics. The energy scales that we will probe range from keV scales, with existing pulsar timing array experiments, all the way to 10^6 TeV with future ground-based experiments.

The structure of this thesis is as follows: In Chap. (II), we present a brief theoretical overview of the SM of particle physics and cosmology, QCD Axions, GWs/SGWBs, and the Gauge/Gravity duality, as these topics constitute the essential cornerstones of this work. Chapter. (III) constitute Part. (I) of the thesis, focusing on the observable prospects arising from cosmological FOPTs occurring in SU(N) pYM theory [5, 6]. In Chap. (III), we consider SU(3) and SU(N_c) pYM theory, where we elucidate the GW prospects from its confinement phase transition using the AdS/CFT correspondence. In particular, we employ the Improved Holographic QCD model to describe the theory. Furthermore we investiage the impact of increasing the number of colors. By using the same model, we address and improve upon the theoretical shortcomings identified in our initial study of SU(3). In Part. (II) of the thesis which comprises Chap. (IV - V), we are looking at two phenomenological consequences of QCD axions in the early universe. Chap. (IV) entertains how axion substructures like mini-clusters and stars would be altered by changing the initial condition of the axion field. In Chap. (V) we elaborate on the observable prospects of GWs from axion strings in the PTA band based on the work [2].

Part. (III) of the thesis governs very weakly interacting or purely gravitationally coupled dark sectors at energies $T \leq 1\,\text{GeV}$ with intrinsic dynamics prone to SGWBs to describe the recent hint of a GW background from the PTA collaborations [7]. We display how a minimal BSM setup consisting of Meta-Stable topological defects i.e. Global Strings (GS) and Domain Walls (DWs) may describe PTA data. These scenarios are known to exhibit large GWs in partial parts of their parameter space, making them prime candidates for observation or constraint by future GW experiments. This study entails Chap. (VI).

In Chap. (VII) we study how density fluctuations in a dark sector can cause μ-distorsions in the CMB by providing an applicable framework in terms of semi-analytic expressions depending on the nature of the anisotropies (stochastic, deterministic). These expressions are then compared against numerical simulations of a toy model for validity of the approach, where we also elaborate on how strong constraints on μ-distortion experiments are against cosmological probes. In doing this, we find a great deal of observational complementarity between μ-distortions in the CMB and GWs in the PTA range for sources keen to admit GWs and large scalar fluctuations like (FOPTs, and meta-stable topological defects). Hence Chap. (VII) in this thesis reveals a clear indication of the dawn of multimessenger probes.

CHAPTER II

Theoretical Background

II.1 The Standard Models of Particle Physics & Cosmology

This section aims to provide a concise overview of the fundamental particles constituting the universe, their associated force carriers, and the evolutionary trajectory of cosmic particle content. While the SM of particle physics and cosmology have enjoyed considerable success in explaining natural phenomena, several key components remain elusive. For instance, in the SM of cosmology, known as the ΛCDM model, CDM and Dark Energy (DE) dominate the universe's energy density, comprising 95% of its content. Yet, the precise nature of CDM and DE remains unknown. Similarly, within the SM of Particle Physics, the unification of gravity with other fundamental forces remains an outstanding challenge.

On a more immediate scale, the understanding of neutrinos and their masses, as well as the hierarchy among fermionic flavors, presents unresolved questions within the SM. Despite these challenges, the SMs serve as foundational frameworks for understanding the universe's behavior, from its smallest constituents to its largest structures. In this thesis, we aim to elucidate these essential constituents, setting the stage for our exploration of more nuanced topics later on.

II.1.1 The SM of Particle Physics

The SM of particle physics [8–11] is the most complete description of our universe so far that describes all known elementary particles and three out of the four fundamental forces the electromagnetic force, the weak, and the strong force. The SM is a gauge theory of non-abelian nature which comprises the following symmetries,

$$SU(3)_c \times SU(2)_L \times U(1)_Y \,. \tag{II.1}$$

The $SU(3)_c$ refers to the color group of Quantum Chromodynamics (QCD) [12–17], whereas the remaining symmetry groups $SU(2)_L$ and $U(1)_Y$ respectively correspond to weak isospin and hypercharge completing the electroweak (EW) force [8–10]. The fact that both the strong and EW forces are gauge interactions is an essential cornerstone of the SM, however, the fourth and final fundamental force, gravity, is not accounted for in this theoretical framework. The SM matter content consists of fermion fields in which there are three generations of (quarks, leptons) with spin-$\frac{1}{2}$, the spin-1 gauge fields (photon, gluon, $W^{\pm}$, Z), and a spin-0 scalar field i.e., the Higgs boson where the fermions constitute the matter content and the gauge bosons mediate interactions among the matter. Excitations of the matter fields are what we call particles. The interactions of the fields in the SM are

Name		Field	Charges		
Spin	Quark/Lepton		$SU(3)_c$	$SU(2)_L$	$U(1)_Y$
$\frac{1}{2}$	Left Quark	q_a	3	2	$\frac{1}{6}$
$\frac{1}{2}$	Right up Quark	u_a	3	1	-$\frac{1}{3}$
$\frac{1}{2}$	Right down Quark	d_a	3	1	$\frac{2}{3}$
$\frac{1}{2}$	Left Lepton	l_a	1	2	-$\frac{1}{2}$
$\frac{1}{2}$	Right Lepton	e_a	1	1	-1
1	Gluons	G	8	1	0
1	Electroweak	W	1	3	0
1	Hypercharge	B	1	1	0
0	Higgs Doublet	ϕ	1	2	$\frac{1}{2}$

Table II.1: Table of the particle content of the SM of particle physics before Electroweak symmetry breaking has occured.

described by a lagrangian density which we in shorthand will denote as lagrangian

$$\mathcal{L}_{SM} = -\frac{1}{4}\mathcal{G}^{\alpha}_{\mu\nu}\mathcal{G}^{\alpha\mu\nu} - \frac{1}{4}\mathcal{W}^{a}_{\mu\nu}\mathcal{W}^{a\mu\nu} - \frac{1}{4}\mathcal{B}_{\mu\nu}\mathcal{B}^{\mu\nu} \tag{II.2}$$

$$-\bar{q}_a\gamma^\mu D_\mu q_a - \bar{u}_a\gamma^\mu D_\mu u_a - \bar{d}_a\gamma^\mu D_\mu d_a - \bar{l}_a\gamma^\mu D_\mu l_a - \bar{e}_a\gamma^\mu D_\mu e_a \tag{II.3}$$

$$(D_\mu\phi)^\dagger(D^\mu\phi) - \mathcal{V}(\phi^\dagger\phi) + \bar{q}^a h_u u^b\tilde{\phi} + \bar{q}^a h_d d^b\phi + \bar{l}h_e e^b\phi + h.c.\,. \tag{II.4}$$

The quark and lepton representations and charge assignments are written out in Table 2 see below. The α, and a are the symmetry generators of $SU(3)_c$, and $SU(2)_L$. The first two lines of Eq. (II.2) describe the kinetic terms of the fields governing the dynamics and self-interactions among the gauge fields. The $(D_\mu\phi)^\dagger(D^\mu\phi) - \mathcal{V}(\phi^\dagger\phi)$ governs the Higgs boson and its self-interactions whereas the last terms in Eq. (II.2) concerns the Yukawa interactions between the fermions and gauge fields to the Higgs. The h_u, h_d, h_e are the Yukawa coupling matrices which are 3×3-matrices. These are the interactions responsible for particle masses under the influence of spontaneous symmetry breaking (SSB), where the fermions and gauge bosons acquire masses proportional to the Higgs VeV.

Provided the Lagrangian of the SM and its large amount of different interactions one can acquire a lot of insights by only considering its symmetry groups and breakings. These symmetries concern the formation of hadrons (Baryons, Mesons) from free quarks and gluons due to confinement, and the generation of particle masses by EW symmetry breaking of $SU(2)_L \times U(1)_Y \to U(1)_{EM}$. We will wrap up this very brief introductionary section with a few comments on each of these symmetry breakings.

1. The strong force mediated by gluons $\mathcal{G}_{\mu\nu}$ possesses a very peculiar behavior called "asymptotic safety", which implies that the nuclear force becomes weaker at shorter distances i.e. higher energies. The consequence for the matter fields and force carriers in the early universe when the energies (temperatures) were high, was that the quarks and gluons propagated freely. This state of matter for the quarks and gluons is known as the Quark-Gluon-Plasma (QGP). As the universe expands and becomes colder at a temperature of about $T \sim 150\,\text{MeV}$ quarks and gluons confine to color neutral objects i.e. (Hadrons) as the $SU(3)_c$ symmetry gets dynamically broken in which the QCD vacua forms a non-zero quark condensate $\langle q_a q_b\rangle \neq 0$. This process i.e. Phase Transition (PT), is a cross-over in the SM where in theories Beyond the SM of particle physics, this can become first order. This exciting phenomenon is

studied later in this thesis, and we will return to this in Chap. (III).

2. To explain the origin of how the elementary particles and the EW gauge bosons gain mass one needs to elaborate on the dynamics of the EW symmetry breaking. To start of the Higgs doublet can be expressed as

$$\phi = \frac{1}{\sqrt{2}} \begin{pmatrix} \phi^+ \\ \phi^0 \end{pmatrix} , \tag{II.5}$$

and the potential is given by

$$V(\phi) = \frac{1}{2}\mu^2\phi^\dagger\phi + \frac{\lambda}{4}(\phi^\dagger\phi)^2 , \tag{II.6}$$

where μ is a parameter with dimension of mass ($\mu^2 < 0$), and λ is a dimensionless quartic coupling constant. As the Higgs field acquires a vacuum expectation value (VeV) at $v_\phi \approx 246\,\text{GeV}$ it spontaneously breaks the EW force into the EM force i.e. $SU(2)_L \times U(1)_Y \to U(1)_{EM}$, this is the renowned Higgs Mechanism and is the responsible mechanism for the fermions and EW gauge bosons to acquire masses. By expanding the SM Lagrangian Eq. (II.2) around the ground state of the broken phase it becomes evident that only one component of the Higgs doublet i.e. the Higgs boson is massive, whereas the other degrees of freedom are massless Goldstone Bosons. This phenomena of EW symmetry breaking takes place in the early universe when the temperatures are around $T \sim 100\,\text{GeV}$ and is also a cross over in the SM.

II.1.2 SM in Cosmology ΛCDM-model

The evolution of the universe is certainly something one may think would be an extremely daunting task to understand, however, the evolution of the universe on very large scales is significantly a lot easier than what one may think. The distribution of galaxies is denser on short scales whereas the scales get larger the distribution of galaxies becomes more and more uniform. In particular on scales larger than $\sim 200\,\text{Mpc}$ the universe appears to look isotropic, which is to say that it looks the same in every direction. Furthermore, the universe is a vast place potentially even infinitely large assuming that neither we on Earth nor anyone/anything else is located at a specific location within the universe provided the observed isotropy on large scales implies that the universe is also thought to be homogeneous.

These two insights regarding the universe on large scales are typically referred to as the cosmological principle and this simplifies the metric structure of spacetimes which respects this principle. The metric that is primarily considered when concerned with the universe on a large scale is the Friedmann-Robertson-Lemaitre-Walker (FRLW) proposed already in the 1920s [18]

$$ds^2 = -dt^2 + a(t)^2 \left[\frac{dr^2}{1-kr^2} + r^2(d\theta^2 + \sin^2\theta d\phi^2) \right] , \tag{II.7}$$

a(t) is the scale factor and $k = -1, 0, 1$ defines the different types of curvature within the space-time. Provided the cosmological principle, what does it imply for the matter content of the universe and what type of fluid structure should it possess? Since the cosmological principle states an isotropic and homogeneous universe its matter content i.e., the energy-momentum tensor will be diagonal whose fluid description will take the form of a perfect fluid.

As a static universe filled with matter and energy is unstable one imposes that the energy density and pressure to be dynamical with time. An energy-momentum tensor for a perfect fluid is diagonal

$$T_\mu^\nu = (\rho + P)u_\mu u^\nu + P\delta_\mu^\nu, \tag{II.8}$$

where $u_\mu = (1, 0, 0, 0)$ is the comoving velocity, i.e. the velocity of a comoving reference frame. The comoving velocity u_μ is the velocity of matter content in a frame of reference where it is at rest. The matter contents are assumed to be of baryonic type, with a linear relationship between the energy density and pressure

$$P = \omega\rho. \tag{II.9}$$

By evaluating the trace of the energy-momentum tensor T_μ^μ the following relation is obtained

$$T_\mu^\mu = -\rho + 3P\,. \tag{II.10}$$

Furthermore one finds

$$\dot{\rho} + 3H(\rho + P) = 0\,, \tag{II.11}$$

where Eq. (II.11) describes how the energy density of a fluid evolves in time with the expansion of the universe encoded in $H = \frac{\dot{a}(t)}{a(t)}$ i.e., the Hubble parameter. Eq. (II.11) is the continuity equation in cosmology. For generic fluids with intermediate values of the equation of state ω between $-1 \leq \omega \leq 1$ and by defining ρ_ω as the energy density as a function of the equation of state parameter ω one then finds

$$\rho_\omega a^{-3(1+\omega)} = constant\,. \tag{II.12}$$

Eq. (II.12) is obtained by combining Eq. (II.11) - (II.9) and then expressing the rate of change in the energy density as a function of ω as a total derivative. One can also find this relation by instead making use of Einstein field equations with the FRLW metric which are stated below

$$\frac{\dot{a}(t)^2}{a(t)^2} = H^2 = \frac{8\pi G}{3}\rho + \frac{\Lambda}{3} - \frac{k}{a^2} \tag{II.13}$$

$$H = \frac{\dot{a}(t)}{a(t)} \tag{II.14}$$

$$\frac{\ddot{a}(t)}{a(t)} = -\frac{4\pi G}{3}(\rho + p) + \frac{\Lambda}{3} \tag{II.15}$$

$$P = \omega\rho \tag{II.16}$$

$$\dot{p} + \frac{3\dot{a}(t)}{a(t)}(p + \rho) = 0\,. \tag{II.17}$$

With this set of equations and insights regarding the universe on large scales we are now in a good place to delve a bit into the current model of cosmology that describes our universe i.e., the so-called ΛCDM model [19, 20]. It is convenient to use the critical energy density, i.e., the energy density today

$$\rho_{c,0} = \frac{3H_0^2}{8\pi G} = 1.9 \cdot 10^{-29} h^2 \frac{g}{cm^3}\,, \tag{II.18}$$

where h^2 is a rescaled version of H_0, the Hubble rate at present. The present energy density can be used to express each component of the total energy density as a fraction of the critical energy density

$$\Omega_{i,0} = \frac{\rho_{i,0}}{\rho_{c,0}}\,. \tag{II.19}$$

In Eq. (II.19), the index i indicates which fluid is being considered, and the subscript 0 refers to the present time.

There is a large uncertainty regarding the present value of the Hubble rate, as its value differs significantly around 5σ difference when inferring its value using different inference measurements. The types of measurements that are performed to evaluate the expansion rate of the universe are either through inference from CMB measurements at redshift $z \sim 1000$ measuring $H_0 \sim 68$km/Mpc or making use of astrophysical standard candels of Cephids at low redshift $z \sim 0.7$ nearby us measuring $H_0 \sim 74$km/Mpc. The discrepancy between the different retrieval of the Hubble parameter H_0 is known as the Hubble tension [21–24] .

The ΛCDM model predicts that the universe is critically flat at large scales i.e. $\Omega_{c,0} \approx 0$, which is confirmed by various simulations and experiments [21,22]. The energy content of the universe is primarily governed by matter and dark energy, with the present fractional matter energy density being $\Omega_{m,0} \simeq 0.31$, and $\Omega_{\Lambda,0} \approx 0.69$. The relic matter density, i.e. $\Omega_{m,0} \simeq 0.31$ is split into two contributions, baryonic matter, and CDM, such that $\Omega_{m,0} = \Omega_{cdm,0} + \Omega_{b,0}$. Baryonic matter incorporates all the ordinary matter of the universe. In the ΛCDM model of the universe, the Friedmann equation reads as

$$\frac{H^2}{H_0^2} = \Omega_\Lambda + \Omega_{m,0} a^{-3} + \Omega_{r,0} a^{-4} + \Omega_{c,0} a^{-2}. \tag{II.20}$$

The present values of the fractional energy densities are taken from [21,22]

$$\Omega_{\Lambda,0} = 0.6889 \pm 0.0056, \tag{II.21}$$
$$\Omega_{m,0} = 0.3111 \pm 0.0056, \tag{II.22}$$
$$\Omega_{r,0} \simeq 9.1476 \cdot 10^{-5}\,. \tag{II.23}$$

The rescaled Hubble rate and fractional matter densities are listed below

$$h = 0.679 \pm 0.006\,, \tag{II.24}$$
$$\Omega_{b,0} h^2 = 0.02242 \pm 0.00014\,, \tag{II.25}$$
$$\Omega_{cdm,0} h^2 = 0.11933 \pm 0.00091\,. \tag{II.26}$$

II.2 Axions

In QCD there is an open problem residing in the discrepancy between the theoretical prediction of CP violation and its experimental absence.

The most popular resolution to this problem is to introduce a new chiral symmetry that dynamically relaxes the presence of CP violation in QCD. This new global chiral symmetry $U(1)_{PQ}$ which is spontaneously broken at an unknown energy scale f_a is denoted as Peccei Quinn (PQ) symmetry from the original authors proposing the solution. Whereas the Axion is the pseudo-Nambu-Goldstone boson (pNGB) associated with the PQ symmetry breaking. However pseudo-goldstone bosons arising from the breaking of global symmetries is a rather generic feature and if the global symmetry is approximate or not determines if the pNGB is massive. In this thesis, we will primarily consider axions whose origin is to resolve the strong CP problem. However the emergence of pNGBs that are not intended to resolve the strong CP problem from the breaking of approximate global symmetries as we refer to as Axion-Like-Particles (ALPs), and regard axions only in the context of the QCD axion.

In this section, we first review the strong CP problem and its resolution with a QCD axion. Secondly, we allure the reader to the different ways cosmological populations of axions/ALPs may have been generated in the early universe and divert further attention to the vacuum misalignment mechanism. Finally, we provide a qualitative discussion about the implications of when the PQ symmetry is broken in the early universe and list some if the phenomenological differences. In Part. (II - III) of this thesis, we will see to what predictable extent either axions or ALPs possess in various cosmological contexts in the early universe.

II.2.1 The QCD Axion

In the theory of strong interactions i.e. QCD there are topological terms more familiar as Chern Simons (CS) terms that are generated when one wants to resolve the $U(1)_A$ problem. Such a term in the QCD Lagrangian takes the following form

$$\mathcal{L}_\theta = \bar{\theta}\frac{g^2}{32\pi^2}\mathcal{G}^a_{\mu\nu}\tilde{\mathcal{G}}^{a\mu\nu}\,, \tag{II.27}$$

where g is the strong coupling constant, $\mathcal{G}^a_{\mu\nu}$ is the field strength of $SU(3)$, and $\tilde{\mathcal{G}}^{a\mu\nu}$ its dual. In the inclusion of such a term to the QCD lagrangian one expects to break both parity P and charge conjugation C i.e. breaking CP. The discrepancy between the theoretical prediction of CP violation in QCD and that it has not been observed experimentally is the strong CP problem of QCD. The primary constraint on CP-violating effects in QCD is the magnitude of the electric dipole moment of the neutron (NEDM), where the magnitude of the NEDM is of the order

$$d_n \propto e\bar{\theta}\frac{m_q}{m_n^2} \leq 10^{-22}\,. \tag{II.28}$$

Where $\bar{\theta}$ is a dimensionless number one would hence, therefore expect it to be of $\mathcal{O}(1)$ but one obtains that $\bar{\theta} \leq 10^{-10}$ making it a severe fine-tuning problem. The first suggestion is to take the lightest quark of the SM to be exactly massless i.e. $m_u = 0$, since then one recovers axial symmetry $u \to exp(i\alpha\gamma_5)u$. However, the SM quarks are not massless so this is not a viable solution to the Strong-CP problem. The second suggestion for resolving the Strong-CP problem would be that $\bar{\theta} = 0$ macroscopically, which generates a CKM angle that at the same time makes $\bar{\theta}$ small. Such a realization can be implemented by adding

a set of vector-like quarks and a set of scalar fields where the scalar fields break CP. This goes under the name of Nelson-Barr mechanisms [25, 26]. The third option suggested by Peccei and Quinn [27, 28] is to promote $\bar{\theta}$ to a dynamical field $\phi(x)$ by introducing an additional chiral symmetry.

We consider a SM-singlet complex scalar field Φ, the PQ field, which extends the SM content and which is described by the effective Lagrangian

$$\mathcal{L} = \mathcal{L}_{\rm QCD} + |\partial_\mu \Phi|^2 - V(\Phi) + \mathcal{L}_{\rm int}\,, \tag{II.29}$$

where $\mathcal{L}_{\rm QCD}$ captures all QCD effects in the SM, the PQ field potential responsible for the SSB of $U(1)_{\rm PQ}$ at the energy scale f_a with coupling λ_Φ,

$$V(\Phi) = \frac{\lambda_\Phi^2}{2}\left(|\Phi|^2 - \frac{f_a^2}{2}\right)^2, \tag{II.30}$$

and where the term $\mathcal{L}_{\rm int}$ is responsible for the interaction of Φ with other beyond-SM physics, leading to an effective coupling of the field with gluons and other SM particles[1]. The Lagrangian in Eq. (II.29) is invariant under the continuous shift symmetry

$$\phi \to \phi + \alpha\, f_a\,, \tag{II.31}$$

for a generic value of α that corresponds to a rotation in the complex plane $\Phi \to e^{i\,\alpha}\,\Phi$. After SSB, the complex scalar field can be decomposed in polar coordinates as

$$\Phi = \frac{1}{\sqrt{2}}\,(S + f_a)\; e^{i\,\phi/f_a}, \tag{II.32}$$

where the angular direction is the axion a and the radial direction is the saxion S, such that the saxion vacuum mass is $m_S = \lambda_\Phi\, f_a$. Once the spontaneous symmetry breaking has occurred the lagrangian of the axion becomes

$$\mathcal{L}_a = -\frac{1}{2}(\partial_\mu\phi)(\partial^\mu\phi) + \frac{g_s}{32\pi^2}\frac{\phi}{f_a/N}\mathcal{G}^a_{\mu\nu}\bar{\mathcal{G}}^{a\mu\nu} - V_{\rm QCD}(\phi), \tag{II.33}$$

where $\phi = \phi(x)$ is the axion field, x is a four-vector, N is the PQ color anomaly which is a sum of all fermionic charges and set to 1. In Eq. (II.33), the three different terms are the kinetic term of the axion field, the interaction between axions and gluons and finally the QCD axion potential $V_{QCD}(\phi)$ which we will elaborate more about later on.

For the final part of the explanation on how the axion resolves the Strong CP problem we only need to pay attention to the contributions of the CS term and the inclusion of an axion to the QCD lagrangian

$$\mathcal{L}_{\theta+\phi} = -\frac{g^2}{32\pi^2}\left(\bar{\theta} + \frac{\phi}{f_a}\right)\mathcal{G}^a_{\mu\nu}\mathcal{G}^{\bar{a}\mu\nu}\,. \tag{II.34}$$

As QCD confines $\mathcal{G}^a_{\mu\nu}\bar{\mathcal{G}}^{a\mu\nu}$ acquires a VeV from instanton effects and generating an axion potential Eq. (II.36) whose minima are at $\bar{\theta} - \frac{\phi}{f_a} = 2\pi n$ for $n \in Z$.

Stated slightly different, the inclusion of the axion ϕ with the θ term of QCD its vacuum energy becomes

$$E(\bar{\theta}) = -m_\pi^2 f_\pi^2 \cos\left(\bar{\theta} + \frac{\phi}{f_a}\right), \tag{II.35}$$

[1]This interaction term in the full lagrangian is where for instance UV models to the axion could be present. In the Kim-Shifman-Vainshtein-Zakharov (KSVZ), this interaction term would have been the yukawa interaction between the additional quark doublet with the PQ field $\mathcal{L}_{int} = -\lambda_Q \Phi Q_L \bar{Q}_R + h.c..$

in which the QCD vacuum energy gets minimized when the axion acquires a VEV that cancels $\bar{\theta}$.

The QCD axion potential is

$$V_{\rm QCD}(\phi) = \chi(T)\left(1-\cos\frac{\phi}{f_a}\right), \tag{II.36}$$

where $\chi(T)$ is the topological susceptibility of QCD and is calculated using lattice QCD. Much of the recent effort has been devoted to the numerical evaluation of the functional form of $\chi(T)$ [29–37]. A fit to the numerical results from lattice simulations is [33]

$$\chi(T) \simeq \chi_0 \times \begin{cases} 1\,, & \text{for } T \lesssim T_{\rm QCD}\,, \\ \left(\frac{T}{T_{\rm QCD}}\right)^{-b}, & \text{for } T \gtrsim T_{\rm QCD}\,, \end{cases} \tag{II.37}$$

where $\chi_0 \simeq 0.0216\,\mathrm{fm}^{-4}$ and $b \simeq 8.16$. At any temperature T, the mass of the axion is $m(T) = \sqrt{\chi(T)}/f_a$, so the axion can be effectively regarded as a massless scalar field as long as the QCD effects can be neglected for $T \gg T_{\rm QCD}$.

Since the axion is shift symmetric one can define the axion misalignment angle as the

$$\theta = \bar{\theta} + \frac{\phi}{f_a/N}\,. \tag{II.38}$$

To conclude, the solution to the strong CP problem with an axion is nothing more than promoting the free parameter $\bar{\theta}$ to a dynamical field i.e. the axion which evolves to the CP conserving minimum through the spontaneous breaking of a global U(1) symmetry. The theoretical technique summarized above can be rephrased in the statement maybe more familiar to some to say that the axion acts as a spurion to $\bar{\theta}$ in the QCD lagrangian. The misalignment angle θ is thought of as a phase of a new complex scalar field $\Phi_a = |\Phi_a|e^{i\theta}$ attaining a non-zero VeV at the energy scale $\frac{f_a}{N}$. The curvature of the axion potential evaluated at the minimum gives the axion mass and it can be calculated using chiral perturbation theory and is

$$m_a(T < T_{QCD}) \approx \mathcal{O}(1) 6\mu\mathrm{eV}\left(\frac{10^{12}\mathrm{GeV}}{\mathrm{f_a}}\right), \tag{II.39}$$

up to an order one prefactor stemming from the PQ color anomaly. As we have now seen how the Axion is a solution to the Strong CP problem we will now briefly discuss different ways on which a cosmological population of axions can become present in the early universe.

II.2.2 Cosmological Population of Axions

A relic population of axions/ALPs can in principle be generated in several ways [38], here we will mention the first three briefly and devote the next subsection to the fourth and final one which for the context of this thesis will be of most importance.

- **Decay of Parent Particle:** Here one can imagine a heavy parent particle with mass $m_X >> m_a(T)$ whose decay produces a relativistic population of axions/ALPs. However, if the decay of the parent particle happens after the axion/ALP has decoupled from the SM plasma they will remain relativistic throughout the history of the universe. Hence in this case the axion would not play the role of CDM but instead act as additional radiation otherwise called dark radiation.

- **Emission of Topological defects:** Since axions/ALPs emerge from the breaking of approximate global symmetries long-lived topological remnants in terms of strings and DWs are formed. These structures however cannot be stable in order to not conflict with the predicted cosmological history of the universe, since strings and DWs energy density scales as $\rho_{DW} \sim a^{-2}$ and would quickly overtake the energy density of the universe. Hence these relics need to have some additional mechanism or model building constraints such that they remain only metastable. For the brief discussion below we will impose the assumption mentioned just above. We will elaborate more on this case in Chapter V concerning the GW emission alongside the axion emission from a network of axion strings.
- **Thermal population from the radiation bath:** If axions/ALPs were to be in thermal contact with the SM radiation bath the creation/annihilation processes could yield a thermal population of axions, for this discussion, we will only focus on the case of the axion since that is the only case in which the couplings are specified. Axions would be produced in the SM plasma through pion scattering processes like $\pi + \pi \to \pi + a$ and would decouple once the rate becomes smaller than the Hubble rate. The abundance of thermal axions is fixed as in thermal freeze-out processes in which larger relic abundances are generated for lower decoupling temperatures. In the case of axions as their couplings to the SM bath scales inversely with f_a and respecting the supernovae bounds on $f_a > 10^9\,\text{GeV}$ the thermal population of axions, in this case, is negligible. However, thermal axions are relativistic as long as the decoupling temperature is larger than their mass $T_D > m_a(T)$, and they become non-relativistic once $T_D < m_a(T)$ in which they will behave as hot CDM and would potentially alter structure formation.

The last mechanism for generating a population of axions/ALPs is through the so-called vacuum realignment mechanism. This is also known under the name misalignment mechanism and is a model-independent production channel of axions/ALPs that only depends on the underlying properties of being a pNGB i.e. emerging from spontaneous global symmetry breaking, whose interactions are merely of gravitational or self-interacting nature in the classical case. But before we elaborate on the misalignment mechanism we first need to discuss the implications and eventual outcomes of when the PQ symmetry in the universe takes place w.r.t., inflation The quantitative behavior of the axion and its evolution in the early universe is governed by two physical processes, the first one is when the early universe is the PQ symmetry broken. As this takes place at some high scale, the immediate question is whether the PQ symmetry breaks during inflation or after. The evolution of the axion and its phenomenological implications are severely different between these two cases and they will be separately discussed in the following subsections.

II.2.2.1 Pre Inflationary Axions

The dubbed "Pre-Inflationary" scenario refers to the case in which the PQ symmetry is broken during inflation. Here we only consider the axion to be a spectator field during inflation even though the axion itself serves as a natural inflationary particle candidate due to its shift symmetry. This scenario occurs more explicitly for when $f_a > \frac{H_I}{2\pi}$ in where H_I is the Hubble rate during inflation and in models of single field cold inflation this takes values around $H_I \sim 10^{14}\text{GeV}$, in agreement with Planck data [21, 22]. PQ symmetry breaking i.e the breaking of an approximately global U(1) symmetry during inflation generates an distribution of values for the initial misalignment angle dubbed θ_i over different hubble patches between $\theta_i \in [-\pi, \pi)$. This would evidently produce

topological defects intersecting between two different Hubble patches, however, due to the rapid expansion of inflation such topological defects would be erased quickly. In the next subsection where the PQ symmetry breaking takes place after inflation these topological defects can remain long-lived and will be discussed further there. Not only would the distribution of different values of θ_i between the Hubble patches be erased its value will be evolved to a uniform value.

However, what value θ_i will attain as our Hubble patch begins to evolve after the end of inflation is entirely random and it is drawn from a distribution. In this case two types of fluctuations in θ_i emerge, first is the contribution of the adiabatic fluctuations stemming from the fact that the axion has a gravitational jeans instability. Secondly, since the axion is essentially a massless field present during inflation in a de-Sitter spacetime it will possess quantum fluctuations of the order $\delta\phi = \frac{H_I}{2\pi}$.
These fluctuations are so-called isocurvature fluctuations and their behavior is similar to the tensorial fluctuations present during slow-roll inflation. However as these fluctuations do not generate the first acoustic peak in the CMB power spectrum they are doomed to at most be subdominant and hence constraints on their magnitude and presence are indicating that $f_a \geq 10^{11}$ GeV axion CDM is excluded in this scenario by the measurements of Planck [21, 22][2].

II.2.2.2 Post Inflationary Axions

Here we focus on the contrary case to the previous subsection i.e. $f_a < \frac{H_I}{2\pi}$. This is the case of prior importance for the QCD axion which we refer to as the axion. Furthermore this is a natural case to bear in mind for the axion in the context of standard high scale inflation $H_I \sim 10^{14}\,\text{GeV}$[3] whereas $f_a \leq 10^{13}\,\text{GeV}$. The PQ symmetry gets broken once the temperature of the universe's radiation bath becomes of the order of f_a, i.e., $T \sim f_a$ in which the PQ field Φ see II.2.1 acquires a VEV and each causally disconnected Hubble patch obtains an initial misalignment angle value $\theta_i \in [-\pi, \pi)$. As in the pre-inflationary case the axion remains massless until instanton effects from QCD emerges at an energy scale of about $T \sim 1$GeV. Since the axion is massless initially there is no preferred value for the θ_i, and hence its value is drawn at random from a uniform distribution between $[-\pi, \pi]$. As the PQ symmetry is a global symmetry its breaking generates topological defects i.e., strings and DWs, and contrary to the previous subsection these relics can be long-lived and have a crucial impact on the phenomenology of QCD axions and their evolution in the early universe [39].

The ramifications of these relics on axion phenomenology have pushed for consistently refining the computations regarding the production and evolution of the PQ field in the early universe and to assess the present relic abundance of the QCD axion. Simulating the formation and decay of the network of strings and DWs on cosmological relevant scales are mainly subject to errors and uncertainties due to the numerical complexity of the simulation [40–45]. An important comment to make is that the defects cannot be stable on large-scale cosmological time scales as they would overclose the universe since their scaling with the energy density is slower than both matter and radiation. Since for instance the energy density of DWs scales with the scale factor as $\rho_{DW} \sim a^{-2}$ leading to a cosmological disaster if they are stable[4].
Due to the presence of the distribution of θ_i as a consequence of the fact that all the

[2] Unless one has a way to deal with the amount of isocurvature perturbations present
[3] here we have single field cold inflation in mind
[4] Unless their surface tension is very small they can be long-lived if that is the case.

different Hubble patches in the early universe were different one can compute the average initial axion misalignment value $\langle | \theta_i^2 | \rangle \simeq 1.4 \frac{\pi^2}{3}$ [46]. With this value at hand, one can realize that this fixates the Axion CDM relic abundance from the vacuum misalignment mechanism. With the initial misalignment angle value at hand there are also $\mathcal{O}(1)$ fluctuations present around the epoch of matter/radiation equality. These fluctuations can give rise to so-called axion mini clusters if their magnitude overcome the jeans lengths for structures to form.

II.2.2.3 Misalignment Mechanism

Provided that one has the initial conditions for the axion field $f_a\theta_i = \phi_i\,, \dot{\theta}_i = 0$ for which by the time of PQ symmetry breaking the Hubble rate is much larger than the axion mass, the axion can be considered massless. The initial field value of the axion is set depending on when the PQ symmetry happens w.r.t., inflation as discussed above. An important feature of this mechanism to remember is that it is a non-thermal mechanism. The terminology misalignment refers to that there is a coherent initial displacement of the field, whereas vacuum realignment refers to the process at which the initial displacement relaxes. Here we will display the misalignment mechanism for the QCD axion bearing in mind that this is even simpler for the case of an ALP since for the ALP the mass and decay constants are free parameters.

The equation of motion for the axion misalignment angle $\theta = \frac{\phi}{f_a}$ in an FRLW metric where we neglect the gradient terms reads reads

$$\ddot{\theta} + 3H\dot{\theta} + m_a^2(T)\sin\theta = 0, \tag{II.40}$$

where a dot indicates a derivation w.r.t, cosmic time t. In Eq. (II.40) we have used the potential $V(\theta) = m_a(T)^2 f_a^2(1 - \cos(\theta))$ arising from the non-perturbative effects present at the PQ symmetry breaking. Neglecting the gradient term means that we are only considering the zero mode which constitutes the CDM component. The temperature dependence of the axion mass is governed by the topological susceptibility of QCD $\chi(T) = m_a^2(T) f_a^2$ and here we use the lattice result of [33]. In Sec. (II.2.1) we saw the expression for a fit of the topological susceptibility of QCD based on [33], which conclude that axion can effectively be regarded as a massless scalar field for temperature well above T_{QCD}. In the opposite limit $T \ll T_{\rm QCD}$, the mass squared of the axion at zero temperature is [47]

$$m_a^2 \equiv m^2(T=0) = \frac{m_u\, m_d}{(m_u + m_d)^2} \frac{m_\pi^2\, f_\pi^2}{f_a^2}\,, \tag{II.41}$$

where m_u, m_d are the masses of the up and down quarks, $m_\pi \simeq 140\,\text{MeV}$ is the mass of the π meson, and $f_\pi \simeq 92\,\text{MeV}$ is the pion decay constant. Numerically, this gives $m_a = \Lambda_{QCD}^2/f_a$, with $\Lambda_{QCD} = \chi_0^{1/4} \simeq 75.5\,\text{MeV}$. The interesting region $T \gtrsim \Lambda_{QCD}$ where the presence of the axion potential is not negligible and the axion gets trapped in a minimum of the potential and starts to oscillate around the minima. This happens when the temperature of the universe becomes of comparable size to the mass of the axion i.e.

$$3H(T_{osc}) \sim m_a(T_{osc})\,. \tag{II.42}$$

At which the solution to the Axion EOM becomes non-trivial at this stage. For a generic value of the initial axion misalignment angle value the solutions are only attainable numerically but in the limit where $\theta_i << 1$ analytic solutions can be found. To find the

oscillation temperature of the axion field we assume the standard radiation-dominated phase, during which the Hubble rate is

$$H(T) = \frac{\pi}{3}\sqrt{\frac{g_\star(T)}{10}}\,\frac{T^2}{M_P}\,, \tag{II.43}$$

in which $g_\star(T)$ is the number of relativistic degrees of freedom at temperature T [48] and M_P is the reduced Planck mass. With this assumption, we obtain (see, e.g. Ref. [49])

$$T_{\rm osc}^{\rm mis} \simeq \begin{cases} \left(\sqrt{\frac{10}{\pi^2\, g_\star(T_{\rm osc}^{\rm mis})}}\, M_P\, m_a\right)^{1/2}\,, & T_{\rm osc}^{\rm mis} \lesssim T_{\rm QCD}\,, \\ \left(\sqrt{\frac{10}{\pi^2\, g_\star(T_{\rm osc}^{\rm mis})}}\, M_P\, m_a\, T_{\rm QCD}^{b/2}\right)^{2/(4+b)}\,, & T_{\rm osc}^{\rm mis} \gtrsim T_{\rm QCD}\,. \end{cases}$$

For example, an axion field of mass $m_a \simeq 26\,\mu$eV would begin to oscillate at $T_{\rm osc}^{\rm mis} \simeq 1.23\,$GeV. In the absence of entropy dilution, the axion number density in a comoving volume after the onset of oscillations is conserved,

$$\frac{\rm d}{{\rm d}t}\left[\frac{\rho_a(T)/m(T)}{s(T)}\right] = 0\,, \tag{II.44}$$

where $s(T) = (2\pi^2/45)\, g_{\star s}(T)\, T^3$ is the entropy density and $g_{\star s}(T)$ is the number of entropy degrees of freedom at temperature T [48]. This last expression gives the present axion density fraction,

$$\Omega_a = \frac{\rho_a(T_\star)}{\rho_{\rm crit}}\,\frac{m_a}{m(T_\star)}\,\frac{g_{\star s}(T_0)}{g_{\star s}(T_\star)}\,\frac{T_0^3}{T_\star^3}\,, \tag{II.45}$$

where $T_\star$ is any temperature such that $T_\star < T_{\rm osc}^{\rm mis}$, T_0 is the present CMB temperature, and the critical density is given in terms of the Hubble constant H_0 as $\rho_{\rm crit} = 3\, M_P^2\, H_0^2$. In the limit where the kinetic energy of the axion field can be neglected and it is reasonable to only consider a quadratic potential for the axion its energy density is then simply

$$\rho_a(T_\star) \simeq \frac{1}{2} m^2(T_\star)\, f_a^2\, \theta_i^2\,, \tag{II.46}$$

where θ_i is the initial value of the misalignment angle at temperatures $T \gg T_{\rm osc}^{\rm mis}$. As an order of estimate, for $f_a \simeq 10^{12}\,$GeV the correct relic density that matches the observed DM is obtained for initial field values $\theta_i \simeq \mathcal{O}(1)$.[5]

The QCD axion misalignment mechanism will be discussed in more detail in Sec. (IV.2) where we will also explore QCD axion CDM when the kinetic energy in the energy density of the axion is non-negligible. The intent with this subsection is only to illustrate the main ideas of the misalignment mechanism.

II.3 Gravitational Waves

One of the profound predictions of the theory of GR is GWs, i.e., ripples in spacetime. They were proposed by Einstein in 1916 as the associated fluctuations of the curvature of spacetime caused by an acceleration of massive objects. At the time of their theoretical prediction, it was not clear what objects and events taking place in space would have been large enough for GWs to have been emitted.

Nevertheless, despite their theoretical prediction Einstein himself also made claims that these waves may never be large enough to witness with an experiment. It took almost

[5] Astrophysical constraints provide a lower bound on the decay constant requiring $f_a \gtrsim 10^7\,$GeV [50,51].

a century for the scientific community to directly detect GWs whose detection is paving into a new era of research in astrophysics and cosmology. As GWs propagate through spacetime they possess information about cataclysmic events such as the binary mergers of black holes and neutron stars, births of supernovae, and possibly also information about the very first moments of the universe.

The quest to directly detect GWs began in the 1960s, spurred by the pioneering work of Joseph Weber, who constructed the first GW detectors known as Weber bars. Weber's concept involved using massive aluminum cylinders vibrating at their resonance frequency of 1660 Hz, accompanied by piezoelectric sensors sensitive enough to detect a minute change in the cylinder's length of 10^{-16} m. Due to the relatively small predicted gravitational waves (GWs), the sensors needed exceptional sensitivity. Weber's experiments, although not conclusive, laid the foundation for future endeavors in gravitational wave astronomy.

However, it wasn't until the 1970s that a more promising approach emerged with the development of laser interferometry by Rainer Weiss, Kip Thorne, and Barry Barish. The concept of this detector involves utilizing lasers as interferometer arms to detect gravitational wave-induced motion in the arm lengths from free-falling test masses. For the first successful gravitational wave detection, the sensitivity within the arm length, which is of the order of a few kilometers, needed to detect a difference of $\Delta L \sim 10^{-21}$ m, which corresponds to the scale at which the Heisenberg uncertainty principle becomes significant. This revolutionary technique formed the basis of modern gravitational wave detectors, such as the Laser Interferometer Gravitational-Wave Observatory (LIGO), which made history in 2015 by detecting the gravitational waves produced by the merger of two black holes [52, 53]. Since then, gravitational wave astronomy has rapidly evolved, opening a new window to observe the universe and offering unprecedented insights into some of the most extreme phenomena in the cosmos.

In this section, we will illustrate the calculations of GWs in flat spacetime for illustrative purpose to the reader. We will introduce SGWBs and how they are especially relevant in cosmological contexts and as a tool to constrain the physics of the early universe. In Sec. (II.3.2) we elaborate on the production channel of SGWBs from cosmological FOPTs in the early universe and the relevant parameters/calculations necessary to make predictions of such signals.

GWs in flat space-time

Here we will display how GWs emerge as a prediction in GR. Let's start of by considering the scenario that there exists a reference frame where the metric can be expressed as the Minkowski metric plus a small perturbation

$$g_{\mu\nu} = \eta_{\mu\nu} + h_{\mu\nu}\,. \tag{II.47}$$

We restrict ourselves to only consider weak gravitational potentials in which the magnitude of the tensor perturbation of the 4-dimensional gravitational potential behaves as $|h_{\mu\nu}| << 1$. Furthermore only keeping terms that are linear in the perturbation due to its smallness. Next, let's consider a general coordinate transformation i.e. $x^{'} = x + t^{\alpha}(x)$ where the magnitude of the gradients is smaller or equal to the magnitude of the gravitational potential. One can show that the perturbed minkowski metric remains invariant under finite Lorentz transformation

$$g_{\mu\nu}(x) \to g_{\mu\nu}(x') = \Lambda^{\rho}_{\mu}\Lambda^{\sigma}_{\nu}(\eta_{\rho\sigma} + h_{\rho\sigma}(x)) = \eta_{\mu\nu} + h^{'}_{\mu\nu}(x')\,. \tag{II.48}$$

Since the metric remains invariant, it can be seen that $h^{'}_{\mu\nu}(x')$ transforms as a tensor among the additional feature that the gravitational potentials are invariant under general transformations $x^{'} = x + a$. From [54] which states that the linearized theory is invariant under the Poincare symmetry, the linearized Einstein field equations can be obtained. We are now ready to derive the Einstein equations for the perturbations by explaining the scenario we have in mind and its assumptions. First, we calculate the associated Christoffel symbol which is defined as

$$\Gamma^{\rho}_{\mu\nu} = \frac{g^{\rho\lambda}}{2}(\partial_\mu g_{\nu\lambda} + \partial_\nu g_{\mu\lambda} - \partial_\lambda g_{\mu\nu}) = \frac{1}{2}\eta^{\rho\lambda}(\partial_\mu h_{\nu\lambda} + \partial_\nu h_{\mu\lambda} - \partial_\lambda h_{\mu\nu}) + \mathcal{O}(h^2). \tag{II.49}$$

Once the Christoffel symbol is calculated, the Riemann tensor is calculated from its definition where all terms constituting higher-order terms in the gravitational potential are being neglected i.e.

$$R^{\rho}_{\mu\nu\sigma} = \partial_\mu \Gamma^{\rho}_{\nu\sigma} - \partial_\nu \Gamma^{\rho}_{\mu\sigma} + \Gamma^{\gamma}_{\sigma\mu}\Gamma^{\rho}_{\gamma\nu} - \Gamma^{\gamma}_{\rho\mu}\Gamma^{\sigma}_{\gamma\nu}, \tag{II.50}$$

$$R^{\rho}_{\mu\nu\sigma} = \frac{1}{2}\eta^{\rho\lambda}(\partial_\nu \partial_{mu} h_{\lambda\sigma} + \partial_\sigma \partial_\lambda h_{\mu\nu} - \partial_\nu \partial_\lambda h_{\sigma\mu} - \partial_\mu \partial_\sigma h_{\lambda\nu}) + \mathcal{O}(h)^2\,. \tag{II.51}$$

Eq. (II.50) can be further simplified by contracting by a Minkowski metric

$$R_{\alpha\mu\nu\sigma} = \eta_{\alpha\rho} R^{\rho}_{\mu\nu\sigma} = (\partial_\nu \partial_\mu h_{\alpha\sigma} + \partial_\sigma \partial_\alpha h_{\mu\nu} - \partial_\nu \partial_\alpha h_{\sigma\mu} - \partial_\mu \partial_\sigma h_{\alpha\nu}) + \mathcal{O}(h)^2. \tag{II.52}$$

Then by contracting with the Minkowski metric once more to obtain the Ricci tensor, and then using $G_{\mu\nu} = R_{\mu\nu} - g_{\mu\nu}R$, with

$$R_{\mu\nu} = \eta^{\alpha\sigma} R_{\alpha\mu\nu\sigma} = \frac{1}{2}(\partial_\nu \partial_\mu h^{\alpha}_{\sigma} + \partial_\sigma \partial_\alpha h^{\mu}_{\nu} - \partial_\sigma \partial_\sigma h^{\nu}_{\alpha} - \partial_\mu \partial_\sigma h^{\alpha}_{\alpha}), \tag{II.53}$$

$$R = \eta^{\mu\nu} R_{\mu\nu} = \partial_\mu \partial_\nu h^{\mu\nu} - \partial_\alpha \partial_\alpha h^{\alpha}_{\alpha}. \tag{II.54}$$

The Einstein tensor becomes

$$G_{\mu\nu} = R_{\mu\nu} - \frac{1}{2}\eta_{\mu\nu} = \frac{1}{2}(\partial_\nu \partial_\mu h^{\alpha}_{\sigma} + \partial_\sigma \partial_\alpha h^{\mu}_{\nu} - \partial_\sigma \partial_\sigma h^{\nu}_{\alpha} - \partial_\mu \partial_\sigma h^{\alpha}_{\alpha}) - (\partial_\mu \partial_\nu h^{\mu\nu} - \partial_\alpha \partial_\alpha h^{\alpha}_{\alpha})\eta_{\mu\nu}. \tag{II.55}$$

From the Einstein tensor, one can simplify further by making use of the trace-reversed Minkowski metric $\bar{h}_{\mu\nu} = h_{\mu\nu} - (1/2)\eta_{\mu\nu}$ whose name is suitable due to its special property that $\bar{h} = -h$. We also adopt Lorentz gauge $\partial^\nu \bar{h}_{\mu\nu} = 0$ on the trace reversed Minkowski metric in which the Einstein equations take the following form

$$\Box \bar{h}_{\alpha\beta} = -\frac{16\pi G}{c^4} T_{\alpha\beta}\,. \tag{II.56}$$

In Eq. (II.56) the $\Box$ operator is nothing more than the d'alembert operator and hence in this gauge for the trace reversed metric perturbation the Einstein equations are nothing more than a set of decoupled wave equations.

II.3.1 Stochastic Gravitational-Wave Background (SGWB)

SGWBs are GW backgrounds that emerge due to the emission of a large set of independent sources of weak magnitude that is only resolved statistically. These GW backgrounds can be thought of as analogous GW backgrounds to the Cosmic Microwave Background and

their origin can either stem from supermassive BH binaries or also be cosmological. In the case where SGWBs stem from a cosmological origin, they can emerge from quantum fluctuations of the inflationary vacuum, cosmic string loops, annihilating DWs, FOPTs, and inhomogeneous field fluctuations generated during the process of reheating.
In the previous section, we displayed how GWs emerge from considering perturbations in a local region of space-time which was assumed to be flat. In this section, we will make use of the prescription shown previously while attributing to the conditions and dynamics of our universe in the context of SGWBs. As we believe that the universe obeys the cosmological principle, which states that on large scales i.e., $\sim$ 200Mpc or larger the universe is homogeneous and isotropic, hence it is natural to assume that an SGWB should obey the same assumptions. Furthermore, as SGWBs come from a large set of independent sources it becomes feasible to assume that such GW backgrounds are statistically Gaussian, however, some sources of SGWBs predict non-gaussian features.
GWs are a form of radiation, hence they are characterized by their fractional energy density Ω_{GW} per logarithmic frequency interval as

$$\Omega_{GW}(f) = \frac{1}{\rho_c}\frac{d\rho_{GW}(f)}{d\log f}\,, \tag{II.57}$$

where experimental limits are usually imposed on $h^2\Omega_{GW}$ and not on Ω_{GW} itself. For the formulation of the fractional energy density of GWs per logarithmic frequency, nothing has been imposed so far regarding at what length scales this formulation is valid. However, as the cosmological principle only remains valid on large scales it certainly does not hold up on short scales, where large inhomogeneities are present. This necessitates the inclusion of going beyond the FRLW metric and doing so by incorporating perturbations[6] to deviate from the FRLW solution.

By employing the same logic as in the previous section to deduce the Einstein equations order by order one finds that at zeroth order in the perturbations one recovers the first Friedmann equation. As in the previous section by only looking at the evolution of the perturbations up to linear order, the first-order equation in the perturbations is nothing else than their corresponding evolution equation. For the calculation machinery, the only difference is that in the metric and the perturbation, one needs to multiply with the scale factor $a(t)$ such that the metric and the perturbation are written out as

$$g_{\mu\nu} = a(t)^2(\eta_{\mu\nu} + h_{\mu\nu})\,. \tag{II.58}$$

As in the previous section, we assume that the magnitude of the perturbation is $|h_{\mu\nu}| << 1$ whereas its composition is in a general form i.e., it contains scalar, vector, and tensor components. In this section, we will primarily focus on the tensor components and we will elaborate further on the scalar components in Sec. (VII.2). To isolate the GWs which are the transverse-traceless components of the tensor components we only consider the spatial components and also impose the same conditions as in the previous section. Accounting for these aspects one obtains

$$h_{ij}^{''} + 2\frac{a'}{a}h_{ij}^{'} - \nabla^2 h_{ij} = \frac{2}{M_p^2}\delta T_{ij}\,, \tag{II.59}$$

where the energy-momentum tensor on the RHS is subject to the same restraints as the perturbations. Sources of SGWBs emerge from the anisotropic components of the stress energy tensor. Before elaborating on a specific source of anisotropic stress in the stress energy tensor we will first mention a few aspects about present and future GW experiments and how a detection is claimed.

[6] These perturbations are however assumed to be statistically homogeneous.

Experiments & Detection

So far in terms of GW experiments, we have mainly mentioned LIGO as it was the detector behind the first discovery of GWs. Here we intend to list various GW experiments both present and future ones. At present the community has two types of experiments taking data as we speak, firstly is the LVK collaboration looking for GW from binary mergers of BHs and neutron stars searching for GW in the frequency range of $f_{LVK} \sim 10{-}10^3$Hz. Secondly, we have PTAs which look for GWs from rotating neutron stars under the influence of a large magnetic field emitting electromagnetic waves that act like cosmic lighthouses. GWs from pulsars are detected by looking for correlated differences between the time of arrival of the EM wave emitted from the pulsar. The current PTA experiments taking data are NANOGrav, IPTA, Parkes Pulsar Timing Array (PPTA), European Pulsar Timing Array (EPTA) and soon, we will have Square Kilometer Array (SKA) as well. PTAs are searching for GWs in the frequency regime $f_{PTA} \sim 1 - 100\,\text{nHz}$ as the observation time of pulsars is of the order of years.
The SGWB sources we consider in this thesis, are not strong enough for potential detection by the LVK collaboration. In principle, the upcoming predecessor the Einstein Telescope [55] could potentially test some regions of parameter space in the frequency regime $f_{ET} \approx 10 - 10^3$Hz. Then one natural question is what about the frequency domain between LVK and PTAs, and also what about below PTAs and above LVK/Einstein Telescope?
Upcoming experiments in the form of space-based laser interferometry experiments will pave into the mHz regime $f_{LISA} \approx 10^{-2} - 10^{-4}\,\text{mHz}$ with the Laser Interferometer Space Antenna (LISA) which is intended to launch the mid-2030s. Other experiments in the frequency regime are TianQin also a space-based interferometer and AION/AEDGE an atomic interferometer utilizing the precision of atomic clocks which are both under construction. Future experiments that are at present on a more speculative level are μAres, Big Bang Observer and DECIGO which would not only close the gap between Interferometers and PTAs but also push the sensitivity by several orders of magnitude.
For an SGWB signal to be detectable in an experiment, the ratio between the signal and the background noise of the detector needs to be sufficiently large. The signal-to-noise ratio (SNR) is given by

$$SNR = \sqrt{\mathcal{T} \int_{f_{min}}^{f_{max}} \left(\frac{h^2 \Omega_{GW}(f)}{h^2 \Omega_{Sen}(f)} \right)^2 df}\,, \tag{II.60}$$

where $\mathcal{T}$ is the observational duration, (f_{min}, f_{max}) is the detectors frequency bandwidth, $h^2 = 0.678 \pm 0.009$ is the reduced Hubble scale today, and $\Omega_{sen}(f)$ is the detector noise. Typically the SNR needs to be at least $SNR \geq 10$ for a realistic chance of claiming detection. When considering an SGWB from a network of detectors like PTAs, one needs to modify Eq. (II.60) with an additional factor of 2, and also replace Ω_{Sen} with the effective noise of the network $\Omega_{eff,n}$.
However, it is impractical to use $h^2\Omega_{eff,n}$ from a representative perspective to have a clear interpretation if a GW signal is detectable or not. Instead one typically uses the so-called power law integrated (PLI) sensitivity curve as a means to provide a simple way of displaying SGWBs detection prospects. To construct the PLI sensitivity curves one assumes that the signal follows a power law like

$$h^2\Omega_{GW}(f) = h^2\Omega_\beta \left(\frac{f}{f_{ref}} \right)^\beta\,, \tag{II.61}$$

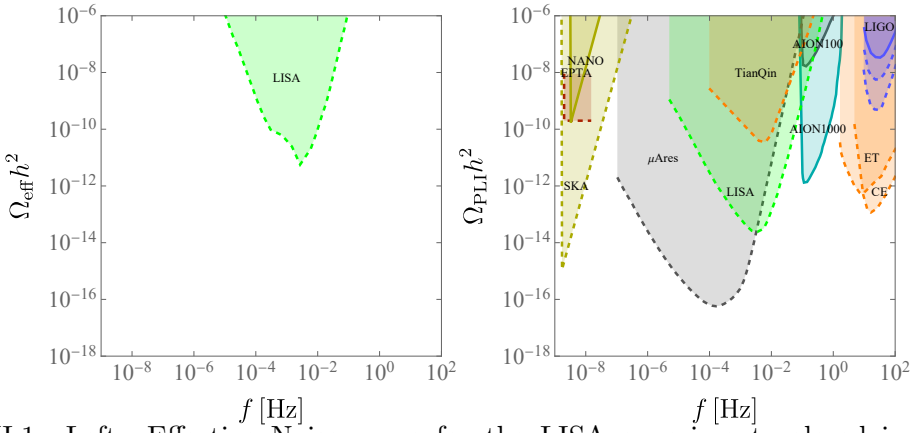

Figure II.1: Left: Effective Noise curve for the LISA experiment colored in green to illustrate the more preferred choice of PLI sensitivity curves. Right:PLI sensitivity curves for a range of experiments over a vast range of frequencies

where f_{ref} is a reference frequency of arbitrary value. Then by fixating the exponent β having a certain experiment in mind, one can invert Eq II.60 to obtain the minimal detectable amplitude $h^2\Omega_{thr}$ at which $SNR = SNR_{thr}$. Then to obtain the PLI sensitivity curve one gathers the envelope of the minimal detectable power law spectra for all values of the exponent β as

$$h^2\Omega_{PLI}(f) = max_\beta \left[h^2\Omega_\beta^{thr}(f) \left(\frac{f}{f_{ref}} \right) \right] . \tag{II.62}$$

A paragraph concerning the interpretation of PLI and figures showing the difference.
In Fig. (II.1) We have presented the projected sensitivities of the previously mentioned GW experiments for illustrative purposes to the reader. With the intent to display the convenience of using the PLI instead of the experimental noise curves by a direct comparison between the left and right figures in Fig. (II.1).
In the peak frequency range of $f_p \approx 10^0 - 10^2\,$Hz we display the projected sensitivity of the Cosmic Explorer (CE) [52], ET [55] and LIGO [53] with its intended updates. In the peak frequency range of $f_p \approx 10^{-1} - 10^{-3}\,$Hz we display the projected sensitivity of TianQin [56] LISA [57] and AION 100-1000 [58]. Finally in the peak frequency range of $f_p \approx 10^{-4} - 10^{-9}\,$Hz we display the projected sensitivity of the μAres [59], EPTA [60], SKA [61] and NANOGrav [62].
In recent years, intriguing evidence for an SGWB has emerged from PTA collaborations such as NANOGrav, EPTA, PPTA, among others, collectively finding evidence of an SGWB in the nHz regime. Previous measurements lacked conclusive evidence on the inter-pulsar correlations, but with the most recent data release, they are closer than ever to establishing a detection. In Chap. (V -VI), we will explore the possibility of interpreting this signal in terms of new physics sources. Furthermore, in Chap. (VII) we find a great deal of observational complementarity between CMB spectral distortions and GWs in the PTA regime.

II.3.2 SGWB from Cosmological First Order Phase Transitions

Phase Transitions (PTs) are ubiquitous in nature, occurring in substances like liquids and solids where their state changes with variations in environmental conditions such as temperature and pressure. A specific type of PT involves changes in the aggregation state

of a substance inhomogeneously under varying environmental conditions until the entire configuration transitions to the new state. A prime example is water, where the different aggregation states and properties are crucial for our existence. Another significant example is ferromagnetism, which underlies the functioning of everyday devices like magnets, engines, generators, and transformers.

To study the characteristic properties of PTs, researchers primarily examine the evolution of a system's free energy concerning an external variable, typically a field, and temperature. This external field, which contains information about the structure of the free energy concerning the field and temperature, is commonly known as the system's order parameter. The characterization of the nature of a PT has one study of how the free energy as a function of the order parameter and temperature evolves and if there are discontinuities in either the value of the free energy itself or in its derivatives w.r.t, the order parameter. The scenarios just mentioned concern if one has a FOPT or Higher-order ones depending on whether the discontinuity in the order parameter appears in the free energy itself or within its derivatives.

Scenarios such as the one just mentioned above also have great importance for the thermal history of the early universe where we have at least undergone two such PTs. The cooling of the SM plasma happens adiabatically, hence, the evolution of the temperature decrease is given by the energy content of the thermal plasma. The thermal plasma underwent at least two PT the electroweak PT, and confinement of QCD. In the SM of particle physics, both of these are believed to be cross-overs.

In this section, we envision the presence of a FOPT in the early universe, either by altering the existing PTs in the SM or that hidden sectors are undergoing such PTs within themselves. In Chap. (III) we will explore this phenomenon of confinement of a pYM theory making use of the AdS/CFT correpsondence.
Given the occurrence of a FOPT in the early universe, a period of bubble nucleation and collision would ensue until the entire universe transitions from the false vacuum to the true vacuum. The expansion and collision of these nucleated bubbles generate anisotropic stress in the energy-momentum tensor, serving as a direct source of GWs. There are three primary sources of GWs from an FOPT: firstly, the anisotropic stress arising from the collision of nucleated bubbles. Secondly, as these bubbles collide and expand, they generate another source of anisotropic stress in the form of sound waves within the thermal plasma due to the developement of pressure gradients during expansion. Finally, the dynamics and evolution of sound waves in the thermal plasma evolve into a non-linear regime, generating vortices and turbulence in the plasma.

The process of bubble nucleation and collision occur randomly in the universe the associated GWs are therefore of stochastic nature, isotropic, unpolarized, and Gaussian i.e., an SGWB. This section is structured as follows in Sec. (II.3.2.1) we will review the tunneling process and how bubble nucleation proceeds[7]. Then in Sec. (II.3.2.2) we will introduce the parameters that are needed to characterize the GW emission of an FOPT. Then in Sec. (II.3.2.3) we elaborate on the different sources of SGWB's from FOPTs and their semi-analytical spectral shapes.

[7]In this thesis we won't have an introductory section on the thermal effective potential since we will make use of holographic techniques presented in Sec. (II.4) and Part I for the construction and utility of the effective potential.

II.3.2.1 Cosmological First Order Phase Transitions & Bubble Nucleation

FOPTs proceed through the nucleation of bubbles of a true vacuum submerged in a universe filled with a false one. One starts in the initial high-T phase which is in the false vacuum phase and as the temperature drops a new vacuum emerges denoted the true vacuum. Eventually, it will become energetically favorable for the field to find itself in the true vacuum, and tunnel from random points in the universe. Nucleation of spherical bubbles takes place at these random sites whose interiors are regions with the true VEV. The amount of energy released in such a FOPT i.e., the latent heat, causes the bubble expansion. The bubble expansion persists as long as the pressure difference between the interior and exterior of the bubble surpasses its surface tension.
Because if this is not the case then the nucleated bubbles would just collapse. Since in principle if the nucleated bubbles were not much smaller than a Hubble horizon then the impact of the expansion of the universe could rip the bubble apart. If the bubble nucleation dynamics is such that one only nucleates a few bubbles per hubble volume, the expansion of the universe may become relevant. However, this turns out not to be the case as in most applicable cases the bubble radius compared to Hubble is typically separated by orders of magnitude. Therefore the effects from the expansion of the universe can in most cases be neglected[8].
The Euclidian action in $D = (3, 4)$ is given by

$$S_3 = \frac{4\pi}{T}\int_0^\infty r^2 dr \left(\frac{1}{2}\left(\frac{d\phi}{dr}\right)^2 + V_{eff}(\phi, T)\right), \tag{II.63}$$

$$S_4 = 2\pi^2 \int_0^\infty r^3 dr \left(\frac{1}{2}\left(\frac{d\phi}{dr}\right)^2 + V(\phi)\right), \tag{II.64}$$

where $V_{eff}(\phi, T)$ is the thermal effective potential, $V(\phi)$ is the vacuum potential, and the prefactors in front of the integrals are the solid angle contributions in $(3, 4)$ dimensions. From the Euclidian actions S_3, S_4 we obtain a set of equations of motion which are

$$V' = \begin{cases} \frac{d^2\phi}{dr^2} + \frac{3}{r}\frac{d\phi}{dr} & \text{For an } \mathcal{O}(4) \text{ Action}, \\ \frac{d^2\phi}{dr^2} + \frac{2}{r}\frac{d\phi}{dr} & \text{For an } \mathcal{O}(3) \text{ Action}, \end{cases} \tag{II.65}$$

where we are in the case of having canonically normalized action i.e., the prefactor in front of the kinetic term is $\frac{1}{2}$[9]. With the EoMs at hand, we need to elaborate on the appropriate set of boundary conditions one needs to impose to find the configurations of our interest i.e., solutions that interpolate between the false vacuum ϕ_{FV} and the true vacuum ϕ_{TV}. However, it is important to notice that we do not necessarily traverse exactly to the ϕ_{TV} but as long the field will find itself somewhere on the other side of the barrier separating the two vacua it is sufficient. With this in mind, a natural choice of a boundary condition is that at

$$\phi|_{r\to\pm\infty} = \phi_{FV}\,, \tag{II.66}$$

and since we do not necessarily need to tunnel directly to the true vacuum we can therefore impose a finite energy condition at the origin such that

$$\frac{d\phi}{dr}|_{r\to 0} = 0\,. \tag{II.67}$$

[8] In [63] a study has been employed to look into what happens when one incorporates geometric effects from GR through the evolution of a nucleated bubble in a FOPT.

[9] Where otherwise an additional term in the equations of motion appears if one cannot reformulate the euclidian action by either a field redefinition or variable substitution

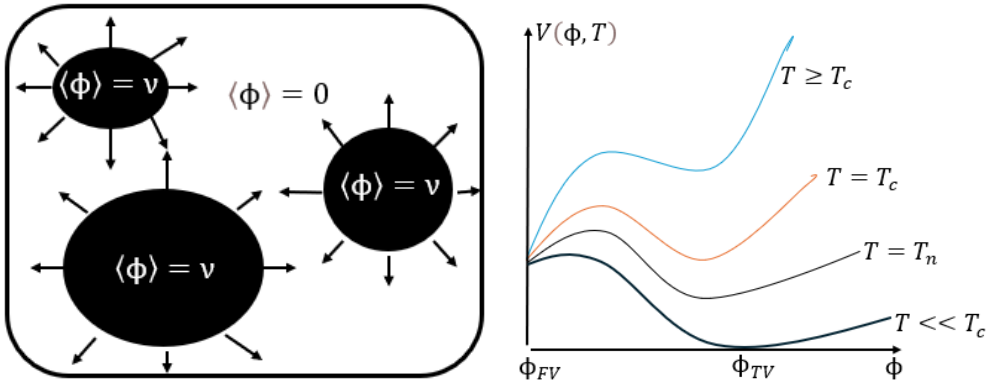

Figure II.2: Left: Illustration of the nucleation of bubbles of true vacuum $\langle\phi\rangle = \nu$ within the false vacuum $\langle\phi\rangle = 0$. Right: Illustration of the evolution of the thermal effective potential as the universe is initially trapped in the false vacuum ϕ_{FV}, and as the temperature decreases it tunnels to the true vacuum ϕ_{TV}.

These boundary conditions seem reasonable for a meta-stable state in the false vacuum and the solution one obtains by imposing these boundary conditions is called the bounce solutions. They are dubbed as the bounce solutions ϕ_b as they are $\mathcal{O}(d)$ field configurations where one starts and ends in the false vacuum but reaches the other side of the barrier with zero velocity [64, 65]. These are primarily the field configurations one aims to find for studies of bubble nucleation dynamics and are mainly the set of solutions one makes use of for studying FOPTs in the semiclassical picture.

Further on in this thesis, we will primarily be interested in $\mathcal{O}(3)$ bounce solutions, and if not stated explicitly from now on we will center our discussion around this case. In a FOPT there are in total three characteristic temperature scales of significant interest, these are the critical temperature T_c when the energy in the false and true vacuum is degenerate, the nucleation temperature T_n when the probability that one has nucleated about one bubble per horizon volume is of order unity, and the percolation temperature T_p when the universe is equally filled with regions of false vacua and true vacua i.e., the probability to find the field in either the false or true vacuum are the same. We will now elaborate further on the nucleation and percolation temperatures and how they are calculated. The nucleation temperature T_n can be naively estimated by comparing the bubble nucleation rate per unit volume with the Hubble rate

$$\Gamma(T) \sim H^4 \,. \tag{II.68}$$

Depending on the nature of the FOPT if it is due to thermal field fluctuations or quantum tunneling the bubble nucleation rate per unit volume is

$$\Gamma = \begin{cases} T^4 \left(\frac{S_3}{2\pi T}\right)^{\frac{3}{2}} e^{-\frac{S_3}{T}} & \text{for Thermal Fluctuations}\,, \\ R_0^{-4} \left(\frac{S_4}{2\pi}\right)^{\frac{3}{2}} e^{-S_4} & \text{Quantum tunneling}\,, \end{cases} \tag{II.69}$$

Where $S_{3,4}$ is the Euclidian d-dimensional action and R_0 is the radius of the nucleated bubble[10]. Considering the case of thermal nucleation $\Gamma \sim T^4 e^{-\frac{S_3}{T}}$, and a radiation-dominated universe one finds that the Euclidian $\mathcal{O}(3)$ action to fulfill nucleation is given

[10]Here we have omitted the contribution from the functional determinant in the formulations of the bubble nucleation rates.

by

$$\frac{S_3(T_n)}{T_n} \sim 146 - 4\log\left(\frac{T_n}{100\,\text{GeV}}\right) - 2\log\left(\frac{g_*(T_n)}{100}\right), \tag{II.70}$$

where g_* is the effective number of degrees of freedom active at temperature T_n normalized to 100. With the nucleation temperature at hand, one can progress further to the percolation temperature T_p i.e., the temperature when an order one fraction of the universe has transitioned to the true vacuum[11]. To calculate the percolation temperature we need to estimate the bubble size as a function of time/temperature in which we need the evolution of the bubble wall velocity v_w. The expression for the probability of being in the false vacua is given by

$$P(T) = e^{-I(T_p)}, \tag{II.71}$$

$$I(T_p) = \frac{4\pi}{3}\int_T^{T_c} \frac{dT'\Gamma(T')}{H(T')T'^4}\left(\int_T^{T'} dT'' \frac{v_w(T'')}{H(T'')}\right)^3, \tag{II.72}$$

where $P(T)$ denotes the probability of being in the false vacua at temperature T and $I(T)$ is the fraction of space-time in the true vacuum. For simplicity, we consider steady state bubbles in which $v_w \sim constant$ and one can pull out the velocity from the integral

$$I(T_p) = \frac{4v_w^3\pi}{3}\int_T^{T_c} \frac{dT'\Gamma(T')}{H(T')T'^4}\left(\int_T^{T'} dT'' \frac{1}{H(T'')}\right)^3. \tag{II.73}$$

A brief comment is in place of how $I(T)$ acquires its form. The input entities are first the bubble nucleation rate per unit volume, secondly, the universe expansion rate, and finally the term within an integral of an integral regards the nucleated bubble size as a function of temperature. Now that we have the nucleation of true vacuum bubbles underway and understand their evolution and governing equations to obtain the bubble profile, we are now ready to delve into the necessary parameters for estimating the amount of gravitational waves an FOPT may emit.

II.3.2.2 The PT Parameters

Remarkably, despite being a highly out-of-thermal equilibrium process, a FOPT can be characterized fairly well by only knowing four parameters. These parameters include the PT's strength, typically denoted as α, i.e., the latent heat, the bubble wall velocity v_w, the inverse PT duration β/H compared to the hubble rate, the kinetic energy fraction in the bubble walls $\kappa(\alpha)$, and the temperature at which the PT occurs or completes, denoted as $T_{n,p}$.

In this thesis, our main focus will be on the nucleation temperature T_n unless explicitly stated otherwise, and all functions of temperature T should be understood as being evaluated at $T = T_n$ The strength of a FOPT is characterized by the latent heat $\mathcal{E} = \Delta V_{eff} - T\frac{\partial \Delta V_{eff}}{\partial T}$ at the time of bubble nucleation

$$\alpha = \frac{\mathcal{E}}{\rho_{rad}}, \tag{II.74}$$

normalized to the energy density of the SM radiation bath content ρ_{rad}. The Δ indicates that one takes the difference in potential energy in the false/true vacuum at the time of

[11] We work with the convention that when P(T)=1/2 we have percolation whereas other works may use slightly different thresholds.

nucleation. The difference in latent heat hence the Δ in the effective potential between the energy values of $V_{eff}(\phi_{FV}, T_n), V_{eff}(\phi_{TV}, T_n)$ describes the height of the potential barrier between the vacua. This is the simplest parameter to get a hold of as it is evaluated directly from the effective potential and its derivative.
The parameter β/H describes the duration and the number of nucleated bubbles the phase transition generates, and is evaluated when the phase transition has completed, i.e. at the percolation temperature T_p. For a fast PT one can approximate $\Gamma \sim \exp[\beta(t - t_p)]$, and the inverse duration of the PT is given by

$$\frac{\beta}{H} = T \left(\frac{d\mathcal{S}_B}{dT} \right) \Bigg|_{T=T_p} . \tag{II.75}$$

For FOPTs at which the approximation above is not valid, one calculates $\beta/H \sim \dot{\Gamma}/\Gamma$ as the logarithmic derivative of the bubble nucleation rate w.r.t., temperature. Hence for FOPTs with tiny to no supercooling $\beta/H \geq 10^4$ indicating that the individual bubbles are small and hence they would not have had much time to expand before. This is the case relevant in this thesis for most of the time. This is also a parameter that is slightly more involved to get a hold of but provided one has an effective action and can solve for the tunneling rate this entity is within one's grasp. Up to now, we have discussed quantities that are evaluated in Thermal quasi/equilibrium, nevertheless the same is not true for the case of the bubble wall velocity which is entirely an out-of-equilibrium quantity.

Bubble wall velocity

The calculation of wall velocity v_w in cosmological phase transitions has received a lot of attention throughout the years. An estimate of v_w is typically obtained by computing the transmission coefficient of particles at the bubble wall [66–74], or assuming local thermal equilibrium LTE [75–77] to simplify the calculations[12]. It is implicitly assumed in the aforementioned techniques that the theories are weakly coupled and that perturbative approaches are valid. However in strongly coupled theories the problem becomes even more complicated and can be addressed using holography in certain models [79–84], and hydrodynamics to certain extents.
The bubble wall velocity is dominantly dependent on the latent heat released during the FOPT. Furthermore, it is also very sensitive to the environment i.e., if the FOPT takes place in a vacuum or if the field undergoing the FOPT couples to a thermal plasma for instance the SM thermal plasma. In vacuum transitions the bubble walls can easily reach luminal velocities and it is quite common to find $v_w \sim 1$ with increasing Lorentz boost factors γ_{v_w}. This is often referred to as a runaway regime in the literature. If however the FOPT takes place in the presence of a thermal plasma then it is crucial to determine the friction the plasma exerts on the bubble walls preventing them from accelerating arbitrarily. This scenario on the other hand is referred to as a non-runaway regime.

For a qualitative prediction of plasma friction, one typically examines the probability of particles being either reflected or transmitted from the bubble wall. It's important to consider whether the particles become massive as they pass through the bubble wall. Specifically, plasma particles become massive as they cross the bubble wall, experiencing a Lorentz boost in the direction along the wall. This process draws energy from the available energy budget of the bubble expansion. The effect mentioned above causes a bulk motion in the plasma, eventually evolving into density waves.

[12] Recently there has been work by [78] which seem to be in conflict of the applicability of the LTE approximation revealing that finding steady state bubble configurations seems potentially unlikely.

One can estimate the latent heat necessary in a FOPT for the bubble walls to reach a runaway regime. The leading order (LO) estimation goes as [66, 85]

$$\alpha_\infty = \frac{1}{\rho_{rad}} \left(\sum_b \frac{\Delta m_b^2 T_n^2}{24} + \sum_f \frac{\Delta m_f^2 T_n^2}{48} \right) , \tag{II.76}$$

which is evaluated at T_n, accounting for all bosons/fermion dof which acquire a mass passing through the wall. If the amount of latent heat in a FOPT exceeds α_∞, the bubble walls are thought to enter the runaway regime. However, recent studies [67] have shown that if the particles that gain mass across the wall are coupled to gauge bosons, Next-to-Leading-Order (NLO) effects from transition radiation of the particles crossing the wall generate a friction force proportional to γ_{v_w}. This renders the possibility of runaway bubbles in this case. This is just the tip of the iceberg when it comes to the complexity of calculating bubble wall velocities. Determining the bubble wall velocity accurately, especially in strongly coupled systems—which is a key focus of this thesis—is highly model-dependent and extremely challenging. Therefore, we recognize that it's beyond the scope of this thesis to provide a comprehensive treatment of this topic.

In this work, we will primarily adopt a phenomenological approach and treat v_w as a free parameter. However, in Part. (I) of this thesis, we will leverage on recent advancements in strongly coupled systems to at least offer an estimate of the wall velocity for a FOPT in an SU(N_c) pYM theory. For prospects related to an observable SGWB, a large bubble wall velocity is necessary. Conversely, in baryogenesis, conventionally, small wall velocities are required for non-equilibrium effects to fully manifest on both sides of the wall. However, recent work [86, 87] has demonstrated that this conventional wisdom may not always hold, and fast bubble walls can sometimes be achieved.

II.3.2.3 The Stochastic Gravitational Wave Spectrum from FOPTs

Around 40 years ago, Witten and Haber [88, 89] were the first to recognize the possibility that GWs could be emitted from a FOPT. Subsequently, it became apparent that during an FOPT, there are not just one, but three potential sources of GWs. These sources include bubble collisions, sound waves in the plasma, and the formation of turbulence due to long-lasting sound waves. The total SGWB from a FOPT is therefore given as

$$h^2\Omega_{GW}(f) = h^2\Omega_\phi(f) + h^2\Omega_{sound}(f) + h^2\Omega_{turb}(f) , \tag{II.77}$$

where Ω_ϕ is the bubble collision contribution, Ω_{sound} the sound wave contribution, and finally Ω_{turb} is for turbulence. Typically the GW spectrum is dominated by the contribution of an individual source, with the dominant contribution depending on the latent heat α, the bubble wall velocity v_w, and the inverse transition rate β/H.
The frequency and the amplitudes of the GW spectra today are related to their corresponding values at the time of production (subscript "*") [90] as

$$f = H_{*,0}\frac{f_*}{H_*} , \qquad h^2\Omega = h^2 F_{GW,0}\Omega_* , \tag{II.78}$$

where $H_{*,0}$ is the Hubble value at the time of production redshifted until today

$$H_{*,0} = H_*\frac{a_*}{a_0} \simeq 1.65\times 10^{-5}\text{Hz}\left(\frac{\text{g}_*}{100}\right)^{\frac{1}{6}}\left(\frac{\text{T}_*}{100\,\text{GeV}}\right) , \tag{II.79}$$

Contribution	Ω_ϕ	Ω_{sound}	Ω_{turb}
Ω	$8.2 \cdot 10^{-7}$	$1.7 \cdot 10^{-6}$	$41 \cdot 10^{-6}$
f_p	$0.11 H_{*,0}(H_*R_*)^{-1}$,	$0.2 H_{*,0}(H_*R_*)^{-1}$	$0.5\Delta_\xi^{-1}(H_*R_*)^{-1}$, $1.4 H_{0,*}(H_*R_*)^{-1}$	$2.2 H_{0,*}(H_*R_*)^{-1}$
κ	$1-\frac{\alpha}{\alpha_\infty}$	$\frac{\alpha}{0.73+0.083\sqrt{\alpha}+\alpha}$	$0.1\kappa_{sound}$
a	2	2	$\frac{3}{2}$
b	2	1	2
$W(v_w)$	~ 1	$max(v_w, c_s)$	$max(v_w, c_s)$
$\mathcal{S}(f)$	$\left(\frac{f}{f_p}\right)^{2.4}\left[\frac{1}{2}+\left(\frac{f}{f_p}\right)^{1.2}\right]^{3.6}$,	$\left(\frac{f}{f_1}\right)^3\left[1+\left(\frac{f}{f_1}\right)^2\right]^{-1}\left[1+\left(\frac{f}{f_2}\right)^4\right]^{-1}$,	$\left(\frac{f}{f_1}\right)^3\left[1+\left(\frac{f}{f_1}\right)^4\right]^{-\frac{1}{2}}\left[1+\left(\frac{f}{f_2}\right)^{2.15}\right]^{\frac{1.33}{2.15}}$
Duration	-	$min\left((H_*R_*/\sqrt{v_f^2}), 1\right)$	-
Reference	[90]	[90]	[90]

Table II.2: GW spectra parameters to be inserted into Eq II.77 for the three different contributions taken from the work of [90]. Have in mind that β is related to the mean bubble separation radius R_* as $R(T_*) = \frac{(8\pi)^{\frac{1}{3}}}{\beta}\max(c_s, v_w)$. Also to emphasize that each contribution will be discussed separatly in the paragraphs below. The validity of the simulation of sound-waves still remains debatable for $\alpha \gtrsim 0.1$. The GW contribution from bubble walls is considered the dominant contribution if $\alpha \gtrsim \alpha_\infty$. We also incorporate the suppression factor in the sound wave contribution and name the feature duration, hence not valid for bubble collisions.

$F_{GW,0}$ is the redshift factor for the fractional energy density

$$F_{GW,0} = \left(\frac{a_*}{a_0}\right)^4\left(\frac{H_*}{H_0}\right)^2 \simeq 1.64\times 10^{-5}\left(\frac{100}{g_*}\right)^{\frac{1}{3}}, \tag{II.80}$$

and g_* is the relativistic dof at the time of GW production.
Analytic calculations are not feasible, and one needs simulations for predictions of the GW spectra. Even simulations are a struggle due to the large separation of scales in the problem, rendering incomplete simulations of the full evolution of the system. Hence the exact GW spectra from FOPTs are not known. For the forthcoming discussions on the individual contributions to the GW spectra, the reader should be aware that it is a rapidly growing field, and what is overviewed here is a part of the state-of-the-art research on the topic. Whereas in the publications [5–7] the GW spectra templates used were the ones in [91, 92]. The GW spectra for the individual contributions in terms of the parameters presented in the previous Sec. (II.3.2.2) can be parametrized as

$$h^2\Omega_i(f) = \Omega\left(\frac{100}{g(T_n)}\right)^{\frac{1}{3}}\left(\frac{\kappa\alpha}{1+\alpha}\right)^a\left(\frac{H}{\beta}\right)^b\mathcal{W}(v_W)\mathcal{S}(f)\,. \tag{II.81}$$

Provided the naive parametrization above a few comments are in place for each respective contribution where we start the discussion with bubble collisions. In all these contributions to the GW spectra, the community has only been able to examine weakly coupled theories. It's important to keep this limitation in mind when considering the level of applicability to strongly coupled theories since many of these findings here may be different.

Bubble collisions

From the first column in Tab. (II.2) in the GW spectra from bubble collisions one shall be aware of the following aspects

- In these FOPTs the fraction of energy that goes into accelerating the bubbles is essentially all the available energy disposed of during the FOPT. The vacuum energy of the scalar field is dominant compared to the energy density of the radiation bath, i.e., $\alpha >> 1$.
- In FOPTs dominated by bubble collisions it is likely to expect superluminal velocities as they can potentially enter runaway regimes, hence a common assumption in these cases is the $v_w \sim 1$.
- The spectral shape for bubble collisions has a simple broken power law shape.
- The current discussion primarily focuses on a scenario where the vacuum energy predominantly drives the scalar field, which couples weakly to the plasma and its dynamics. This scenario has been analyzed using the envelope approximation in conjunction with the thin wall approximation, thereby neglecting the collided parts of the walls. Recently it has been found that the collided bubble parts cannot be neglected, this has to be since these shells cannot lose all their momenta instantaneously.
- Supercooled FOPTs can also proceed by primarily transferring vacuum energy into highly relativistic fluid shells. In these cases, particle splitting plays an important role. Naively one would expect the SGWB from such a case to be very different from sound waves as these fluid shells tend to accumulate very close to the wall. Recently in [92] they simulated highly relativistic fluid shells and estimated the SGWB from them, to find that their spectra resemble the one from bubble collisions in which a gauge symmetry is broken. This can then justify the reasoning of modeling both these GW contributions of bubble walls equally.

Sound Waves

Here, one considers a scenario where the coupling between the bubble walls and the surrounding plasma is significantly strong, facilitating the transfer of latent heat into bulk motion of the plasma. Upon bubble collision, compression waves arise, serving as the source of gravitational waves in this context. These compression waves propagate in the plasma at the speed of sound and depending on what velocity the bubble wall obtains one usually makes three distinctions, First if $v_w < c_s$ then a shock wave is built up ahead of the bubble wall ("deflagration"), whereas if $v_w > c_s$ then the compression waves partially or entirely travels behind the bubble wall ("Hybrid", "Detonation"). Numerical simulations, particularly those employing the sound shell model, support this explanation. For sound waves, the following aspects should be emphasized.

- The SGWB originating from sound waves exhibits a characteristic double-broken power law (DBPL), which contains details regarding the thickness of the fluid shells and the bubble size. The pivot frequencies for this SGWB, being described by a DBPL, are determined by power of β/H. Additionally, the second pivot frequency contains information about the thickness of the sound shell, denoted as $\delta_\xi = \xi_{\text{shell}}/\max(v_w, c_s)$, where ξ_{shell} represents the dimensionless sound shell thickness.
- The thickness of the sound shell $\xi_{shell} = \xi_{front} - \xi_{rear} = |\xi_{wall} - c_s|$ is calculated from the profile of an expanding bubble, where the last equality holds for subsonic deflagrations or detonations.
- The sound wave contribution of the SGWB spectra is typically a long-lasting source and if present as a contribution it tends to be the dominant one. The duration of the GW contribution is either set by its decay time into turbulence $H_* \tau_{sound} =$

$min[(H_* R_*/v_f^2), 1]$, or to the Hubble time if the onset of turbulence happens very slowly. So for short-lasting sound waves, one needs to multiply Eq. (II.81) with the suppression factor due to the short duration of the sound waves being present.

Turbulence

Due to the bulk fluid motion resulting from bubble expansion, not only are sound waves generated, but there are also contributions from vortical motion in the plasma and eddy currents. These arise when the sound waves enter a nonlinear dynamical regime. The presence of vortical motion and eddy currents in the plasma serves as sources of gravitational waves through magnetohydrodynamical turbulence (MHD), where the gravitational waves are directly sourced through the combination of the anisotropic stresses from the velocity and magnetic fields. This contribution is often considered negligible if the duration of the sound-wave source is long-lasting, accounting for only around 10% of the energy budget compared to the kinetic energy in the sound-wave contribution. In this thesis, we will mainly consider sound waves and hence omit further discussion about turbulence.

II.4 Introduction to AdS/CFT

The Anti de-Sitter/Conformal Field Theory (AdS/CFT) correspondence, as formulated by Maldacena in 1997 [93], represents the first realization of the holographic principle conjectured by 't Hooft [94] and Susskind [95]. This principle posits:

> "A theory of quantum gravity in a manifold $\mathcal{M}$ is equivalent to a nongravitational field theory living on the corresponding boundary $\partial\mathcal{M}$."

The key insight of this conjecture is that the entropy of a black hole scales with its surface area (known as the Bekenstein-Hawking entropy) rather than its volume. With this insight in mind, 't Hooft conjectured that the nature of gravity might be holographic, suggesting that non-gravitational field theories could be described on the boundary of a theory of quantum gravity existing in the interior. Maldacena provided the first explicit realization of this principle by establishing an exact correspondence in string theory. The correspondence he discovered is between closed strings in Type IIB string theory on $AdS_5 \times S_5$ and open strings describing $\mathcal{N} = 4$ Supersymmetric Yang-Mills theory. This correspondence is now recognized as the AdS/CFT correspondence. Subsequently, Witten [96,97] and Gubser [98] embraced this correspondence and established an exact relationship between the partition functions and fundamental observables of these theories. Further developments in the correspondence and its applications extend to cases where both supersymmetry and conformal invariance are absent.

In this thesis, we are particularly interested in such scenarios to describe non-supersymmetric Yang-Mills theories at finite and large N_c. We aim to employ these constructions to model QCD-like theories and their confinement phase transitions to search for such sectors using gravitational waves. In Chap. (III), we will explore how such holographic constructions are available and closely resemble SU(N_c) pYM theory. Before this, we will provide a brief introduction to the essential ingredients of the correspondence, and proceed by introducing Maldacenas conjecture. Furthermore, we will also elaborate on the continuation of the conjecture regarding the field/operator correspondence and how one identifies quantities in the bulk theory as entities in the field theory. Finally we will also elaborate briefly on the gravitational interpretation of considering CFTs at finite temperature.

II.4.1 Fundamentals in Gauge/Gravity Duality

In order to sketch Maldacenas conjecture and its great ramifications we first need to introduce some of the constituent building blocks to the correspondence. This is the intent here where we will introduce some insights from string theory like D-branes, and their corresponding energy limit.

Unlike a QFT where elementary particles are pointlike, in string theory the elementary particles are instead one-dimensional objects i.e. strings generating a 2-D worldsheet as strings propagate in space-time. Strings are primarily governed by two intrinsic parameters which are their tension, and their interaction strength

$$T = \frac{1}{2\pi\alpha^{'}}\,, \qquad \alpha^{'} = \ell_s^2\,, \qquad g_s = e^{\phi_\infty}\,, \tag{II.82}$$

where T is the string tension, ℓ_s is the string length, and g_s is the coupling constant given as the asymptotic value of the spin-zero scalar field in the theory. Analogous to the case of the action of a point-particle the action is proportional to its length i.e., trajectory, instead for a string the action becomes proportional to the worldsheet area spanned by the string propagating in space-time. The action for a string moving in the worldsheet therefore takes the form

$$S = -T\int_\Sigma d^2\tilde{\sigma}\sqrt{-g_{MN}\partial_\alpha X^M \partial_\beta X^N}\,, \tag{II.83}$$

where $\tilde{\sigma} = (\sigma_1, \sigma_2) = (\sigma, \tau)$ are the worldsheet coordinates, Σ denotes the worldsheet area, and g_{MN} is the metric on the (d+1) dimensional spacetime[13].
As bosonic string theory only has two different topologies for the strings which are either open or closed one needs to elaborate further on the impact of the topologies of the strings. For the case of open strings, one needs to impose boundary conditions on their endpoints which are either of Dirichlet or Neumann form. One can also have objects denoted as D-branes at which open strings can also end but we will get to their importance later on and their puzzle piece to the correspondence. For the case of closed strings, there is no need to impose boundary conditions and one can essentially go ahead and quantize that theory. In doing so one finds within the spectrum a massless spin-two field which can be identified as the graviton. Therefore closed strings in bosonic string theory is considered to be a theory of gravity. Meanwhile for open strings to end with either Dirichlet or Neumann boundary conditions one introduce a new set of dynamical objects which are called D-branes or Dp-branes where the D stands for Dirichlet, and the p denotes the number of spacetime dimensions the endpoints live on.
The naive purpose of D-branes is to possess an object at which boundary conditions on open strings can be imposed properly. When quantizing bosonic string theory one finds a uniquely remarkable feature that the spacetime dimension of the theory needs to be $D = 26$. This is called the critical dimension of the theory and it can be found in two ways. First by looking at the string spectrum provided one has quantized the theory and by requirment to not have any non-physical states the dimension necessarily needs to be $D = d+1 = 26$. Secondly by considering a scale transformation[14] on the worldsheet where

[13]The action displayed above has a clear physical interpretation however it suffers the drawback that it is harder to quantize an action of such a formulation, this can be resorted by instead considering the polyakov action. The aforementioned comment will not have any impact on our discussion here as we will primarily be interested in the low energy limit and the classical regime of string theory.

[14]Scale transformation refers to metrics which are conformal i.e., $g_{\mu\nu}(x) \to g^{'}_{\mu\nu}(x^{'}) = \Omega(x) g_{\mu\nu}$, where $\Omega(x)$ is the scaling transformation.

one finds that the trace of the energy-momentum tensor behaves as

$$T^{\mu}_{\mu} \propto (D-26)R\,, \tag{II.84}$$

where R is the Ricci scalar, and to cancel the trace anomaly $D = 26$ is required.
So far we have only mentioned bosonic string theory which is insufficient to fully describe nature as we also have fermions. In string theory, the inclusion of fermions is made by making use of supersymmetry (SUSY) and one finds that the critical dimension gets reduced from 26 to 10. For our purposes of illustrating the basics of AdS/CFT conjecture, it is sufficient to consider the low energy limit of type IIB string theory which is 10d supergravity (SUGRA). The SUGRA action is

$$\mathcal{S}_{SUGRA} = \frac{1}{16\pi G_{10}} \int d^{10}x\sqrt{-g}\left(R - \partial_\mu\phi\partial^\mu\phi - \frac{1}{2}\frac{1}{5!}F_5 + \dots\right)\,, \tag{II.85}$$

where R is the Ricci scalar, ϕ is the dilaton, F_5 is the field strength of the 4-form field C_4 and the dots represent the fermionic fields and other so-called Ramond-Ramond forms which for our purposes are irrelevant. The 10-d gravitational constant G_{10} can be related to the string length ℓ_s and the coupling constant g_s[15] as

$$16\pi G_{10} = (2\pi)^7 g_s^2 \ell_s^8\,. \tag{II.86}$$

With this very brief introduction of some of the fundamental concepts, and objects in bosonic string theory we are now ready to start elaborating on Maldacenas conjecture.

II.4.1.1 Maldacena Conjecture

The conjecture proposed by Maldacena as the first explicit realization of the holographic principle ancres around the different interpretations of D3-branes in type IIB string theory. Where in the case of the closed string theory in the low energy limit the D3-branes are solutions to the SUGRA action. Meanwhile for the open string theory case the presence of a stack of D3-branes form a non-abelian gauge theory. A crucial point in type IIB string theory key is that the strength of gauge interactions and gravitational interactions in these constructions are different. This allows for the possibility of evaluating one realm of interactions meanwhile the other one remains small.
As it was mentioned in the previous section that closed strings describe theories of gravity, open strings hence describe gauge interactions. To disentangle the type of interactions of interest a typical procedure is to consider a low energy limit. For instance the low energy limit of the open string sector of the theory reduces to a gauge field theory. In other string theories this is not necessary the case as for instance in Heterotic String theory. Here we will elaborate on each string sector separately to then bring maldacenas argument together with its constituents.

Closed Strings

One can show that a set of Dp-branes can be identified as black p-brane solutions in SUGRA which Polchinski did in [99]. Black p-branes are a kind of higher dimensional generalizations of black hole solutions in GR. One can find the D3-brane solution with an appropriate metric ansatz in which its solution to the SUGRA action Eq. (II.85) is found, by imposing self-duality for the field strength $F_5 = *F_5$. See [100] for a concrete derivation, however it is more useful to consider the stack of D3 branes simultaneously,

instead of looking at the solution for a single D3 brane. The metric for the stack of D3-branes with the dilaton can be shown to take the following form

$$ds^2 = H(r)^{-\frac{1}{2}}\left(-dt^2 + d\bar{x}^2\right) + H(r)^{\frac{1}{2}}\left(dr^2 + r^2 d\Omega_5^2\right)\,, \tag{II.87}$$

where

$$H(r) = 1 + \frac{\mathcal{L}^4}{r^4}\,, \tag{II.88}$$

in the case where one considers $p = 3$ i.e., D3 branes. Here the geometric warp factor is related to the dilaton as

$$e^{\phi} = 1\,. \tag{II.89}$$

Furthermore the AdS curvature length scale $\mathcal{L}$ is given by

$$\mathcal{L}^4 = 4\pi g_s N \ell_s^4\,, \tag{II.90}$$

where g_s is the string coupling, N is the number of coincident D3 branes, and ℓ_s is the string scale. Considering the two limits off r, when $r \to \infty$ one retrieves 10-d flat Minkowski space as $H \to 1$, whereas in the limit $r \to 0$ where $H \to \frac{\mathcal{L}^4}{r^4}$ the metric for a coincident stack of D3 branes reduces to

$$ds^2 = \frac{r^2}{\mathcal{L}^2}\eta_{\mu\nu}dx^\mu dx^\nu + \frac{\mathcal{L}^2}{r^2}dr^2 + \mathcal{L}^2 d\Omega_5^2\,. \tag{II.91}$$

By imposing the coordinate transformation $r^2 = \mathcal{L}^2/z$ one obtains

$$ds^2 = \frac{\mathcal{L}^2}{z^2}\left(dt^2 + d\bar{x}^2 + dz^2\right) + \mathcal{L}^2 d\Omega_5^2\,, \tag{II.92}$$

where the first part of the metric is pure AdS_5 and the second part is a five sphere of radius $\mathcal{L}$. Hence the metric for a stack of D3 branes has reduced into the topological product of AdS_5 and an $\mathcal{S}_5$ sphere

$$AdS_5 \times \mathcal{S}_5\,. \tag{II.93}$$

This decoupling of closed strings is illustrated in Fig. (II.3) for the decoupling of Type IIB string theory in the background geometry of a stack of D3-branes into Type IIB String

[15]The string coupling constant is not a free parameter but it is set as the asymptotic expectation value of the dilaton.

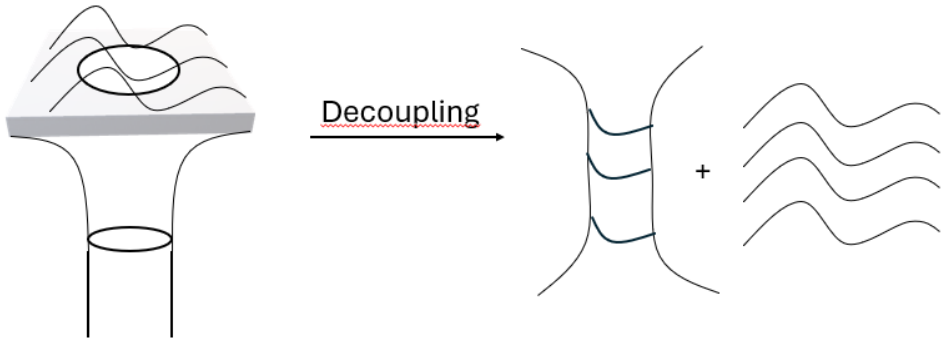

Figure II.3: Left: Type IIB string theory on the background geometry of the stack of D3 branes where the throat depicts the geometry. Right: In the low energy limit one retrieves Type IIB string theory on $AdS_5 \times \mathcal{S}_5$ which is decoupled from 10d SUGRA modes.

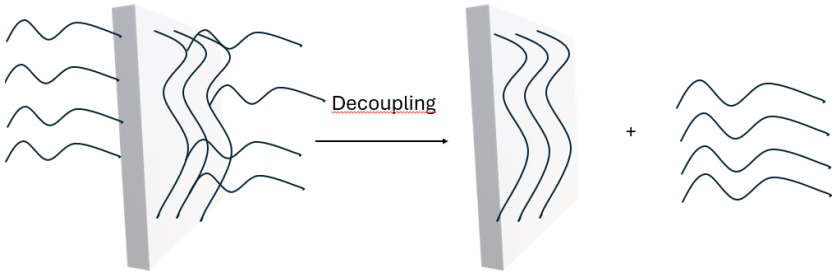

Figure II.4: Left: Stack of D3-branes pictured by the squared block with open strings attaching the D3-branes, along with open string which attach the D3 branes at both ends. Right: In the low energy limit i.e., decoupling of the open strings on the stack of D3-branes one obtains $\mathcal{N} = 4$ SUSY YM which is decoupled from 10d SUGRA modes.

theory on $AdS_5 \times \mathcal{S}_5$ with decoupled 10d massive SUGRA modes. It is important to remember that SUGRA is a valid approximation of Type IIB string theory in the low energy limit provided string and quantum effects can be neglected. String effects are negligible if the string scale is small in comparison to the AdS length $\mathcal{L}$ whereas quantum effects can be omitted if the 10-D gravitational constant is considered small compared to the AdS length $\mathcal{L}$. These limits are formulated as follows

$$\ell_s << \mathcal{L}\,, \qquad \frac{G_{10}}{\mathcal{L}^8} << 1\,. \tag{II.94}$$

From the perspective of the bakground SUGRA solutions, the gauge theory is present in the original metric before concerning with the $r \to 0$ limit. Hence in our new $AdS_5 \times \mathcal{S}_5$ geometry the gauge theory will "live" in the limit $r \to \infty$ or $z \to 0$, which corresponds to nothing else than Minkowski space. This can be shown by analyzing pure AdS space in this limit where it becomes global AdS and in Poincare coordinates this corresponds to Minkowski space. So the gravitational theory is within AdS_5 whereas the gauge theory is on the boundary of AdS_5 which is Minkowski space.

Open Strings

Here the D-3 branes are perceived as 4-D hypersurfaces at which open strings can end with Dirichlet boundary conditions [100]. The associated action for the open strings can be written terms of its separate contributions as

$$\mathcal{S} = \mathcal{S}_{brane} + \mathcal{S}_{bulk} + \mathcal{S}_{int} \tag{II.95}$$

where $\mathcal{S}_{brane}$ is the 4d action on the brane, $\mathcal{S}_{bulk}$ is the action in the bulk space-time, and $\mathcal{S}_{int}$ describes the interactions amongst the brane with the bulk. Surprisingly the bulk action $\mathcal{S}_{bulk}$ is the corresponding SUGRA action with massive string modes. In the low energy limit i.e., $\alpha' \to 0$ we may only consider terms linear in α', hence omitting the interaction term $\mathcal{S}_{int}$ as it scales like α'^2. Furthermore one also finds that the massive string modes drop out at which the bulk theory becomes free SUGRA. This is illustrated in Fig. (II.4) for the decoupling of open strings on the stack of D3-branes. We find that by considering a stack of N coincident D-3 branes in a low energy limit, the theory of the brane is described by the lagrangian

$$\mathcal{L} = \frac{1}{4\pi g_s} Tr\left(\frac{1}{4}\mathcal{G}_{\mu\nu}\mathcal{G}^{\mu\nu} + \frac{1}{2}D_\mu\phi^i D^\nu\phi^i + [\phi^i, \phi^j]^2\right)\,. \tag{II.96}$$

Provided the lagrangian presented just above one may realize that this lagrangian is nothing else than the lagrangian for $\mathcal{N} = 4$ SYM with the symmetry group $SU(N_c)$, and coupling constant $g_s = 4\pi g_{YM}^2$. An interesting fact is that one can make the identification between the number of D3-branes and the number of colors in the symmetry group of SYM

$$N = N_c \,. \tag{II.97}$$

Conjecture & t'Hooft Limit

Maldacenas conjecture is the exact equivalence between

$$\mathcal{N} = 4, \text{SUSY SU}(N_c) \text{ YM } = \text{ IIB String theory on } AdS_5 \times S_5 \,. \tag{II.98}$$

From the previous subsections we have seen that for N coincident D-3 branes in the closed string perspective are described by IIB string theory on $AdS_5 \times \mathcal{S}_5$, whereas in the open string perspective they are equivalent to $\mathcal{N} = 4$ SYM with $SU(N_c)$ gauge symmetry. With this conjecture at hand, it becomes very useful to relate the parameters between the different theories.
On the LHS of the conjecture, we have the gauge theory, that is primarily determined by the number of colors N_c, it's t'hooft coupling, and its gauge coupling g_s. Whereas on the RHS of the conjecture in the low energy limit we have classical SUGRA on $AdS_5 \times S_5$. The intrinsic parameters of the theory are the string length ℓ_s, the 10-d gravitational constant G_{10}, and the size of the AdS space $\mathcal{L}$. The parameters of the theories are related to each other in the following ways, first, the string coupling constant is related to the gauge coupling of SYM like

$$g_s = \frac{g_{YM}^2}{4\pi} \,, \tag{II.99}$$

whereas the t'Hooft coupling is related to the fraction of sizes between the string scale and AdS

$$\left(\frac{\mathcal{L}}{\ell_s}\right)^4 = g_{YM}^2 N_c = \lambda_t \,. \tag{II.100}$$

From this limiting case one may ask what can one learn from it? Lets first consider the case when the field theory is weakly coupled i.e., small values of the t'Hooft coupling which implies that the curvature radius $\mathcal{L}$ needs to be much smaller than the string scale. The conclusion from this is that the gravitational side of the correspondence strongly curved in the regime when the field theory is weakly coupled. Whereas in the limit where the gravitational theory is weakly curved one realizes that this means on the field theory side that it is strongly coupled.
A few remarks are in place, first of that the conjecture is claimed to be true for all couplings however, we understand neither gravity or gauge theories at arbitrary large couplings. However we have elaborated that classical SUGRA is a good approximation to type IIB string theory in the low energy limit, where we also elaborated on what regime in the parameters of SUGRA this persists. Then one can immediately ask what regime of parameter space does this correspond to in the gauge theory

$$\left(\frac{\mathcal{L}}{\ell_s}\right)^4 = g_{YM}^2 N_c = \lambda_t \,, \qquad \frac{G_{10}}{\mathcal{L}^8} \propto N_c^2 \,. \tag{II.101}$$

The second relation comes from the realization of two facts, first that the 10-d gravitational constant is proportional to the string coupling constant g_s. This in turn one can relate

to the t'Hooft coupling and directly to the number of colors in the gauge group. This imposes the following limits

$$N_c \to \infty\,, \qquad \lambda_t >> 1\,, \tag{II.102}$$

which is the t'Hooft limit of $\mathcal{N}=4$ SYM in the strong coupling regime. This result is of utmost importance as it states that one can understand a strongly coupled gauge theory in the large N_c limit using a classical gravitational theory in one dimension higher and in particular for this case using classical SUGRA. One can conclude that the AdS/CFT correspondence is a strong/weak duality. The possible exploration into strongly coupled Non-Abelian gauge theories with the aid of the AdS/CFT correspondence has been one of the biggest theoretical triumphs of the present generation in theoretical physics.
One crucial advancement facilitated by the correspondence has been the ability to describe gauge theories that are not conformal. Initially, this was accomplished by considering small perturbations of $\mathcal{N}=4$ supersymmetric Yang-Mills theory in the ultraviolet (UV), which then evolves into interacting non-conformal field theories (CFTs) in the infrared (IR). In certain cases, these interacting non-CFTs exhibited behavior reminiscent of confinement. In the gravitational dual theory, the solutions are asymptotically AdS near the UV boundary and are deformed within the bulk. For example, in cases of confinement-like behavior in the gauge theory, this is associated with bulk deformation caused by the presence of a black hole in the interior of the five-dimensional (5D) space.
Since QCD is neither an actual CFT nor is it supersymmetric a huge amount of research has been put into the question of whether the ADS/CFT correspondence can aid our understanding of QCD and theories that closely resemble it.

II.4.1.2 Field/Operator Correspondence & Holographic Dictionary

The intent of this section is to overview how to relate observables between the gauge theory and the gravitational theory [101, 102]. This great achievement of utilizing Maldacenas conjecture was done by the works of Witten and Gubser [96, 98] . We will formulate this here as a holographic dictionary, which is of utmost necessity provided that we want to understand how quantities in the field theory to their gravitationally equivalent theory. To start things off we state the famous W-GKP (Witten- (Gubser, Klebanov, Polyakov))[16] relation

$$\mathcal{Z}_{\mathcal{O}}[\phi_0]_{\mathcal{N}=4} = \mathcal{Z}_{\phi}[\phi_0]_{IIB}\,, \tag{II.103}$$

which states the equivalence between the partition functions of the two theories[17]. Where the boundary operator $\mathcal{O}$s are related to the partition function of Type IIB string theory for the field ϕ evaluated at its UV boundary ϕ_0. The field value in the bulk theory at the UV boundary ϕ_0 in the string theory corresponds to the source of the operator $\mathcal{O}$ in the $\mathcal{N}=4$ SUSY YM theory. To concretize our discussion we will concern ourself with the t'hooft limit of the gauge theory and hence in the gravitational theory omit string/quantum corrections. On the LHS of Eq. (II.103) we have the partition function of $\mathcal{N}=4$ SUSY YM, which we can formulate as

$$\mathcal{Z}_{\mathcal{N}=4} = \int \mathcal{D}[\dots]\exp\left[-\mathcal{S}_{\mathcal{N}=4} + \int d^4x \mathcal{O}(x)\phi_0(x)\right], \tag{II.104}$$

[16] The formulation of W-GKP presented above is the most powerful formulation as it states an exact equivalence between the partition functions of a CFT in D dimensions living on the boundary of D+1 AdS space. Here we will discuss it in its somewhat less powerful formulation for convenience.
[17] This equivalence was performed in Euclidian space

where $\mathcal{D}[\dots]$ is a functional integration over all the SUSY YM fields, and $\mathcal{S}_{\mathcal{N}=4}$ is the SUSY YM action. We will formulate the partition function of SUSY YM as follows

$$\mathcal{Z}_{\mathcal{N}=4} = \left\langle \int d^4x \mathcal{O}(x)\phi_0(x) \right\rangle \tag{II.105}$$

where $\langle \dots \rangle$ is to be understood that an intergration over all SUSY YM fields have been made. On the RHS of Eq. (II.103) we can in the absence of string or quantum effects employ the fact that Type IIB string theory simplifies to classical SUGRA and reformulate the partition function as

$$\mathcal{Z}_{\phi}[\phi_0]_{IIB} = e^{-\mathcal{S}_{SUGRA}(\phi_0)} \,. \tag{II.106}$$

By combining our brief statements regarding the LHS/RHS of Eq. (II.103) We find the following reformulation of the W-GKP

$$\left\langle \int d^4x \mathcal{O}(x)\phi_0(x) \middle| \int d^4x \mathcal{O}(x)\phi_0(x) \right\rangle = e^{-\mathcal{S}_{SUGRA}(\phi_0)} \,. \tag{II.107}$$

In Eq. (II.107) we have on the LHS of the equivalence the generating functional of an operator $\mathcal{O}(x)$ acting on the source ϕ_0, whereas on the RHS we have the partition function of the evaluated on shell action of SUGRA. Now one can attain a direct relation between n-point correlation functions for the operators $\mathcal{O}(x)$ w.r.t., functional derivatives of the bulk fields with ϕ_0 being the source

$$\langle \mathcal{O}(x_1) \dots \mathcal{O}(x_n) \rangle = \frac{\delta^n \mathcal{S}_{SUGRA}}{\delta\phi(x_1) \dots \delta\phi(x_n)} |_{\phi \to \phi_0} \,. \tag{II.108}$$

An important caveat with the above-stated equivalence is that the correlation functions most often contain singularities that must be cured. This can be done in two ways, one possible solution is to tune the boundary conditions such that no singularities appear, and secondly resort to holographic renormalization, in which one renormalizes the gravitational action by adding local counter terms. In this thesis, we will mainly resort to holographic renormalization which will be further elaborated on in a future chapter of this thesis.

At this point, it is worthwhile to embrace the immense power of the above-mentioned equivalence. With this at hand, one can calculate n-point correlation functions of strongly coupled gauge theories only by knowing SUGRA in a weakly curved regime. As the AdS/CFT correspondence itself, is a duality of a strong/weak nature it may also be used in the reverse to understand strong SUGRA by looking at n-point correlation functions at weak coupling.

Now it is due time to start relating the observables on each side of the equality i.e.,. the matter fields in the SUGRA and the operators of the field theory. This procedure just described above is what is known as the field/operator correspondence. In the following, we will demonstrate this for the simplest case of a massive scalar field whose equation of motion (EoM) is

$$\left(\frac{1}{\sqrt{g}} \partial_\mu \sqrt{-g} g^{\mu\nu} \partial_\nu - m^2 \right) \phi(t, \bar{x}, z) \,, \tag{II.109}$$

and by Fourier transforming the EoM with a plane wave decomposition i.e., $\phi(t, \bar{x}, z) = e^{ip_\mu x^\mu} \phi_p(z)$, one find

$$z^2 \partial_z^2 \phi_p(z) - z(d-1)\partial_z \phi_p(z) - (\eta_{\mu\nu} p^\mu p^\nu z^2 + m^2 \mathcal{L}^2)\phi_p(z) = 0 \,. \tag{II.110}$$

We are mainly interested in the UV regime i.e., $z \to 0$ for the mode equation, where one finds the behavior $\phi_p(z) \sim z^{\Delta}$. Then by substituting it back into the mode equation one can obtain relations for the exponents Δ like

$$\Delta_{\pm} = \frac{d}{2} \pm \sqrt{\left(\frac{d}{2}\right)^2 + m^2\mathcal{L}^2}\,, \tag{II.111}$$

where $\Delta_{\pm}$ are the roots to the equation $\Delta(\Delta - d) = m^2\mathcal{L}^2$. We can now expand our solution for ϕ in the UV regime as

$$\phi(t, \bar{x}, z) = \phi_1(t, \bar{x}) z^{\Delta_-} + \phi_2(t, \bar{x}) z^{\Delta_+}\,, \tag{II.112}$$

where the functions ϕ_1, ϕ_2 are yet undetermined. From the AdS metric one can observe that it possesses a dilatation invariance under the simultaneous set of transformations [18] $x \to \lambda x$, and $z \to \lambda z$. By applying this to the UV expansion on the solution of ϕ, one realizes that if the scalar field ϕ shall respect the dilatation invariance ϕ_1, ϕ_2 must transform as $\phi_1(x) \to \lambda^{-\Delta_-}\phi_1\,, \phi_2 \to \lambda^{\Delta_- - d}\phi_2$. At this point, one can realize that there is a relationship between scalar fields of mass m in AdS space whose boundary data corresponds to a conformal scalar operator $\mathcal{O}$ of dimension Δ. Then by dimensional analysis also conclude that ϕ_1 corresponds to the source of the operator $\mathcal{O}$, with ϕ_2 being the vacuum expectation value of $\mathcal{O}$. In realizing this one can show that the two-point correlator behaves as

$$\langle \mathcal{O}(x1)\mathcal{O}(x_2)\rangle \sim \frac{1}{(x_1 - x_2)^{2\Delta}}\,. \tag{II.113}$$

As an example, it is worthwhile mentioning what the interpretation is of the two-point correlator for the case when the scaling dimension $\Delta = 4$, what its interpretation is on the gravitational side. To consider operators with scaling dimension 4 implies that in the gravitational theory, one is considering a massless scalar field, which in the case of SUGRA can be identified as the dilaton. In the case of $\mathcal{N} = 4$ SUSY YM the operator with scaling dimension $\Delta = 4$ has been shown to correspond to $\mathcal{O} = TrF^2$. This is known as the first explicit example of the relation between bulk fields and boundary operators. This logic concerning bulk fields and boundary operators can be applied to for instance higher spin fields, fermionic fields, and interpretations of the metric itself. This provides what we denote here as a holographic dictionary on what corresponding field content in the bulk theory is interpreted as in the dual QFT. Below we present a table at which we provide a comprehensive table of the relevant quantities on both sides of the correspondence and how to think of them on the other side.

Field Theory	Bulk Theory
Generating Functional	Partition Function
Scalar Operator $\mathcal{O}$	Scalar Field ϕ
Fermionic Operator $\mathcal{O}_\psi$	Dirac field ψ
Energy Momentum Tensor $T_{\mu\nu}$	Metric fluctuation $\delta g_{\mu\nu}$
Scaling Dimension Δ	Mass of bulk scalar m

II.4.1.3 Finite Temperature & Phase Transitions in AdS/CFT

So far, in our discussions of the AdS/CFT correspondence, whether concerning the equivalence of different theories or relating physical observables between the two theories, we

[18] For clarification and completeness $x = x_\mu = (t, \bar{x})$

have exclusively focused on zero temperature scenarios. While this serves as an excellent starting point for testing and establishing the correspondence, numerous physical phenomena occur in the presence of temperature. Consequently, the AdS/CFT correspondence at zero temperature lacks direct phenomenological applications.
Therefore, we need to elaborate on how the inclusion of temperature is achieved. In QFT, when examining a physical process at finite temperature as opposed to zero temperature, a Wick rotation of the time direction is necessary. This rotation compactifies the temporal direction onto a circle. So what is the analogue of performing a Wick rotation on the time direction in a QFT on the gravitational theory of the correspondence? One finds a rather remarkable feature that the inclusion of large temperatures in the gravitational theory of the correspondence on obtains black hole like solutions. Particularly in String Theory one finds that the stack of D3-branes becomes a stack of black D3 branes, which is the string theoretical description of black holes in extra dimensions. In Sec. (II.4.1.1) we claimed that one can show that a stack of D3 branes can be identified as black 3-brane solutions in SUGRA with the metric being

$$ds^2 = H(r)^{-\frac{1}{2}}\left(-f(r)dt^2 + d\bar{x}^2\right) + H(r)^{\frac{1}{2}}\left(f(r)^{-1}dr^2 + r^2 d\Omega_5^2\right)\,, \tag{II.114}$$

where $H(r)$ defined as before, whereas $f(r)$ is the geometrical blacking factor

$$H(r) = 1 + \frac{\mathcal{L}^4}{r^4}\,, \qquad f(r) = 1 - \frac{r_h^4}{r^4}\,. \tag{II.115}$$

By performing an analogous analysis of the various limits of the 5-d coordinate r we find that in $r \to \infty$ we recover 10-D Minkowski on the boundary. Whereas in the $r \to 0$ limit we find that the Eq.(II.114) metric for the stack of D3 branes becomes

$$ds^2 = \frac{\mathcal{L}^2}{z^2}\left(-f(z)dt^2 + d\bar{x}^2 + f(z)^{-1}dz^2\right) + \mathcal{L}^2 d\Omega_5^2\,, \tag{II.116}$$

where we have used the same substitutions as before with $f(z) = \left(1 - \frac{z^4}{z_h{}^4}\right)$. For the AdS_5 part of the metric we can by inspection see that it is almost identical up to the blackning factor and one can therefore realize that the AdS_5 geometry now has the inclusion of a Black Hole. The metric space of $AdS_5 \times \mathcal{S}_5$ has been modified to $AdS_5 - Schwarzchild \times \mathcal{S}_5$ by the inclusion of temperature effects [97]. The black hole present in the AdS_5 geometry one can assign an associated temperature to it and an entropy from the governing laws of black hole thermodynamics by Hawking [103–105]. In doing so one finds that the temperature and entropy are given by

$$T_h = \frac{1}{\pi z_h} \qquad S(z_h) = \frac{\mathcal{L}^3}{4 z_h^3 \mathcal{G}_5}\,, \tag{II.117}$$

where z_h is the location of the BH horizon, and $\mathcal{G}_5$ is the 5-d gravitational constant. Since temperature and entropy are physical quantities, it is natural to identify the temperature and entropy of the black hole to the temperature and entropy of the gauge theory, i.e., $\mathcal{N} = 4$ SUSY YM. As temperature is independent of couplings this can be done directly, however for the entropy this is not as straight forward let us delve more into this. The 5-d gravitational constant is defined as $\mathcal{G}_5 = \frac{\pi}{2}\frac{\mathcal{L}^3}{N_c^2}$, the BH entropy can be simplified into

$$S_{BH} = \frac{1}{2}\pi^2 T^3 N_c^2\,, \tag{II.118}$$

Field Theory	Bulk Theory
Finite T QFT	AdS Schwarzchild
Temperature T	BH Hawking Temperature T_h
Entropy	Hawking Beckenstein Entropy S_h
Phase Transition	Black Hole Instability.

Table II.3: Extention of the table of the Holographic dictionary to QFT's at finite temperature.

where we also replaced the expression of temperature to have entropy as a function of temperature for clarity. Lets compare this with the Stefan Boltzmann entropy density of an ideal plasma of $\mathcal{N} = 4$ SUSY YM in the large N_c limit

$$S_{YM} = \frac{2}{3}\pi^2 T^3 N_c^2 \,. \tag{II.119}$$

This is already quite striking that they are very similar and only off by a prefactor of 3/4, then one may wonder is this a shortcoming of the correspondence or have we missed something? One important detail to bear in mind here, when matching the entropy densities between the BH and SB plasma of $\mathcal{N} = 4$ SUSY YM, we must not forget that the BH entropy is matched to what the corresponding entropy density is for $\mathcal{N} = 4$ SUSY YM at strong coupling. Hence not in the weak coupling regime which is what the expression above is accounting for. By including the leading order $\frac{1}{\lambda}$ correction to the entropy density of weakly coupled $\mathcal{N} = 4$ SUSY YM [106] one finds

$$\frac{S_{BH}}{S_{YM}} = \frac{3}{4} + \frac{1.69}{\lambda^{\frac{3}{2}}} + \dots \,, \tag{II.120}$$

where one can conjecture that if all the $1/\lambda$ corrections were to be accounted for one would obtain an exact result. A striking aspect is that there are lattice results [107–109] which support this claim where they find that the ratio of entropy densities between a strongly coupled plasma and the BH entropy are close to 1.
With the identifications of temperature, entropy and by employing the fundamental laws of thermodynamics, we have the possibility of formulating the thermal evolution of a Strongly coupled QFT. This is achieved by utilizing the thermal description of a black hole in a gravitational theory with d+1 dimensions. One may ask how does a phase transition in the thermal QFT translate into for a gravitational theory with a black hole. This certainly depends on the type of PT of interest but in general terms a PT in the field theory is described by the indication of an instability of the black hole. To conclude this section we state that the AdS/CFT correspondence in thermal contexts by performing a wick rotation of the time direction in the field theory one end up introducing a BH on the other side. We will add these finding to our holographic dictionary table written out above with the additions A few final remarks to conclude this section

- In the discussion above, we have outlined a thermodynamic theory of $\mathcal{N} = 4$ SUSY YM through a particular string theory in its corresponding low-energy limits. This approach, known in the literature as a top-down approach, starts from the string theory and derives the corresponding field theory. Conversely, in a bottom-up approach, one starts with a field theory of interest and attempts to construct a string theory that approximates it.
- In the previous subsection we also looked at the procedure of obtaining correlation functions of the field theory, and this is straightforwardly extended to correlation

functions at finite temperature by substituting the vacuum solution metric with the BH one [110,111].

- Finally as the energy momentum tensor of the field theory is dual to the fluctuations of the metric one can also study hydrodynamics of the field theory by doing a fluctuation analysis of the BH metric on the gravitational side of the correspondence. This was shown explicitly by [110, 112–115] for $\mathcal{N} = 4$ SUSY YM, and has had large amount of success in the paradigm of using holography for hydrodynamics and ultimately Heavy Ion Collisions.

In this thesis we will work in the bottom up approach for studying the confinement phase transition of non SUSY SU(N_c) Yang-Mills theory in hope to calculate its associated GW spectra making use of the gauge/gravity duality.

Part I

GWs at Strong Coupling

CHAPTER III

Gravitational Waves from Dark Yang-Mills with Holography

III.1 Motivation

FOPTs in the early universe can emit GWs with sufficient strength for detection in present and future experiments [57, 61, 116]. This would serve as a compelling evidence of new physics, considering that both the Electroweak and QCD phase transitions in the SM are understood to be crossovers. Such GWs could enable exploration of otherwise inaccessible sectors, such as dark sectors where interactions with the SM are merely gravitational or extremely weak [117–119]. One compelling scenario where dark sectors are at play regards CDM – a particle interacting with the standard model solely through gravity or weakly via a mediator. The specific sector describing CDM remains elusive, with numerous models proposed in the literature for strongly interacting models [120–128].

In this realistic context, GWs emerge as an essential tool for shedding light on the properties of these otherwise inaccessible dark sectors. In this Part of the thesis which is comprised of [5, 6], we analyze the confinement FOPT in SU(N_c) pYM theory using Improved Holographic QCD (IhQCD) for $N_c \geq 3$. IhQCD is a non-critical string theoretical model whose intent is to approximate SU(N_c) pYM theory whose holographic construction is of the bottom up type. SU(N_c) pYM theories are frequently appearing in model building for BSM physics, for instance, in string theory [129–133], Composite Higgs/Twin Higgs models for resolving the EW hierachy problem [134–136], and in dark matter model building [117, 126, 137–139]. These theories are minimal in the sense that the theory involves only the confinement scale Λ and the number of colors, N_c as free parameters.

Therefore theys serve as good benchmark models for understanding GWs from FOPTs of strongly coupled theories. To initiate this exploration, we perform a fit of the free parameters of IhQCD to the equilibrium thermodynamical properties obtained from Lattice QCD, focusing on the groups $N_c = 3, 8$. This provides with crucial insight of what to expect as N_c grows. The equilibrium thermodynamics computed with Lattice QCD exhibit only minor changes between the groups $SU(3)$ and $SU(8)$.

Initially, regarding the kinetic term of the effective action, we relied on a phenomenological ansatz from [140], which we used in [5]. Here we will present a well-founded ansatz for the kinetic term based on qualitative calculations, which potentially encompasses a sizable uncertainty factor. This refinement is expected to significantly influence the outlook for GW observability in future experiments, such as μAres DECIGO and BBO.

The outline of this chapter is as follows: In Sec. (III.2), we will review the IhQCD model and compute its equilibrium thermodynamics. Then, in Sec. (III.3), we will discuss some

properties of the large SU(N_c) plasma, and outlining the procedure for fitting to SU(8) data.

Then we will proceed to construct an effective potential using the free energy landscape approach [5, 140–144], and for the kinetic term, we will impose an ansatz based on direct calculations. Utilizing our effective action, we will calculate the GW signal by employing the LISA Cosmology Working Group (CWG) [91] template for the PT parameters β, α, v_w, and $\kappa(\alpha)$.

Given that we are dealing with strongly coupled theories, one may question the validity of the LISA CWG semi-analytic templates, which were verified only for simulations of weakly coupled theories. We will not address this concern in this thesis, but instead we will simply make use fo what is available having these concerns in mind. We will however demonstrate how the dynamics of large N_c impact, the PT parameters, including the wall velocity, drawing upon recent works by [83, 84].

Finally, we will discuss our results and outline prospects for future work.

III.2 Review of Improved Holographic QCD

The gauge/gravity duality [93, 97] has emerged as one of the most powerful tools for understanding strongly coupled gauge theories, with notable successes in fields such as Heavy-ion collisions [145, 146]. This duality hinges on the remarkable correspondence between strongly coupled gauge theories in D dimensions and weakly coupled gravitational theories in D+1 dimensions. While the original formulation of the conjecture was based on a conformal SUSY theory, recent advancements have extended its applicability to non-conformal scenarios. The IhQCD model, which is the focus of interest here, represents a significant step forward in constructing gravitational duals for QCD-like theories.
IhQCD [147–150] is a 5-D bottom-up model of holographic QCD theories inspired by non-critical string theory for describing the gluon sector of pYM theories. The model is designed to reconstruct many features of observed in QCD like linear confinement, resembling hadron spectrum, asymptotic freedom in the UV and a finite temperature phase diagram structure that matches SU(N_c) pYM theory. The inclusion of matter fields for chiral symmetry breaking are doable by adding tachyonic D-branes or for instance an axion. However, here we will omit such an inclusion and study the SU(N_c) deconfinement phase transition with varying the number of colors N_c. The model IhQCD is composed of a 5-D Einstein-Dilaton theory with a non-trivial Dilaton potential. The model consists of a metric $g_{\mu\nu}$ whose fluctuations are dual to the energy-momentum tensor, the dilaton Φ which is dual to (λ_{YM}, TrF^2) and an axion dual to (θ_{YM}, $TrF \wedge F$).

The axion part of the theory can be neglected here as its contribution to the action is N_c^{-2} suppressed and does not come to play for the thermodynamics [1]. In the Einstein frame, the 5-D action which describes this model both at zero and finite temperature is given by

$$\begin{aligned}\mathcal{S}_5 = &- M_p^3 N_c^2 \int d^5x\sqrt{g}\left(R - \frac{4}{3}(\partial\Phi)^2 + V(\Phi)\right) \\ &+ 2M_p^3 \int_{\partial\mathcal{M}} d^4x\sqrt{h}\mathcal{K}\,,\end{aligned} \tag{III.1}$$

where M_p is the plank mass, N_c is the number of colors, R the Ricci scalar, g the metric and $V(\Phi)$ is the dilaton potential. The second term in the action is the Gibbons Hawking term

[1] In the large N_c which is the case of study here these effects becomes completely negligible.

that depends on the induced metric h on the boundary, and $\mathcal{K}$ is the extrinsic curvature

$$K_{\mu\nu} = \nabla_\mu n_\nu = \frac{1}{2} n^\rho \partial_\rho h^{\mu\nu} \quad , \mathcal{K} = h^{ab} K_{ab} \, . \tag{III.2}$$

The quantity governing the dynamics of the theory is the dilaton potential $V(\Phi)$, which is partially chosen by non-critical string theory, and also chosen such to generate a qualitatively accurate phenomenology of the theory. The dilaton potential is employed in the same manner as by the original authors [148, 150] defined as

$$V = \frac{12}{\ell^2} \left(1 + V_0 \lambda + V_1 \lambda^{\frac{4}{3}} (\log[1 + V_2 \lambda^{\frac{4}{3}} + V_3 \lambda^2]^{\frac{1}{2}}) \right) \, , \tag{III.3}$$

where $\lambda = \exp(\Phi)$, and ℓ is the AdS length that sets the scale of the fifth dimensional coordinate. The parameter V_0 and V_2 are related to the coefficients of the SU(3) YM β-function

$$V_0 = \frac{8}{9} b_0 \, , \qquad V_2 = b_0^4 \left(\frac{23 + 36 \frac{b_1}{b_0^2}}{81 V_1} \right)^2 \, , \tag{III.4}$$

with $b_0 = 22/(3(4\pi)^2)$ and $b_1/b_0^2 = 51/121$. These values emerge from imposing a linear relation between λ and the the 't Hooft coupling λ_t of the YM theory in the UV, $\kappa\lambda = \lambda_t$. Other normalizations are possible, but do not influence the physical results [150]. The free parameters of the potential $(V1, V3)$ will be the primary discussion of the next section of how to determine these with available lattice data. As previously mentioned the dynamics of the model are encoded in $V(\lambda)$, where the small/large λ limits determines the solution of the system in the UV/IR. Here we mention the most important features encoded in $V(\lambda)$ in Eq. (III.3). For more details about the vacuum solutions and its structure we refer to [147, 149] and also section 2 in [148].
From the identification of the dilaton with the t'Hooft coupling in the UV, one can infer that for $\lambda \ll 1$, the Yang-Mills (YM) theory is in a weakly coupled regime where asymptotic freedom prevails. Conversely, in the limit $\lambda \gg 1$, corresponding to the deep infrared (IR), one expects to encounter confinement-like behavior. However, directly comparing the t'Hooft coupling λ_t with the profile of λ in the deep IR is less straightforward due to the intricate nature of the latter.

- **I**n the UV i.e. small λ: $V(\lambda)$ needs to have a power law expansion in the UV

$$V(\lambda) \sim \frac{12}{\ell^2} (1 + v_0 \lambda + v_1 \lambda^2 + ...) \, , \tag{III.5}$$

  in which the coefficients of this expansion are the ones related to the YM β-function as in Eq. (III.3). From Eq. (III.5) the relations between the coefficients v_i to the YM β-function are

$$b_0 = \frac{9}{8} v_0 \, , \qquad b_1 = \frac{9}{4} v_1 - \frac{207}{256} v_0^2 \, . \tag{III.6}$$

  In the vicinity of the UV boundary at $r \to 0$ the geometry asymptotes to AdS with logarithmic corrections:

$$b(r) = \frac{\ell}{r} \left[1 + \frac{4}{9} \frac{1}{\log r\Lambda} - \frac{4}{9} \frac{b_1}{b_0^2} \frac{\log(-\log r\Lambda)}{(\log r\Lambda)^2} + \dots \right] \, , \tag{III.7}$$

$$b_0 \lambda(r) = -\frac{1}{\log r\Lambda} + \frac{b_1}{b_0^2} \frac{\log(-\log r\Lambda)}{(\log r\Lambda)^2} + \dots \tag{III.8}$$

The scale Λ can be used to set the energy scale of the theory. Λ can be thought of as the holographical analog to the strong coupling scale in perturbative YM theory. Alternatively, one can fix the energy scale by choosing the mass of the lightest glueball or the critical temperature of the confinement phase transition, This is the prescription we have employed in this thesis for phenomenological purposes.

- **I**n the IR i.e. large λ: For accurate behavior of confinement, and no bad singularities $V(\lambda)$ shall maintain the form

$$V(\lambda) \sim \lambda^{4/3}(\log\lambda)^{1/2}. \tag{III.9}$$

With these powers in the exponents of $\lambda, \log\lambda$ one obtains a linear glueball spectra $m_n^2 \sim n$, we will only consider this case here. Furthermore for the scale factor and the dilaton with such a potential in the IR limit where $r \to \infty$ becomes

$$b(r) \sim e^{-\left(\frac{r}{r}\right)^2}, \qquad \lambda(r) \sim e^{\left(\frac{r}{r}\right)^{3/2}} \left(\frac{r}{L}\right)^{4/3}. \tag{III.10}$$

L remains fixed once Λ is determined as L is the lengths scale of the IR physics.

As our intention is to study the confinement phase transition, we need to consider the finite-temperature counterpart of this theory. As discussed in Sec. (II.4.1.3), introducing finite temperature in the field theory entails invoking a black hole (BH) solution on the gravity side. In the holographic interpretation, the confinement phase transition manifests as the instability of the BH solution, transitioning from a stable BH solution to a thermally excited vacuum state[2]. By performing a Wick rotation of the field theory to compactify time on a circle of size $\beta = \frac{1}{T}$, two distinct solutions emerge.

- **T**hermal Gas Solution: This solution is equivalent to the vacuum solution except for the compactification along the time direction

$$ds^2 = b_0^2(r)(dr^2 - dt^2 + dx^m dx_m). \tag{III.11}$$

This solution corresponds to a thermal excitation above the vacuum and is often referred to as a thermal gas of gravitons at temperature T. This is a thermal ensemble of the same original solution, in which it inherits all the correct non-perturbative features like (confinement, glueball spectra, etc..)

- **A**dS Black Hole Solution: are of the form

$$ds^2 = b^2(r)\left(\frac{dr^2}{f(r)} - f(r)dt^2 + dx^m dx_m\right), \tag{III.12}$$

these solutions are characterized by their black hole horizon r_h where $f(r_h) = 0$. These solutions, provided they exist correspond to a deconfined phase. To realize this one can consider the confining string tensions analog in the holographic picture [**?**], doing so one finds that it is proportional to $Min_r(\sqrt{g_{tt}\cdot g_{rr}}) = 0$. The temperature of the system is given by the hawking temperature of the black hole i.e.

$$T_h \equiv \frac{|\dot{f}(r_h)|}{4\pi}, \tag{III.13}$$

The picture of this system for an arbitrary temperature T in the gravity theory is that one has the black hole solution which is surrounded by the thermal gas. By considering the canonical ensemble partition function in the large N_c limit, it becomes the sum over

[2]This type of PT is known as a Hawking-Page Phase Transition [151]

saddle points evaluated at temperature T, in which one determines the governing phase by the contribution which dominates the partition function at that temperature. This therefore imposes a regularity condition at the BH horizon that the temperature of the BH is equal to that of the thermal gas i.e.

$$T_h = T\,. \tag{III.14}$$

If the aforementioned condition is not fulfilled a conical singularity appears which needs to be dealt with accordingly. More about this in Sec. (III.4). By inspecting Eq. (III.13) one can realize that because the blackening factor $f(r_h)$ is absolute valued, there are either zero or two values of r_h at each temperature T_h.
These BH horizon position values r_h identifies two branches, there is the Big BH (BBh) branch for small values of r_h and the corresponding small BH (SBh) branch for large values of r_h. The Big BH branch is thermodynamically stable whose evolution with decreasing temperature describes the SU(N_c), whereas the Small BH branch is thermodynamically unstable see Fig. (III.1). However, the Small BH branch and its dynamics are essential for the tunneling [5] between the different vacua. More about this in the upcoming sections. A firm requirement on the AdS BH in Einstein-Dilaton gravity is that their UV asymptotics are equal to those in the thermal/vacuum solution.
Hence to impose this practically one needs to set $f(0) = 1$, such that the BH metric coincides with the thermal gas/vacuum one. As the metrics of the BH/TG coincide in the UV by requirement of the solutions this also imples that they must obey the same UV boundary conditions. To phrase the aforementioned statement in a different way this means that the integration scale Λ i.e. the holographic correspondence to the strong coupling scale needs to be equal. Starting from the black hole ansatz of Eq. (III.12), the Einstein equations are written as

$$6\frac{\dot{b}^2}{b^2} + 3\frac{\ddot{b}^2}{b^2} + \frac{\dot{b}}{b}\frac{\dot{f}}{f} = \frac{b^2}{f}V \tag{III.15}$$

$$6\frac{\dot{b}^2}{b^2} - 3\frac{\ddot{b}^2}{b^2} = \frac{4}{3}\dot{\Phi}^2 \tag{III.16}$$

$$\frac{\ddot{f}}{f} + 3\frac{\dot{b}}{b} = 0 \tag{III.17}$$

$$\ddot{\Phi} + \left(\frac{\dot{f}}{f} + 3\frac{\dot{b}}{b}\right)\dot{\Phi} + \frac{3b^2}{8f}\frac{dV}{d\Phi}0 \tag{III.18}$$

where the dilaton potential is given in Eq. (III.3). The thermal gas equations of motion are obtained by setting $f(r) = 0$ and replacing $b(r) \to b_0(r)$. From the equations of motions Eq. (III.15) and the action Eq. (III.57) of the theory we start to elaborate on how one attains the thermodynamics of this system. Recalling from Sec. (II.4.1.3) we have the physical temperature in terms of the hawking temperature of the BH, where the entropy is given by the Hawking-Beckenstein [152] formula

$$S = \frac{\text{Area}}{4G_5} = 4\pi M_p^3 N_c^2 V_3 b(r_h)^3\,, \tag{III.19}$$

where $G_5 = 1/(16\pi M_p^3 N_c^2)$ is the 5D Newton constant and V_3 is the volume of 3D space. The free energy difference at a fixed temperature β^{-1} is given by the difference of regularized on-shell actions of the respective solutions i.e.

$$\mathcal{F} = \frac{\beta}{V_3}(\mathcal{S}_{\text{dec.}} - \mathcal{S}_{\text{conf.}})\,. \tag{III.20}$$

In Eq. (III.20) the respective on-shell actions are regulated by regulators $\epsilon, \tilde{\epsilon}$ which are not necessarily evaluated at the same r. By taking the difference between the on-shell actions one can avoid the calculation of counter terms which for more involved geometries such as the ones we study renders a major simplification[3]. This regularization technique is guaranteed to work even for finite values of the regulators $\epsilon, \tilde{\epsilon}$ since they are constructed by invariants of the induced boundary metric and the boundary values of the dilaton λ. One can even go further to say that the explicit form of the counter terms are not even needed at all due to the aforementioned reasoning.
A simplification concerning the solutions to this systems is that one can realize that since the dilaton profile $\lambda(r)$ grows monotonically from 0 at $r \to 0$ to $\lambda \to \infty$ at large r. This also implies that the horizon position r_h corresponds to a finite value λ_h. This allows one to make use of the so-called gubser gauge [153], where λ is used as the radial coordinate along the fifth dimension.[4] To get back to the thermodynamics of the system we can note that the sign of $\mathcal{F}$ indicates the energetically favorable phase, with $\mathcal{F} < 0$ corresponding to the deconfined phase. The critical temperature T_c is defined at $\mathcal{F} = 0$. In practice, the free energy can be computed by integrating the thermodynamic relation $\mathrm{d}\mathcal{F} = -\mathrm{d}S/\mathrm{d}T$ along both black hole branches [148]:

$$\mathcal{F} = -\int_{\infty}^{\lambda_h} b(\tilde{\lambda}_h)^3 \frac{\mathrm{d}T}{\mathrm{d}\tilde{\lambda}_h} \mathrm{d}\tilde{\lambda}_h \,. \tag{III.21}$$

Fig. (III.1) shows the temperature and the free energy of the BH solutions. Once the essentials for quantities of a system i.e. $(T, S, \mathcal{F})$ are obtained, the remaining thermodynamics are obtained using standard relations

$$P = -\mathcal{F} \,, \qquad \rho = \mathcal{F} - TS \,, \qquad \Delta = \rho - 3P \,. \tag{III.22}$$

The remaining relevant thermodynamic properties of the plasma are for instance

$$c_v = -T\frac{d^2\mathcal{F}}{dT^2} \,, \qquad c_s^2 = \frac{s}{c_v} \,, \qquad \omega = \frac{P}{\rho} \,. \tag{III.23}$$

With the thermodynamics at hand, one can perform comparisons with lattice data. For a rigorous introduction to lattice gauge theory and how their observables are constructed we refer the reader to Refs. [154–157]. Fig. (III.1) displays the equilibrium thermodynamics of the system in which the Big BH branch describes the thermodynamics of the deconfined phase of pure SU(N_c) to the limit of meta-stability at T_{min}. The states on the small BH branch emerge the Big BH branch at T_{min} that is profound to observe at the maximum value of the free energy in Fig. (III.1). The thermodynamic states along this branch are both locally thermodynamically unstable and also dynamical unstable. This is evident by observing the specific heat $c_v = s/c_s^2$ along this branch, implying that the sound speed is $c_s^2 < 0$ in the small BH branch. For explicitness we point out that we are here only plotting the high T phase its metastable region, and spinodal region [158, 159] where it traverses the small BH branch as we assume that the energy and entropy density in the confined phase to quickly drop to zero[5]. For recent studies about the evolution of the small BH branch and its implications on PT phenomenology see [158–161].

[3] As a regularization scheme this often goes under the name subtraction scheme

[4] This coordinate frame choice will together with the 5-D coordinate r be the prior ones used in this work, they may be interchanged at certain places.

[5] As the Dof in the confined phase scales as $\mathcal{O}(N_c^0)$ are neglected even modeling the low T phase with [?], one quickly realizes that in the large N limit it becomes negligible

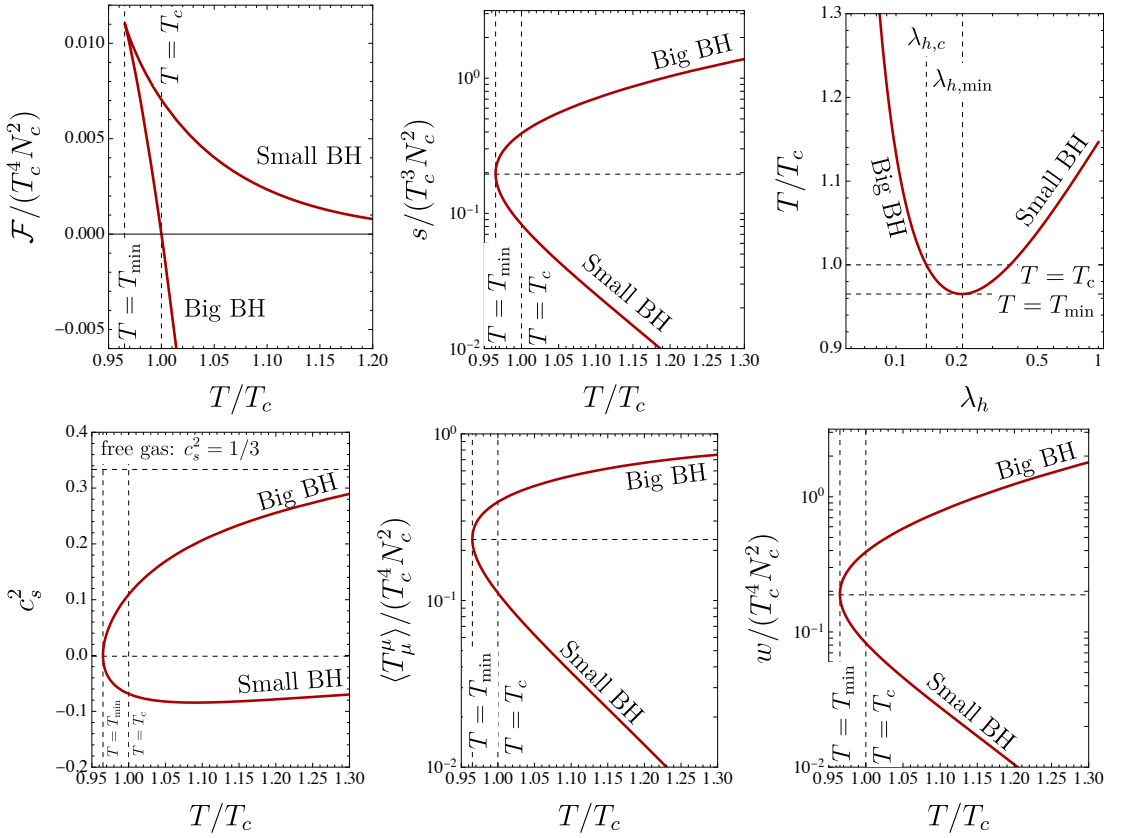

Figure III.1: Thermodynamical properties for the pYM deconfined plasma being depicted by the BBH branch of the solutions. In the top row we have the free energy as a function of temperature, the entropy density, and the temperature evolution as a function of the dilaton field value at the BH horizon. Bottom row we have the speed of sound of the plasma as a function of temperature, trace of the EM tensor, and finally the equation of state. Figures created by E.Morgante

III.3 Quark Gluon Plasma Thermodynamics and Lattice Observables

In first principle approaches for understanding the confinement phase transition, the conventional order parameter is the vacuum expectation value of the Polyakov Loop. This exhibits a jump at T_c [157, 162, 163] indicating a FOPT for $N_c \geq 3$. Here we argue that in holographic setups the relevant order parameter is λ_h i.e., the dilaton field value at the horizon position.[6] Here we elaborate on how the equilibrium thermodynamics from lattice can be used to infer an accurate behavior for IhQCD, and what impact different SU(N) groups have on the model parameters of IhQCD i.e., $(V_1\,, V_3)$.

The QGP fairly close to confinement $T_c \leq T \simeq 3.5 T_c$ has the characteristic feature that the pressure posessess a steep increase from approximately zero in the confined phase and approaches the Stefan Boltzmann (SB) limit of a free gas[7]. We address our focus to this region and in particular consider the region $T_c \leq T \simeq 2.5 T_c$, as our available data

[6] Since we have made a calculation of the polyakov loop vev within holography to see that by changing λ_h one obtains a jump in the polyakov loop VEV.

[7] It shall be emphasized that we refer to $p/p_{SB}|_{T=T_c} \sim 0$, which quickly rises to the SB limit $P_{SB} = (N_c^2 - 1)\pi^2/45$

is centered around this regime. So our focus of this section is to elaborate on how the IhQCD model parameters i.e., $(V_1\,, V_3)$ are fitted against lattice data as in [150] and how this procedure can potentially be improved. We will illustrate the approach by providing a direct comparison between it and the approach used in [150]. This is described in the gravitational theory as follows

In the gravitational theory the dynamics of the QGP at tmperatures $T > T_c$ is governed by the Big-Black hole branch of solutions. As the QGP cools down and reaches the critical temperature $T = T_c$ where the deconfined phase becomes meta-stable is encoded in the gravitational theory by the presence of a BH instability. This can be seen from top left figure in Fig. (III.1) of how the free energy crosses zero at $T = T_c$. The QGP for $T_c \gtrsim T$ enters a supercooled regime which is observed in the gravitational theory by following the BBH branch of the free energy in Fig. (III.1).

The thermodynamical observables for fitting the parameters V_1, V_3 are the Latent heat per unit volume and the pressure per unit volume. The main dimensionfull parameter of pure SU(N_c) YM theory is the strong coupling scale Λ_{QCD} which fixes the overal energy scale of the theory. One can rescale the actual strong coupling scale to adjust for considering the theory/dynamics to take place at different energy scales. In [150] values of the parameters $V1, V3$ were obtained by looking at the dimensionless Latent heat, and pressure at a fixed temperature which they took to be $T = 2T_c$. With the dilaton potential where V_0, V_2 are related to the YM beta function coefficients, where it was found in [150] that for SU(3) with V_1, V_3 $V_1 = 14, V_3 = 170$ quantitatively matches the data fairly well. Here the intent is to compare the strategy presented by [150] with a χ^2 fit on the available SU(8) lattice data used in [164]. By calculating the thermodynamics for different values of (V_1, V_3) one can understand that for increased V_1 the thermodynamics reaches the Free Gas limit faster, whereas for decreasing V_3 the latent heat increaces. This understanding was also emphasized in [150]. Recent work on how adequate fitting procedures should be done in holographic QCD models were recently presented in [165].

To perform the χ^2 fit we proceed by using the scalar variables and their numerical relations to the thermodynamic functions $T, S, \mathcal{F}$ introduced in Sec. (III.8.1). We generate a set of BH solutions for a large range of λ_h values for an array of values of the free parameters (V_1, V_3). Then for this set of λ_h values given certain values of $V_1\,, V_3$ we find the critical temperature T(λ_h^c,V_1,V_3) in which $\mathcal{F}(\lambda_h^c, V_1, V_3) = 0$ by using a bisectional method to find the corresponding λ_h^c[8]. Provided this data we evaluate the thermodynamic quantitites i.e., $P(T)/T^4, L_h/T^4$ at the lattice data points as a function of T/T_c which we compute for each set of parameter values (V_1, V_3) in the array. We make a discrete array due to computational complexity. Then we perform the χ^2 estimation of all the parameter combinations (V_1, V_3) at all points and take the (V_1, V_3) values whose averaged value of the χ^2 is minimized.

[8]This one can certainly improve by implementing some gradient descent method but for our purposes the aforementioned technique is sufficient

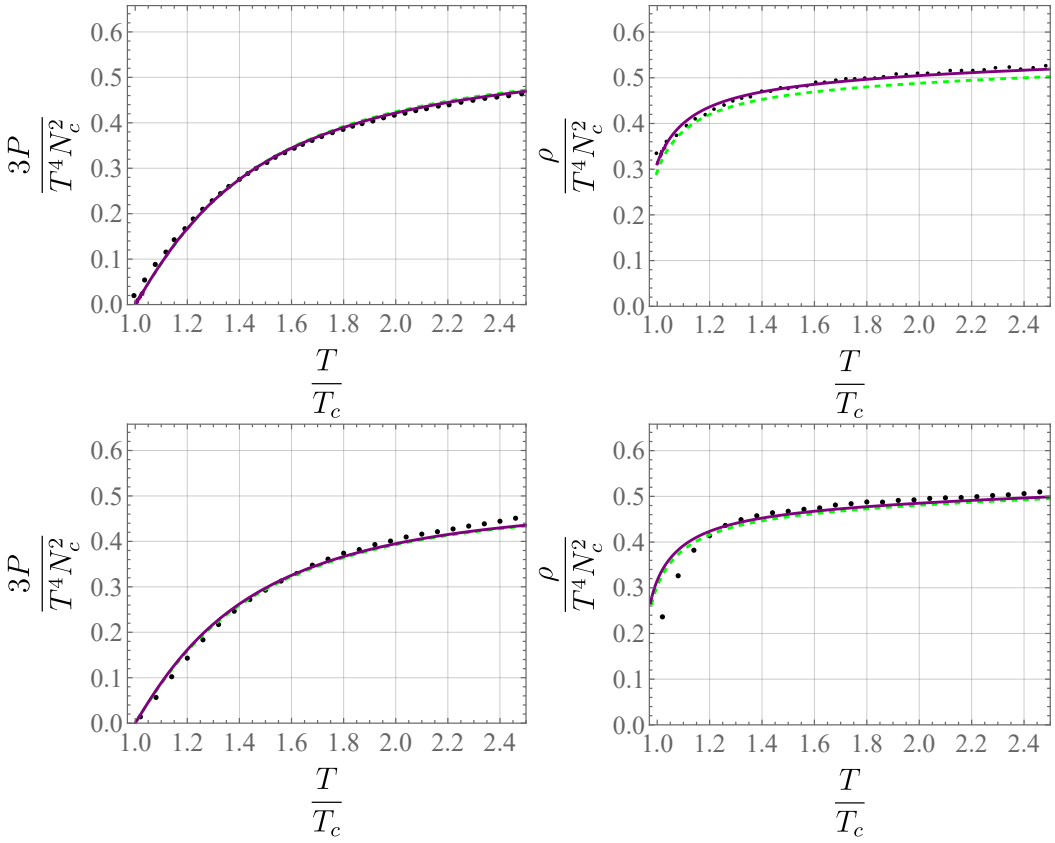

Figure III.2: The outcome of the different fitting procedures. To the upper figures we display the pressure/energy density in the continium limit of the available lattice data for SU(8) in [164]. The purple line is the one in which we perform the χ^2 parameter scan, and in green is with only fitting to a point. To the right we can see how the fitting procedures affect predictions of thermodynamics, for instance the energy density ρ. The lower figures display the available lattice data of [166] for SU(3) with the same color coding.

For the case of SU(8) we find the following values

$$V1 = 12.0\,, \qquad V3 = 150\,. \tag{III.24}$$

The thermodynamics of the system by going from SU(3) to SU(8) is not expected to change very much as indicated in various literature [164]. In the figure above we show the overall difference in the different fitting procedures. We can directly observe that there is not a significant difference by performing a fit by inspection to a point in comparison with a full χ^2 estimator. The overall χ^2 estimation is improved by roughly a factor of 2 by performing the parameter scan over $V1, V3$ in the pressure/latent heat. We find that for the quantities that are fitted the difference is minor but that the effect of the different fitting procedures becomes more evident for the TD observables we predict. Nevertheless this is still not a significant effect however the outcome could potentially have been anticipated. In Fig. (III.2) the upper plots are for the SU(8) case whereas the lower figures are for SU(3). We consider the continiuum limit of the pressure in the left figures which we fit against, whereas in the right figures, we illustrate the effect the different fitting strategies have on an observable. However, going from SU(8) to arbitrary large N_c is only possible through the lattice but due to the numerical daunting task of going to very large N_c we will resort to the AdS/CFT correspondence. Nevertheless, to perform

the fit for SU(8) as it is the largest group currently accessible in finite T, we use it as a benchmark point for what would to be expected for an even larger N.

III.4 Effective action

As explained previously in [5], the most natural order parameter is the horizon position λ_h. The effective action with order parameter λ_h is obtained in several steps and this section intends to elaborate on these steps. First, it is necessary to discuss how the actions are regularized as we have not explicitly emphasized any direct counterterms in the actions. This will be discussed in Sec. (III.4.1) which explains the regularization procedure in these holographic constructions. Then we explain the assumptions for the BH/TG metrics needed to calculate the effective potential using a free energy landscape approach, similar to Refs. [140–142, 144][9]. Finally, we elaborate on how to calculate a kinetic term to fully formulate our effective action given our imposed metric assumptions and calculated effective potential at hand.

III.4.1 Regularized Action

We define the effective action as the difference between the classical action of a black hole solution and that of the thermal gas solution with the same ambient temperature T:

$$\mathcal{S}_{\text{eff}} = \mathcal{S}_{\text{BH}} - \mathcal{S}_{\text{TG}} \,. \tag{III.25}$$

When discussing the tunneling rate, we want to interpolate between the small and big BH solutions with a fixed temperature T. Hence, we consider metric-field configurations for the order parameter λ_h (or, equivalently, r_h), that solve the Einstein equations up to a possible conical singularity at the BH horizon. The conical singularity arises whenever the Hawking temperature T_h differs from the ambient temperature T of the thermal graviton gas. Since we will ultimately discuss bubble nucleation, we assume the order parameter r_h is a function of position in 3-space, and, assuming spherical symmetry, we will write $r_h = r_h(\rho)$. To simplify the problem, we will assume that the r dependence of the solution is not affected by the fact that r_h is not constant in space. In other words, we will take

$$\lambda(r, \rho) = \lambda_{r_h}(r) \,, \tag{III.26}$$

where on the RHS we indicated the solution of the EoM obtained for a constant r_h, as it was obtained in [5,148], and the ρ dependence is intrinsic through $r_h(\rho)$. This is consistent with an expansion in the powers of spatial derivatives. An analogous equation holds for the scale factor $b(r)$.

Both terms on the RHS of Eq. (III.25) are divergent as $r \to 0$. They thus need to be regularized with a cut-off at some small $r = \epsilon$, which can be sent to 0 after the subtraction has been taken. For the divergence to cancel in the difference, two conditions have to be met:

1. First, the intrinsic geometry of the 4-dimensional boundary must coincide for the BH/TG solutions, up to terms that vanish in the UV limit [168].
2. In IhQCD, one also has to assume that the value of the dilaton field at the cutoff must be the same. Furthermore, since we want the BH and TG to represent two phases of the same physical theory, the strong coupling scale Λ needs to be the same for both theories [148]. This is analogous to the statement that the strong coupling scale Λ does not shift due to finite T effects.

[9] See also [167] for an interesting example applied to the Hawking-Page phase transition

The first condition implies that the proper length of the time circle and the proper volume of 3-space must be the same at the cut-off,

$$\beta b_0(r)|_{\rm cut-off} = \tilde{\beta} b(r)\sqrt{f(r)}|_{\rm cut-off} \tag{III.27}$$

$$V_3 b_0^3(r)|_{\rm cut-off} = \tilde{V}_3 b^3(r)|_{\rm cut-off} \tag{III.28}$$

The second condition, instead, can only be met if the two solutions are evaluated at *different* positions of the cut-off, such that [10]

$$\lambda_0(\epsilon) = \lambda(\tilde{\epsilon})\,, \tag{III.29}$$

where $\tilde{\epsilon} = \epsilon + \delta\epsilon$ and $\delta\epsilon \ll \epsilon$ is of higher order in the ϵ expansion, and must be determined taking into account the UV expansion of λ_0 and λ.

The conditions above can now be applied to refine the metric ansatz for the BH and the TG backgrounds. Our starting point is the thermal gas metric

$$ds^2 = b_0^2(r)\left(dr^2 - dt^2 + d\vec{x}^2\right)\,, \qquad \phi = \phi_0(r) \tag{III.30}$$

and the AdS black hole one

$$ds^2 = b^2(r)\left(\frac{dr^2}{f(r)} - f(r)d\tilde{t}^2 + d\vec{\tilde{x}}^2\right)\,, \qquad \phi = \phi(r)\,. \tag{III.31}$$

We left implicit the dependence of the functions b_0, b, f, ϕ_0, ϕ on r_h. The conditions (III.27) and (III.28) imply that

$$d\tilde{t} = \frac{b_0(\epsilon)}{b(\tilde{\epsilon})\sqrt{f(\tilde{\epsilon})}}dt\,, \qquad d\tilde{\rho} = \frac{b_0(\epsilon)}{b(\tilde{\epsilon})}d\rho\,, \tag{III.32}$$

where $\rho = (\vec{x}^2)^{1/2}$. The UV behavior of the metric and field configuration can be derived from the Einstein equation applied to the ansatz Eq. (III.53), (III.31), neglecting the $\vec{x}$ dependence of these functions. Up to the first logarithmic correction, one obtains [148]:

$$b_0(r) = \frac{\ell}{r}\left[1 + \frac{4}{9}\frac{1}{\log r\Lambda} + \dots\right]\,, \tag{III.33}$$

$$\lambda_0(r) = -\frac{1}{b_0}\frac{1}{\log r\Lambda} + \dots\,, \tag{III.34}$$

for the thermal gas and, for the black hole,

$$b(r) = b_0(r)\left[1 + \mathcal{G}(r_h)\frac{r^4}{\ell^3} + \dots\right]\,, \tag{III.35}$$

$$\lambda(r) = \lambda_0(r)\left[1 + \frac{45}{8}\mathcal{G}(r_h)\frac{r^4\log r\Lambda}{\ell^3} + \dots\right]\,, \tag{III.36}$$

$$f(r) = 1 - \frac{C(r_h)}{4}\frac{r^4}{\ell^3}\,. \tag{III.37}$$

Solving for $\lambda_0(\epsilon) = \lambda(\tilde{\epsilon})$ using Eqs. (III.34) and (III.36), one obtains

$$\delta\epsilon \equiv \tilde{\epsilon} - \epsilon = \frac{45}{8}\frac{\mathcal{G}(r_h)}{\ell^3}\epsilon^5(\log\epsilon\Lambda)^2\,. \tag{III.38}$$

[10] We employ a different convention w.r.t., Ref. [148], indicating with a tilde quantities related to the BH metric, instead of to the TG one. This leads to an opposite sign in Eq. (III.38), which anyway does not affect the result for the effective potential.

III.4.2 Metric Ansatz for the Effective action

In the previous subsection, we reviewed how the regularized on-shell action is retrieved in the IhQCD model which relies on the so-called subtraction scheme to not have to resort to counter terms. Furthermore, we set the stage for the calculations in the coming subsections where we will take the reader through how we obtain our effective action. First, we have to allure the reader of what the appropriate metric ansatz is for the BH and the TG as we construct the effective action employing the strategy as the original authors of the model i.e. by working in the subtraction scheme.

III.4.2.1 Black Hole Metric

In this section, we will construct the correct ansatz for the black hole metric. Let us first analyse its behaviour in the vicinity of the horizon. We start from the case of constant r_h. We can expand f, b as

$$f(r) \approx \dot{f}_h(r - r_h)\,, \qquad b(r) \approx b_h\,, \tag{III.39}$$

obtaining

$$ds^2 = b_h^2 \left(\frac{dr^2}{\dot{f}_h(r - r_h)} + \dot{f}_h(r - r_h)dt^2 + (d\vec{x})^2 \right)\,. \tag{III.40}$$

We can now define

$$y = \frac{2b_h}{(\dot{f}_h)^{1/2}}\sqrt{r_h - r} \qquad \text{with } y > 0\,, \tag{III.41}$$

$$\varphi = 2\pi T t \qquad \text{with } 0 < \varphi < 2\pi\,, \tag{III.42}$$

In terms of which the metric (restricting ourselves to the r, t directions) is

$$ds^2 = dy^2 + y^2 \left(\frac{\dot{f}_h}{4\pi T} \right)^2 d\varphi^2\,. \tag{III.43}$$

This is the metric of a cone, y being the distance from the tip, φ the angular direction and the opening angle α of the cone is

$$\sin\alpha = \frac{\dot{f}_h}{4\pi T} = \frac{T_h}{T} \tag{III.44}$$

For $\sin\alpha = 1$ the singularity at the cone tip disappears, and the metric becomes flat. Otherwise, the metric can be regularized by cutting the cone surface close to the tip, at some small y_s, and smoothly gluing a spherical cap of radius $R_s = y_s \tan\alpha$, as shown in Fig. (III.3). In polar coordinates, the metric on the spherical cap is

$$h_{\mu\nu}^{\text{cone}} = \text{diag}\left(R_s^2, R_s^2 \sin\theta^2, b(y)^2, b(y)^2, b(y)^2\right)\,, \tag{III.45}$$

with $0 < \theta < \pi/2 - \alpha$. The regularized region contributes to the total action as

$$\mathcal{S}_{\text{cone}}^{BH} = -M_p^3 N_c^2 \int d^5x \sqrt{g}[\mathcal{R} - \frac{4}{3}(\partial\phi)^2 + V(\phi)]\,. \tag{III.46}$$

The matter contribution is regular, and goes to zero as the cap is shrunk. The relevant term is the Einstein-Hilbert one, which can be easily evaluated using

$$\sqrt{g} = R_s^2 \sin\theta b(y)^3 \approx R_s^2 \sin\theta\, b_h^3 \tag{III.47}$$

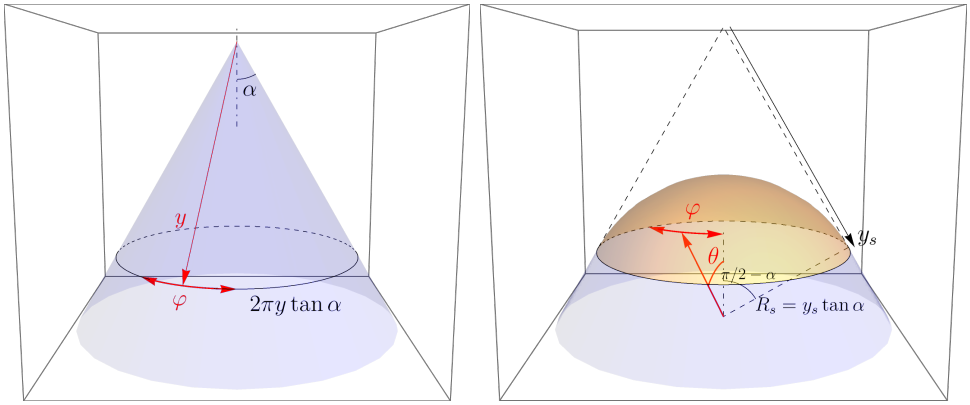

Figure III.3: Visualization of the cone singularity at the BH horizon and of its regularization by means of a spherical cap. Figures created by E.Morgante

and

$$\mathcal{R} = 2/R_s^2 + \dots\,, \tag{III.48}$$

where the dots are terms containing the derivatives $\partial_\theta b \propto R_s \to 0$. The integral extends over the area of the spherical cap, which is $2\pi R_s^2(1-\sin\alpha)$. The resulting action is thus

$$\mathcal{S}^{BH}_{\text{cone, geom}} = -M_p^3 N_c^2 V_3 b_h^3 \,\text{Area}\,(2/R_s^2) = -4\pi M_p^3 N_c^2 V_3 b_h^3 \left(1 - \frac{T_h}{T}\right)\,. \tag{III.49}$$

We now let r_h be position-dependent, $r_h(\rho)$, following a procedure described in Ref. [144]. The coordinate y in Eq. (III.42) now depends on ρ:

$$y = \frac{2b_h(r_h(\rho))}{(\dot{f}_h(r_h(\rho)))^{1/2}}\sqrt{r_h(\rho) - r}\,. \tag{III.50}$$

If we start from the metric of Eq. (III.31) and perform the change of coordinates from r to y in the usual way, the non-vanishing derivative $\partial_\rho y$ induces off-diagonal terms that are not present in Eq. (III.45). The manifold is not a cone anymore, and the above discussion is not valid.

In order to have a tractable conical singularity, we proceed as follows. We start from the metric in Eq. (III.31), and perform the change of variable of Eq. (III.42) with constant r_h, without restricting it to the region $r \to r_h$. We obtain

$$ds^2 = b(r)^2\,\text{diag}\left(\frac{\mathcal{Q}^4}{4}\frac{y^2}{f(r)}, -\frac{f(r)}{4\pi^2 T^2}, 1, \rho^2, \rho^2\sin^2\theta\right)\,, \tag{III.51}$$

with $\mathcal{Q} = \dot{f}_h^{1/2}/b_h$. Now we can promote $r_h \to r_h(\rho)$ and change coordinates using Eq. (III.50), obtaining the new metric $g^{\text{BH}}_{\mu\nu}$ with entries

$$\begin{aligned}
g^{\text{BH}}_{rr} &= \frac{b(r)^2}{f(r)} \\
g^{\text{BH}}_{tt} &= -b(r)^2 f(r) \\
g^{\text{BH}}_{\rho\rho} &= b(r)^2\left[1 + \frac{r_h'(\rho)^2}{f(r)}\left(\frac{\mathcal{Q}(r_h) - 2(r_h - r)\mathcal{Q}'(r_h)}{\mathcal{Q}(r_h)}\right)^2\right]
\end{aligned}$$

$$
\begin{aligned}
g^{\rm BH}_{\rho r} = g^{\rm BH}_{r\rho} &= -b(r)^2\,\frac{r_h'(\rho)}{f(r)}\,\frac{\mathcal{Q}(r_h)-2(r_h-r)\mathcal{Q}'(r_h)}{\mathcal{Q}(r_h)}\\
g^{\rm BH}_{\theta\theta} &= b(r)^2\rho^2\\
g^{\rm BH}_{\varphi\varphi} &= b(r)^2\rho^2\sin^2\theta\,,
\end{aligned}
\tag{III.52}
$$

where, once again, we left implicit the dependence of $b(r), f(r)$ on r_h, which is now a function of ρ. Anyway, we stress that, neglecting the ρ dependence in the Einstein equations, the asymptotic behaviour of Eqs. (III.33)-(III.37) is still valid, and, in the UV, the only dependence of $b(r), f(r)$ on $r_h(\rho)$ is through $\mathcal{G}(r_h)$ and $C(r_h)$. This is important because, as we are going to see, the UV behaviour of the metric is the only relevant entity for determining the action. Notice that, for simplicity of notation, and in contrast to the discussion in Sec. (III.4.1), we do not distinguish between ρ and $\tilde{\rho}$ coordinates. Rather, we will explicitly rescale the relevant metric components in the thermal gas metric discussed below.

III.4.2.2 Thermal Gas Metric

We now turn the attention to the metric of the thermal gas. Even though, in this case, there is no horizon and no order parameter r_h, one must reintroduce it in such a way that the solution matches the UV behaviour of the BH one, in the sense discussed in Sec. (III.4.1).

We start from the simple metric of Eq. (III.53). As discussed in Sec. (III.4.1), we need to modify it to have, at the UV cut-off $r=\epsilon$, the same physical 3-volume and the same proper length of the time circle as for the BH metric. Thus, we improve the metric as follows:

$$
ds^2 = b_0^2(r)\left(dr^2 - \frac{b(\tilde{\epsilon})^2}{b_0(\epsilon)^2}f(\tilde{\epsilon})\,dt^2 + \frac{b(\tilde{\epsilon})^2}{b_0(\epsilon)^2}\,d\vec{x}^2\right)
\tag{III.53}
$$

This ansatz is enough to get a finite effective action for constant r_h. Notice that, assuming ϕ_0 only depends on r, the equations of motion for ϕ_0 and thus their solution are not affected by the new metric.

In the next step, one would like to further improve this metric, including terms that depend on $r_h'(\rho)$, vanish in the $r_h'(\rho)\to 0$ limit, and reproduce the divergent behaviour of the BH metric in the UV, in such a way that the difference of the two actions remains finite also at order $r_h'(\rho)$. Unfortunately, we were not able to determine such a metric. We discuss below in Sec. (III.4.4) how we circumvented this problem for to obtain the kinetic term. Following the logic above, we nevertheless define a "best guess" for the TG metric, which will use to validate our estimate of the kinetic term in Sec. (III.4.4):

$$
\begin{aligned}
g^{\rm TG}_{rr} &= b_0^2(r)\\
g^{\rm TG}_{tt} &= -b_0^2(r)\,\frac{b(\tilde{\epsilon})^2}{b_0(\epsilon)^2}f(\tilde{\epsilon})\\
g^{\rm TG}_{\rho\rho} &= b_0^2(r)\,\frac{b(\tilde{\epsilon})^2}{b_0(\epsilon)^2}\left[1+\frac{r_h'(\rho)^2}{f(\tilde{\epsilon})}\left(\frac{\mathcal{Q}(r_h)-2(r_h-\frac{\tilde{\epsilon}}{\epsilon}r)\mathcal{Q}'(r_h)}{\mathcal{Q}(r_h)}\right)^2\right]\\
g^{\rm TG}_{\rho r} = g^{\rm TG}_{r\rho} &= -b_0^2(r)\,\frac{b(\tilde{\epsilon})^2}{b_0(\epsilon)^2 f(\tilde{\epsilon})}\,r_h'(\rho)\,\frac{\mathcal{Q}(r_h)-2(r_h-\frac{\tilde{\epsilon}}{\epsilon}r)\mathcal{Q}'(r_h)}{\mathcal{Q}(r_h)}\\
g^{\rm TG}_{\theta\theta} &= b_0^2(r)\,\frac{b(\tilde{\epsilon})^2}{b_0(\epsilon)^2}\rho^2
\end{aligned}
$$

$$g^{\rm TG}_{\varphi\varphi} = b_0^2(r)\,\frac{b(\tilde\epsilon)^2}{b_0(\epsilon)^2}\rho^2\sin^2\theta\,, \tag{III.54}$$

III.4.3 Effective potential

We compute the effective action as the classical action of the system evaluated on a particular field and metric configuration:

$$\mathcal{S} = -\,M_P^3N_c^2\int \mathrm{d}^5x\sqrt{g}\left[R - \frac{4}{3}(\partial\phi)^2 + V(\phi)\right] + 2M_P^3N_c^2\int_{\partial M}\mathrm{d}^4\sqrt{h}K + \mathcal{S}_{\rm ct}\,, \tag{III.55}$$

where the second piece is the Gibbons-Hawking action computed on the boundary surface and the last one is the counterterms action. The latter cancels when subtracting the thermal gas contribution, and we will neglect it in the following. On a BH solution, the spherical cap term in Eq. (III.49) has to be included in $\mathcal{S}$. Taking the trace of the Einstein equation, the Ricci scalar becomes

$$R = \frac{4}{3}(\partial\phi)^2 - \frac{5}{3}V(\phi)\,. \tag{III.56}$$

and the action simplifies to

$$\mathcal{S} = \frac{2}{3}M_P^3N_c^2\int \mathrm{d}^5x\sqrt{g}\,V(\phi) + 2M_P^3N_c^2\int_{\partial M}\mathrm{d}^4\sqrt{h}K\,. \tag{III.57}$$

Equation (III.57) is valid everywhere except, in the BH case, on the regularized tip of the cone, the action of which has to be added separately.

The Einstein equations can be used to further simplify the first term. Being interested in the effective potential $V_{\rm eff}(\lambda_h)$, we can neglect the ρ dependence of $b, f, g_{\mu\nu}$ and all derivatives ∂_ρ in the eom. One can use the eom for constant r_h, derived in App. A of Ref. [148]:

$$6\frac{\dot b^2}{b^2} + 3\frac{\ddot b}{b} + 3\frac{\dot b}{b}\frac{\dot f}{f} = \frac{b^2}{f}V \tag{III.58}$$

$$6\frac{\dot b^2}{b^2} - 3\frac{\ddot b}{b} = \frac{4}{3}\dot\Phi^2 \tag{III.59}$$

$$\frac{\ddot f}{f} + 3\frac{\dot b}{b} = 0\,. \tag{III.60}$$

The Einstein-Hilbert (bulk) term of Eq. (III.57) is a total derivative ([148], App. C)

$$\begin{aligned}\mathcal{S}^{r_h'=0}_{\rm EH,BH} = \frac{2}{3}M_P^3N_c^2\int \mathrm{d}^5x\sqrt{g}\,V(\phi) &= 2M_P^3N_c^2\,\beta\int \mathrm{d}^3x\int_{\tilde\epsilon}^{r_h}\mathrm{d}r\frac{d}{dr}(f\,b^2\,\dot b)\\ &= -2M_P^3N_c^2\,\beta\int \mathrm{d}^3x f(\tilde\epsilon)\,b(\tilde\epsilon)^2\,\dot b(\tilde\epsilon)\end{aligned} \tag{III.61}$$

for the BH and

$$\begin{aligned}\mathcal{S}^{r_h'=0}_{\rm EH,TG} &= 2M_P^3N_c^2\,\beta\int \mathrm{d}^3x\,\frac{b(\tilde\epsilon)^4 f(\tilde\epsilon)^{1/2}}{b_0(\epsilon)^4}\int_\epsilon^\infty \mathrm{d}r\frac{d}{dr}(b_0^2\,\dot b_0) =\\ &= -2M_P^3N_c^2\,\beta\int \mathrm{d}^3x\,\frac{b(\tilde\epsilon)^4 f(\tilde\epsilon)^{1/2}}{b_0(\epsilon)^2}\,\dot b_0(\epsilon)\end{aligned} \tag{III.62}$$

for the TG, where the contribution at $r \to \infty$ vanishes as the singularity is of a "good" type [148].

The Gibbons-Hawking term is computed as follows. One starts from defining the boundary manifold as $F = 0$ with $F = \epsilon - r$ in the thermal gas case and $F = \tilde{\epsilon}(r_h(\rho)) - r$ for the black hole. Then the definition of the outgoing normal vector follows: $n_\alpha = \partial_\alpha F$. The trace of the extrinsic curvature K is defined as $K = -\nabla_\alpha n^\alpha$, where ∇ is a covariant derivative. We then obtain the Gibbons-Hawking action

$$\mathcal{S}^{r_h'=0}_{\rm GH,BH} = M_p^3 N_c^2 \beta \int \mathrm{d}^3x\, b(\tilde{\epsilon})^2 \left(8 f(\tilde{\epsilon}) \dot{b}(\tilde{\epsilon}) + b(\tilde{\epsilon}) f'(\tilde{\epsilon})\right) , \tag{III.63}$$

for the black hole and

$$\mathcal{S}^{r_h'=0}_{\rm GH,TG} = 8 M_p^2 N_c^2 \beta \int \mathrm{d}^3x\, \frac{b_0'(\epsilon) b(\tilde{\epsilon})^4 \sqrt{f(\tilde{\epsilon})}}{b_0(\epsilon)^2} , \tag{III.64}$$

in the thermal gas case. Note that these two results do not match those of [148], because of the different definition of $\epsilon, \tilde{\epsilon}$ and of the 3-space coordinate rescaling. Anyway, taking the difference, we find the same result.

Finally, the effective action for $r_h' = 0$ is

$$\mathcal{S}^{r_h'=0}_{\rm eff} = \int \mathrm{d}t \int \mathrm{d}^3x\, V_{\rm eff}(\lambda_h) = \mathcal{S}^{r_h'=0}_{\rm BH} - \mathcal{S}^{r_h'=0}_{\rm TG} \tag{III.65}$$

where $\mathcal{S}^{r_h'=0}_{\rm BH}$ is obtained as the sum of Eqs. (III.61), (III.63) and (III.49), and $\mathcal{S}^{r_h'=0}_{\rm TG}$ is the sum of Eqs. (III.62), (III.64). After expanding the functions $b, b_0, f, \tilde{\epsilon}$ as in Eqs. (III.33)-(III.38) one finds a finite value after subtraction:

$$\mathcal{S}^{r_h'=0}_{\rm eff} = M_P^3 N_c^2 \beta \int \mathrm{d}^3x \left[\left(15\mathcal{G}(r_h) - \frac{C(r_h)}{4}\right) - 4\pi b(\lambda_h)^3 \left(1 - \frac{T_h}{T}\right)\right] \tag{III.66}$$

III.4.4 Kinetic term

In this section, we discuss how we can estimate the kinetic term for the order parameter λ_h, inspired by the calculation performed in Ref. [144] for the Randall-Sundrum and for the Witten-Sakai-Sugimoto models. Furthermore in appendix. (III.8.2) we will also display the kinetic term and effective action used in [5] for estimating the GW spectra of SU(3) YM theory.

We allow r_h varying in position $\vec{x}$, and the dependence of b, f, λ on $r_h(\vec{x})$ must be taken into account. We assume that, for a given value of r_h, the metric functions take the same value as in the case where r_h is constant. In other words, we neglect in the equations of motion all the derivatives with respect to $\vec{x}$. We instead include these derivatives in the action, in particular in the calculation of the Ricci scalar, the kinetic term of ϕ and the extrinsic curvature.

Compared to Ref. [144], in IhQCD, the task is complicated by the fact that the functions b, b_0, f are not known analytically, and by the logarithmic corrections to AdS in the UV, which require extra care when taking the expansion. In addition, and differently from the constant r_h case, the prescriptions in Eqs. (III.27), (III.28) are not sufficient to determine

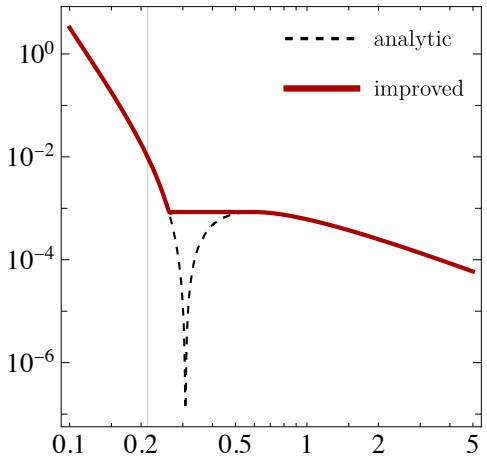

Figure III.4: Normalization coefficient of the kinetic term, in function of λ_h. Shown in black dashed, the analytic ansatz of Eq. (III.67). In red, the improved ansatz, cutting off the region where the former goes to zero. Figures created by E.Morgante

unambiguously a valid ansatz for the thermal gas metric, such that the divergences in the action $\mathcal{S}_{\rm BH} - \mathcal{S}_{\rm TG}$ cancel at order $(\nabla r_h)^2$.

Given the above difficulties, we limit ourselves to an educated guess of the kinetic term, which we will validate below. Firstly, the action is proportional to $M_p^3 N_c^2$. A factor of β comes from integrating along the time component $\int \mathrm{d}t$. Next, we notice that the terms depending on $r_h'(\rho)$ in Eq. (III.52) are, in the UV limit $r \to 0$, proportional to $(1 - 2r_h \mathcal{Q}'/\mathcal{Q})^2$. Finally, the kinetic term, after subtracting the actions of the BH and of the TG solutions, must come from the behaviour in the UV of the scale factor, the cut-off ϵ, and the blackening factor f. These are parametrized in terms of $45/8\,\mathcal{G}$ and $C/4$. Hence, our ansatz for the kinetic term is

$$\mathcal{S}_{\rm eff}^{r_h'=0} = M_p^3 N_c^2\, \beta \int \mathrm{d}^3x\, (\vec{\nabla}\lambda_h)^2 \left(\frac{\partial r_h}{\partial \lambda_h}\right)^2 \left(\frac{45}{8}\mathcal{G}(r_h) + \frac{C(r_h)}{4}\right) \left(1 - 2r_h \frac{\mathcal{Q}'(r_h)}{\mathcal{Q}(r_h)}\right)^2 , \tag{III.67}$$

where we left implicit the dependence of r_h on $\vec{x}$.

A final improvement to our ansatz can be made by noticing that the second term in parentheses in Eq. (III.67) becomes zero around $\lambda_h \sim 0.3$. Although this is not a problem in principle, around that point higher order terms can change this result. Hence, we consider an improved kinetic term obtained by glueing a constant piece around this spurious zero.

In order to compare with existing literature, [5, 140], it is useful to write the action as

$$\mathcal{S} = \frac{4\pi}{T} \int \mathrm{d}^3x \left(c(\lambda_h) \frac{N_c^2}{16\pi^2} (\vec{\nabla}\lambda_h(\vec{x}))^2 + V_{\rm eff}(\lambda_h(\rho), T) \right) \tag{III.68}$$

The coefficient c, which in Ref. [5] was allowed to vary in the range $0.3 - 3$ and is often assumed to be 1 in other models [140], varies between 10^{-6} and 10^{-2} in the range of interest, depending on λ_h. The numerical value is plotted in Fig. (III.4).

We can use the coefficient c to define a canonically normalised field $\tilde{\lambda}_h$ as

$$\mathrm{d}\tilde{\lambda}_h = \sqrt{2c}\frac{N_c}{4\pi}\mathrm{d}\lambda_h\,, \qquad \tilde{\lambda}_h = \frac{N_c}{4\pi}\int_0^{\lambda_h} \mathrm{d}\lambda_h' \sqrt{2c(\lambda_h')} \tag{III.69}$$

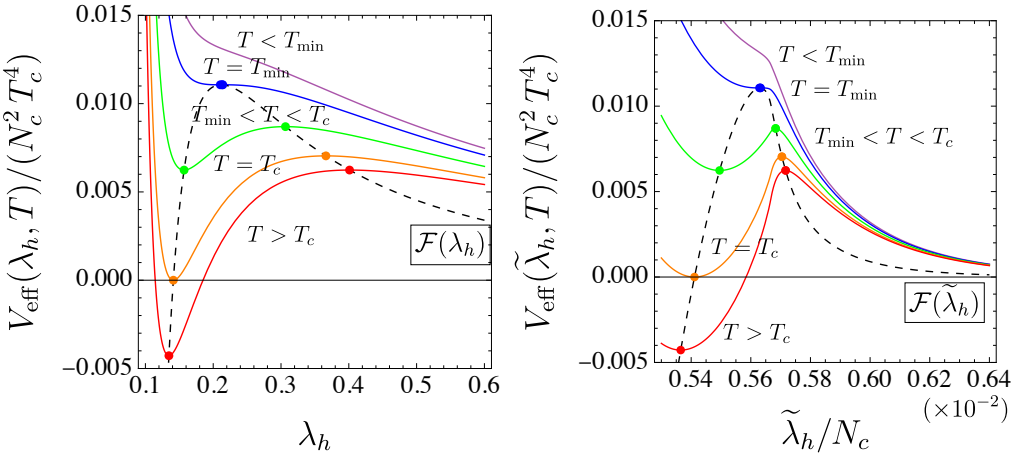

Figure III.5: Effective potential as a function of λ_h (left) and of the canonically normalized field $\tilde{\lambda}_h$ (right). Figures created by E.Morgante

such that the action takes the form

$$\mathcal{S} = \frac{4\pi}{T}\int \mathrm{d}^3x \left(\frac{1}{2}(\vec{\nabla}\tilde{\lambda}_h(\vec{x}))^2 + V_{\rm eff}(\tilde{\lambda}_h(\vec{x}), T)\right) \tag{III.70}$$

where, with slight abuse of notation, we wrote $V_{\rm eff}(\lambda_h(\tilde{\lambda}_h(\vec{x})), T)$ as simply $V_{\rm eff}(\tilde{\lambda}_h(\vec{x}), T)$. Fig. (III.5) show the effective potential, plotted as function of λ_h and of $\tilde{\lambda}_h$.

We check the validity of our ansatz Eq. (III.67) as follows. We use Eq. (III.56) to write the action without referring to the potential $V(\phi)$. We then compute the action on the BH and the TG solution, with the metric of Sec. (III.4.2.1, III.4.2.2), including the dependence of $b, f, \tilde{\epsilon}$ on $r_h(\vec{x})$:

$$b = b(r, r_h(\rho))\,, \quad f = f(r, r_h(\rho))\,, \quad \tilde{\epsilon} = \tilde{\epsilon}(r_h(\rho))\,, \tag{III.71}$$

where $r_h(\rho)$ can be seen as a boundary condition in solving for b, f, λ. Again, at any given position $\vec{x}$ and for a fixed value of $r_h(\vec{x})$, we assume for b, f, λ the same value that they take in the constant r_h case. In particular, the UV dependence is that of Eqs. (III.33)-(III.38). Being interested in spherical bubble configurations, we use spherical coordinates with $\rho = (\vec{x}^2)^{1/2}$ but this is not essential for our result.

Once specified the metric, the computation of the action is straightforward, although tedious. The result can be expanded to second order in $r_h'(\rho)$, with $r_h''(\rho) \sim \mathrm{O}(r_h'^2)$, integrating by parts the terms containing r_h'', thus obtaining the kinetic term from the piece proportional to $(r_h')^2$.

The Gibbons-Hawking action is a boundary term, and has to be evaluated at the UV cutoff. The Einstein-Hilbert action, instead, involves a bulk integral, which requires some extra work. In obtaining the effective potential, a key step was to recognize that the integrand was a total derivative with respect to r, in Eq. (III.61). This allowed us to rewrite the action as a boundary term, evaluated at the UV cutoff. Including the space dependence of r_h, we were not able to prove this explicitly in this case. We nevertheless assumed this was the case. We then expand the metric and λ inside the integral, and integrated in $\mathrm{d}r$ the resulting expression, obtaining a valid boundary term evaluated at the UV cutoff. The action computed this way contains terms diverging as ϵ^{-n} with $n \leq 4$, as $\log\epsilon$ and as $\log(-\log\epsilon)$. The latter are not computed consistently, in the sense that

they arise from integrating the UV expansion, but are of higher order compared to the UV expansion of Eqs. (III.33)-(III.38).

We finally consider the finite part of the action obtained in this way. The result agrees with Eq. (III.67) up to a factor $\mathcal{O}(1-10)$, depending on the precise choice made for the r_h' terms in the TG metric. Although we could not derive a finite and scheme independent result, we consider Eq. (III.67) a valid ansatz, possibly up to an $\mathcal{O}(1-10)$ uncertainty factor.

III.5 Bubble Nucleation and Large N_c dependence

The motivation of extensively working toward formulating an effective action [169, 170] is to understand phase transitions of field theories. The process of nucleating bubbles of true vacuum in a universe filled with false vacua is controlled by the effective action which we have just found in the previous section. The bubble nucleation is driven by two different types of fluctuations either thermal or quantum, that are considered in the different temperature regimes and leads to considering two different actions for the nucleation. For instance, in the high-temperature regime, one works with a $\mathcal{O}(3)$ symmetric action which is always present and incorporates both thermal and quantum fluctuations, meanwhile, in the low/zero temperature limit there are only quantum fluctuations and one then obtains a $\mathcal{O}(4)$ symmetric action. In this work, we will primarily work with the $\mathcal{O}(3)$ symmetric action. The $\mathcal{O}(3)$ symmetric action accounting for spherical symmetry in Eq. (III.70), and performing the integration along the angular directions (θ, ϕ) and the time direction becomes

$$\mathcal{S} = \frac{4\pi}{T} \int d\rho \rho^2 \left(\frac{1}{2} (\vec{\nabla} \tilde{\lambda}_h(\rho))^2 + V_{\text{eff}}(\tilde{\lambda}_h(\rho), T) \right) . \tag{III.72}$$

In which we are working with the canonically normalized field $\tilde{\lambda}(\rho)$ introduced in the previous Sec. (III.4.4). Before we can evaluate Eq. (III.72) we need to solve for the bubble profiles acquired by tunneling between the BBH and the confined Phase. This is done by solving the so-called bounce equation which is nothing else than the associated equations of motion from the effective action, for our case of relevance of $\mathcal{O}(3)$ symmetric solutions the equations of motion are

$$\frac{d^2 \tilde{\lambda}_h}{d\rho^2} + \frac{2}{\rho} \frac{d\tilde{\lambda}_h}{d\rho} - \frac{dV_{eff}(\tilde{\lambda}_h, T)}{d\tilde{\lambda}_h} = 0 . \tag{III.73}$$

Eq. (III.73) is solved by imposing the following boundary conditions that $\tilde{\lambda}_h(0) = \tilde{\lambda}_0 , \tilde{\lambda}_h(\infty) = 0$, for each temperature T where the derivative conditions are set as $\tilde{\lambda}_h(0, \infty) = 0$. Studying the bubble profiles whose shapes entails information about the bubble wall thickness if one is in a thin, intermediate, or thick wall regime. With the bubble profiles at hand and being able to evaluate the integral for the effective action, we are now ready to explore the bubble nucleation dynamics with increasing N_c. The probability of nucleating a bubble of true vacuum out of the meta-stable vacuum is initially governed by the bubble nucleation rate per unit volume [170] for a thermal transition $\mathcal{O}(3)$

$$\Gamma(T) = T^4 \left(\frac{\mathcal{S}}{2\pi T} \right)^{\frac{3}{2}} e^{-\frac{\mathcal{S}}{T}} . \tag{III.74}$$

In Eq. (III.74) the effective action that goes into that is given by Eq. (III.70), where the explicit N_c^2 dependence is in Eq. (III.68). Eq. (III.70) is the action used for calculating the bounce action and the bubble nucleation rate per unit volume is calculated with

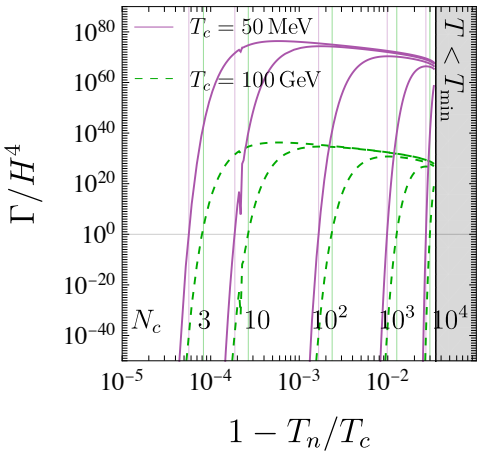

Figure III.6: Nucleation rate per Hubble volume Γ/H^4, for an increasing number of colors N_c. In the $N_c = 10$ purple line the jagged edge is due to numerical difficulty at that intermediate value. Figure created by E.Morgante

Eq. (III.74) [170–172].[11] Hence one may realize that in the strict large N_c limit bubble nucleation will not occur as the instanton action mediating the phase transition i.e. $\mathcal{S}$ becomes infinite. In practice we are mainly interested in two aspects of upscaling the number of colors, first that we work with a large enough N such that we dont have to account for finite N_c corrections, finally to understand at what limit does bubble nucleation become so suppressed that the PT cant complete.
The first consequence of looking at what happens in the large N_c limit governs the nucleation temperature T_n, which is determined by the condition that the nucleation rate per Hubble volume per Hubble time equals 1, i.e.,

$$\frac{\Gamma(T)}{H^4} = 1\,. \tag{III.75}$$

From Eq. (III.75) one can deduce that this condition is satisfied for $\Gamma(T) \sim 150$[12]. In the next section we will visualize explicitly what the impact on the PT parameters are with increasing $N_c = 3...1000$. This will also have crucial impact on the percolation temperature, that roughly indicates the end of the phase transition. It is defined as the time when the probability $\mathcal{P}$ of remaining in the false vacuum is reduced by $\mathcal{O}(30)\%$ [175–177]

$$\mathcal{P}(t) = e^{-I(t_p)}, \tag{III.76}$$

$$I(t) = \frac{4\pi}{3}\int_{t_c}^{t} dt' \Gamma(t') a(t')^3 r(t,t')^3\,, \tag{III.77}$$

where

$$r(t,t') = \int_{t'}^{t} dt'' \frac{v_w}{a(t'')} \tag{III.78}$$

[11] Here we have omitted the contribution from the functional determinant which could potentially have sizable effects see for instance [171–173].

[12] Analogous discussion of looking at large N for phase transitions with holography can be found in [81, 174]. However in this work we will show explicitly when bubble nucleation becomes completely suppressed with increasing N_c

is the radius at time t of a bubble emitted at t'. In this work we have treated the bubble wall velocity to be a constant. One region of special interest is the case right when the bubble nucleation rate becomes so suppressed that it becomes close to/reach T_{min}. T_{min} is the minimal temperature at which the BH solution exists and posessess the interpretation that the confinement PT shall have completed before the system reaches T_{min}. An essential point regarding evaluation of the nucleation/percolation temperatures for N_c values such that one supercools down to T_{min}, is that the instanton action must vanish at the turning point since there is no barrier for nucleation.
When the system has supercooled down to $T_{\min}$, and traversing the TD-unstable Small Black Hole (SBH) branch, it signifies entry into the spinodal instability regime [158, 159]. Recent work [159] has demonstrated that completing the phase transition (PT) in this manner can serve as a potent source for gravitational waves (GWs). The study reveals that the emitted GWs and amplification period of the unstable modes can be qualitatively understood through a hydrodynamic approximation of the dynamics.

Moreover, the authors provide a parametric estimate of the degrees of freedom (DoF) required to suppress bubble nucleation to the extent that the system reaches the metastable limit. Their findings suggest this limit could be achieved for $N \sim 10^5$. In contrast, our model suggests the potential attainment of this limit at $N_c \sim 10^4$. This is indicative as around here it becomes more and more challenging to compute the percolation temperature T_p.

III.6 Gravitational Waves

We now focus on calculating the GW spectrum based on the results and studies presented in the previous sections, where we formulated an effective action valid for all N_c and explored the dynamics of bubble nucleation. To estimate the power and spectral shape of the GW spectrum, we adopt the semi-analytic templates provided by the LISA Cosmology working group LISA (CWG) [90, 91, 178]. We also display in Appendix. (III.8.2) the calculated PT parameters with the effective action we had at hand by the time of that publication. That shall serve as a direct comparison to the change in results by comparing the SU(3) case presented here in this section with the result from [5]. In Appendix. (III.8.2) we also elaborate on the LISA CWG template which was used for calculating the GW spectras presented here.

To compute the GW spectrum with the templates provided by the LISA CWG, we must specify the energy scale of the theory. Pure YM theories are characterized by a single energy scale, with all other scales being proportional to this one. Equivalent choices include the mass of the lightest glueball, the strong coupling scale Λ[13] the confining string tension, or the critical temperature T_c. In SU(3) IhQCD, one finds $m_0 \approx 5.1\Lambda$ and $m_0 \approx 6T_c$, which align well with lattice results [149, 150]. In the subsequent analysis, we will employ T_c to set the energy scale, as it facilitates natural comparisons with the nucleation and percolation temperatures.

An immediate caveat with this approach is that the templates from the collaboration may not be adequate or accurate for strong phase transitions occurring in strongly coupled theories. Nonetheless, we must rely on these results for now, awaiting hydrodynamic simulations in cases where the phase transitions are stronger. The semi-analytic GW spectra templates require only four parameters, a noteworthy simplicity given the highly non-linear dynamics of phase transitions. The essential phase transition parameters for

[13] defined as the energy at which the perturbative coupling constant formally diverges

utilizing these semi-analytic templates include the inverse duration of the phase transition in units of the Hubble time (β/H), the energy liberated during the phase transition (α), the kinetic energy of the bubble walls ($\kappa(\alpha)$), and finally, the bubble wall velocity (v_w). In this study, our focus lies on a dark confining sector devoid of matter, i.e., dark pYM theory. In this scenario, the true vacuum bubbles are expected to experience substantial plasma friction due to strong interactions. As a result, we find it reasonable to assume that the confining phase transition proceeds via non-runaway bubbles, allowing us to solely consider the contribution from sound waves to the GW spectra [179,180]. Our results below will support this claim. While it is theoretically possible to account for turbulence, the uncertainties surrounding this contribution remain debatable. Consequently, we regard our assumption as a conservative estimate. Additionally, we acknowledge the presence of a short-lived source, introducing a suppression effect on the magnitude of the GW spectra [181–184] .

From the previous section of studying the bubble nucleation dynamics and its corresponding large N_c dependence, we have access to the nucleation and percolation temperature of the PT. With these essential results, we can calculate the first of four PT parameters, i.e., β/H which characterizes the number of nucleated bubbles per Hubble volume and it is evaluated at the percolation temperature T_p. For a fast phase transition, one can approximate $\Gamma \sim \exp[\beta(t-t_p)]$, and the inverse duration of the phase transition is given by

$$\frac{\beta}{H} = T\left(\frac{d\mathcal{S}_B}{dT}\right)\Big|_{T=T_n}. \tag{III.79}$$

In Fig. (III.7) we demonstrate explicitly how β/H varies with N_c. In our case for $N_c = 3\ldots1000$ we observe that $\beta/H \propto N^{-1}$ which is in agreement lattice simulations for the surface tension [185], which may indicate that a thin wall approximation might be valid. This is also visible in Fig. (III.7) in which we also performed a fit to the data and obtained a similar scaling. For $N_c = 10^4$ we see an indication that we are entering a different bubble wall profile as the nucleation temperature $T_n \simeq T_{min}$ in which the scaling for $\beta/H \neq N_c^{-1}$. These results are in alignment with [174,186] in their figure 13, to the right. The implication of our results regarding the scaling of β/H as a function of N_c indicates that in the regime of $N_c = 3\ldots1000$ for SU(N) pYM theory the scaling for the surface tension would go linearly with N_c. We will discuss below about the connection between the evolution of the kinetic term $c(\lambda)$ and the emerging relation between β/H and N_c as this makes the discussion more intricate.
Secondly, we need to compute the strength of the phase transition α, i.e. the amount of energy released during the phase transition that is available to convert into the fluid motion of the plasma. We define it as

$$\alpha = \frac{4}{3}\frac{\Delta\theta}{\Delta w} = \frac{1}{3}\frac{\Delta\rho - 3\Delta p}{\Delta w}. \tag{III.80}$$

where θ is the trace of the energy-momentum tensor, w is the enthalpy, and Δ indicates that we take the difference of the corresponding values in the deconfined and confined phases. As well here in Fig. (III.7) we demonstrate how the strength of the transition increases by additional colors in the plasma. A somewhat surprising result from that is the moderately small effect of $\sim \mathcal{O}(30)\%$ for an increase in the dof by 4 orders of magnitude.
In a cosmological phase transition the parameter which is the hardest one to predict is the bubble wall velocity v_w and has obtained large attention over recent years. To calculate the wall velocity even in weakly coupled theories is a daunting task where many recent

advances has emerged [66–74]. Recently it has been been realised that making use of local thermal equilibrium (LTE) can aid the calculations of the wall velocity significantly [75,77]. The calculated wall velocity obtained using the LTE approximation can always be thought of as an upper limit to the wall velocity since external friction forces are omitted in these calculations. LTE has been shown to be a viable tool for bubble wall velocity estimation in both weakly and strongly coupled theories [75–77, 84].Besides LTE in the case of strongly coupled theories holography has also been shown to be a valuable tool for predictions of the wall velocity [79–83].

It was shown in [83, 84] that in the case of small amount of supercooling in a strongly coupled FOPT using Eq 8 in [83] may provide a reasonable estimate of the wall velocity. Here we intend to use this formula as a means to try to provide with an estimate of the bubble wall velocity as a function of N_c. Here we write out the "fits" to the data of how the different PT parameters like nucleation temperature, β/H and the wall velocity in the simple wall approximation Eq. 8 [83].

$$1 - \frac{T_n}{T} \approx 3 \times 10^{-5}\, N_c^{0.9} \tag{III.81}$$

$$\frac{\beta}{H} \approx 10^{7}\, N_c^{-0.85} \tag{III.82}$$

$$v_{\omega,s.w} \approx 8 \times 10^{-5} N_c^{0.9} \tag{III.83}$$

The fits are only properly valid for $N_c = 3 \ldots 1000$, meanwhile for $N_c = 10^4$, the results start to deviate from the fit. This is related with the fact that the nucleation temperature in this case comes very close to the minimal temperature. Provided a direct comparison between the result presented here and in [5] for the PT parameters and their intricate dependence on the input data i.e., $c(\lambda_h)\,, N_c$. Therefore we emphasize the utmost necessity for an even more careful study in order to reveal all the dynamics at play. Hence given the intricate structure and partially spurious features of our kinetic term we find it necessary to also study the impact of the kinetic term throughout the process of tunneling.
We will perform this study in two steps first we will calculate the PT parameters and GW spectra with the full kinetic term and its evolution with λ_h. In the second part we will make a comparison with setting the kinetic term parameter c to three fixed values and evaluate the GW spectra in these cases. The values of c we will take under consideration are $c = 1\,, 10^{-3}\,, 10^{-5}$. These values represent important point in the variation of the full kinetic term and its value troughout the tunneling process and for the positions of the barrier. We will discuss each parameter point individually

- **$c = 1$:** This is a natural parameter point and a direct extension of our previous study in [5] to explore the large N_c dependence and how the dynamics of the PT changes and hence what is the expected amplification of the GW spectrum due to additional supercooling. We illustrate these effects in figure ... where one can find several important insights, first that already at $N_c \sim 10^2$ one hits the limit of supercooling i.e., nucleation becomes so suppressed that the false minima will have enough time to evolve into a saddle point. The effective enhancement in the peak of the GW spectra is not significantly large in the case which is due to primarily two reasons. There would effectively not be any significant magnification in the amount of latent heat released in the FOPT in this case as
- $c = 10^{-3}$**:** In Fig. (III.4) of the improved curve, one can see that this value of the

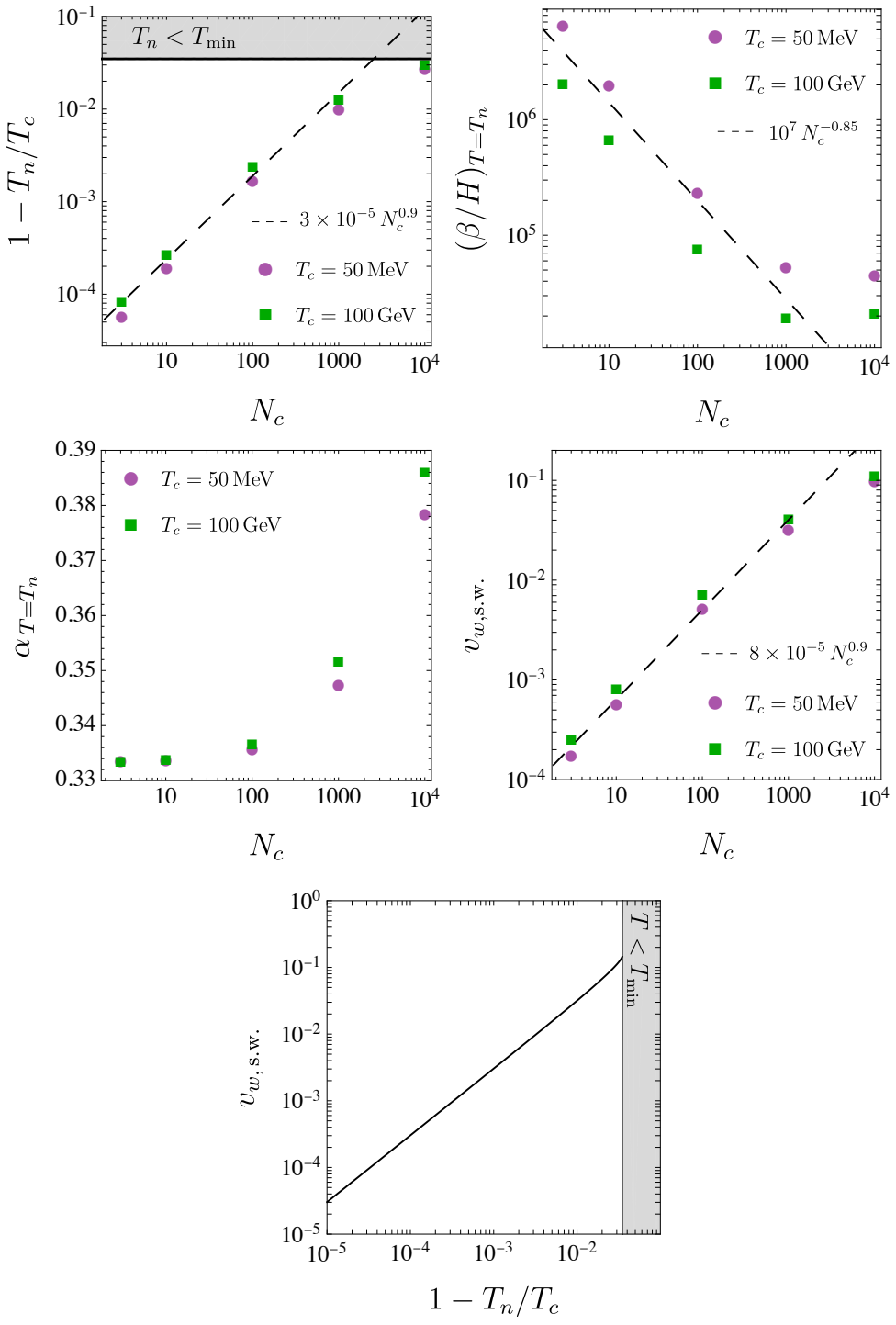

Figure III.7: Phase transition parameters (α , β/H , $v_{w,s.w}$ from [83] both as a function of N_c and nucleation temperature T_n). The grey region $T_n \leq T_{min}$, is marked out as T_{min} is the lowest temperature at which the meta-stable deconfined phase can exist. Figures created by E.Morgante

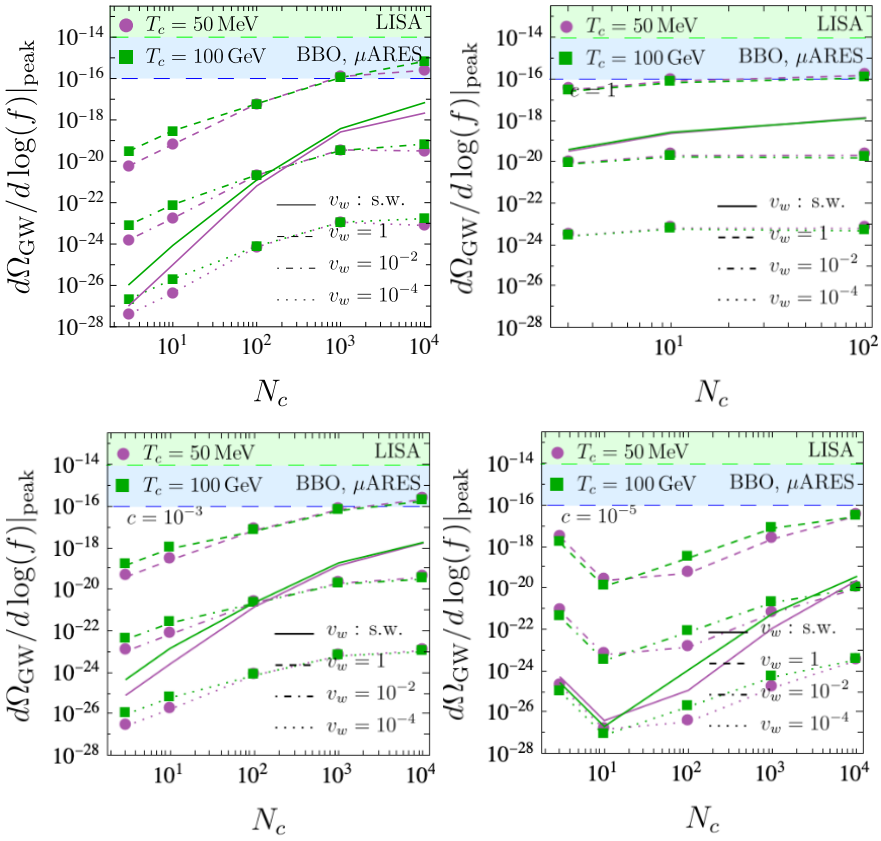

Figure III.8: The evaluated peak frequency of the GW spectra [91] where we analyze the kinetic term and the magnitude of its prefactor. The top left plot is the full kinetic term incorporating its evolution see Fig. (III.4). In the top right figure we have analyzed the value $c = 1$, in the bottom left we have $c = 10^{-3}$, bottom right $c = 10^{-5}$. We display each curve for two choices of the critical temperature $T_c = 0.05, 50$ GeV, and for in total 4 different values of the wall velocity $v_w = 1\,, 10^{-2}\,, 10^{-4}\,, v_{s.w}$ where $v_{s.w}$ is obtained using results from [83, 84]. Figures created by E.Morgante

kinetic term coefficient for the values of λ_h is mainly the dominant one throughout the tunneling process. This also displays itself directly as we can see that it closely resembles the scenario when the full kinetic term is accounted for. Hence it reveals the insight that what matters is the magnitude of the value of the kinetic term coefficient at the temperature of $T_c\,, T_{n,p}$ of the false vacua.

- $c = 10^{-5}$**:** Since we can see from Fig. (III.4) that the analytic evolution of the kinetic term coefficient has the spurious feature of having a "pole" like structure at $\lambda_h = 0.3{-}0.4$ which is around the regimes where the maxima of the effective potential is. Hence it is of utmost importance to proceed with future investigations of this matter to resolve this issue, and an alternative approach by the author of this thesis is in the making by utilizing hydrodynamical quantities to formulate an effective action. Therefore we wanted to investigate the qualitative features of the FOPT in the regime of very small c to try to understand its impact on the bounce calculations. Some non-trivial features present themselves, like an intermediate decrease in the GW spectra between $N_c = 3 - 100$. One possible reason for this spurious feature may be due to numerical issues as the tunneling becomes more and more intractable to calculate as the PT becomes so fast that one essentially tunnels right at T_c.

Statement of a potential upper limit on GWs from these models due to the presence of a minimal temperature and hence a "cap" on the amount of supercooling. This bound on the FOPT is therefore a potential upper bound on the predicted GW spectra. In the case which $N_c, c(\lambda_h)$ are valued such that one is close to have $T_n \simeq T_{min}$ shall imply from the value of $\beta/H \sim 2 \cdot 10^4, \alpha \sim 0.38, v_{w,(s.w)} \simeq 0.2$ [83, 84] in the case with the full kinetic term. However the interplay between the Nc scaling and the value of the kinetic term however by comparing the cases with $c = 1, c = 0.001$ becomes more interesting as their relative scalings against each other to counteract their impact may be more non-trivial.

III.7 Discussion & Conclusions

GWs resulting from FOPTs in the early universe serve as clear indicators of new physics, especially considering that phase transitions in the SM of particle physics—specifically, the EW and QCD phase transitions—are known to be cross-overs. In this study, we explore a well-motivated theory that inherently predicts a FOPT, namely SU(N_c) YM theory for $N_c \geq 3$. We treat this theory as decoupled from the SM plasma, with interactions limited to gravity, which is a plausible scenario, particularly in the context of particle candidates for CDM, and in the string landscape.

Building upon our prior research [5], we address some of its limitations and expand the scope of study from SU(3) to SU(N_c). Each section and its contents are elaborated on in chronological order. In Sec. (III.2), we start off with a brief review of the IhQCD framework, which successfully reproduces lattice results for the equilibrium thermodynamics of SU(N_c) YM theory. We delve into the solution of the associated equations of motion and reveal how basic thermodynamic relations are derived from a holographic construction.

Moving on to Sec. (III.3), we present a qualitative overview of the temperature evolution of the plasma. Additionally, we provide insights into the fitting process for the lattice data of equilibrium thermodynamics. Initially, we revisit the fitting methodology employed in [150], where the free parameters of the dilaton potential were determined to ensure pressure and latent heat per unit volume matched the data for a point at $T = 2T_c$. While this approach yielded satisfactory results, our goal was to assess potential improvements. Introducing a χ^2 minimization with parameters V_1 and V_3, we observed an enhanced overall fit with a reduction in χ^2 by a factor of 2.

In Sec. (III.4), we guide the reader through the step-by-step calculation of the effective action. The qualitative picture that the reader should have in mind is that here we construct the effective action on the gravity side of the correspondence i.e., the dual to the 4-D quantum effective action. We begin by reviewing on-shell regularized actions within the subtraction scheme, offering the necessary motivation for the correct black hole/thermal gas (BH/TG) metric ansatz. Following this, we calculate the effective potential and conclude by determining the kinetic term. In comparison to our previous work in [5], we find that the coefficient $c(\lambda_h)$ associated with the kinetic term is roughly three orders of magnitude smaller than our initial assumption[14]. The derivation of the effective action with a justified kinetic term constitutes the primary result of this work. The subsequent results of this paper explore the implications of this finding on bubble nucleation, the large N_c dependence, phase transition parameters, and the GW spectrum.
In Sec. (III.5), we leverage our effective action to scrutinize bubble nucleation, exploring its large N_c dependence and the influence of the new kinetic term coefficient. We calculate both nucleation and percolation temperatures as functions of N_c and employ these values

[14] In our previous work we imposed a kinetic term of the form [140]

to compute the GW spectra, discussed in Sec. (III.6). Here, we elucidate how the PT parameters, the PT rate β/H, the amount of latent heat α, the wall velocity v_w, and the nucleation temperature T_n—depend on N_c. Striking results emerge, such as the nearly linear increase in the duration of supercooling with N_c, in comparison to the results found in [174, 186]. Additionally, we find that $\beta/H \propto A/N_c$, where A is a constant.

Despite considering the very large N_c regime, we observe that α experiences only a $\sim \mathcal{O}(10)\%$ correction for $N_c = 3...1000$, suggesting a mild dependence on latent heat with increasing N_c, in alignment with quantitative arguments in the lattice community. Moreover, we illustrate the N_c dependence on $v_w(N_c)$ through recent advancements [83,84], indicating a small wall velocity, as suggested by various works [82, 83, 159]. We combine these findings to illustrate the GW peak frequencies dependency on the number of colors, as depicted in Fig. (III.8). It becomes evident that despite additional supercooling with increasing N_c, the impact of the small kinetic term in the effective action dominates, resulting in an overall suppression of the GW spectra by roughly three orders of magnitude. The precise correlation between the evolution of the kinetic term coefficient $c(\lambda_h)$ and the predicted N_c^2 scaling in the effective action remains intriguing.

As we have seen in this work that an understanding of the relation among the two is essential for an understanding of the types of bubbles one nucleates and the potential GW phenomenology of these theories. The fact that in these holographic constructions of pYM the excistence of a cut-off in the amount of supercooling which was also emphasized in [84] to understand the prohibitance of obtaining very large wall velocities. This allures the question what would the "optimal" configuration for the kinetic term coefficient $c(\lambda_h)$, and N_c^2 with $T_p \gtrsim T_{min}$ for maximizing the potential GW spectra. Could this be a universal upper bound on the GW spectra in these models? Furthermore the fact that as the PT can supercool down until T_{min} and enter a spinodal instability regime in which the modes with the lowest β/H were to be within the instability band in which one may ask how much would this alter the GW phenomenology for SU(N_c) pYM theories. We plan to elaborate on this in the enar future.

Although the signals presented here are considerably weaker than previously anticipated by the community [5, 187–190]. The conclusions drawn from calculations of the effective action, the amount of supercooling, and the relatively small wall velocities [81, 83, 84], the overall motivation for using GWs to probe dark sectors remains compelling. This is particularly true since gravitational interactions are guaranteed to be present between visible and dark sectors, making GWs a robust avenue for exploration.

Main result: Previous estimates regarding the GW signal from SU(3) YM theory have been demonstrated to be overestimated by as much as five orders of magnitude. This discrepancy arises when incorporating a more precise formulation of the effective action and an actual estimate of the bubble wall velocity instead of imposing phenomenological optimism. Notably, the GW template formulas provided by the LISA CWG suggest utilizing the maximum velocity between the terminal velocity and the sound speed. This underscores the critical importance of theoretical accuracy in predicting stochastic GW backgrounds if our community hopes to have a realistic chance of observation. While we do not assert that our work fully addresses this need, it unequivocally highlights significant gaps in our understanding.

III.8 Appendix

III.8.1 SU(3) Thermodynamics with IhQCD using Scalar Variables

To solve the system of the equation given by Eq. (II.9)-(II.7) we employ the approach of scalar variables introduced in section 7 in [148], where the number of equations and the order of the equations get reduced into an equation system comprised of 2 equations which are both first order. To employ this mathematical trick one first has to go over to using $\lambda = N_c e^{\Phi}$, and the main idea is to use λ as the radial coordinate since the way the scalar functions are defined they are invariant under diffeomorphisms of the radial coordinate. The scalar variables defined as

$$X(\lambda) = \frac{\lambda'(\lambda)}{3A'(\lambda)}\,, \qquad Y(\lambda) = \frac{f'(\lambda)}{4f(\lambda)A'(\lambda)}\,, \tag{III.84}$$

then by performing these substitutions into the equations of motion and manipulating them one obtains the following set of first-order equations

$$\lambda\frac{dX}{d\lambda} = -\frac{4}{3}\left(1 - X^2 + Y\right)\left(1 + \frac{3}{8X}\frac{\lambda d\log V}{d\lambda}\right) \tag{III.85}$$

$$\lambda\frac{dY}{d\lambda} = -\frac{4}{3}\left(1 - X^2 + Y\right)\frac{Y}{X} \tag{III.86}$$

$$Y \to \frac{Y(\lambda_h)}{\log\left(\frac{\lambda_h}{\lambda}\right)}, Y(\lambda_h) = \frac{9\lambda_h V'(\lambda_h)}{32V(\lambda_h)} \tag{III.87}$$

$$X \to -\frac{4}{3}Y(\lambda_h). \tag{III.88}$$

The first two equations are the evolution equations for X, Y, meanwhile, the last two lines describe the Boundary condition one imposes at the black hole horizon position λ_h (BHH) position.So given our potential $V(\Phi)$ expressed in $V(\lambda)$ to solve the above system of equations one numerically integrates from an initial value denoted λ_0 which shall set to be small such that one remains deep in the UV to the dilaton field value at the black hole horizon λ_h. The zero temperature solution is retrieved in this set of equations by simply setting $Y = 0$.

The boundary conditions one imposes at the horizon is a series expansion in λ for values very close to the set BH horizon value λ_h so one can incorporate more terms for higher precision. The numerical technique is that one integrates from a value ϵ away from the actual value of the horizon λ_h which is indicated by the arrows that for X, Y given a particular λ_h one approaches these values. The numerical procedure used here is that for a λ_0 value, which remains fixed and chosen to be small provided that the solutions X, Y remain in numerical control. Having the previously mentioned property in mind, then perform numerical integration of the equations for a large set of λ_h values, and interpolate between different solutions given that the step-size is small enough not to induce any possible errors. Once the functions X, Y are determined with enough BH solutions such that the interpolation in between them does not induce errors the metric functions are then determined as

$$A(\lambda) = A(\lambda_0) + \int_{\lambda_0}^{\lambda}\frac{d\tilde{\lambda}}{3X(\tilde{\lambda})\tilde{\lambda}}, \tag{III.89}$$

$$g(\lambda) = \log f(\lambda) = \int_{\lambda_0}^{\lambda}\frac{4Y(\tilde{\lambda})}{3X(\tilde{\lambda})\tilde{\lambda}}d\tilde{\lambda} \tag{III.90}$$

$$\frac{f'(\lambda)}{f(\lambda)} = g'(\lambda) = -\frac{4Y(\lambda)}{l}\exp\left\{\left(-\frac{4}{3}\int_{\lambda_0}^{\lambda}\frac{X(\tilde{\lambda})}{\tilde{\lambda}}d\tilde{\lambda}\right)\right\}. \tag{III.91}$$

From the set of equations Eq. (III.89) -Eq. (III.91) provided the solutions for X, Y i.e. Eq. (III.85) - (III.86), for a large enough set of λ_h values along with the appropriate boundary conditions at the horizon i.e. Eq. (III.88), Eq. (III.87), the metric functions $b(\lambda) = \exp\{A(\lambda)\}, f(\lambda)$ are determined by knowledge of X, Y. By combining Eq. (III.90), Eq. (III.91) one can determine $f'(\lambda)$ so that the metric functions $A(\lambda), f(\lambda), f'(\lambda)$ are unambiguously determined as functions of the scalar variables X, Y. Furthermore with the equations Eq. (III.89) - Eq. (III.91) we can use the expressions previously showed in Sec. (III.2) to calculate the relevant thermodynamical properties in terms of the scalar variables. From the thermodynamical basic quantities like $S, T, \mathcal{F}$ we can also go further and reduce a direct equation for $\frac{s}{T^3}$ in terms of the dilaton potential and the scalar variables. This is Eq 7.38 in [148] which we illustrate here

$$\frac{s}{T^3} = \frac{4\pi^2(12M_p\ell)^3}{\ell^6}\frac{e^{-4\int_0^{\lambda_h}\frac{d\lambda}{\lambda}X(\lambda)}}{V(\lambda_h)^3}\,. \tag{III.92}$$

This equation allows one to directly get access to one of the lattice observables only by knowledge of the scalar variable X, and the dilaton potential. One can also find an equally useful relation regarding the temperature of the system

$$T(\lambda_h) = \frac{Y(\lambda_0)}{\pi\ell}e^{A_0-\int_{\lambda_0}^{\lambda_h}\frac{1}{\tilde{\lambda}}\frac{1}{X(\tilde{\lambda})}d\tilde{\lambda}}\,, \tag{III.93}$$

where one obtains the temperature at a fixed λ_h from the initial condition on A_0, the UV value of the scalar variable $Y(\lambda_0)$ and integration of the scalar variable X. These equations are more under control numerically and provided that one has imposed a UV numerical cutoff value i.e. λ_0 and accounted for appropriate normalization the solution remains numerically stable. One can obtain the system's free energy by using the first law of thermodynamics once one has the entropy of the system which is given by the Beckenstein Hawking formula Eq. (III.19). The free energy is given by

$$\mathcal{F}(\lambda_h) = \int_{\lambda_h}^{\infty} d\bar{\lambda_h} S(\bar{\lambda_h})\frac{dT(\bar{\lambda_h})}{d\bar{\lambda_h}}\,, \tag{III.94}$$

where one in practice imposes a cut-off for the integration range at some value $\Lambda_h >> \lambda_{h,min}$. Hence the value of Λ_h provides a systematic check on the validity of Eq. (III.94). Nevertheless with these formulas and expressions at hand and how they are related to the scalar variables one has everything that is needed to study the equilibrium thermodynamics of the system. To determine the critical temperature $T_c = T(\lambda_{h,c})$, one finds the corresponding λ_h value which makes $\mathcal{F}(\lambda_h) = 0$. Even though one has the relation for the entropy density directly expressed in terms of the scalar variable X and the dilaton potential one cannot circumvent the fact that one needs T_c to set the appropriate scale. In the last part of this section we intend to illustrate the findings of the fit-to-lattice data found in [5] making direct use of the scalar variables illustrated here.

With $(T, \mathcal{F}, S)$ given by Eq. (III.92) - Eq. (III.94), we can calculate the energy density ρ, pressure P, and $\theta = \rho - 3P$ and compare them to lattice results. Lattice observables of equilibrium thermodynamical quantities are extracted mainly in the continuum limit[15],

[15] For an extensive introduction into lattice gauge theory and how their observables are constructed we refer to Refs. [154–157].

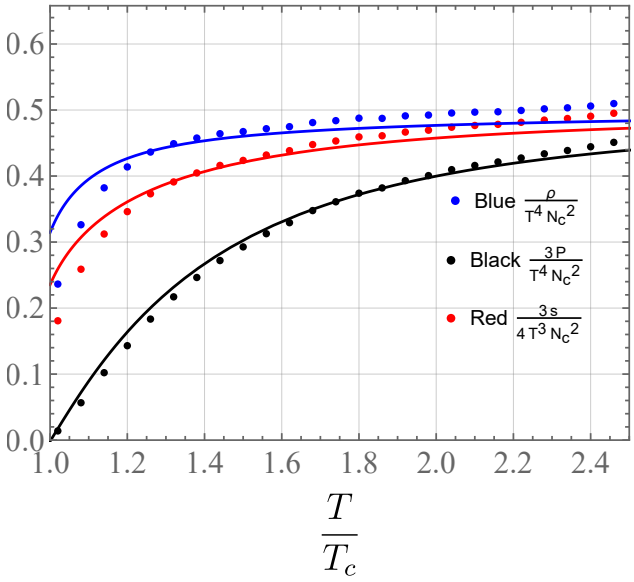

Figure III.9: SU(3) equilibrium thermodynamics from [166] in dotted points and where the lines are the prediction from IhQCD for the dilaton potential parameters $V_1 = 14$ $V_3 = 170$. The y-axis ends at the SB-limit for the thermal gas limit of $\frac{\pi^2}{15}$.

where the error induced by the lattice spacing gets minimized. As shown in this thesis by performing a more quantitative fitting procedure one may obtain better results for the overall fit. The results of the fit to the lattice data in [5] are shown in Fig. (III.9), together with the parameter values for $V_1\,, V_3$.

III.8.2 GW spectra from SU(3) pYM with old kinetic term.

The intent here is to provide a comparison to the results regarding the GW spectra shown above from the results obtained in [5]. Here we employed the same strategy as explained above where instead of calculating the kinetic term imposed the phenomenological ansatz as in [140]

$$c\frac{T_c^2 N_c^2}{16\pi^2}(\vec{\nabla}\lambda_h)^2\,, \tag{III.95}$$

and we varied c in the range, of $0.3-3$. The bounce action here was the sum of Eqs. (III.66) and (III.95), computed on the bounce solution:

$$\mathcal{S}_B = \frac{4\pi}{T}\int \mathrm{d}r\, r^2 \left[c\frac{N_c^2}{16\pi^2}(\partial_r\lambda_h(r))^2 + V_{\text{eff}}(\lambda_h(r), T)\right] \tag{III.96}$$

where we assumed an $\mathcal{O}(3)$ symmetric action, as we were interested in thermal tunneling. The bounce solution is obtained using the shooting method with boundary conditions $\lambda_h(r\to\infty) = \lambda_h^{\text{BBH}}$ and $\partial_r\lambda_h(r)|_{r=0} = 0$. We double-checked our results using the publicly available code FindBounce [191]. The tunneling rate per unit volume and time is then [170]

$$\Gamma = T^4\left(\frac{\mathcal{S}_B}{2\pi}\right)^{3/2} e^{-\mathcal{S}_B}\,. \tag{III.97}$$

We start by estimating the nucleation and percolation temperatures as functions of the critical temperature T_c. The nucleation temperature T_n is determined by the condition that the nucleation rate per Hubble volume per Hubble time equals 1, i.e., $\Gamma(T)/H^4 = 1$.

	α	$\beta/H\,(v_w = 1)$	$\beta/H\,(0.1)$	$\beta/H\,(0.01)$
$T_c = 50\,\text{MeV}$	0.343	9.0×10^4	8.6×10^4	8.2×10^4
$100\,\text{GeV}$	0.343	6.8×10^4	6.4×10^4	6.1×10^4

Table III.1: Values of β/H and α for different wall velocities and critical temperatures. All entities are evaluated at the percolation temperature $T_p = 0.993 T_c$.

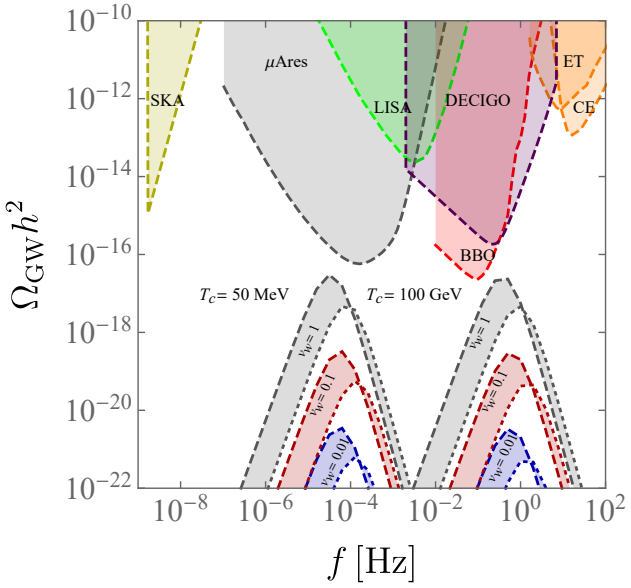

Figure III.10: Gravitational wave spectra estimated with our effective action for IHQCD and the projected sensitivity curves for future GW experiments: Square Kilometer Array (SKA) [61], μAres [59], LISA [57], DECIGO/BBO [116], Einstein Telescope (ET) [55], and Cosmic Explorer (CE) [53]. For illustration, we choose a critical temperature $T_c = 50\,\text{MeV}$ and $T_c = 100\,\text{GeV}$, and the contours denote $v_w = 1$ (gray), $v_w = 0.1$ (red) and $v_w = 0.01$ (blue).

For $c = 1$, we obtain $T_n = 0.992 T_c$ for $T_c = 100\,\text{GeV}$ and $T_n = 0.993 T_c$ for $T_c = 50\,\text{MeV}$. Having T_n close to T_c is not unexpected, as it could be estimated from thermodynamics using some lattice input (see e.g. Ref. [192]). At that point we were able to calculate $\alpha\,, \beta/H$, and $\kappa(\alpha)$ in the case where the wall velocity is assumed to be close to one with Eq. (III.100). At the time of this publication, we treated the bubble wall velocity as a free parameter due to its significant intricateness and large spread of what one may expect within the community at the time. In Tab. (III.1) we present the calculated values for $\alpha\,, \beta/H$ evaluated at the percolation temperature T_p.

Here, we only concerned ourselves with the sound wave contribution to the GW spectrum [179, 180], also including the suppression of having a short-lived source [181–184]. We employed the templates presented in the works of the LISA Cosmology Working Group [91, 178].

In the context of gravitational waves emitted from FOPT's numerous numerical studies [91, 178, 180, 193, 194] provides the literature with an estimated GW spectrum based on knowledge of the parameters α, β/H, v_w, g_*, T_*. The GW spectra in [91] is parametrized

as a broken power-law

$$\frac{d\Omega_{GW,0}}{d\ln f} = 0.687 F_{GW,0} K^{\frac{3}{2}} \left(H(T_*)R(T_*)\right)^2 \tilde{\Omega}_{GW} C\left(\frac{f}{f_{p,0}}\right), \tag{III.98}$$

where the prefactor $F_{GW,0} = (3.57 \pm 0.05) \cdot 10^{-5} \left(\frac{100}{g_*}\right)^{\frac{1}{3}}$ accounts for the redshift. The expression for K describes the fraction of kinetic energy available during the transition

$$K = \frac{\kappa(\alpha)\alpha}{1+\alpha}, \tag{III.99}$$

where

$$\kappa(\alpha) = \frac{\alpha}{0.73 + 0.083\sqrt{\alpha} + \alpha}, \tag{III.100}$$

is the efficiency factor for wall speeds $v_w \approx 1$, which gets modified for lower wall velocities [85]. The scaling of K in Eq. (III.98) indicates that we in this work have a short lived source which induces a suppression to the spectrum of GWs. Furthermore the term $R(T_*)$ is the mean bubble separation evaluated at the percolation temperature, can be related to the inverse transition rate β, as

$$R(T_*) = \frac{(8\pi)^{\frac{1}{3}}}{\beta} \max\left(c_s, v_w\right). \tag{III.101}$$

The term $\tilde{\Omega}_{GW} \approx 10^{-2}$ stems from the numerical simulation as a residual prefactor, and the function $C(f/f_{p,0})$ describes the spectral shape

$$C(x) = x^3 \left(\frac{7}{3+4x^2}\right)^{\frac{7}{2}}, \tag{III.102}$$

$f_{p,0}$ being the peak frequency redshifted until today

$$\begin{aligned} f_{p,0} =& 26 \left(\frac{\beta}{v_w (8\pi)^{\frac{1}{3}} H(T_*)}\right) \left(\frac{z_p}{10}\right) \times \\ & \times \left(\frac{T_*}{100\,\mathrm{GeV}}\right) \left(\frac{g(T_*)}{100}\right)^{\frac{1}{6}} \mu\mathrm{Hz}\,. \end{aligned} \tag{III.103}$$

The term $z_p \approx 10$ appears from the numerical simulation, and T_* denote the temperature when the PT has completed and the GW's are being emitted at this temperature. The aforementioned set of equations are valid when the duration of the sound waves are less than a Hubble time.

Part II

Early Universe Axions

CHAPTER IV

QCD Axions and Mini-Clusters

IV.1 Introduction

The QCD axion [47, 195] is a hypothetical pseudo-scalar particle that emerges within the solution to the strong-CP problem proposed by Peccei and Quinn (PQ) [27, 28, 196]. As reviewed in Sec II.2.1 one introduces a new global $U(1)_{PQ}$ symmetry with a scalar field which is PQ charged. The axion is the angular direction of the scalar Φ after the spontaneous symmetry breaking (SSB) of the $U(1)_{\rm PQ}$ symmetry. QCD anomalies explicitly break the PQ symmetry, reducing it to an approximate global symmetry. More generally, pseudo-scalar particles that couple derivatively to Standard Model (SM) fields are referred to in the literature as axion-like particles (ALPs) [197]. Axions and ALPs arise in various SM extensions through SSB or from string compactification [198].
Along with this theoretical motivation, the QCD axion is also an excellent particle candidate for explaining the missing dark matter CDM observed [199–202]. Here we will consider the QCD axion as the particle candidate of CDM produced through the misalignment mechanism which was introduced in Sec II.2.2.3. We will allure the possibility that the axion possesses a large initial velocity a mechanism referred to as kinetic misalignment [203, 204], despite the conventional assumptions regarding the misalignment mechanism.
In this case, the PQ symmetry is broken explicitly not only by QCD anomalies but also by the radial direction of the PQ field. For instance, a global symmetry is generally not a fundamental field property and gets spoiled by quantum effects. Nevertheless the *quality* of the PQ symmetry has to be protected from these effects in order not to jeopardize the solution of the strong-CP problem [205–207], models in which the PQ symmetry is an accidental symmetry explicitly broken by quantum effects have been constructed [208–212]. In particular, we intend to explore if there are distinct properties of axion-mini clusters emerging from pre-inflationary QCD axions within the kinetic misalignment (KM) mechanism. Here we have remained agnostic about the UV dynamics that source the non-zero initial axion velocity but have merely focused on potential observational signatures. Since KM can be accessibly realized in the pre-inflation scenario, we focus on this case, which consists of invoking non-standard scenarios for the formation of the axion inhomogeneities [213–215].

As the relic abundance of axions becomes immensely altered for specific benchmark values of its initial velocity, we utilize this property in the context of the mass function of axion mini clusters (AMCs). In this work, we explore how the characteristic mass of AMCs is affected by different axion production mechanisms. We first provide a brief review of the production of axion DM in the standard misalignment and the KM mechanisms. Then, we

elaborate on the motivation concerning different regimes of the KM mechanism before analyzing its various impacts on the characteristic minicluster mass function as a function of the axion mass. After AMCs form around matter-radiation equality (MRE), the clumping of these structures proceeds to present time. The merging process of the clumping of the matter is a complicated and numerically extensive process typically comprising of N-body simulations [216]. Even though numerical simulations are in place to be able to make confident predictions, the intention here is to draw attention to a scenario that could serve as a motivation for N-body simulations in the future. Here we employ a semi-analytic approach from the evolution of a linear density contrast such as the Press-Schechter (PS) formalism [217, 218].

IV.2 Standard scenario

We consider a SM-singlet complex scalar field Φ, the PQ field, which extends the SM content and which is described by the effective Lagrangian

$$\mathcal{L} = \mathcal{L}_{\rm QCD} + |\partial_\mu \Phi|^2 - V(\Phi) + \mathcal{L}_{\rm int}\,, \tag{IV.1}$$

where $\mathcal{L}_{\rm QCD}$ captures all QCD effects in the SM. The PQ field potential responsible for the SSB of $U(1)_{\rm PQ}$ at the energy scale v_a with coupling λ_Φ,

$$V(\Phi) = \frac{\lambda_\Phi^2}{2}\left(|\Phi|^2 - \frac{v_a^2}{2}\right)^2, \tag{IV.2}$$

and where the term $\mathcal{L}_{\rm int}$ is responsible for the interaction of Φ with other beyond-SM physics, leading to an effective coupling of the field with gluons and other SM particles. The Lagrangian in Eq. (IV.1) is invariant under the continuous shift symmetry

$$a \to a + \alpha\, v_a\,, \tag{IV.3}$$

for a generic value of α that corresponds to a rotation in the complex plane $\Phi \to e^{i\,\alpha}\,\Phi$. After SSB, the complex scalar field can be decomposed in polar coordinates as

$$\Phi = \frac{1}{\sqrt{2}}\,(S + v_a)\; e^{i\,a/v_a}, \tag{IV.4}$$

where the angular direction is the axion a and the radial direction is the saxion S, such that the saxion vacuum mass is $m_S = \lambda_\Phi\, v_a$.

After SSB, the Lagrangian in Eq. (IV.1) reads

$$\mathcal{L} = \mathcal{L}_{\rm QCD} + \frac{g_s^2}{32\pi}\frac{a}{v_a}\,{\rm Tr}\,G_{\mu\nu}\tilde{G}^{\mu\nu} + \frac{1}{2}(\partial_\mu a)^2 - V_{\rm QCD}(a)\,, \tag{IV.5}$$

where g_s is the QCD gauge coupling of the strong force, and $G_{\mu\nu}$ is the gluon field with dual $\tilde{G}_{\mu\nu}$. The effective QCD axion potential $V_{\rm QCD}(a)$ arises from the interaction of the axion with QCD instantons around the QCD phase transition [219] and leads to a mass term for the axion, which would otherwise remain massless in the absence of an explicit breaking of the $U(1)_{\rm PQ}$ symmetry. QCD terms break the continuous symmetry in Eq. (IV.3) explicitly, while leaving a residual $\mathbb{Z}_N$ discrete shift symmetry with N vacua, $a \to a + n\,\pi\,f_a$, with n a natural number and $f_a = v_a/N$ is the axion decay constant. Here, we set $N = 1$. Because of this, the exact form of the axion potential is periodic around the temperature at which the QCD phase transition occurs, $T_{\rm QCD} \simeq 150$ MeV. At high temperatures, the shape of

the potential is well approximated by a cosine potential meanwhile, for $T \ll T_{\rm QCD}$ the shape of the potential is well approximated by its zero temperature prediction which can be computed at the next-to-leading order within perturbation theory [220–222]. Here, we adopt the parametrization

$$V_{\rm QCD}(a) = \chi(T)\ (1 - \cos\theta)\ , \tag{IV.6}$$

where $\theta(t) \equiv a(t)/v_a$ is the axion angle and $\chi(T)$ is the QCD topological susceptibility. Much of the recent effort has been devoted to the numerical evaluation of the functional form of $\chi(T)$ [29–37]. A fit to the numerical results from lattice simulations is [33]

$$\chi(T) \simeq \chi_0 \times \begin{cases} 1\,, & \text{for } T \lesssim T_{\rm QCD}\,, \\ \left(\frac{T}{T_{\rm QCD}}\right)^{-b}\,, & \text{for } T \gtrsim T_{\rm QCD}\,, \end{cases} \tag{IV.7}$$

where $\chi_0 \simeq 0.0216\,{\rm fm}^{-4}$ and $b \simeq 8.16$. At any temperature T, the mass of the axion is $m(T) = \sqrt{\chi(T)}/f_a$, so the axion can be effectively regarded as a massless scalar field as long as the QCD effects can be neglected for $T \gg T_{\rm QCD}$. In the opposite limit $T \ll T_{\rm QCD}$, the mass squared of the axion at zero temperature is [47]

$$m_a^2 \equiv m^2(T=0) = \frac{m_u\, m_d}{(m_u + m_d)^2}\frac{m_\pi^2\, f_\pi^2}{f_a^2}\,, \tag{IV.8}$$

where m_u, m_d are the masses of the up and down quarks, $m_\pi \simeq 140\,{\rm MeV}$ is the mass of the π meson, and $f_\pi \simeq 92\,{\rm MeV}$ is the pion decay constant. Numerically, this gives $m_a = \Lambda_a^2/f_a$, with $\Lambda_a = \chi_0^{1/4} \simeq 75.5\,{\rm MeV}$.

The equation of motion for the axion field obtained from the Lagrangian in Eq. (IV.1) is

$$\ddot\theta + 3\,H(T)\,\dot\theta - \frac{1}{R^2(T)}\nabla^2\theta + m^2(T)\,\sin\theta = 0\,, \tag{IV.9}$$

where a dot is a differentiation with respect to the cosmic time t, $R = R(T)$ is the scale factor, and $H(T) \equiv \dot R/R$ is the Hubble expansion rate. This expression for the evolution of the axion field is a Klein-Gordon equation in the potential of Eq. (IV.6). At any time, the axion energy density is

$$\rho_a(T) = \frac{1}{2}\,f_a^2\,\dot\theta^2 + \frac{1}{2}\,\frac{1}{R^2}\,f_a^2\,(\partial_\mu\theta)^2 + m^2(T)\,f_a^2\,(1-\cos\theta)\ . \tag{IV.10}$$

Equation (IV.9) is solved by evolving the axion field starting from the initial conditions $\theta = \theta_i$ and $\dot\theta = \dot\theta_i$ which are imposed when the saxion field begins to oscillate [203]. We refer to θ_i as the initial misalignment angle, while the initial velocity is usually set as $\dot\theta_i = 0$.[1] In the naive estimation of the axion abundance, Eq. (IV.9) gets solved by considering super-horizon modes for which the gradient term is negligible. More elaborate treatments have to rely on the lattice simulation of Eq. (IV.9) and the interaction of the axion with the radial component of the PQ field. These computations are extremely demanding and lead to conflicting results in the literature. The string network that develops in fully solving Eq. (IV.9) has a spectrum that spans all frequencies from the infrared cutoff $\sim H$ to the ultraviolet (UV) cutoff $\sim f_a$, with a spectral index q. Current simulations can explore scales down to a size in which the behavior seems to be dominated by the UV spectrum

[1] An alternative production mechanism which is valid for a large initial value of the saxion field is parametric resonance [223–226].

with $q < 1$ [41], however recent results seem to be challenged once even more refined grids are used [45]. In this work, we qualitatively remark the differences between the various misalignment scenarios, for which we rely on solving Eq. (IV.9) for super-horizon modes, and we neglect the contribution from strings.

In the misalignment mechanism, the axion field starts to roll about the minimum of the potential once the Hubble friction is overcome by the potential term [199–202]. This occurs around the temperature $T_{\rm osc}^{\rm mis}$ defined implicitly as

$$3\,H(T_{\rm osc}^{\rm mis}) \approx m(T_{\rm osc}^{\rm mis})\,, \tag{IV.11}$$

where generally $m(T_{\rm osc}^{\rm mis}) \ll m_a$. We assume the standard radiation-dominated phase, during which the Hubble rate is

$$H(T) = \frac{\pi}{3}\sqrt{\frac{g_\star(T)}{10}}\,\frac{T^2}{M_P}\,, \tag{IV.12}$$

in which $g_\star(T)$ is the number of relativistic degrees of freedom at temperature T [48] and M_P is the reduced Planck mass. With this assumption, we obtain (see, e.g. Ref. [49])

$$T_{\rm osc}^{\rm mis} \simeq \begin{cases} \left(\sqrt{\frac{10}{\pi^2\,g_\star(T_{\rm osc}^{\rm mis})}}\,M_P\,m_a\right)^{1/2}\,, & T_{\rm osc}^{\rm mis} \lesssim T_{\rm QCD}\,, \\ \left(\sqrt{\frac{10}{\pi^2\,g_\star(T_{\rm osc}^{\rm mis})}}\,M_P\,m_a\,T_{\rm QCD}^{b/2}\right)^{2/(4+b)}\,, & T_{\rm osc}^{\rm mis} \gtrsim T_{\rm QCD}\,. \end{cases}$$

For example, an axion field of mass $m_a \simeq 26\,\mu$eV would begin to oscillate at $T_{\rm osc}^{\rm mis} \simeq 1.23\,$GeV. In the absence of entropy dilution, the axion number density in a comoving volume after the onset of oscillations is conserved,

$$\frac{\rm d}{{\rm d}t}\left[\frac{\rho_a(T)/m(T)}{s(T)}\right] = 0\,, \tag{IV.13}$$

where $s(T) = (2\pi^2/45)\,g_{\star s}(T)\,T^3$ is the entropy density and $g_{\star s}(T)$ is the number of entropy degrees of freedom at temperature T [48]. This last expression gives the present axion density fraction,

$$\Omega_a = \frac{\rho_a(T_\star)}{\rho_{\rm crit}}\,\frac{m_a}{m(T_\star)}\,\frac{g_{\star s}(T_0)}{g_{\star s}(T_\star)}\,\frac{T_0^3}{T_\star^3}\,, \tag{IV.14}$$

where $T_\star$ is any temperature such that $T_\star < T_{\rm osc}^{\rm mis}$, T_0 is the present CMB temperature, and the critical density is given in terms of the Hubble constant H_0 as $\rho_{\rm crit} = 3\,M_P^2\,H_0^2$. The energy density in Eq. (IV.10) is approximated in the limit in which the kinetic energy can be neglected and for a quadratic potential such as

$$\rho_a(T_\star) \simeq \frac{1}{2}m^2(T_\star)\,f_a^2\,\theta_i^2\,, \tag{IV.15}$$

where θ_i is the initial value of the misalignment angle at temperatures $T \gg T_{\rm osc}^{\rm mis}$. As an order of estimate, for $f_a \simeq 10^{12}\,$GeV the correct relic density that matches the observed DM is obtained for initial field values $\theta_i \simeq \mathcal{O}(1)$.[2]

The left panel of Fig. (IV.1) shows the axion relic abundance $\Omega_a h^2$ as a function of θ_i for $f_a = 10^{15}\,$GeV, corresponding to the axion mass $m_a \approx 5.7\,$neV, in the standard misalignment case (i.e., taking $\dot\theta_i = 0$). Since the axion potential is symmetric, hereafter without loss of generality we assume $\theta_i \geq 0$. The solid black and the dotted blue lines in

[2] Astrophysical constraints provide a lower bound on the decay constant requiring $f_a \gtrsim 10^7\,$GeV [50,51].

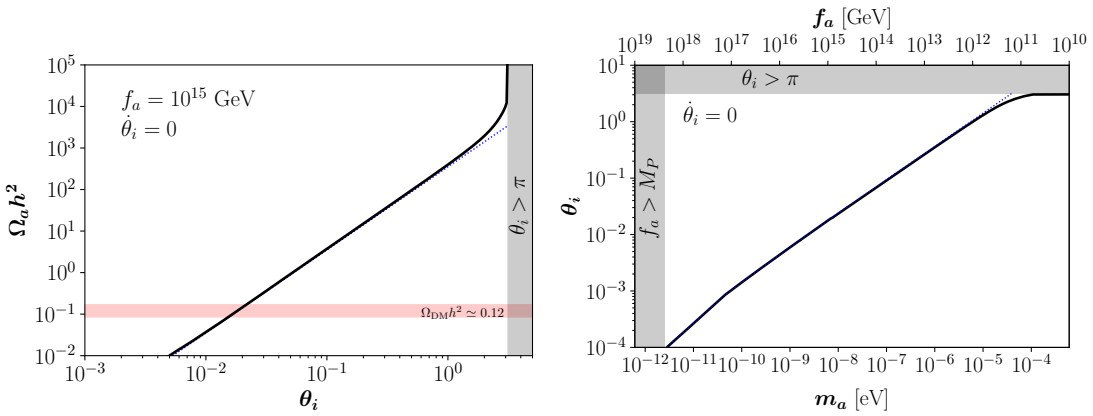

Figure IV.1: Standard scenario. Left panel: Axion relic abundance for $f_a = 10^{15}\,\text{GeV}$, taking $\dot{\theta}_i = 0$. Right panel: Misalignment angle required to match the whole observed DM abundance. The two lines show the comparison between numerical (solid black) and analytical (dotted blue). Figure made by B.Barman

Fig. (IV.1) correspond to the results obtained from the numerical solution of Eq. (IV.9) and the analytical solutions in Eq. (IV.14), respectively. The analytical solution with the quadratic approximation in Eq. (IV.15) underestimates the relic abundance when $\theta_i \simeq \pi$, due to the presence of the non-harmonic terms in the QCD axion potential [49, 227–229]. The red horizontal band showing to $\Omega_a h^2 \simeq \Omega_{\rm DM} h^2$, where $\Omega_{\rm DM} h^2 \approx 0.12$ is the DM abundance today from the *P*lanck satellite measurements [21]. The right panel of Fig. (IV.1) depicts the misalignment angle required to produce the whole observed DM abundance in the standard scenario as a function of the QCD axion mass. The slope changes for $m_a \approx 4.8 \times 10^{-11}\,\text{eV}$, corresponding to the DM axion mass at which the oscillations in the axion field begins around the QCD phase transition $T_{\rm osc}^{\rm mis} = T_{\rm QCD}$. For $f_a \gg 10^{12}\,\text{GeV}$, the initial misalignment angle must be tuned so that $f_a\,\theta_i^2$ is approximately constant to give rise to the observed abundance. For $f_a \ll 10^{12}\,\text{GeV}$, the abundance of cold axions is much smaller than that of DM unless the initial misalignment angle gets tuned to $\theta_i \approx \pi$. In this region of the parameter space, the relevant non-harmonic contributions to the QCD axion potential break the analytic derivation sketched in Eq. (IV.15), and a numerical solution of Eq. (IV.9) is needed.

IV.3 Kinetic misalignment mechanism

A non-negligible initial rotations of complex scalar fields could arise through the Affleck-Dine mechanism [230]. When applied to the PQ field, baryogenesis can be addressed by transferring the PQ charge associated to the rotation of the PQ field to the SM chiral asymmetries, which in turn generate the baryon asymmetry through baryon number-violating processes such as electroweak sphaleron processes [231]. For the sake of generality, we remain agnostic about the detailed mechanism that generate the initial kick of the axion and study the implication caused by such an assumption, although various scenarios have been discussed in the literature in relation with the pre-inflation QCD axion, see e.g. Refs. [51, 203, 204, 231–237].

Our intention with this work is neither to elaborate on how the initial kick is generated in the early Universe nor extensively work out its detailed dynamics once different patches

reach causal contact. We assume that the initial kick is provided by some mechanism acting around the phase transition and we look into what observational consequences this provides.

IV.3.1 Overview

So far, we have reviewed the computation of the DM abundance in the standard scenario in which the initial value of the axion field velocity gets set to zero. Recently, the possibility has been considered that the axion field possesses a non-zero initial velocity $\dot{\theta}_i \neq 0$, which is so large that the potential barriers can effectively be ignored, in the so-called kinetic misalignment (KM) mechanism [203, 204].

In the KM mechanism, the axion possesses an initial velocity $\dot{\theta}_i \neq 0$ corresponding to the rotation of the PQ field Φ in the complex field plane and an overall asymmetry of the PQ charge. At any time, the Noether charge density associated to the shift symmetry of the axion field in Eq. (IV.3) is

$$n_\theta = i\left[\Phi\dot{\Phi}^* - \Phi^*\dot{\Phi}\right] = \dot{\theta}\, f_a^2\,, \tag{IV.16}$$

with the corresponding yield $Y_\theta \equiv \dot{\theta} f_a^2/s(T)$. A necessary condition to generate an initial velocity of the axion field consists in the field value of the radial mode S to be initially much larger than the axion decay constant, $S \gg f_a$, as it occurs in the early Universe. Provided that the PQ potential is sufficiently flat, the desired conditions can be realized by either imposing the appropriate initial conditions of inflation, primordial quantum fluctuations, or in supersymmetric models with flat directions in the superpotential. Another possibility to generate the initial misalignment velocity $\dot{\theta}_i \neq 0$ can emerge from axion models where the axion potential becomes tilted by introducing an explicit symmetry breaking term induced by a higher-dimension potential of the form

$$V_{\rm PQ-break} = M_P^4 \left(\frac{\Phi}{M}\right)^n + \text{h.c.}\,, \tag{IV.17}$$

where $n > 0$ is an integer and M is a new energy scale lying well beyond the SM. The addition of the potential in Eq. (IV.17) would lead to an explicit breaking of the PQ symmetry, and would provide an initial kick to the angular direction of Φ [203].

Two distinct regions exist for this mechanism: in the *w*eak KM regime, the initial velocity allows the axion to explore a few different minima of the potential, while in the *s*trong KM regime the initial axion velocity is so large that the potential barriers can effectively be ignored, and the onset of coherent oscillations gets delayed. In the following subsections, we discuss DM production in these different regimes.

IV.3.2 Weak kinetic misalignment

At high temperatures $T \gg T_{\rm osc}^{\rm mis}$, the potential term in Eq. (IV.9) can be safely neglected and the oscillations in the axion field are damped by the Hubble friction. Therefore, the expression $\ddot{\theta} + 3H(T)\,\dot{\theta} \simeq 0$ predicts $\dot{\theta} \propto R^{-3}$ for any cosmological model. This result can also be obtained from the conservation of the Noether charge n_θ in Eq. (IV.16) [203]. For this reason, if the field possesses a non-zero initial velocity, the kinetic energy term would dominate over the potential energy term and the total energy density would scale as a kination field [238],

$$\rho_a \propto \dot{\theta}^2 \propto R^{-6}\,. \tag{IV.18}$$

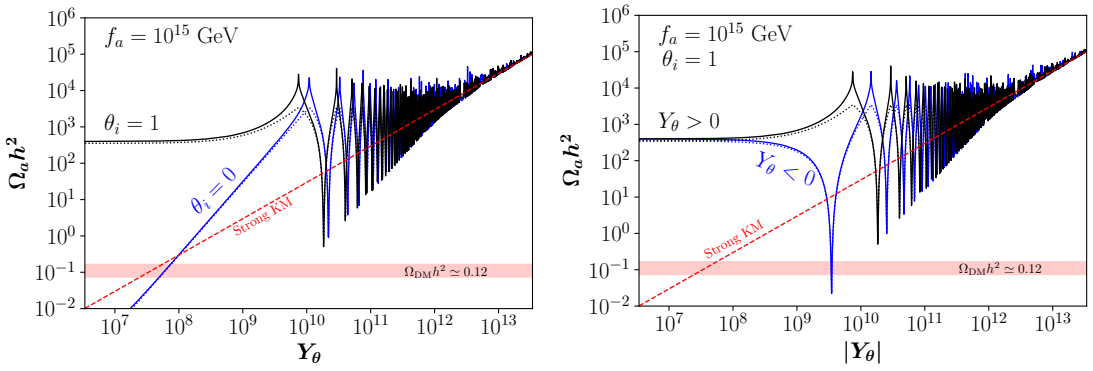

Figure IV.2: Weak KM. Axion relic abundance for $f_a = 10^{15}\,\text{GeV}$. Left panel: $\theta_i = 1$ (black) and $\theta_i = 0$ (blue) for $Y_\theta > 0$. Right panel: $Y_\theta > 0$ (black) and $Y_\theta < 0$ (blue), for $\theta_i = 1$. We show a comparison between numerical results (solid) and the analytical approximation with a quadratic QCD axion potential (dotted). The dashed red line shows the limit of strong KM. Figure made by N.Bernal

Since in a radiation dominated cosmology $H(R) \propto R^{-2}$, the axion field in this configuration would scale as [204]

$$\theta(R) \simeq \theta_i - 2n\,\pi + \frac{\dot\theta(R_i)}{H(R_i)}\left[1 - \frac{R_i}{R}\right], \tag{IV.19}$$

with n being a natural number that counts how many times the axion crosses a potential barrier, and $\theta_i = \theta(R_i)$ is the initial misalignment angle. Equation (IV.19) can be restated in terms of the the dimensionless redshift-invariant yield $Y_\theta \equiv f_a^2\,\dot\theta/s(T)$ as

$$\theta(T) \simeq \theta_i - 2n\,\pi + \frac{Y_\theta}{f_a^2}\frac{s(T_i)}{H(T_i)}\left[1 - \left(\frac{s(T)}{s(T_i)}\right)^{1/3}\right], \tag{IV.20}$$

where T_i is the photon temperature at $R = R_i$. The standard misalignment scenario in Eq. (IV.15) is recovered in the limit $Y_\theta = 0$ and $n = 0$. In this case, $T_{\rm osc}^{\rm mis}$ does not vary with respect to the standard misalignment scenario and Eq. (IV.11) holds. At later times, the Hubble rate dampens the oscillations and the QCD potential becomes relevant.

In the weak KM regime, the value of the misalignment angle θ_i in Eq. (IV.19) required to match the observed DM abundance is modified by the presence of the initial velocity term $\dot\theta(R_i)/H(R_i)$. The parameter space for the KM mechanism is non-trivial and depends on the direction of the velocity $\dot\theta_i$ which changes the sign of the yield Y_θ.

Fig. (IV.2) (left panel) shows the dependence of the axion relic abundance $\Omega_a h^2$ on the redshift-invariant yield $Y_\theta > 0$, for a fixed PQ breaking scale $f_a = 10^{15}\,\text{GeV}$ and for the choices $\theta_i = 1$ (black) or $\theta_i = 0$ (blue). The solid and the dotted lines correspond to the numerical solution and its analytical approximation obtained by considering a quadratic QCD axion potential instead of Eq. (IV.6). The approximation is in good agreement with the numerical result unless for values of the misalignment angle in Eq. (IV.20) near $\theta \simeq (1{+}2n)\pi$, corresponding to the peaks in the cosine potential. For small initial velocities, the axion energy density is dominated by the potential, therefore a larger initial misalignment angle $\theta_i \approx 1$ gives rise to a higher relic abundance as in the case of standard misalignment. However, when the kinetic energy starts to dominate, the energy density rapidly grows as $\Omega_a h^2 \propto Y_\theta^2$. This behavior halts once the initial kinetic energy is large enough so that the field climbs the top of the potential, $\theta = (1{+}2n)\pi$. A higher value for Y_θ allows the crossing

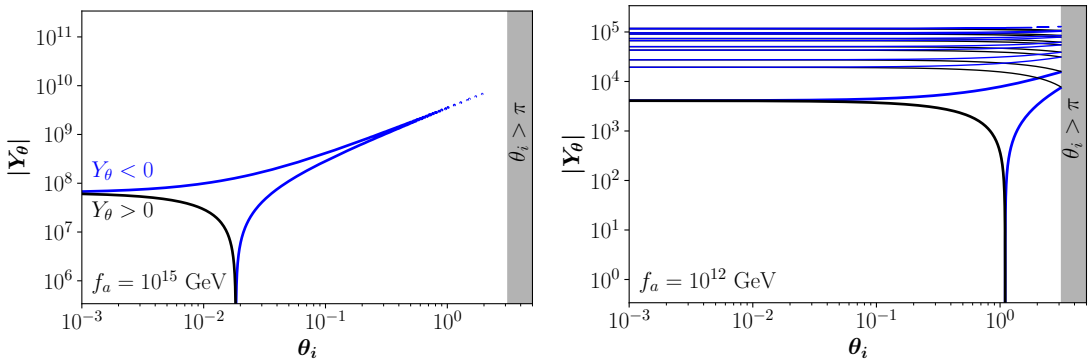

Figure IV.3: Kinetic misalignment. Parameter space that reproduces the whole observed DM abundance for $f_a = 10^{15}\,\text{GeV}$ (Left) and $f_a = 10^{12}\,\text{GeV}$ (Right). Black and blue lines correspond to $Y_\theta > 0$ and $Y_\theta < 0$, respectively. Figures created by N.Bernal.

of the potential barrier, oscillations taking place when the axion starts to roll down the potential, and hence a smaller relic abundance in generated. A minimum for $\Omega_a h^2$ occurs when oscillations start at the minimum of the potential where $\theta = 2n\,\pi$. Increasing values for Y_θ allow the axion field excursion to cross several potential barriers, and therefore the relic abundance experiences the oscillating behavior shown in Fig. (IV.2). Furthermore, when the kinetic energy completely dominates over the potential, $\Omega_a h^2$ loses its dependence on the initial misalignment angle θ_i, and it asymptotically approaches the strong KM regime, see Eq. (IV.24) in the following section. The right panel of Fig. (IV.2) shows the results for $\Omega_a h^2$ once fixing $\theta_i = 1$ and for the yields $Y_\theta > 0$ (black) or $Y_\theta < 0$ (blue). For positive values of the misalignment angle, the choices $Y_\theta > 0$ and $Y_\theta < 0$ correspond to an axion climbing up or rolling down further in the potential well, respectively. We emphasize that in the case of weak KM, the oscillation temperature is the same as in the standard misalignment scenario, so that there is no delay the onset of oscillations.

We now fix the relic abundance of axions to that of the observed DM, and study the corresponding parameter space $\{\theta_i, |Y_\theta|\}$ for which this is achieved. This is shown in Fig. (IV.3) for the different choices $f_a = 10^{15}\,\text{GeV}$ (left panel) and $f_a = 10^{12}\,\text{GeV}$ (right panel). In both panels, the black lines correspond to $Y_\theta > 0$, while blue lines correspond to $Y_\theta < 0$. For $f_a = 10^{15}\,\text{GeV}$, the axion is confined in the potential well containing its minimum and it is not able to explore other minima, i.e. there are only solutions corresponding to $n = 0$ in Eq. (IV.19). For $Y_\theta < 0$, the solution features a spike-like behavior, corresponding to the first funnel-shaped region appearing in the right panel of Fig. (IV.2). In the case $Y_\theta < 0$, the axion field has a negative moderate initial velocity that makes it roll down further in the potential well so that the field value becomes smaller than θ_i when the oscillations begin; this leads to a suppression in the relic abundance and, as a consequence, a larger θ_i is required to compensate. A similar behavior is shown for $f_a = 10^{12}\,\text{GeV}$, however in this case different solutions to Eq. (IV.19), corresponding to higher values of n, give rise to the observed DM abundance. In this scenario, the axion has enough kinetic energy to explore different minima, and therefore different solutions corresponding to the same initial axion angle appear. As the total axion energy density is dominated by the kinetic term, the new solutions tend to be independent of θ_i.

A similar behavior occurs when plotting the contours describing axion DM over the plane $\{m_a, Y_\theta\}$, see Fig. (IV.4). The left panel shows the region $Y_\theta > 0$ for the initial axion angles $\theta_i = 0$ (blue) and $\theta_i = 1$ (black), whereas the right panel shows the cases

for $Y_\theta > 0$ (black) and $Y_\theta < 0$ (blue) assuming $\theta_i = 1$. To reproduce the same observed abundance in the KM scenario, the case for $\theta_i = 0$ requires a larger value of Y_θ compared to the case $\theta_i = 1$. The dotted lines mark the area, to the left of the line, for which the weak KM regime holds, while the strong KM regime applies to the right, see Eq. (IV.23) below. All solutions with different initial values of θ_i (left panel) or the yield Y_θ (right panel) converge to the solution given by the red solid line in the strong KM regime.

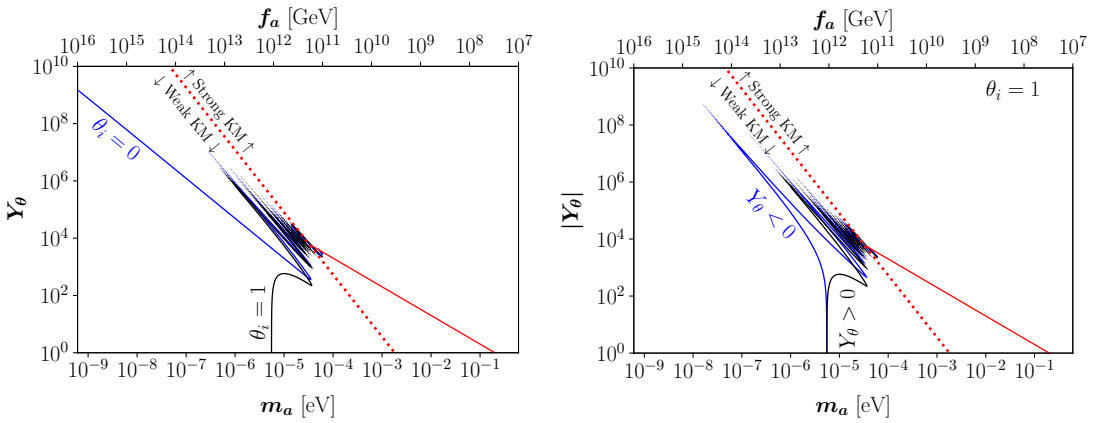

Figure IV.4: Weak kinetic misalignment. Left panel: Yield Y_θ as a function of the DM axion mass m_a, for the values of the initial misalignment angle $\theta_i = 0$ (blue) and $\theta_i = 1$ (black). Right panel: $|Y_\theta|$ as a function of the DM axion mass m_a, assuming $\theta_i = 1$ and considering either $Y_\theta > 0$ (black) or $Y_\theta < 0$ (blue). In both panels, the red dotted line separates the regimes of weak (to left) and strong (to right) KM. Figures created by N.Bernal.

IV.3.3 Strong kinetic misalignment

Contrary to the previous case where an initial velocity allows the axion to explore a few minima, in the strong KM the kinetic energy is so large compared to the potential barrier that the potential is effectively flat. In this scenario, the oscillations in the axion field are delayed with respect to the cases of the standard misalignment and weak KM [203, 204]. The initially dominant axion kinetic energy $K = \dot{a}^2/2$ eventually becomes equal to the maximum of the potential barrier $V_{\rm max} = 2\, m^2(T)\, f_a^2$ at the temperature $T_{\rm osc}^{\rm skm}$, defined implicitly by the equality

$$|\dot{\theta}(T_{\rm osc}^{\rm skm})| \equiv 2\, m(T_{\rm osc}^{\rm skm})\,. \tag{IV.21}$$

If at $T = T_{\rm osc}^{\rm mis}$ the kinetic energy density is larger than the potential barrier, the axion oscillations are delayed until the kinetic energy falls below the potential energy. With $m(T_{\rm osc}^{\rm mis}) \approx 3H(T_{\rm osc}^{\rm mis})$, this condition is satisfied for

$$|\dot{\theta}(T_{\rm osc}^{\rm mis})| = |\dot{\theta}(T_i)|\,\frac{s(T_{\rm osc}^{\rm mis})}{s(T_i)} = \frac{|Y_\theta|}{f_a^2}\, s(T_{\rm osc}^{\rm mis}) \gtrsim 6\, H(T_{\rm osc}^{\rm mis})\,, \tag{IV.22}$$

which corresponds to the red dotted line appearing in the panels of Fig. (IV.4). In terms of the yield, this gives

$$|Y_\theta| > 6\, f_a^2\, \frac{H(T_{\rm osc}^{\rm mis})}{s(T_{\rm osc}^{\rm mis})}\,. \tag{IV.23}$$

To obtain the present relic abundance, we employ the conservation of $n(T)/s(T)$ from the onset of field oscillations to present time,

$$\begin{aligned}\rho_a(T_0) &= \mathcal{C}\,\rho_a(T_{\rm osc}^{\rm skm})\frac{m_a}{m(T_{\rm osc}^{\rm skm})}\frac{s(T_0)}{s(T_{\rm osc}^{\rm skm})}\\ &\simeq \mathcal{C}\,|\dot\theta(T_{\rm osc}^{\rm skm})|\,f_a^2\,m_a\,\frac{s(T_0)}{s(T_{\rm osc}^{\rm skm})} = \mathcal{C}\,|Y_\theta|\,m_a\,s(T_0)\,,\end{aligned} \tag{IV.24}$$

where we used the fact that in the strong KM scenario, the axion energy density is completely dominated by the kinetic energy. Although the analytical estimate predicts $\mathcal{C}=1$, a numerical analysis favors $\mathcal{C}\simeq 2$ [203]. The result in Eq. (IV.24) is the red dashed line in Fig. (IV.2), and the red solid lines in Fig. (IV.4). As evident from Eq. (IV.24), in this limit the axion DM relic abundance is independent of the initial misalignment angle and the sign of Y_θ. The transition between the weak and the strong KM regimes occurs at $f_a\simeq 2.2\times 10^{11}\,\text{GeV}$, corresponding to $m_a\simeq 26\,\mu\text{eV}$.

The KM mechanism allows us to explore the region of the parameter space corresponding to relatively large values of the axion mass.[3] Equations (IV.21)–(IV.24) allow us to compute the value of $T_{\rm osc}^{\rm skm}$ required to match the observed DM abundance, via the relation

$$\frac{\sqrt{\chi(T_{\rm osc}^{\rm skm})}}{s(T_{\rm osc}^{\rm skm})} \simeq \frac{\rho_{\rm DM}}{2\,\mathcal{C}\,s(T_0)\,\sqrt{\chi(T_0)}}\,, \tag{IV.25}$$

which, setting $\mathcal{C}=2$, yields a value that is independent on the axion mass,

$$T_{\rm osc}^{\rm skm} = \left[\frac{4\,g_{\star s}(T_0)}{g_{\star s}(T_{\rm osc}^{\rm skm})}\frac{\chi_0}{\rho_{\rm DM}}\,T_{\rm QCD}^{b/2}\,T_0^3\right]^{\frac{2}{6+b}} \simeq 1.23\,\text{GeV}\,. \tag{IV.26}$$

Thus, in the strong KM scenario, axions start to oscillate at a smaller temperature $T=T_{\rm osc}^{\rm skm}$ instead of the value obtained in the conventional scenario $T_{\rm osc}^{\rm mis}$ given in Eq. (IV.13) and, as a consequence, the onset of coherent oscillations is delayed.[4] We have shown the value of the temperature at which the axion field is set into motion as a function of its mass in Fig. (IV.5). The line denoted "Strong KM" is the value given in Eq. (IV.26), and the two tilted lines to the left denote the result in Eq. (IV.13). A summary of the conditions satisfied by the three different misalignment mechanisms discussed is given in Tab. (IV.1).

Mechanism	Initial velocity	Oscillation temperature
Standard scenario	$\dot\theta_i = 0$	$3H(T_{\rm osc}^{\rm mis}) = m(T_{\rm osc}^{\rm mis})$
Weak KM	$\dot\theta_i \neq 0$	$3H(T_{\rm osc}^{\rm mis}) = m(T_{\rm osc}^{\rm mis})$
Strong KM	$\dot\theta_i \neq 0$	$\lvert\dot\theta(T_{\rm osc}^{\rm skm})\rvert = 2\,m(T_{\rm osc}^{\rm skm})$ with $\lvert\dot\theta(T_{\rm osc}^{\rm mis})\rvert > 2\,m(T_{\rm osc}^{\rm mis})$

Table IV.1: Conditions for the various scenarios of misalignment mechanism discussed in the text.

[3] Axions heavier than $\mathcal{O}(10^{-1})\,\text{eV}$ are in tension with observations from horizontal branch stars and other astrophysical measurements [239].

[4] A delay in the onset of oscillations also occurs in the *t*rapped misalignment case [240, 241].

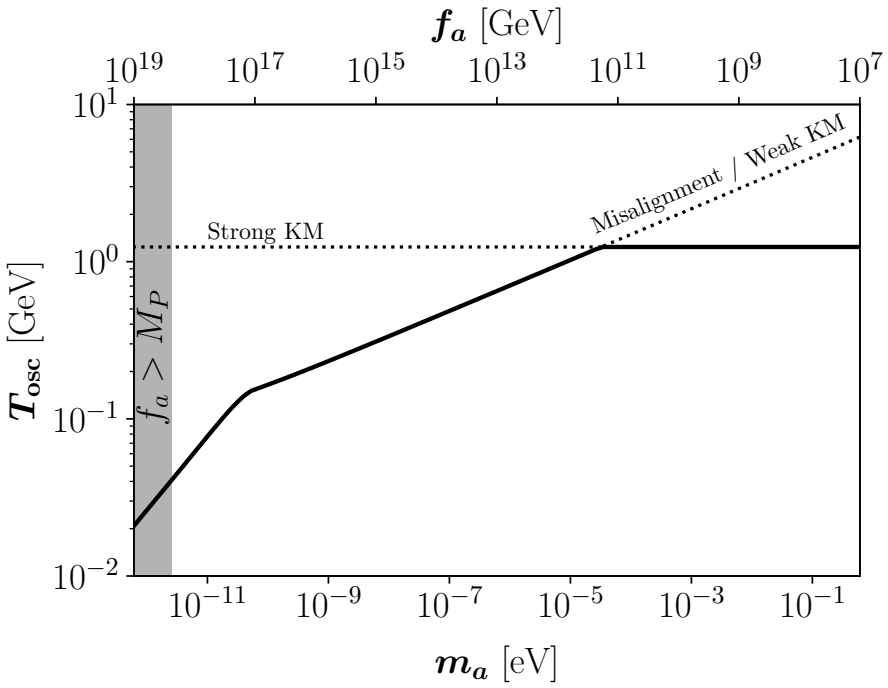

Figure IV.5: The temperature of the primordial plasma at the onset of axion field oscillations $T_{\rm osc}$ as a function of the axion mass. The tilted dotted line corresponds to the cases of standard misalignment or weak KM regimes in Eq. (IV.13), while the horizontal dotted line is the result in the strong KM regime in Eq. (IV.26).Figure made by N.Bernal

IV.4 Axion miniclusters

An axion minicluster is a dense, virialized clump of axions described by a mass M_0 and an overdensity δ parametrizing the local overdensity in the axion energy density. AMCs are generally discussed within the post-inflation framework, in which the PQ symmetry is spontaneously broken after inflation and the axion field at the time of the onset of oscillations is spatially inhomogeneous over different Hubble patches. However, such a scenario is difficult to realize as the KM is easily accommodated within the inflation period and due to the properties of the PQ potential in Eq. (IV.2). In more detail, if the PQ scalar field is driven to large values after the post inflationary PQ breaking, its angle will be randomized over different Hubble patches, leading to a net $Y_\theta \approx 0$ and to an absence of KM effects in this picture. In addition, since the initial velocity $\dot{\theta}_i$ cannot exceed the mass of the radial mode $m_S = \lambda_\Phi f_a$, where the coupling is bound to be $\lambda_\Phi^2 \leq 4\pi$ by perturbativity arguments, the energy scale f_a is severely constrained in this scenario. At the same time, the argument does not hold if the PQ symmetry is spontaneously broken before or during inflation and it is not restored afterwards (the pre-inflation scenario), because the assumption that $H \propto R^{-2}$ does not apply.

For the reasons above, we focus on the pre-inflation scenario, in which the axion field is homogeneous over the observable Universe and would not generally exhibit defects or seeding substructures. In this scenario, the axion field experiences the same initial conditions across the whole observable Universe; in particular, the axion would have the same initial velocity potentially leading to KM. Nevertheless, miniclusters can arise if additional features are considered. For example, a subdominant population of primordial

black holes could trigger the nucleation of axion overdensities around them [242, 243]. Overdensities with $\delta \sim \mathcal{O}(1)$ can also arise from tachyonic instability and/or resonance instability if the axion potential contains a small explicit breaking term [244,245], although the present analyses have been carried out only for the standard scenario and in the linear regime.

In the scenario depicted above, a sizable overdensity can be formed when the axion field starts rolling close to the hilltop of the potential [246]. This is a configuration that is accompanied with the formation of domain walls not attached to strings and thus extremely dangerous cosmologically, even for $N_{\rm DW} = 1$ [227, 247]. Nevertheless, the fine tuning required for the initial conditions is relaxed once the thermal effects from the interactions with the QCD sector are taken into account [245], so that axion clumps also form for a wider range of initial conditions avoiding the fine tuning. This is consistent with the requirements imposed on the axion decay constant f_a: in this regime, quantum fluctuations induce perturbations in the axion field of size $\sigma_a = H_I/(2\pi)$, where H_I is the Hubble scale during inflation, so that the PQ symmetry is restored whenever $\sigma_a > f_a$ [227, 247]. However, this region is not within the values of interest in this analysis, since we consider a relatively large axion decay constant $f_a \sim 10^{15}$ GeV while the energy scale of inflation for a single-field slow roll model is bound as $H_I \lesssim 2.5 \times 10^{-5}\, M_P$ at 95% confidence level (CL) [22].

IV.4.1 Formation and properties

The energy density associated with an AMC at formation is [248]

$$\rho_{\rm AMC} \approx 140\,(1+\delta)\,\delta^3\,\rho_{\rm eq}\,, \tag{IV.27}$$

where $\rho_{\rm eq}$ is the energy density in DM at MRE. The comoving size of the fluctuations at the onset of oscillations is $r_H = 1/(R\,H)_{\rm osc}$,[5] leading to an AMC of radius $r_{\rm eq} = r_H\,R_{\rm eq}/\delta$ at the time when the overdensity perturbations decouple from the Hubble expansion and start growing by gravitational instability, rapidly forming gravitationally bound objects [89,248–252], with the corresponding mass

$$M_0 = \frac{4\pi}{3}(1+\delta)\,\rho_{\rm DM}\,\frac{s(T_{\rm osc})}{s(T_0)}\left(\frac{1}{H(T_{\rm osc})}\right)^3. \tag{IV.28}$$

The mass scale in Eq. (IV.28) corresponds to the heaviest AMCs that are formed at MRE. Bound structures are formed with all masses below M_0, down to the smallest physical scales at which the oscillatory behavior of the axion field exerts an effective "quantum" pressure which prevents further clumping. This so-called Jeans length $\lambda_J = 2\pi/\lambda_J$ corresponds to the wave number [253, 254]

$$k_J = \left(16\pi G\rho_{\rm DM} m_a^2 R\right)^{1/4} \simeq 710\left(\frac{m_a}{\mu{\rm eV}}\right)^{1/2}{\rm pc}^{-1}, \tag{IV.29}$$

where the last expression holds at MRE. Perturbations grow for modes $k > k_J$.

Numerically, Eq. (IV.28) in different regimes reads

$$M_0 = \begin{cases} 1.7\times10^{-14}\,M_\odot\,(1+\delta)\,\left(\frac{m_a}{\mu{\rm eV}}\right)^{-3/2}, & \text{for } T_{\rm osc} \lesssim T_{\rm QCD}\,, \\ 1.1\times10^{-10}\,M_\odot\,(1+\delta)\,\left(\frac{m_a}{\mu{\rm eV}}\right)^{-\frac{6}{4+b}}, & \text{for } T_{\rm QCD} \lesssim T_{\rm osc} \lesssim T_{\rm osc}^{\rm skm}\,, \\ 2.1\times10^{-11}\,M_\odot\,(1+\delta)\,, & \text{for } T_{\rm osc} \gtrsim T_{\rm osc}^{\rm skm}\,, \end{cases} \tag{IV.30}$$

[5] In the following, we generally refer to $T_{\rm osc}$ to indicate either Eq. (IV.11) or Eq. (IV.21).

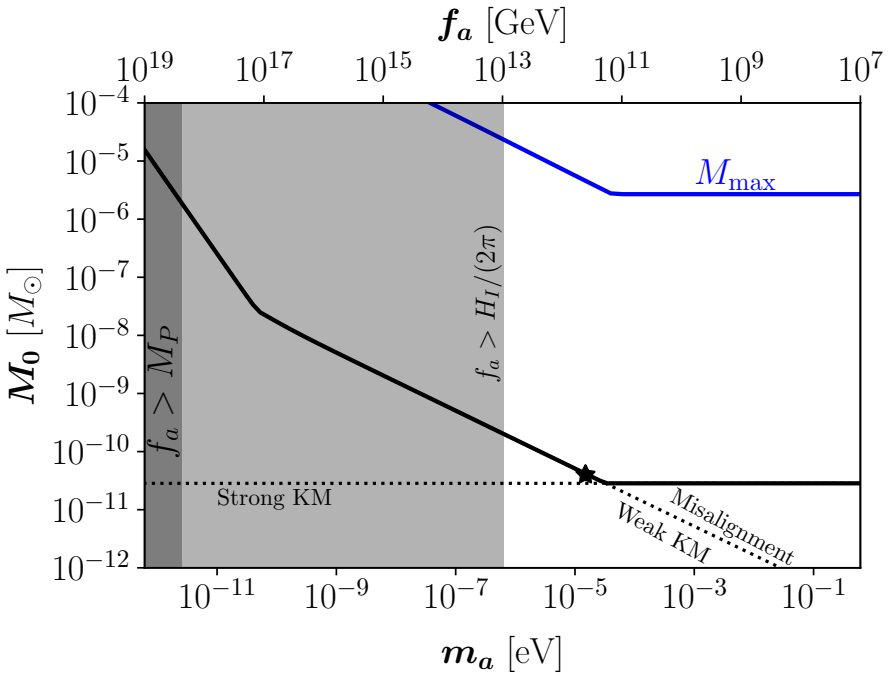

Figure IV.6: The characteristic minicluster mass, for $\delta = 1$. The two dotted lines correspond to the cases of standard scenario or the weak KM regime, and to the strong KM regime. Figure made by L.Visinelli

where the first two lines are found in the case where the onset of oscillations is not delayed by the presence of KM so that Eq. (IV.13) holds, while the third line is obtained in the strong KM regime where Eq. (IV.26) holds.

The first two lines of Eq. (IV.30) apply in the pre-inflation scenario which, although less explored, could nevertheless lead to the formation of miniclusters as discussed in Sec. (IV.3). The first line in Eq. (IV.30) corresponding to the case $T_{\rm osc} < T_{\rm QCD}$ is realized for an initial misalignment angle $\theta_i \ll 1$ which, in the pre-inflation scenario, corresponds to relatively large values of f_a. This is consistent with the requirement that the Hubble rate at the end of the inflation epoch for single-field inflation models is bound as $H_I \lesssim 2.5 \times 10^{-5}\, M_P$ at 95% CL [22] at the wave number $k_0 = 0.002\,{\rm Mpc}^{-1}$ which, together with the bound $f_a \gtrsim H_I/(2\pi)$ valid for the pre-inflationary scenario, implies $m_a \lesssim 0.6\,\mu$eV. The KM regime allows achieving different values of the DM axion mass according to the initial velocity, with a wider possibility for the AMC mass ranges. In particular, AMCs can be as heavy as $\sim 10^{-9}\, M_\odot$. This effect is ultimately due to the delayed onset of oscillations occurring in the KM regime, where the AMC mass is independent of the DM axion mass since the temperature in Eq. (IV.26) is constant.

The results in Eq. (IV.30) for the AMC mass M_0 are sketched as a function of the DM axion mass m_a by the black solid in Fig. IV.6. The star labels the typical AMC mass obtained with a DM axion of mass $m_a = 20\,\mu$eV using the second line in Eq. (IV.30). The first kink to the left corresponds to the change in the behavior of the susceptibility in Eq. (IV.7) near $T \sim T_{\rm QCD}$, while the second kink at heavier axion masses corresponds to the change from the weak to the strong KM regimes, see Fig. (IV.5). The moment where the axion field begins to oscillate coincides with the transition from being frozen at the configuration $\theta = \theta_i$ to an oscillatory behavior with dust-like equation of state $w_a \approx 0$.

In the KM scenario, the axion initially behaves as a kination field with $w_a \approx 1$ and the transition could occur at lower temperatures, i.e. at $T = T_{\rm osc}^{\rm skm} < T_{\rm osc}^{\rm mis}$, as discussed in Sec. (IV.3.3). For this reason, axion mini clusters formed in the strong kinetic regime are heavier than those formed in the standard scenario. The gray band to the left of the plot marks the mass region in the post-inflationary scenario which is excluded by the non-observation of tensor modes in single-field inflation by the *P*lanck satellite collaboration.

The lighter gray band marks the region where the bound $f_a > H_I/(2\pi)$ applies, which is a condition that describes the breaking of the PQ symmetry occurring during inflation. Note that, this bound applies for the quartic coupling $\lambda_\Phi = \mathcal{O}(1)$ appearing in the "Mexican hat" potential in Eq. (IV.2) that is invoked to parametrize the symmetry breaking of the PQ field. Since $\lambda_\Phi = m_S^2/f_a^2$, where m_S is the mass of the radial mode S, this requirement applies when m_S is of the same order as f_a. For lighter modes, the PQ symmetric phase can alternatively be obtained by adding a term describing a non-minimal interaction $\xi\, R\, |\Phi|^2$ to the Lagrangian in Eq. (IV.1), where ξ is the non-minimal coupling strength, along with a new scale M that couples to the Ricci scalar so that $M^2 = M_{\rm Pl}^2 - \xi\, |\Phi|^2$ (see Refs. [255–257] for applications of the non-minimal coupling).

So far, the treatment has overlooked the role of density fluctuation growth, which is referred in the literature as the "fragmentation" of the field. It has been shown that fragmentation might play an important role in the dynamics, as it introduces an additional scale which could alter the description above [258]. For a model of the axion-like particle, fragmentation occurs in a sizable part of the parameter space, leading to heavier miniclusters than in the standard scenario [259]. Fragmentation is expected to occur also for the QCD axion [258], although a study of this is not yet available. The picture is complicated by the fact that the analytical tools used to study the linear regime could not suffice when the axion mass largely exceeds the Hubble rate at the trapping temperature in Eq. (IV.21) (for which fragmentation is "complete"), and a more sophisticated analysis in terms of lattice computation has to be invoked.

IV.4.2 Growth of structures

At around MRE, axion miniclusters form at scales below the threshold in Eq. (IV.28), populating the decades in mass according to a halo mass function (HMF) $\mathrm{d}n/(\mathrm{d}\ln M)$ which provides the number density n as a function of the logarithmic mass M. The bottom-up clumping of axion miniclusters begins already around the time of matter-radiation equality when these structures form. Recent progress on the merging process has focused on the formation of axion "minihalos" with a HMF derived from N-body simulations [216, 260], which can be understood in terms of semi-analytical modeling [217, 218, 261, 262], and is well approximated by using the standard Press-Schechter (PS) and Sheth-Tormen formalisms.

Even though numerical simulations are in place to be able to make confident predictions, the intention here is to draw attention to a scenario that could serve as a motivation for N-body simulations in the future. Here, we intend to estimate how the HMF becomes modified in the KM case to the standard case, following the PS formalism [263]. The PS formalism is based on two key assumptions: *i*) at any time, the density contrast of a spherically-symmetric overdense region of size R collapses into a virialized object once it evolves above a critical overdensity δ_c. For the critical value of the linear density contrast for spherical collapse during the matter domination is $\delta_c \approx 1.686$. To quantify

this criterion, we introduce the overdensity fuzzed over the spherical region,

$$\delta_s(\mathbf{x},t) = \int \mathrm{d}^3\mathbf{x}'\,\delta(\mathbf{x}')\,W(\mathbf{x}+\mathbf{x}',R)\,, \tag{IV.31}$$

where $W(\mathbf{x},R)$ is a kernel function that smooths the spatial overdensity over the spherical region of radius R. *ii*) The density contrast is distributed as a normal distribution, specified by the variance

$$\sigma^2(z,R) = \int \frac{\mathrm{d}^3\mathbf{k}}{(2\pi)^3}\,|\delta_k(R)|^2\,\mathcal{T}^2(\mathbf{k},z)\,|W(\mathbf{k},R)|^2\,, \tag{IV.32}$$

where $|\delta_k(R)|^2$ is the power spectrum of the fluctuations, $\mathcal{T}(\mathbf{k},z)$ is the transfer function, and $W(\mathbf{k},R)$ is the Fourier transform of the kernel function $W(\mathbf{x},R)$ that smooths the density field $\delta(\mathbf{x})$ over the spherical region of radius R.

The HMF derived from these premises is parametrized as

$$\frac{\mathrm{d}n}{\mathrm{d}\ln M} = \frac{\rho_{\rm DM}}{M}\,f(\sigma)\,\Big|\frac{\mathrm{d}\sigma}{\mathrm{d}\ln M}\Big|\,, \tag{IV.33}$$

where the multiplicity function $f(\sigma)$ is defined within the PS formalism as

$$f(\sigma) = \sqrt{\frac{2}{\pi}}\,\frac{\delta_c}{\sigma}\,e^{-\frac{1}{2}\frac{\delta_c^2}{\sigma^2}}\,. \tag{IV.34}$$

The method described above is extremely efficient in describing the distribution of the high-end mass spectrum of the HMF. Since our interest is in the heaviest virialized objects that form within the theory, we specialize the treatment to find an approximate solution for the maximal mass of the minihalo $M_{\rm max}(z)$ at redshift z. The power spectrum of the fluctuations $|\delta_k(R)|^2$ is accessible from lattice simulations in the early Universe [43,44] and from N-body simulations [216]. Since we are interested in estimating the maximal mass of axion structures at redshift z, we adopt the approximation in Ref. [218] of a white-noise power spectrum truncated at the comoving scale $k_{\rm osc}$ at which coherent field oscillations begin. Normalization of the power spectrum ensures that the integral of the power spectrum equates the square of spatial fluctuations averaged over different horizons [264] and it is here set as $P_0 = (24\pi^2/5)\,k_{\rm osc}^{-3}$ [218]. In principle, the transfer function depends on the relative value of k for the Jeans wavelengths at MRE and today. In practice, these Jeans lengths are too small to yield a significant modification over the white-noise spectrum. Here, we use the fact that in the spherical collapse model, the fluctuations collapse and grow to size M at redshift $z < z_{\rm eq}$ as isocurvature modes with $\delta(M) \propto a$ so that the transfer function can be approximated as a linear scale factor. Finally, we assume a Gaussian kernel function, whose Fourier transform is again a Gaussian function in $k = |\mathbf{k}|$ of the form

$$W(\mathbf{k},R) = \exp\left(-k^2R^2/2\right)\,. \tag{IV.35}$$

With this choice, the mass of a structure today that extends to a region of size R is $M = (2\pi)^{3/2}\rho_{\rm DM}R^3$.

With this parameterization, the standard deviation in Eq. (IV.32) is approximated by the analytic function

$$\sigma(z,R) = \frac{1+z_{\rm eq}}{1+z}\sqrt{\frac{3}{5}\frac{\sqrt{\pi}\,\mathrm{erf}(x) - 2x\,e^{-x^2}}{x^3}}\,, \tag{IV.36}$$

where $x = k_{\rm osc} R$ and $\mathrm{erf}(x)$ is the error function. Collapse occurs when $\sigma(z, R) \geq \delta_c$. More generally, the mass of the heaviest objects that form at redshift z, $M_{\rm max}(z)$, is found implicitly from the expression

$$\sigma(z, M_{\rm max}(z)) = \delta_c \,, \tag{IV.37}$$

where $\sigma^2(z, M)$ is the variance corresponding to Eq. (IV.32) once R is expressed in terms of M. The results for $z = 0$ are reported in Fig. (IV.6) (blue line), where the kink at $m_a \sim 10^{-5}\,\mathrm{eV}$ corresponds to the effects of the kinetic term in the initial conditions. Whenever there exists a mechanism that grants a large initial kinetic energy for the axion field, the field would begin coherent oscillations in a colder universe, allowing for heavier axion miniclusters at MRE. The clumping of such heavier building blocks also leads to an increased value of the maximal mass, with observational consequences. Note, however, that these large miniclusters would probably not survive tidal stripping from other astrophysical objects such as brown dwarfs and main sequence stars, especially in high-density regions such as the Galactic center [265–267].

IV.4.3 Stripping

It is not guaranteed that AMCs survive tidal stripping from compact objects in galaxies, such as brown dwarfs and stars. In all DM models, tidal interactions destroy small-scale clumps [268,269], such as axion miniclusters [265]. Recent N-body simulations have proven that the stripping mechanism is crucial for the population of miniclusters in galaxies [266]. In general, it could be expected that the larger and heavier miniclusters produced in the strong KM regime would be more prone to get tidally disrupted by compact objects.

The effect of the encounter of the minicluster with an individual compact object of mass M with relative velocity $v_{\rm rel}$ is that of increasing the velocity dispersion of the bounded axions. An encounter that occurs close enough would deposit sufficient energy so that the minicluster is completely disrupted. This occurs for an impact parameter b smaller than the critical value [270, 271]

$$b < b_c \equiv \left(\frac{G M R_{\rm AMC}}{v_{\rm rel}\, v_{\rm AMC}} \right)^{1/2} , \tag{IV.38}$$

where the velocity dispersion of the minicluster is $v^2_{\rm AMC} = G\, M_{\rm AMC}/R_{\rm AMC}$. The probability of disruption for a minicluster moving in a stellar field of column mass density S is [265]

$$p_{\rm disr} = 2\pi\, S\, \frac{G\, R_{\rm AMC}}{v_{\rm rel}\, v_{\rm AMC}} \,. \tag{IV.39}$$

In the vicinity of the solar system, it is generally found $p_{\rm disr} = \mathcal{O}\left(10^{-2}\right)$ and miniclusters generally survive the stripping process. However, this result depends on the density of the minicluster and not on its mass or radius separately. Since the density of miniclusters given in Eq. (IV.27) is related to the spherical collapse model and not to the cosmological history, we generally expect that at the lowest order in which this approximation holds, the probability of disruption would not change among the different scenarios of misalignment mechanisms. Near the Solar system, Eq. (IV.39) yields $p_{\rm disr} \approx 2\%$.

IV.4.4 Microlensing

Now we discuss a possible method to distinguish between the different misalignment scenarios using microlensing. Bound structures made of axions such as miniclusters, minicluster halos, and axion stars can impact lensing from distant sources. For a point-like lens

of mass M, the characteristics of the microlensing event are determined by the Einstein radius [272, 273]

$$R_E(x) = \sqrt{\frac{4\,G_N\,M}{c^2}\frac{D_L\,D_{LS}}{D_S}} \approx 4.3\times10^3\,\mathrm{km}\left[x(1-x)\frac{D_S}{\mathrm{kpc}}\frac{M}{10^{-10}M_\odot}\right]^{1/2}, \tag{IV.40}$$

where D_S, D_L, and D_{LS} are the distances between the source and the observer, the lens and the observer, and the source and the lens, respectively, and $x = D_L/D_S$.

Although lensing can occur from axion miniclusters and halos [218, 266, 274, 275], these structures can generally not be modeled as point lenses, as their Einstein radius lies within their mass distribution, so that the internal density profile must be known to estimate the lensing power. Extended objects generally lead to weaker limits due to the smaller magnification of the lens [276, 277].

Here, we focus on the lensing of light coming from a distant source when the lensing object is an axion star, which is generally a much more compact object than a minicluster [278–282]. Axion stars belong to the class of real scalar field oscillatons [283–286] in which the field occupies the lowest energy state that is allowed by the Heisenberg uncertainty principle. An axion star of mass $M_{\rm as}$ is generally produced in the dense core of axion miniclusters through the mechanism of gravitational cooling [287] with the relaxation time $\tau_{\rm as}$ [288]. Although the decay rate in two photons does not significantly affect the stability of axion stars on a cosmological time scale, self-interactions of type $3\,a \to a$ can lead to the decay of axion stars with a decay rate that depends on $(m_a/f_a)^2$ [289].

An axion star can efficiently lens the light from a distant source, as their radius is typically smaller than their corresponding Einstein radius. Recently, a single microlensing event observed by the Subaru Hyper Suprime-Cam (HSC) collaboration after observing in M31 ($D_S = 770\,\mathrm{kpc}$) for 7 hours [290] has been interpreted in terms of an axion star of planetary mass [291] (see also Ref. [243]). However, the result is of difficult interpretation in the standard scenario of the misalignment mechanism, since such massive stars would only form for the lightest QCD axions, for which the post-inflation scenario does not hold. Although the AMCs formed in the strong KM regime are generally much heavier, the axion stars formed within them are not expected to differ much from those of the standard scenario, since the mass of the axion star is only mildly dependent on that of the host AMC as $M_{\rm as} \propto M_{\rm AMC}^{1/3}$ [292]. For this reason, the KM regime cannot be invoked to produce the heavy axion stars which are needed to explain the microlensing results in Ref. [291]. One issue with the derivation of the axion star properties is that the formulas used rely on the results of Ref. [292] which are obtained for ultralight axions for which the mass scale greatly differs from that of the QCD axion. Although this can be justified since the set of equations describing the system (the Newton-Poisson equation) possesses a scaling property, a dedicated simulation proving this is yet lacking.

IV.5 Conclusions

An explicit breaking term in the Peccei-Quinn (PQ) symmetry could give rise to a non-zero velocity term for the axion field. This scenario, called kinetic misalignment (KM), has been explored in the literature in relation with baryogenesis. Even if the models of KM presented in the literature typically correspond to a PQ symmetry breaking happening during inflation, in this work we focused on the low-energy dynamics of an axion featuring a non-zero velocity, being agnostic about how it was produced in the early Universe.

Here, we have discussed further implications for the delayed onset of the oscillations in the axion field that appear in the KM scenario. In the standard scenario, the DM axion mass depends on the relative size of the inflation scale with respect to the axion energy scale: in the pre-inflation regime, the initial misalignment angle can be tuned to achieve a specific mass scale according to the result in Fig. (IV.1), while in the post-inflation regime the mass is fixed by the dynamics of the axion field that yields $\theta_i = \mathcal{O}(1)$. In KM scenarios, different values of the DM axion mass can be explored because of the presence of the non-zero initial velocity as a new parameter upon fixing θ_i, see Fig. (IV.4).

One aspect that has been explored here is the formation of axion miniclusters (AMCs) and minihalos in KM regimes, as a possible tool that leads to distinctive signatures from the standard scenario. AMCs are generally formed in the post-inflation regime with typical mass $M_0 \sim 10^{-11}\ M_\odot$. In KM scenarios, the non-zero velocity term allows for a wider mass range for the AMCs: the mass of the AMCs is larger than what is obtained in the standard scenario because the axion field begins to oscillate in a colder universe with a larger comoving scale, as shown in Fig. (IV.6). In this regime, AMCs are more diffuse and heavier, so assuming that the fraction of axions in bounded structures is the same, there would be fewer of them and they would be affected by tidal stripping the same way as in the standard scenario. The clumping of heavier AMCs would lead to larger halos of mini clusters, with the typical mass today that could be orders of magnitude above what has been expected so far, and could affect the analysis of the microlensing events from minicluster halos.

Future directions would involve employing a numerical solution of the equation of motion, including the effects of explicit symmetry breaking. For example, the dynamics of the axion can be resolved by modifying the recent open-source numerical routine `MiMeS` [293]. The properties of AMCs can only be assessed through more sophisticated analyses that account for the evolution of the PQ field and require modification of existing open-source codes that are already available [43]. A similar analysis involving the implementation of a Boltzmann solver can be performed in the pre-inflationary scenario, where the KM regime would be additionally constrained by isocurvature fluctuations, as has been discussed in Ref. [51].

CHAPTER V

QCD Axion Strings and Gravitational Waves

V.1 Introduction

The recent discovery of GWs by the LIGO/Virgo collaborations have catapulted the search for GW signals in various frequency domains that are already taking data and more will emerge in the next decade. One of these regimes regards GW searches in the nanohertz regime by the aid of PTA experiments such as European Pulsar Timing Array [294], the Parkes Pulsar Timing Array [295] and the North American Nanohertz Observatory for Gravitational Waves (NANOGrav) collaboration [296, 297]. PTA data allow probing the SGWB in the nHz frequency range by keeping track of the correlated GW fluctuations from millisecond pulsars at the time of arrival. Here we analyze the next to most recent data set given by the NANOGrav collaboration which is their 12.5-year [1] data set and interpret the data as an SGWB of primordial origin. Recently, the NANOGrav collaboration reported the evidence for a stochastic process from analyzing 12.5 years based on 45 pulsars [298]. The reported signal may be interpreted as an SGWB signal of amplitude $A_* \sim \mathcal{O}(10^{-10} - 10^{-15})$ for frequencies $f \sim 30\,\mathrm{nHz}$ and a mild spectral index. At present, it is not clear whether the detected signal truly originates from an SGWB process due to i) the tension with previous PTA SGWB upper limits in the same frequency range, and ii) the lack of quadrupole correlations, a smoking gun for SGWB [299][2].

If the detected signal found by the PTA collaborations is indeed a component of the SGWB, it could be explained by various processes such as PBH formation [300, 301], phase transitions in the early Universe [302, 303], models of inflation in the early Universe [304, 305], or the GW signal emitted by a network of cosmic strings [306–308]. Here we explore a model that is able to predict both an SGWB but also provides with a CDM candidate which is a missing tile in the cosmic puzzle. In this work, we provide a possible explanation of the NANOGrav detection in light of the model we studied in Ref. [2], where the QCD axion is the CDM and GW emission from axionic strings are studied in light of an NSC in the early Universe. Our work intends to shed light on the possible models of the QCD axion and of the NSC that has the capability of being probed in future GW detectors.

This chapter is organized as follows. We introduce non-standard cosmological models in

[1] By the time this work was done, we only had the NANOGrav 12.5-year data release and hence we will center the discussion about that whereas in the ed of the paper we will mention how the results of this paper may change by considering the latest data releases.

[2] In the most recent data release further evidence for a quadrupole correlation amongst the pulsars are becoming more evident, which is a crucial step towards an SGWB detection.

Sec. (V.2), and we review the axion model in Sec. (V.3). The method to compute the GW spectrum within the theory is explained in Sec. (V.4). We show the results in Sec. (V.5), which are further discussed and concluded in Sec. (V.6).

V.2 Setup of the cosmological model

In the standard picture, the expansion of the Universe is governed by the energy density of the relativistic bath produced right after inflation, until radiation is red-shifted away and matter domination begins. Within this picture, BBN successfully reproduces the abundance of various light elements with extreme precision, provided that the standard cosmological model holds up to temperatures $T_{\rm BBN} \sim 5\,{\rm MeV}$ [309–314]. The content of the Universe for temperatures $T > T_{\rm BBN}$ has not been explored, since a relic from the pre-BBN period has yet to be identified. One such relic could be the DM particle if it decouples from the plasma, or the GW spectrum released by some process in the pre-BBN era. Proposed probes comprise the effects on the chemical [315–319] and kinetic [320] decoupling temperatures of the weakly interacting massive particle, as well as the altered energy density of thermal [321] and non-thermal axions [49]. Gravitational waves from early phase transitions or from topological defects could also be a gateway to explore the pre-BBN epoch [322, 323].

Here, we model the pre-BBN era as follows. Soon after inflation ends, the expansion rate of the Universe is dominated by an exotic (non-radiation) component ϕ, whose energy density ρ_ϕ is larger than that of the relativistic species at temperature T. We refer to this early stage as the NSC period. Candidates for the exotic component which is responsible for the NSC period include massive moduli fields [46, 201, 324, 325] and fast "kination" fields [238, 326–330].

The NSC period lasts until the exotic component either dilutes or decays away. Here, we focus on this latter case in which the details of the NSC are determined by the value of the decay rate Γ and the equation of state w_ϕ of the exotic component. We treat the equation of state as a free parameter ranging over $-1/3 < w_\phi < 1/3$, excluding a post-inflation accelerated epoch where $w_\phi < -1/3$. We also do not consider the case in which the exotic fluid redshifts faster than radiation $w_\phi > 1/3$, because in this scenario the energy density of axionic strings is not enhanced with respect to the standard results [2].

For a massive scalar field, the shape of the self-interacting potential determines the value of w_ϕ. For example, the equation of state for a massive moduli field moving in the potential $V(\phi) \propto \phi^{2j}$ with $j > 0$ is $w_\phi = (j-1)/(j+1)$ [46], so that for $j = 1$ the field rolls in a quadratic potential and the dust-like case $w_\phi = 0$ is recovered. The effective equation of state for a massive field can attain negative values when the massive field dominates the expansion rate under the exponential potential [331–334]

$$V(\phi) = V_0 \, \exp\left(-\lambda\phi/M_{\rm Pl}\right) \,, \tag{V.1}$$

where V_0 and λ are constant and $M_{\rm Pl}$ is the reduced Planck mass. The self-interaction potential of the form as in Eq. (V.1) arises in string models for the moduli fields associated with the geometry of the extra dimensions [e.g. Ref.][]Green:1987sp, in theories of modified gravity [335–337], or from supersymmetry breaking in models of gaugino condensation [338–340]. In particular, for $2 < \lambda^2 < 3$, the Universe expands with the equation of state $-1/3 < w_\phi < 0$ [333, 341].

Depending on the nature of the exotic component, its interaction with radiation can be described by the Lagrangian term $\mathcal{L} \propto g\phi\bar{\psi}\psi$ if ϕ is a massive scalar field, where ψ

is the spinor describing an electron and g a new coupling. Here, we do not include the details of the coupling between radiation and the exotic component ϕ; instead, we describe the conversion of the energy density ρ_ϕ into radiation ρ_R through energy conservation as [342–347]

$$\dot{\rho}_\phi = -3(1+w_\phi)H\rho_\phi - \Gamma\rho_\phi\,, \tag{V.2}$$
$$\dot{\rho}_R = -4H\rho_R + \Gamma\rho_\phi\,, \tag{V.3}$$
$$3H^2 = 8\pi G(\rho_\phi + \rho_R)\,. \tag{V.4}$$

The decay rate Γ regulates the conversion rate of the exotic component into radiation. This set of equations describes a NSC in which the energy density ρ_ϕ dominates the expansion rate of the pre-BBN Universe before decaying into radiation, which thermalizes on timescales $\ll 1/\Gamma$. When ρ_ϕ equates the energy density in radiation, the Universe transitions to the radiation-dominated period at the temperature T_ϕ. In order not to alter the results of BBN, we require $T_\phi > T_{\rm BBN}$.

V.3 The QCD axion

The QCD axion is a hypothetical pseudo-scalar particle of zero-temperature mass [47]

$$m_a = 6.2\,\mu{\rm eV}\left(\frac{10^{12}{\rm GeV}}{f_a/N_{\rm DW}}\right)\,, \tag{V.5}$$

where f_a is the axion decay constant and $N_{\rm DW}$ is the "domain wall number", see e.g. Sec. 2.7.1 in Ref. [252]. Here, we set $N_{\rm DW}=1$. The mass of the axion arises from QCD instanton effects and depends on temperature so that $m_a(T) = \sqrt{\chi(T)}/f_a$, where the QCD topological susceptibility is normalized at zero-temperature as $\chi(0) = m_a^2 f_a^2$ [219].

The abundance of axions produced through non-thermal mechanisms after the PQ symmetry breaking occurs could explain the missing DM in the Universe [199,201,202].[3] The computation of the present abundance proceeds through the vacuum realignment mechanism, for which the axion field a in units of f_a, the so-called axion angle $\theta = a/f_a$, reads

$$\ddot{\theta} + 3H\dot{\theta} + m_a^2(T)\sin\theta = 0\,. \tag{V.6}$$

Given an initial value of the axion angle, θ_i drawn randomly from the uniform distribution $[-\pi,\pi]$ when the PQ phase transition occurs, the solution to Eq. (V.6) is a constant value of $\theta=\theta_i$ as long as the Hubble friction is much larger than the axion mass. Coherent oscillations in the axion field begin at around the time $t_{\rm osc}$ given by

$$H(t_{\rm osc}) \approx m_a(t_{\rm osc})\,, \tag{V.7}$$

after which the number of axions in a comoving volume is fixed and the axion energy density evolves as a matter-like field. The temperature of the plasma at $t_{\rm osc}$ is $T_{\rm osc}$.

V.3.1 Axions from strings

If PQ symmetry broke either after inflation or was temporarily restored right after inflation, an emergence of topological defects that eventually decay will contribute to the DM axion budget [39,349]. The string network contains about one axionic string per Hubble

[3] A thermal axion component is also expected from processes scattering off pions and nucleons [348].

volume and is approximated to have a linear mass distribution of string core size $\sim 1/f_a$ and a linear mass density [39, 350]

$$\mu_{\rm eff}(t) = \pi f_a^2 \ln(f_a t) \ . \tag{V.8}$$

The string network evolves by emitting a spectrum of axions and GW, either by wiggles on long open strings or self collapse of closed strings. The cold portion of the spectrum of axions emitted from axionic strings might significantly contribute to the present energy density of axions [39–41, 43–45, 350–367].

To describe the power loss of the network into radiation, we consider the dissipation of the energy $E_{\rm loop} = \mu_{\rm eff}\ell$ of a closed loop with length ℓ into axions and gravitational waves [356–359],

$$P_{\rm loop} = \frac{{\rm d}E_{\rm loop}}{{\rm d}t} = \kappa\mu_{\rm eff} + \gamma_{\rm GW} G\mu_{\rm eff}^2, \tag{V.9}$$

where $\gamma_{\rm GW} \approx 65$ and $\kappa \approx \mathcal{O}(0.1)$ are *dimensionless* quantities describing strings moving at relativistic speed [368–370]. Contrarily to the previous literature, we have set $\kappa \approx 0.15$ which characterizes the predominant energy loss into axions, instead of using the value $\kappa = 0$ which would describe the predominant release of energy into gravity wave modes. Since the ratio of the power loss in gravity waves and axions is of the order of $Gf_a^2 \ll 1$, the string network mainly dissipates energy into axions. While sub-Planckian, the value of f_a is larger than in the standard scenario for an equation of state $w_\phi < 1/3$, leading to an enhanced GW emission.

Using Eq. (V.9), the shrinking of a loop with initial size ℓ_i is described by the expression

$$\frac{{\rm d}\ell}{{\rm d}t} = \kappa - \ell\,\frac{{\rm d}\ln\mu_{\rm eff}}{{\rm d}t}, \tag{V.10}$$

where $\ell = \ell(t, \ell_i)$ is the size at time t. Although the loop length could vary between arbitrary sizes, numerical simulations show that the initial length of the large loop at its formation tracks the time of formation as $\ell(t_i) = \alpha t_i$, where α is an approximately constant loop size parameter which gives the fraction of the Hubble horizon size at which loops predominantly form [358, 371, 372].

Owing to the small power loss in GWs, we approximate the evolution of the string network in a scaling regime with the emission proceeding through axions. The energy density of the radiated axions follows the evolution $\rho_a + 4H\rho_a = \Gamma_{\rm str\to a}$, where $\Gamma_{\rm str\to a}$ is the energy lost in the emission of axions per unit time. The number density of axions emitted from strings within the modes of angular wavenumber $k \approx 1/\ell(t_i) \approx H(t_i)/\alpha$ to infinity is [41]

$$n_a^{\rm str} = \int^t {\rm d}t' \frac{\Gamma_{\rm str\to a}(t')}{H(t')} \left(\frac{R(t')}{R(t)}\right)^3 \int \frac{{\rm d}k}{k}\, F(k), \tag{V.11}$$

where $R(t)$ is the scale factor at t and the spectral energy density is defined in terms of a spectral index $q > 1$ as [41, 356, 357]

$$F(k) = \frac{q-1}{\alpha^{q-1}} \left(\frac{k}{H}\right)^{-q}. \tag{V.12}$$

The spectral energy density $F(k)$ is properly normalized over the frequency range considered.

It has been alternatively assumed that strings efficiently shrink emitting all of their energy at once, leading to a flat power spectrum per logarithmic interval with a harder spectral index $q = 1$, an infrared cutoff at the wave mode $k \approx H$ and a ultraviolet cutoff at $k = f_a$ [354, 373, 374].

V.3.2 Gravitational Waves from Axionic String Loops

Here, we compute the subdominant SGWB emitted from axionic string loops. The fraction of the critical energy density released into the GW spectrum per unit logarithmic interval of frequency is

$$\Omega_{\rm GW}(t,f) = \frac{1}{\rho_c(t)}\frac{{\rm d}\rho_{\rm GW}}{{\rm d}\ln k}. \tag{V.13}$$

The evolution of the string loop is described by Eq. (V.10), where the shrinking rate is not driven by the emission into GWs but rather into Goldstone bosons. GWs emitted at time t' with the modal frequency $f_{\rm emit}$ redshift to $f = f_{\rm emit}R(t')/R(t)$ at a later time $t > t'$.

The axionic string network emits GWs as long as the axion is massless. When coherent axion oscillations begin, the string network dissipates due to the formation domain walls, and the energy density of GWs emitted so far redshifts as radiation to present time,

$$\Omega_{\rm GW}(t_0,f_0) = \frac{\rho_c(t_{\rm osc})}{\rho_c(t_0)}\left(\frac{R(t_{\rm osc})}{R(t_0)}\right)^4 \Omega_{\rm GW}(t_{\rm osc},f)\,, \tag{V.14}$$

where $\rho_c(t)$ is the critical density of the Universe at time t and the frequency $f_0 = fR(t_{\rm osc})/R(t_0)$ accounts for the redshift of the peak wavelength.

We decompose the fractional energy density of GWs emitted by the string network loops in terms of the distribution of power mode of emission n as

$$\Omega_{\rm GW}(t_{\rm osc},f) = \gamma_{\rm GW}\sum_n \frac{n^{-4/3}}{\mathcal{N}}\,\Omega^{(n)}_{\rm GW}(t_{\rm osc},f)\,, \tag{V.15}$$

where $\mathcal{N} = \sum_n n^{-4/3}$, the power spectrum of index $q = 4/3$ characterizes the emission of GW modes from loops with cusps [372, 375], and the contribution from the mode n at time t reads [376]

$$\begin{aligned}\Omega^{(n)}_{\rm GW}(t_{\rm osc},f) \;=\; & \frac{1}{\rho_c(t)}\frac{2n}{f}\frac{\xi}{\alpha}\times \\ & \int_{t_s}^{t_{\rm osc}} {\rm d}t'\,\frac{G\mu^2_{\rm eff}(t')}{t_i^4}\left(\frac{R(t')}{R(t)}\right)^5\left(\frac{R(t_i)}{R(t')}\right)^3 .\end{aligned} \tag{V.16}$$

In Eq. (V.16), the time t_i at which the loop forms is obtained from inverting the redshift expression for the emitted frequency. Since the sum in the expression for the total emission converges slowly, higher emission modes significantly contribute to the total power. The thermal history of the Universe prior $t_{\rm osc}$, thus the choice of the NSC, enters Eq. (V.16) through the scale factors appearing in the integrand.

V.4 Method

We have solved numerically the set of coupled kinetic equations describing the decay of the exotic field ϕ into radiation in Eqs. (V.2)-(V.4), as a function of the parameters (T_ϕ, w_ϕ) and assuming that the radiation energy density is negligible at temperatures well above T_ϕ. We recover the time dependence of the Hubble rate H, which is fed into the equation of motion for the QCD axion field in Eq. (V.6) which describes the vacuum realignment mechanism (vrm). Since we are considering temperatures well above those at which matter-radiation equality occurs, the axion is a subdominant field during the pre-BBN epoch and does not appear in Eqs. (V.2)-(V.4).

The axion angle $\theta = a/f_a$, where a is the axion field, evolves according to Eq. (V.6), starting from the initial condition $\theta(t_i) = \theta_i$ and $\dot{\theta}(t_i) = 0$ (a dot is a derivation with respect to cosmic time) at some time t_i well before the time $t_{\rm osc}$ at which the axion acquires a non-zero mass, see Eq. (V.7). The initial value of the axion angle is fixed as $\theta_i = \pi/\sqrt{3}$ [377, 378]. The evolution of the axion field is sensitive to the total energy content of the Universe through the value of $t_{\rm osc}$, which depends on the value of the Hubble rate H. If coherent oscillations begin during a NSC, the abundance of axions differs from the standard result for a given value of f_a. This is extremely relevant if the transition temperature T_ϕ lies below the GeV [49].

The present number of axions per comoving volume resulting from the vacuum realignment mechanism just described, $n_a^{\rm vrm}$, and from axionic string emission $n_a^{\rm str}$. For the string contribution, we have integrated Eq. (V.11) numerically to include the time-varying linear mass density in Eq. (V.8) that characterizes the axionic string. The total number density of cold axions gets contributions from both string decay and vacuum realignment mechanism, and the resulting present energy density of axions is a function of f_a, w_ϕ, and T_ϕ. The value of f_a is then fixed by assuming that the axion is the DM particle, so that the value of the DM axion mass and the axion energy constant depend on the parameters w_ϕ and $T_{\rm RH}$ [2].

V.5 The QCD axion and NANOGrav

The results from NANOGrav-12.5 yr searches from PTA data [298] are reported in terms of the power-law spectrum of the characteristic strain

$$h_c(f) = A_* \left(\frac{f}{f_{\rm yr}}\right)^{\frac{3-\gamma}{2}} , \tag{V.17}$$

where $f_{\rm yr} = 1\,{\rm yr}^{-1}$ is a reference frequency, A_* is the amplitude at $f_{\rm yr}$, and the parameter γ is related to the spectral tilt. The fractional energy density in GWs associated with the strain is [306]

$$\Omega_{\rm GW}(f) = \frac{2\pi^2}{3H_0^2} f^2 h_c^2(f) \equiv \Omega_{\rm GW}^{\rm yr} \left(\frac{f}{f_{\rm yr}}\right)^{5-\gamma} , \tag{V.18}$$

where $\Omega_{\rm GW}^{\rm yr} = 2\pi^2 f_{\rm yr}^2/(3H_0^2)$.

The NANOGrav collaboration reports the fit of the strain in Eq. (V.17) to thirty bins within the frequency range $f \in (2.5, 90)\,{\rm nHz}$. However, the excess is reported by fitting only the first five bins in the signal-dominated frequency range $f \in (2.5, 12)\,{\rm nHz}$, while bins of higher frequencies are assumed to constitute of white noise. The constraint derived on the (A_*, γ) space of parameters reads approximately $\log_{10} A_* \in (-15.8, -15.0)$ and $\gamma \in (4.5, 6.5)$ at 68% confidence level (CL).

We assess the cosmological scenario presented against these experimental results, considering the GW signal from axionic strings given in Eq. (V.14). We obtain the spectral tilt and the amplitude by inverting the relations in Eqs. (V.17)-(V.18) as [306]

$$\gamma = 5 - \left.\frac{{\rm d}\ln \Omega_{\rm GW}(t_0, f)}{{\rm d}\ln f}\right|_{f=f_*} , \tag{V.19}$$

$$A_* = \sqrt{\frac{3H_0^2}{2\pi^2} \frac{\Omega_{\rm GW}(t_0, f_*)}{f_{\rm yr}^2} \left(\frac{f_{\rm yr}}{f_*}\right)^{5-\gamma}} , \tag{V.20}$$

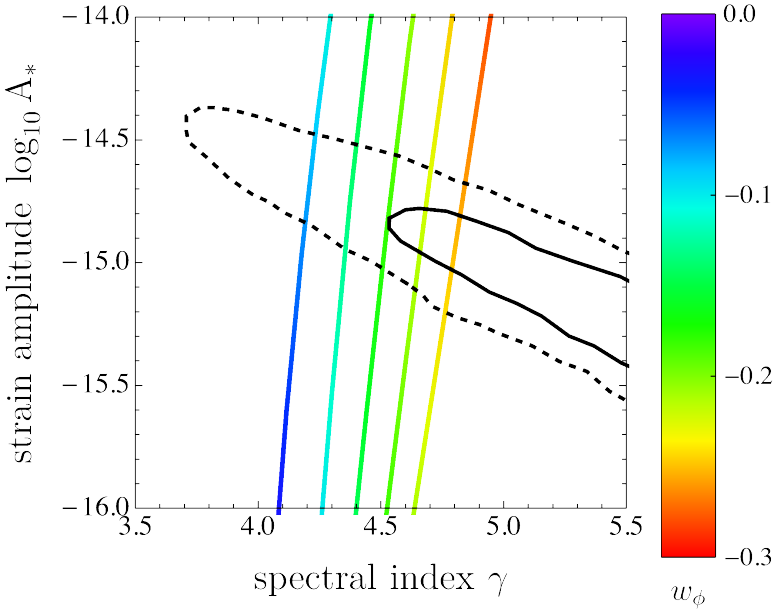

Figure V.1: The colored curves represent the amplitude A_* (vertical axis) and the spectral tilt γ (horizontal axis) of the SGWB predicted from axionic string, for different values of T_ϕ. From left to right, $T_\phi \in (5, 10, 15, 20, 25)$ MeV. The color codes different values of the equation of state w_ϕ along each line, as given by the color bar to the right of the figure. The solid and dashed black lines indicate the detection of (A_*, γ) respectively at 68% and 95%, as inferred by the analysis of the NANOGrav collaboration [298]. Figure made by L.Visinelli

where the quantities are computed at the reference frequency $f_* = 5.6\,\text{nHz}$ which is the geometric average of the signal-dominated frequency range considered.

In Fig. (V.1) we compare the results of the NANOGrav collaboration with the prediction of the SGWB from axionic strings in our model. The constraints on the strain A_* (vertical axis) and the spectral tilt γ (horizontal axis) from the NANOGrav collaboration are shown at 68% CL (solid black line) and 95% CL (dashed black line). Each color curve is a prediction of the model for different values of T_ϕ. From left to right, $T_\phi \in (5, 10, 15, 20, 25)\,\text{MeV}$. The color codes the value of the equation of state w_ϕ of the exotic component that controls the NSC, which varies within the region $w_\phi \in (-0.3, 0)$. Lines in blue represent models with a dust-like equation of state, $w_\phi \approx 0$, for which the model predicts a SGWB signal within 95% limit reported with a relatively low value of the transition temperature $T_\phi \lesssim 10\,\text{MeV}$. For these models, the GW strain amplitude lies between $\log_{10} A_* \in (-14.9, -14.4)$ with a spectral index $\gamma \sim 4.3$. Lines with a red shade represent models with $w_\phi \lesssim -0.2$. For these models, the expected SGWB from the axionic string network is within 68% limit, with the amplitude in the range $\log_{10} A_* \in (-15.3, -14.6)$ and a spectral tilt $\gamma \approx (4.7 - 4.8)$. The NANOGrav data then favor a negative equation of state $w_\phi \lesssim -0.2$.

Note, that the QCD axion is the DM particle in the model we consider, with the value of m_a sensibly differing from the result expected in a standard cosmological model. In particular, for the target parameter space that reconciles the NANOGrav results, we expect $m_a \in (0.01, 1)\,\mu\text{eV}$ [2]. In turns, the axion energy scale in our model is expected to be larger than the corresponding quantity in the standard cosmology, yielding to a sizable

SGWB which could potentially be detected by next-generation detectors across different GW frequencies. The predictions of the model would need to be confirmed through a direct detection of the QCD axion, whose light mass is in reach of "A Broadband/Resonant Approach to Cosmic Axion Detection with an Amplifying B-field Ring Apparatus" (ABRACADABRA) [379, 380] and "UPconversion Loop Oscillator Axion Detection experiment" (UPLOAD) [381, 382].

V.6 Discussion & Conclusion

If the SGWB signal is confirmed, we will have a precious insight into the physics of the early Universe. More data is needed to confirm the result and, in this case, to distinguish different models that candidate to explain the results in either astrophysical or cosmological setups. Models in which a spontaneous symmetry breaking leads to a string network whose GW emission can potentially explain the NANOGrav results in terms of a SGWB have been recently discussed in the literature [262, 307, 383]. Our model presents key differences from these models since i) the axionic string in our model does not last until the present time and it is dissipated in the early Universe as soon as the QCD axion acquires a mass, and ii) the axionic string network predominantly emits axions before decaying, with a subdominant spectrum of GWs. While the GW spectrum from axionic strings can be generally neglected, the GW strain is potentially detectable in future detectors for the region of the parameter space we consider in this work, $w_\phi \leq 0$.

The results are summarized in Fig. (V.1), where we show the prediction of the axionic string model proposed in light of the NANOGrav-12.5 yr results (solid black line is for 68% detection, and dashed black line is for 95% detection), for different values of the transition temperature T_ϕ (colored lines) and of the equation of state for the exotic field governing the NSC (color scale). Our model predicts an SGWB within the 95% limit of the PTA data when considering dust-like scenarios with $w_\phi \approx 0$ and a relatively low transition temperature $T_\phi \lesssim 10\,\mathrm{MeV}$. For these models, the GW strain amplitude lies between $\log_{10} A_* \in (-14.9, -14.4)$ with a spectral index $\gamma \sim 4.3$. For the case of a background model whose equation of states satisfies $w_\phi \lesssim -0.2$, the expected SGWB from the axionic string network is within 68% limit, with the amplitude in the range $\log_{10} A_* \in (-15.3, -14.6)$ and a spectral tilt $\gamma \approx (4.7 - 4.8)$. The preferred region of the parameter space hints at background models $w_\phi \lesssim -0.2$, with a transition temperature $T_\phi \lesssim 100\,\mathrm{MeV}$. Although we have not specified the underlying model for the exotic component that drives the background cosmology during NSC, a theory for the self-interacting potential of a scalar field that leads to $w_\phi < 0$ has been presented in Eq. (V.1).

At the time of conducting this work, we analyzed the NG 12.5-year data set [62, 384]. Subsequently, newer data releases from NG and other PTA collaborations have emerged [385–388], presenting a significant update since the 12.5-year dataset. It is important to reassess our findings in light of these recent data, given the potentially transformative insights they offer. The latest data indicate a softer spectral index, around 3, with a comparable strain amplitude. For our model, this suggests an earlier reheating temperature, together with a softer equation of state, and the potential scenario of $\omega_\phi \geq 0$. However, these hypotheses require validation through data analysis. Nevertheless, this qualitative understanding unveils intriguing possibilities and points towards a more phenomenologically viable regime for our model. Furthermore, such analysis could illuminate preferred mass regions for the DM axion. This work hinted at a preferred mass range of $\mathcal{O}(10^{-8})eV$ for the QCD axion to constitute the CDM abundance right in range for the ABRACADABRA experimental setup [379, 380]. Hence there is a potential great deal of

complementarity between the time of reheating of the universe and its equation of state, together with the preferred mass range for a CDM candidate and all of this can be inferred from the interpretation of the PTA data. Finally, the revelation of the axion theory can appear by considering its associated gravitational wave relics, which in fact might be the "smoking gun" because present axion experiments are very model-dependent.

Part III

PTA's & μ-Distortions

CHAPTER VI

Primordial Gravitational Waves from Pulsar Timing Arrays (PTAs)

VI.1 Introduction

The discovery of the first GW signal by the LIGO/VIRGO [52] collaboration has started a new era in astrophysics and cosmology. GWs offer a new avenue to explore the physics of the very early universe, since they travel almost entirely undisturbed through space-time. While LIGO and other ground based GW detectors are most sensitive to GWs with kilo-Hertz frequencies, here we focus on much longer wavelengths down to nano-Hertz (nHz). GWs in that frequency range are searched for by PTA experiments such as the EPTA [389, 390], NANOGrav [296, 384] and PPTA [391, 392], as well as their joint collaboration, the IPTA [393, 394].

In fact, there is now mounting evidence for a stochastic gravitational wave background (SGWB) in the nHz range from the observation and timing of pulsars by several PTA collaborations (NANOGrav [62, 395], PPTA [396], EPTA [397] and IPTA [388]). Such a signal is expected from GW emission from supermassive black hole binaries (SMBHBs) [398–400], but it can also be due to so far unknown new physics sources such as FOPTs [5, 302, 303, 395, 401–403], annihilating DW networks [404], CSs [306–308, 405–407], axion dynamics [303, 408], or induced by large scalar fluctuations [300, 301, 409–411].

An interesting aspect of the PTA frequency range is that, due to causality, it requires sources which are active down to cosmological temperatures of a few Mega-electronvolt (MeV). This is exactly the time when we start to have, at least indirect, constraints on the content and dynamics of the universe, from observations of the CMB, BBN and neutrino decoupling. Thus, while there are many mechanisms known to produce sufficiently large GW signals to explain the PTA data, it is non-trivial to write down concrete models which satisfy all existing constraints.

In this chapter we identify a few well defined benchmark models that can be confronted with both the GW data and cosmological constraints. Our focus here is on simplicity, i.e. to introduce as few new fields, parameters and couplings as possible, that nevertheless allow a consistent cosmological history. This also reduces the penalty for having too many parameters in Bayesian model comparison, which can in particular plague models of FOPTs, for which the signal parameterisation can be quite complicated even for simple underlying models. Some open questions that motivate this work is whether the frequency spectrum of the PTA observations can already discriminate between different models, whether the data from different PTAs can be consistently explained within these models, and which other cosmological observables can be used to identify or rule out different

explanations of the signal. In this thesis we will only provide with a summarized version of manuscript [7], mainly highlighting the parts the author of this thesis contributed. Therefore the other benchmark models like an FOPT, scalar induced GWs and the part on bosonic instability are omitted here. A brief summary of the findings of [7] for these explanations will be found in Sec. (VI.5).

In Sec. (VI.2), we introduce the models and their GW spectra. These are axion and ALP models that serve as benchmarks for GWs from global CSs, DWs. The GW spectra of these models are confronted with the PTA data using the `enterprise` software suite [412, 413] and the rapid fitting tool `ceffyl` [414], as discussed in more detail in Sec. (VI.3). Cosmological constraints in general and also separately for each model are discussed in Sec. (VI.4). There we also present the results of our fits to the PTA data and identify the regions of parameter space that satisfy all cosmological constraints. We conclude with some thoughts about the necessary steps for addressing the GW inverse problem [415], in anticipation of upcoming data releases by the PTA collaborations.

VI.2 Primordial sources of GWs in the nano-Hertz regime

A variety of models and scenarios can give rise to a primordial SGWB, see e.g. Ref. [416] for a review. Our goal here is not a comprehensive overview, but to study a selection of simple, but concrete, models that can produce a GW signal compatible with the current PTA data. This allows us to also confront the models with cosmological and laboratory constraints which provide complementary insight into their viable parameter space.

An important consideration is the magnitude and frequency range of the signal. To fully explain the observed excess noise, the GWs should today have a fractional energy density $\Omega_h^2 \sim 10^{-9}$ in the $(10^{-9} - 10^{-8})$ Hz range. GWs of this frequency are produced before matter-radiation equality, and thus subject to dilution by a redshift factor $\mathcal{F} \sim 10^{-5}$ between production and today. The largest possible amplitude is further constrained by the fraction of the total energy density carried by the source at the time of production Ω_S, and by the ratio of the typical length scale of the source divided by the Hubble radius at production, (LH_*), to some power. Thus, the expressions for the peak amplitude can all be cast in a form

$$\Omega h^2 \sim \mathcal{F}\,\Omega_S^2 (LH_*)^n\,, \tag{VI.1}$$

where the power n depends on the type of source and the expression should be evaluated at the time of GW production. Consistency and causality imply that these factors cannot exceed unity, but they can easily suppress the signal by several orders of magnitude in realistic models. Said differently, most scenarios that give rise to primordial GWs will fail to produce a sufficiently large signal.

We therefore focus on models and scenarios that are known to produce large GW signals at least in parts of their parameter space, which are also the models that will first be observed, or constrained, by future GW searches.[1] Since it will appear frequently below, let us also define the reduced Planck scale here as $M_{\rm P} = 2.4 \times 10^{18}$ GeV.

VI.2.1 Meta-stable topological defects, remnants of symmetry breaking

Spontaneous symmetry breaking in the early universe is accompanied, in many extensions of the SM, by the production of topological defects such as CSs and DWs [352, 418]. If

[1] In the context of LHC searches for new physics, the term "supermodels" was used for such scenarios [417].

symmetry breaking happens after inflation, these topological defects can carry a significant fraction of the total energy density in the early universe, and they give rise to GW spectra with distinct features.

Of particular relevance for GW production are networks of CSs from the breaking of a global U(1) symmetry, or networks of annihilating DWs from the breaking of a discrete symmetry. A simple and well studied model that gives rise to CSs is that of ALPs with post-inflationary Peccei-Quinn (PQ) breaking. For DWs, we consider two scenarios. In aligned axion models [419,420] the QCD axion is accompanied by several heavier partners, which necessarily couple to photons and gluons and thus reheat the visible sector after DW annihilation. Instead in heavy ALP models [421] the ALPs could also decay to dark radiation after DW annihilation, thus leading to a "dark DW" scenario [422]. In the following we introduce these scenarios in more detail.

VI.2.1.1 Global (ALP) Strings

CSs are one-dimensional objects originating from the spontaneous breaking of a U(1) symmetry. Here we will solely discuss global strings, i.e. strings stemming from breaking a global U(1) symmetry, for instance, an ALP string network. The core of the CS has a typical size that is of the order of the inverse of the symmetry-breaking scale, usually much smaller than the horizon scale. This allows us to employ the Nambu-Goto approximation, where CSs are one-dimensional infinitely thin objects whose tension μ is in units of energy per unit length. The string tension of ALP strings is given by

$$\mu = 2\pi n\, f_a^2\, \log(f_a t)\,, \tag{VI.2}$$

where f_a is the symmetry-breaking scale for an ALP string network with winding number $n = 1$. The network forms when the temperature of the universe is of the order of the PQ symmetry-breaking scale through the Kibble mechanism [423],

$$T_f \simeq f_a\,. \tag{VI.3}$$

This implies that there is a UV cut-off for the network associated with the time of formation, but this is in frequency ranges far above our region of interest. Once the network is formed it evolves towards an attractor solution that is independent of the initial conditions, the so called scaling regime. This is the result of equilibration between the competing effects of string recombination and the Hubble expansion.

GWs from strings are primarily radiated off loops. For global strings, this happens shortly after the loops are produced. GWs are only a subcomponent of the total emission from CS networks, with the main radiation emitted from long strings and loops going into axions. We base our quantitative analysis on the GW spectrum that was obtained in Ref. [45] from numerical simulations. In the scaling regime, it takes the form

$$\Omega^{\text{scaling}}(f)h^2 \simeq 0.8\times 10^{-15}\left(\frac{f_a}{10^{14}\,\text{GeV}}\right)^4\left(1+0.12\,\log\left[\left(\frac{f_a}{10^{14}\,\text{GeV}}\right)\left(\frac{10^{-8}\,\text{Hz}}{f}\right)^2\right]\right)^4. \tag{VI.4}$$

If the U(1) symmetry was exact, the string network would exist until today and would be subject to strong bounds from the non-observation of gravitational imprints on the CMB. We therefore consider a scenario where the U(1) is only approximately realized. The amount of symmetry breaking can be parameterized by the axion mass m_a (the Goldstone boson associated with the symmetry). Once the Hubble rate falls below the mass, DWs

form and lead to the rapid annihilation of the string network given that there is only one minimum in the axion potential (see below for multiple minima). The time of the decay can be related to a pivot frequency today at which the spectrum deviates from the form given above and transitions to a $\propto f^3$ slope in the IR. The pivot frequency can be expressed in terms of the mass as

$$f_{\rm pivot} \sim 3 \times 10^{-9}\,{\rm Hz} \left(\frac{m_a}{10^{-14}\,{\rm eV}}\right)^{\frac{1}{2}} , \tag{VI.5}$$

which is the annihilation frequency of the string network. We use a smooth step function for interpolating the GW spectra between the regime $f > f_{\rm pivot}$ described by Eq. (VI.4) and a $\propto f^3$ dependence in the IR regime.

Before moving on, let us note that in the literature there is an ongoing debate about whether the GW spectrum features the log enhancement that is apparent in Eq. (VI.4). When these simulations are carried out, technical constraints force one to only consider times close to the creation of the network when $\log(f_a/H) = \mathcal{O}(1-10)$. While there are many simulations in this regime [41,383,424,425] that agree up to order one factors, there is disagreement on how one should extrapolate these results to $\log(f_a/H) = \mathcal{O}(10-100)$ which is the relevant regime for predictions on GWs in PTAs. Suggestions reach from an exactly scale invariant spectrum [425, 426] to the $\log^4$ enhanced one [41, 383] that we are showing. The analytic observation that the string tension is expected to have a log enhancement together with other considerations on the scaling of the number of strings per Hubble patch leads semi-analytic approaches to suggest an in-between behavior [427–429].

The main consequence of this choice is that it changes the value of f_a towards larger values by a factor of up to $\mathcal{O}(10)$ to explain the amplitude. When comparing the PTA fit to the strength of other constraints these effects partially cancel, however, since also other observables such as the axion abundance are predicted to be log enhanced if the GW amplitude is (see Sec. (VI.4.1.1) for more details). A minor effect is that a log enhancement leads to a small slope in the scaling regime.

VI.2.1.2 Annihilating ALP/Axion DWs

DWs are two-dimensional topological defects that form due to the spontaneous breaking of a discrete symmetry. We refer the reader to Ref. [418] for a review of their cosmology, which we briefly summarize here. After the breaking of the symmetry, different patches in the universe populate the different degenerate minima. At the intersections of the patches the field has to interpolate between these ground states, which leads to a concentration of energy in thin two-dimensional sheets, the DWs. They carry a characteristic energy per area, or surface tension, σ. Subsequently, these networks evolve to minimize the area of the DWs, while radiating the majority of the released energy as particles and a small fraction as GWs.

Numerical simulations show that the evolution rapidly reaches a scaling regime, with roughly one DW per Hubble volume. The typical curvature radius is on the order of $\mathcal{O}(H^{-1})$ and the energy density is given by

$$\rho_{\rm DW} \simeq \mathcal{A}\,\sigma H\,, \tag{VI.6}$$

where H is the Hubble rate and the area parameter $\mathcal{A} \simeq \mathcal{O}(1)$ is a numerical prefactor extracted from simulations. In a model with a single real scalar field with broken Z_2 symmetry, its value is $\mathcal{A} = 0.8 \pm 0.1$ [430]. For larger numbers of degenerate minima,

$N_{\rm DW} > 2$, it is slightly bigger [431], but we will restrict our discussions to the case of $N_{\rm DW} = 2$ below.

As the universe cools down and the Hubble rate decreases, the total energy $\propto H^2$ is depleted faster than the one in the DW network. Thus the energy fraction in the DW network is growing as

$$\Omega_{\rm DW} \simeq \frac{\mathcal{A}\,\sigma}{3M_{\rm P}^2 H}\,, \tag{VI.7}$$

and eventually comes to dominate the energy density at a temperature

$$T_{\rm dom}^2 = \frac{\mathcal{A}\,\sigma}{\pi M_{\rm P}}\sqrt{\frac{10}{g_*(T_{\rm dom})}}\,. \tag{VI.8}$$

In order not to overclose the universe, DWs must be unstable and decay at temperatures above $T_{\rm dom}$. This requires an explicitly symmetry-breaking term in the Lagrangian, lifting the degeneracy between the vacua. We denote by $V_{\rm bias}$ the energy difference between minima. This difference generates a volume pressure which leads to the annihilation of the network once the pressure becomes comparable to the surface tension in the walls. In a radiation-dominated universe, the network then annihilates at a temperature [431]

$$T_{\rm ann} \simeq 20\,{\rm MeV}\left(\frac{\sigma}{{\rm TeV}^3}\right)^{-\frac{1}{2}}\left(\frac{V_{\rm bias}}{{\rm MeV}^4}\right)^{\frac{1}{2}}\,. \tag{VI.9}$$

In order to avoid overclosure, $V_{\rm bias}$ has to satisfy $V_{\rm bias}^{1/4} \gtrsim 0.03\,{\rm MeV}\,\left(\sigma/{\rm TeV}^3\right)^{1/2}$. The network's energy is located in the DWs that are moving at relativistic velocities. Additionally, the scalar particles that get radiated from the DWs also possess large inhomogeneities. Both contribute to an anisotropic stress that leads to the emission of GWs. The majority of GWs get emitted right before the network annihilates, when its energy $\Omega_{\rm DW}$ is largest. The GW spectrum can be found from numerical simulations [418] and its peak amplitude and frequency are found to be

$$\begin{aligned}\Omega_{\rm GW}^{\rm peak}h^2 &\simeq 2.8\times10^{-18}\left(\frac{\sigma}{{\rm TeV}^3}\right)^2\left(\frac{T_{\rm ann}}{10\,{\rm MeV}}\right)^{-4}\,,\\ f_{\rm peak} &\simeq 1.1\times10^{-9}\,{\rm Hz}\left(\frac{T_{\rm ann}}{10\,{\rm MeV}}\right)\,.\end{aligned} \tag{VI.10}$$

Here we included redshift factors assuming that annihilation takes place during radiation domination at temperatures close to 10 MeV that lead to the correct frequencies for PTAs. We follow Ref. [404] and assume that away from the peak the spectral shape is given as

$$\Omega_{\rm GW}(f)h^2 = \Omega_{\rm GW}^{\rm peak}h^2 \times S(f/f_{\rm peak})\,, \qquad S(x) = \frac{4}{x^{-3}+3\,x}\,. \tag{VI.11}$$

The behavior for frequencies below the peak as f^3 is dictated by causality, while the f^{-1} above the peak is found in numerical simulations. Additionally, there will be a cutoff at much larger frequencies that is correlated with the time when the network is first formed. These frequencies are, however, way too large to be relevant for the PTA data we consider.

So far, the discussion has been fairly model-independent. We will now explore two explicit models, where the DWs arise in a generic ALP model or in a clockwork realization of the QCD axion. While the two scenarios lead to almost identical GW spectra, their cosmological signatures are quite distinct.

We first consider the case of an ALP as the pseudo Nambu-Goldstone boson generated from the spontaneous breaking of an anomalous U(1) symmetry, which we will refer to as a Peccei-Quinn symmetry, at a scale f_a. The Lagrangian takes the form

$$\mathcal{L} = \partial_\mu \Phi^\dagger \partial^\mu \Phi - \lambda \left(\Phi^\dagger \Phi - \frac{v_a^2}{2} \right)^2 - V(a) \,, \tag{VI.12}$$

where $\Phi = \rho/\sqrt{2} \exp\{(ia/v_a)\}$ is a complex scalar field and the axion a is its angular part. The potential of Eq. (VI.12) is such that the U(1) symmetry is spontaneously broken, with a vev $\langle \Phi \rangle = v_a/\sqrt{2}$ and $a \in [0, 2\pi v_a)$. The term $V(a)$ in Eq. (VI.12) is the anomaly-induced U(1) breaking under the influence of a strongly coupled gauge theory with dynamical scale $\Lambda \simeq \sqrt{m_a f_a}$. This explicitly breaks the U(1) symmetry into its $\mathcal{Z}_{N_{\rm DW}}$ subgroup. The conventional form of such explicit breaking at zero temperature is

$$V(a) = \Lambda^4 \left(1 - \cos \frac{a}{f_a} \right) \,, \tag{VI.13}$$

where $f_a = v_a/N_{\rm DW}$. The tension of ALP DWs in the absence of finite temperature effects can be estimated as [418]

$$\sigma = 8 m_a f_a^2 \,. \tag{VI.14}$$

We will work under the assumptions that $v_a < T_{\rm rh}$, such that the U(1) symmetry is restored after inflation and the network forms as the universe cools down, and that there is a large separation of scales between v_a and Λ. This initially leads to the formation of a CS network which persists until the time of DW formation when $H \approx m_a$. Since $N_{\rm DW} \geq 2$, there are multiple DWs attached to every string and the network is stable. Shortly after this time, the combined network is dominated by the dynamics of the DWs and one can neglect any effect the remnant strings have on the evolution. GWs produced by strings, as well as cosmological constraints such as those coming from $N_{\rm eff}$, are negligible with respect to the contributions from DWs. This is because, as will be clear from Sec. (VI.4.1.2), the decay constant f_a is much lower than in the CS scenario discussed above.

In addition, the global U(1) symmetry is expected to be broken quantum gravity effects. Therefore, additional breaking terms, if not accidentally aligned with the anomalous breaking, lift the degeneracy between the minima. They provide the necessary $V_{\rm bias}$ for the network to annihilate, with the temperature of annihilation given by Eq. (VI.9).

In addition to the generic ALP model, we consider DWs in models of the QCD axion, i.e. models that solve the strong CP problem. One such scenario is that of axion alignment [419] realized by a clockwork mechanism. Here a collection of N axions that individually respect a shift symmetry

$$\phi_i \to \phi_i + C_i \,, \tag{VI.15}$$

is considered, where C_i is a real-valued transformation parameter. One then assumes that $N-1$ of these shift symmetries get explicitly broken into their discrete subgroups, giving rise to the potential for $N-1$ linear combinations of the axions. The remaining flat direction is then identified as the QCD axion with its associated gluon coupling in, for instance, the Kim-Shifman-Vainshtein-Zakharov (KSVZ) model.

The main advantage of this scenario is that it gives a light QCD axion with an exponentially enhanced effective decay constant $F_a \sim f_a e^N$, while the actual symmetry breaking scales f_a can be much lower, e.g. around the TeV-PeV scale, thus making the model

testable at particle physics experiments. This also ensures that the symmetry breaking can take place after reheating, and thus a DW network, made from the $N-1$ heavy axions predicted by the model, can form. Ref. [419] found that the DWs are long-lived and survive until the QCD axion potential becomes relevant. For simplicity we take equal masses m_a and equal decay constants f_a for all the heavy axions. In terms of these, the DW tension is again given by Eq. (VI.14).

Different from the generic ALP model, here the network is destabilized by QCD instantons at the time of the QCD phase transition. This lifts the degeneracy between the different minima by $\Delta V \simeq \Lambda_{\rm QCD}^4$, and the annihilation temperature can be predicted as [419]

$$T_{\rm ann} \sim 1\,{\rm GeV} \left(\frac{g_*(T_{\rm ann})}{80}\right)^{-\frac{1}{4}} \left(\frac{\Lambda_{\rm QCD}}{400\,{\rm MeV}}\right)^2 \left(\frac{10^7\,{\rm GeV}}{f_a}\right) \sqrt{\frac{10\,{\rm GeV}}{m_a}}\,. \tag{VI.16}$$

Up to order-one factors, the GW spectrum obtained in Ref. [419] agrees with Sec. (VI.10), and we will therefore use the latter for both models. The main difference instead is that in the aligned axion model, also the heavy axions couple to the SM via the usual axion couplings [432]. Shortly after DW annihilation, the energy is therefore transferred back to the visible sector via decays of the heavy axions into SM particles. As discussed in more detail in section VI.4.1.2, these two DW scenarios are therefore subject to very different cosmological constraints.

VI.3 PTA data and fitting method

Since 2020, three of the currently operating PTA observatories, NANOGrav [62], EPTA [397] and PPTA [396] have reported strong evidence for a common-spectrum red process across pulsars in their data. Similar results were found by the joint IPTA [388] collaboration combining previous data releases of the former three. Although the evidence for the interpulsar Hellings-Downs correlations [299] required for establishing the observation of a GW signal is still not conclusive, it is intriguing to attribute this signal to a SGWB.

We here operate upon the assumption that the putative SGWB signal is of cosmological origin and assume that the potential SGWB from SMBHBs is subdominant in the frequency range we consider. We fit the GW signals produced by the sources discussed in Sec. (VI.2) to pulsar timing data. For PTA data this fit is typically done in terms of the timing-residual cross-power spectral density,

$$S_{ab} = \Gamma_{ab} \frac{H_{100}^2}{8\pi^4} \frac{\Omega h^2(f)}{f^5}\,. \tag{VI.17}$$

Here, Γ_{ab} denotes the overlap reduction function between two pulsars a and b and $H_{100} = 100\,{\rm km\,s^{-1}\,Mpc^{-1}}$. However, a thorough Bayesian analysis of this quantity for PTA data is a computationally expensive task. Hence, fast refitting techniques have been developed to reinterpret free-spectrum fits (to the entire PTA or for each pulsar individually) in terms of arbitrary SGWBs, resulting in the development of the `ceffyl` analysis suite [414]. In this vein, we perform a PTA free-spectrum refit in `ceffyl` to the NANOGrav 12.5 year dataset [384] and the second data release (DR2) of IPTA [388,394]. The kernel density estimator (KDE) representation required by `ceffyl` for the NANOGrav dataset is provided by the collaboration [433]. For the IPTA data, the KDE is created reproducing the 30-frequency-bin free-spectrum fit with `enterprise` [412] and `enterprise_extensions` [413].

We verified that `ceffyl` reproduces the best-fit regions for a simple power-law SGWB that were obtained by NANOGrav and IPTA. Furthermore we also checked that this remains true for broken power-law signals by comparing the best-fit regions obtained with `ceffyl` to those from a full `enterprise` run for the bosonic instability scenario in [7]. We use `PTMCMCSampler` [434] to sample the respective parameter spaces of our signal models, except for the CW model for which we evaluate the likelihood on a regular grid. An overview of the priors we use in our Bayesian analysis can be found in Sec. (VI.7.1).

Following the NANOGrav searches for a general common-spectrum signal [62] and for a SGWB from FOPTs [395], we use only the five lowest-frequency bins of the NANOGrav data, corresponding to frequencies below $f \lesssim 12.5\,\mathrm{nHz}$. These bins give the strongest contribution to the signal-to-noise ratio (SNR) of the NANOGrav signal [62]. For consistency, we cut the IPTA data at the same frequency. Due to the longer observation period of 30 years, this corresponds to twelve bins in the IPTA 30-component free-spectrum fit.

Intuitively, the most robust insight into the low-frequency regime can be obtained by combining data from different PTA collaborations. However, this is a very challenging task. The different datasets comprise pulsars observed by multiple collaborations,[2] timed over various observation periods at different times and with different telescopes. A considerable amount of care has to be taken to properly account for all correlations between the individual measurements due to overlaps in the timing data as well as instrument-specific noise contributions. In order to address this, EPTA, NANOGrav and PPTA, as well as the Indian Pulsar Timing Array (InPTA) project, have formed the joint IPTA consortium. While the current evidence in the individual PTAs could only be established with the respective latest data releases, IPTA was able to detect the common spectrum combining data available in 2016 and before. Hence, the question arises what can be expected when all currently available measurements are taken into account.

Clearly, a forecast with a proper account of pulsar overlaps is beyond the scope of this work. To approximate the signal reconstruction obtained in a future IPTA release, we here employ a naive combination by multiplying the likelihoods of the NANOGrav 12.5 year data and IPTA DR2, where we again evaluate the likelihood of each experiment using `ceffyl`, i.e. treating the two datasets as independent. In addition to the overlap discussed above, this procedure evidently double-counts pulsars, as IPTA includes the nine-year NANOGrav data. However, not all pulsars in the nine-year dataset have been observed for a sufficient amount of time to contribute to the frequency bins we consider, somewhat reducing the number of double-counted pulsars. Nonetheless, a significant overlap between the two datasets remains. Consequently, while we still present the naive combination as a rough indicator for how the results might change in the near future, the corresponding fit should be taken with caution.

VI.4 Cosmological constraints and final results

As discussed in Sec. (VI.2), to explain the large observed signal, the GW sources should constitute a significant fraction of the total energy density in the universe at the time of GW production, and are therefore likely to be subject to other cosmological constraints. Furthermore, the frequency range puts the time of GW production close to that of nucleosynthesis and neutrino decoupling at $T \lesssim 1\,\mathrm{MeV}$ and $T \approx 2\,\mathrm{MeV}$, respectively. More

[2] Currently, IPTA includes timing measurements of 65 millisecond pulsars, of which 24 are observed by more than one PTA.

precisely, the frequency today can be written as [435]

$$f_0 = \frac{a_*}{a_0} H_* \frac{f_*}{H_*} \approx 10^{-9}\,\mathrm{Hz} \times \frac{T_*}{10\,\mathrm{MeV}} \frac{f_*}{H_*}\,, \tag{VI.18}$$

where T_* is the temperature of the universe at the time of production. Causality requires the last factor to be larger than unity, therefore GWs in the frequency range probed by NANOGrav cannot be produced much before the time of nucleosynthesis.

Overall, the following constraints are considered for each model:

- The abundance of **relativistic degrees of freedom**, commonly expressed as $\Delta N_{\rm eff}$, should satisfy the current constraints $\Delta N_{\rm eff}^{\rm BBN} \leq 0.39$ at 2σ and $\Delta N_{\rm eff}^{\rm CMB} \leq 0.29$ at 2σ [21] confidence level (CL), at the relevant temperatures.
- **Big Bang Nucleosynthesis** should not be affected significantly, which roughly implies that the universe should look standard model like at temperatures below 1 MeV. More precise constraints on the allowed amounts of energy influx into the SM thermal bath during and after BBN are available e.g. in Refs. [310, 436] and are taken into account when relevant.
- If the energy in the GW source leads to significant **late time reheating**, then the universe should reheat to $T_{RH} \gtrsim 2\,\mathrm{MeV}$ such that also the neutrino sector is re-thermalised [436, 437]. Furthermore the **dilution of previously produced baryon and dark matter (DM) abundances** has to be taken into account.
- **Spectral distortions of the CMB** can be induced by late decays of particles [438, 439] or by large fluctuations in the plasma or even decoupled sectors [4, 440], and thus can both directly and indirectly constrain models that produce large GW signals at low frequencies. The current limit on μ-type spectral distortions from COBE/FIRAS is $\mu < 4.7 \times 10^{-5}$ [441], which could be improved to $\mu < 3 \times 10^{-8}$ by future missions such as PIXIE [442].
- If the energy stored in the GW source is partially converted to non-relativistic **dark matter**, its abundance should not exceed the observed value today $\Omega_{\rm DM} h^2 \leq 0.12$. If this becomes a significant fraction of the total dark matter, also isocurvature constraints apply.
- The large energy anisotropies typically required to produce GWs may lead to the formation of **primordial black holes or dark matter mini-clusters**. Their abundance should obviously agree with observational constraints.

While above these cosmological observations are discussed as constraints, more precise measurements in the future will allow us to discriminate between different sources of GWs. Below we show this in particular for the case of constraints on $\Delta N_{\rm eff}$, which is expected to improve by an order of magnitude in the coming decade [443, 444], and for the case of CMB spectral distortions, which could be improved by several orders of magnitude in the not too distant future [445, 446].

VI.4.1 Meta-stable topological defects, remnants of symmetry breaking

VI.4.1.1 Global (ALP) Strings

In Fig. (VI.1) we show the preferred parameter space in which cosmic strings from the spontaneous breaking of a U(1) symmetry can explain the PTA signal. This region changes slope around $m_a \approx 10^{-14}\,\mathrm{eV}$. For lower masses, the network decays at temperatures below 1 MeV and the PTA signal is due to the almost scale invariant part of the spectrum, for larger masses the $\propto f^3$ tail of the spectrum that gets created in the decay of the network

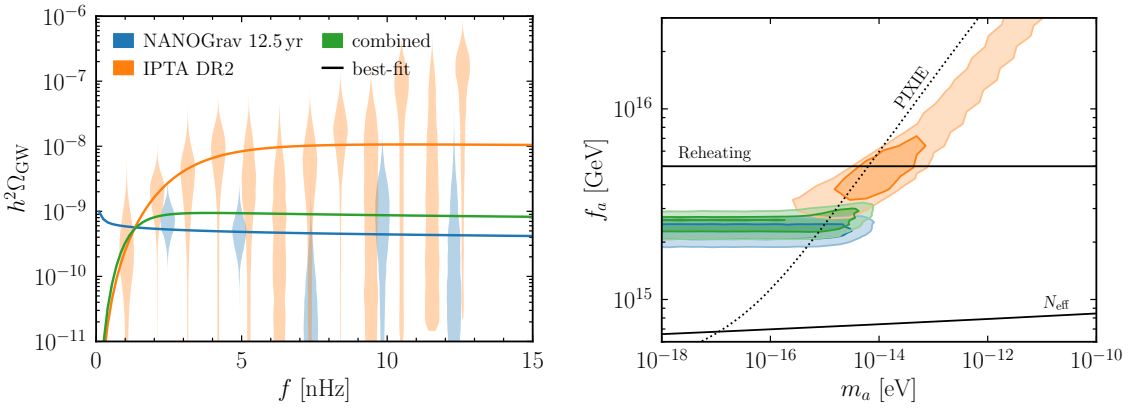

Figure VI.1: Best-fit regions from fitting the GW signal from an ALP string network (cf. Sec. (VI.2.1.1) to NANOGrav (blue) and IPTA (orange) data, as well the naive combination of both (green). *Left:* Fitted GW spectrum and input data for the refitting (violins). *Right:* Contours of the ALP mass m_a and decay constant f_a. The regions above the solid lines are excluded by constraints from reheating and $N_{\rm eff}$, as discussed in the text. The projected sensitivity of PIXIE is indicated by the dotted line. The full triangle plot including 1D posteriors is shown in Sec. (VI.4). Figures were created by S.Schenk

gives the signal. The NANOGrav data seems to prefer the former scenario, while IPTA favors the latter.

In a minimal scenario ALPs in this parameter space are expected to be cosmologically stable with negligible SM interactions. As the ALP strings continuously radiate ALPs during the evolution of the network, they create an abundance of both relativistic and non-relativistic ALPs contributing to $N_{\rm eff}$ and DM respectively. For the contribution towards $N_{\rm eff}$ we obtain using Eq. (21) of Ref. [383],

$$\Delta N_{\rm eff} = 0.4 \left(\frac{f_a}{10^{15}\,\text{GeV}}\right)^2 \left(\frac{\log(f_a/m_a)}{80}\right)^3 . \tag{VI.19}$$

Using this relation, the present bound on $\Delta N_{\rm eff}$ corresponds to an ALP decay constant of $f_a \lesssim 10^{15}\,\text{GeV}$. It is therefore at tension with all of the parameter space favored by the fit. At this point it is however worth mentioning that other predictions concerning the log scaling as discussed in Sec. (VI.2.1.1) might lead to a milder tension. Assuming that this is a viable explanation, the non-relativistic ALPs also contribute to DM.[3] In order to not overproduce DM, very small masses of $m_a \sim 10^{-22}\,\text{eV}$ are required. At least the NANOGrav data would still be consistent with such a scenario, our figure only ends at $m_a \sim 10^{-18}\,\text{eV}$ due to our choice of priors. Alternatively, also a period of late matter domination can improve the viability of the model, while still yielding observable GWs [2, 427, 429, 447]. For completeness, let us also mention one further constraint, even though it is always weaker than $N_{\rm eff}$. In order for the string network to form, the global symmetry should be broken after inflation and reheating. The current Planck bound on the Hubble scale [21] at the end of inflation, $H_{\rm inf} \leq 6 \times 10^{13}\,\text{GeV}$, one finds that the highest temperature of the post-inflationary universe is $T_{\rm max} \sim 5 \times 10^{15}\,\text{GeV}$. The constraint $f_a \leq T_{\rm max}$ is therefore also indicated in Fig. (VI.1).

[3] This Ultralight DM is too fuzzy however to allow for the observed structure formation and can therefore only constitute a small fraction of the total dark matter [383].

Overall, it appears that the global CS scenario is not a viable explanation for the current PTA data. Nevertheless, future GW probes in the nHz range will be able to test viable regions of parameter space (see e.g. Fig. 11 of [4]), and it could easily be that most of the current signal is of astrophysical origin. A complementary probe of such a scenario would also be provided by future measurements of μ-distortions, as shown by the dotted line in Fig. (VI.1). We therefore decided to keep it in our list of simple benchmark models.

VI.4.1.2 Annihilating ALP/Axion DWs

To explain the available PTA data with DWs, the network needs to annihilate close to BBN. In order to produce a sufficient amount of GWs, it needs to comprise at least a fraction of the total energy, $\Omega_{\rm DW} \sim 0.1$. Annihilating DWs mainly decay into non-relativistic particles, which in our models are the heavy axions and ALPs. They necessarily have to decay further, in order to not overclose the universe. At this point we have to distinguish between the ALP and the aligned axion model.

In the ALP model, for simplicity, we assume that the ALPs subsequently decay to some form of dark radiation, which will contribute to ΔN_{eff}. Assuming efficient annihilation, we can set $\rho_{\rm DW} \simeq \rho_d$ where ρ_d is the energy density in dark radiation, and obtain

$$\Delta N_{eff} \simeq 1.6 \left(\frac{g_s(T)}{10}\right)^{5/6} \frac{m_a f_a^2}{M_{\rm P} T^2}\,, \tag{VI.20}$$

where the temperature should be taken at the time of annihilation, $T = T_{\rm ann}$. Besides $\Delta N_{\rm eff}$ constraints, DW networks that are decoupled from the SM were shown in Ref. [4] to exhibit μ-distortions. We follow their approach to compute the induced μ-distortions and impose the constraints from FIRAS as well as the expected sensitivity of the PIXIE proposal. There are two more technical constraints that we impose. First we require that the DW network annihilates sufficiently before it would start to dominate the energy density of the universe, $T_{\rm dom} \lesssim 4\,T_{\rm ann}$. On the other hand we also require that $T_{\rm dom} \gtrsim T_{\rm ann}/4$, to ensure that plasma effects on the DWs are negligible [421]. This should ensure that our results are in the region where the simulations of the GW spectra can be trusted.

Fig. (VI.2) shows the range of axion masses and annihilation temperatures $T_{\rm ann}$ preferred by the fit of the ALP DW GW spectrum to NANOGrav (blue) and IPTA (orange) data, as well as the combined fit (green). Here f_a takes values between 5×10^4 GeV and 10^7 GeV, with smaller values preferred for larger m_a and for NANOGrav, while IPTA prefers values closer to the upper end of the range, as can be seen in the full triangle plot in Fig. (VI.5). Only a small part of the parameter space is disfavored by $N_{\rm eff}$ limits. We indicate them for two characteristic values of f_a in the figure. As discussed above, our estimate of the GW signal is only reliable in a certain window, which here is the region between the dashed lines. Finally PIXIE would be able to probe the region below the dotted line. It is apparent that especially at small annihilation temperatures μ-distortions provide a strong independent probe of the model going much beyond the $N_{\rm eff}$limit. Within the range of decay temperatures favored by the fit their reach is however limited.

In the aligned axion model, we expect instead that the heavy axions rapidly decay to SM particles after DW annihilation. Therefore, we do not expect constraints from $N_{\rm eff}$ or spectral distortions. Instead, one needs to make sure that the decay products of the heavy axions do not jeopardize BBN. To estimate this, we compare their decay rate into gluons

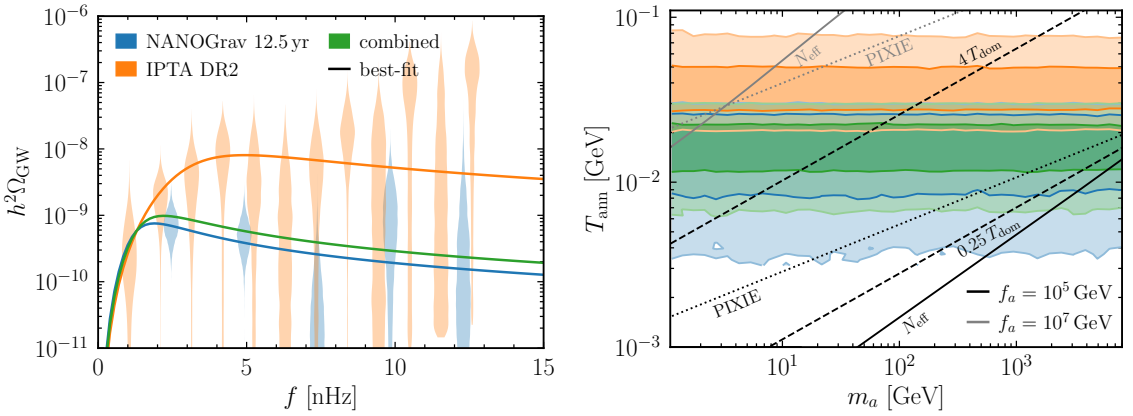

Figure VI.2: Fit results of the ALP DW model from Sec. (VI.2.1.2) to NANOGrav (blue), IPTA (orange) and their combination (green). *Left:* Best-fit GW spectrum alongside the free-spectrum fit (violins). *Right:* 68 % and 95 % CL fit region in terms of the axion mass m_a and annihilation temperature $T_{\rm ann}$. In the region between the dashed lines, our description of the GW spectrum in terms of the scaling regime is valid. The region below the solid lines is excluded by $N_{\rm eff}$ for $f_a = 10^5$ GeV (black) and for $f_a = 10^7$ GeV (grey). The dotted line shows the projected sensitivity of PIXIE. The full triangle plot including 1D posteriors is shown in Fig. (VI.5). Figures were created by S.Schenk

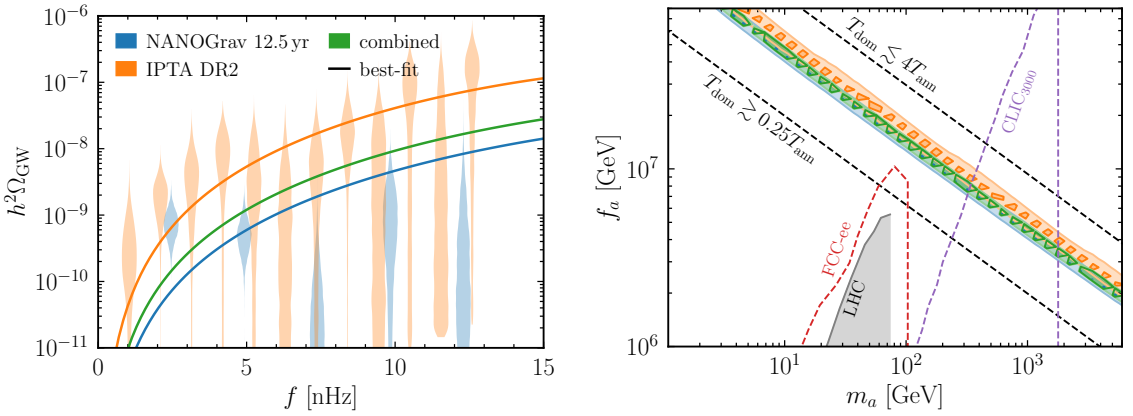

Figure VI.3: Fit results of the aligned QCD axion DW model from Sec. (VI.2.1.2) to NANOGrav (blue), IPTA (orange) and their combination (green). *Left:* Best-fit GW spectrum alongside the free-spectrum fit (violins). *Right:* 68 % and 95 % CL fit region in terms of the axion mass m_a and decay constant f_a. In between the dashed lines our description of the GW spectrum in terms of the scaling regime is valid. The full triangle plot including 1D posteriors is shown in Fig. (VI.6). The collider projections from LHC Run 2 in grey are taken from Ref. [448], whereas the projections from searches by FCC and CLIC are from Ref. [449]. Figures were created by S.Schenk

and photons with the Hubble rate, i.e. $\Gamma_{a\to gg/\gamma\gamma} \simeq H(T)$, where the decay rate at leading order of an axion into two gluons is given by

$$\Gamma_{a\to gg} \sim \frac{1}{64\pi}\left(\frac{\mathcal{C}_{gg}\alpha_s}{2\pi}\right)^2 \frac{m_a^3}{f_a^2} \simeq 1.67\times 10^{11}\,\mathrm{s}^{-1}\left(\frac{m_a}{10\,\mathrm{GeV}}\right)^3\left(\frac{10^7\,\mathrm{GeV}}{f_a}\right)^2, \qquad \text{(VI.21)}$$

with $\alpha_s = 0.1$ and $\mathcal{C}_{gg} = 1$. Our primary concern will be the decay into gluons for $m_a \geq 1\,\mathrm{GeV}$. This rate is fast enough to ensure decays before the onset of nucleosynthesis. In fact it guarantees that the relic axions will almost instantly decay after the DW network annihilates for all values of m_a and f_a considered here.

We show the 68 % and 95 % CL contours as a function of the axion mass and decay constant in Fig. (VI.3). The technical constraints discussed for the ALP case also apply here. Again we see that the best-fit region fully agrees with the range of validity of the DW simulations we are using, and there are no conflicts with cosmological bounds. It should be noted though that the best-fits shown on the left of Fig. (**??**) disagree substantially. This difference is due to the heavy axion model possessing effectively only one parameter, with the surface energy $\sigma \propto f_a^2 m_a$ and the annihilation temperature $T_{\mathrm{ann}} \propto 1/(f_a\sqrt{m_a})$ both being controlled by the same combination of parameters. This leads to the peak of the spectrum sitting at higher frequencies than the range probed by PTAs, while for the ALP model the peak can be freely adjusted and the fit prefers parameters where it falls into this range.

Furthermore, it can be interesting to ask whether the heavy axions in this model can be probed in the laboratory, in particular at the LHC. It was shown in Ref. [448] that the production of axions in the decay of electroweak bosons provide a particularly sensitive probe for heavy axions in the $(1 - 100)\,\mathrm{GeV}$ mass range. While the projected collider reach of the LHC (grey shaded region) is not sufficient to probe the best-fit region, it is still interesting to see that collider probes of such scenarios are in principle possible. In particular, a future linear electron-positron collider such as CLIC with a center-of-mass energy of 3 TeV can explore the best-fit region for axion masses above $m_a \gtrsim (10 - 100)\,\mathrm{GeV}$, whereas a circular collider like FCC-ee would not be able to probe the required decay constants [449].

A potentially important constraint on DWs as a source for the PTA signal comes from the formation of PBH during the annihilation of the domain-wall network. Closed domain walls of typical radius $r \sim H^{-1} \sim t$ will form a BH when their linear size becomes smaller than their Schwarzschild radius $r_S \propto M \propto r^3$ [450–452]. According to a recent study [452], in the parameter space where the PTA signal is reproduced an overabundance of PBH is produced. Still, we believe that the current understanding of this process does not allow to claim the exclusion. First, the scaling regime $r \sim t$ is expected to be violated when the Schwarzschild radius becomes comparable to r, but dedicated simulations are lacking. Secondly, the assumption $r = t$ implies a monochromatic spectrum, which is not expected to be realized in a consistent cosmological history. Last, the evolution from the start of the annihilation process T_{ann} until the time of BH formation T_* is still very uncertain, and its impact on f_{PBH} is parametrized by the ratio $(T_*/T_{\mathrm{ann}})^\alpha$, with $\alpha \simeq 7 - 28$. Given these large uncertainties, we refrain from showing these constraints in our figures, but we stress their potential relevance and encourage a dedicated analysis, which goes beyond our current scope.

VI.5 Summary of remaining Benchmark models

As stated in the declaration of the author's contributions to the paper this section is intended as a brief summary of the omitted section of [7] in which the author did not contribute. The other benchmark models of interest in [7] were an Abelian Higgs model with classical scale invariance as a benchmark for GWs from supercooled FOPTs, ALP models featuring bosonic instabilities, and a single field inflationary model for secondary GWs from large density fluctuations. These benchmark models were challenged against the same or other relevant cosmological constraints as for the axion/alp strings and DW cases. We will discuss the results of the fits to the PTA data for each benchmark model separately. The most recent data release by the PTA collaborations are in overall agreement with the IPTA dataset presented here so the summarized results will mainly revolve around that dataset. In table Tab. (VI.1) the best-fit data point is presented for all benchmark models as in table 1 in [7]. For details on the models and the fitting procedures of the benchmark models to the PTA data we refer the reader to [7].

- **Supercooled FOPT:** The model of concern here was the Coleman-Weinberg model by considering the loop corrections to the potential for radiative symmetry breaking. The results of this benchmark model is revealed in figure 3 of [7] where the right figure displays 2-d contour plots of the posteriors of the PTA data regions by IPTA and 12.5 year NANOGrav data. The axis are for different values of the gauge coupling g and the mass scale $M = e^{-\frac{1}{3}+\gamma_E}\frac{\mu_R}{4\pi}$ such that the zero T VeV and mass of scalar can be related to the mass scale M. In the right plot in figure 3 of [7] several statments can be made first these FOPTs needs to be very supercooled and hence one may imagine that the bubble wall collision contribution is the dominant one in this setup. Furthermore to be compatible with the the IPTA data large amounts of entropy dilution is present so many DM and baryogenesis mechnanism may be spoiled due to the large initial dilution of order $\mathcal{O}(10^{10})$. Interesting consequence of the model presented in [7] is that the percolation temperature is so low that nucleosynthesis would have already started and as the plasma reheats after the PT a second epoche of nucleosynthesis would be necessary. The reheating dynamics here one needs to elaborate on is the fact that there is a light scalar present close to BBN so its decay is necessary. the authors in [7] discuss some possibilities for viable decay channels and illustrate the point that future colliders may be able to test such a scenario like FCC-ee.
- **Bosonic Instability late preheating:** Here an alp coupled to a dark photon was considered which produces GWs by a tachyonic instability in the production of dark photons due to the oscillations of the alp. This setup possessess two components the alp being a CDM candidate meanwhile the Dark Photon will act as extra relativistic degrees of freedom. One can see from figure 7 in [7] that there is a tension between ΔN_{eff} and the preferred parameter points by the PTA collaborations. There has also been recent works realizing that the alp in these models also tend to overproduce CDM [453–455] and these issues have also been spotted when concerned with models with parametric resonances instead of a tachyonic instability [258, 456, 457]. One may also ask if one could instead deplete the energy into the SM plasma, however in such a scenario as this it is very hard as the axion is very light with a large decay constant hence very long lived and perturbative decay rates will be very tiny.
- **Scalar Induced GWs:** In this scenario to reproduce the PTA signal one needs an amplitude of the scalar perturbations of the order $A_\zeta \sim 10^{-2} - 10^{-1}$, which peak momenta around $(10^6 - 10^7)Mpc^{-1}$. The qualitative difference here is that these

GWs are generated during inflation so the constraints on these sources can be slightly different. In the right figure 8 of [7] one can note that μ- distortions puts contraints on a large region of available parameter space in these scenarios. Furthermore the impact of Primordial Black hole Production and their intrinsic gaussianities may play a crucial role for this source of SGWBs to being able to reconcile the PTA data without being excluded. In [7] they made a case study for a single field inflation model with an inflection point, known to have large scalar fluctuations and PBH production however they were not able to fulfill CMB contraints with this model.

VI.6 Conclusions

In this chapter, we have proposed and studied benchmark models that can produce GWs in the frequency bands probed by PTA experiments. By focusing on models with a minimal set of free parameters, we were able to identify the best-fit regions for each model directly in terms of the model parameters such as the masses of the new particles and their couplings.

Fitting a large variety of models to two different PTA datasets was in particular enabled by using the new tool `ceffyl`, which dramatically speeds up obtaining the viable parameter regions. We fit our models to two datasets, the 12.5 year NANOGrav search and the data from IPTA DR2 (which includes the NANOGrav nine-year data). For some models, the best-fit regions disagree at 95% CL. This was more pronounced for models that feature a sharper peak, since IPTA seems to prefer a flatter spectrum. It will be interesting to see if this discrepancy disappears with more data, or if there is a difference in the way the noise is subtracted.

In addition to the PTA data, we include a variety of cosmological constraints on the models. The main results are shown in Fig. (VI.1 -VI.3), where the constraints are superimposed on the regions preferred by PTA data. Let us briefly summarise the results for the individual models. GWs from topological defects also provide a good fit of the PTA data, however constraints from N_{eff} rule out the global cosmic string scenario, while domain walls are viable both if they annihilate into a dark sector or into the visible sector. In the former case, CMB spectral distortions are predicted in range of future probes, while the latter case future colliders will be sensitive to parts of the parameter space preferred by the PTA signal.

On more general grounds, we observe the following. First, since the signal is very large, the source must at some point carry a significant fraction of the total energy density in the universe. Hiding this energy in a dark sector fails in most models due to $N_{\rm eff}$ constraints, with the exception of the dark ALP DW model, which seem to be a very efficient source of GWs. This bound might tighten in the future and will remain an important constraint (or hint) for these models. The obvious alternative is to transfer the energy back to the visible sector after the GWs are produced. If this happens through particle decays, as in the domain wall scenarios, the models may be probed by laboratory experiments in the future.

One aspect that should not be neglected is naturalness, or how likely these models can be realised in nature. Often, a large separation of scales is implicitly required in these models. An example is the bias term in DW models, which is many orders of magnitude smaller than the other mass scales that appear there, and which has to be tuned such that the DWs annihilate shortly before they start to dominate the energy density of the universe. There are also typically more parameters required in each model than those which determine the GW signal, but which could impact other observables.

model	parameter		best-fit value
CS, ALP	m_a	axion mass	unconstrained
	f_a	axion decay constant	$2.3^{+0.1}_{-0.2} \times 10^{15}\,\mathrm{GeV}$
DW, ALP	m_a	axion mass	unconstrained
	f_a	axion decay constant	$3.0^{+2.3}_{-2.6} \times 10^{15}\,\mathrm{GeV}$
	T_{ann}	annihilation temperature	$18.9^{+7.3}_{-9.1}\,\mathrm{MeV}$
DW, heavy axion	m_a	axion mass	unconstrained
	f_a	axion decay constant	unconstrained

Table VI.1: Best-fit values of the model parameters obtained in `ceffyl` for the NANOGrav 12.5-year dataset. The corresponding models are presented in Sec. (VI.2 - VI.4).

While here we have taken the next step in establishing simple and testable models, in most cases additional model building and more detailed phenomenological studies will be required. Furthermore, the prediction of the GW signal is still affected by large uncertainties, which are at least of order one in most models, and which often rely on extrapolation from complicated numerical simulations that are only available for a limited set of parameters. The large fluctuations in energy density associated with GW production can also have other observable consequences like the formation of dark matter substructures and mini-clusters. One may also wonder if the tension in the Hubble rate determination can be improved in one of these scenarios.

An important question that we have not addressed here is what happens if an astrophysical background of GWs is included in the fit. It will probably open up the parameter space in most models, since not all of the GW signal has to be explained. Furthermore it will be interesting to see if a primordial component of the stochastic GW background can be distinguished from the contribution of SMBHBs. Certainly precise predictions of the spectral shape of the GW signals are essential for this task.

VI.7 Appendix

VI.7.1 Priors, full fit results and best-fit parameters

For completeness, here we show the full results of our fits of PTA data to the various model parameters, including the 1D posterior probabilities. The best-fit results of the model parameters for the NANOGrav 12.5-year dataset are shown in Tab. (VI.1). The priors used for the fits in `ceffyl` are listed in Tab. (VI.2). The results for CS from ALPs are shown in Fig. (VI.4). The posteriors for DW networks from ALPs and heavy axions are depicted in Fig. (VI.5-VI.6), respectively.

model	parameter		prior type	prior range
CS, ALP	m_a	axion mass	log-uniform	$(10^{-21} - 10^{-9})$ eV
	f_a	axion decay constant	log-uniform	$(10^{12} - 10^{18})$ GeV
DW, ALP	m_a	axion mass	log-uniform	$(1 - 10^{4})$ GeV
	f_a	axion decay constant	log-uniform	$(10^{3} - 10^{8})$ GeV
	$T_{\rm ann}$	annihilation temperature	uniform	$(3 - 100)$ MeV
DW, heavy axion	m_a	axion mass	log-uniform	$(1 - 10^{4})$ GeV
	f_a	axion decay constant	log-uniform	$(10^{5} - 10^{8})$ GeV

Table VI.2: Parameter priors used in `ceffyl` for the models presented in Sec. (VI.2 - VI.4).

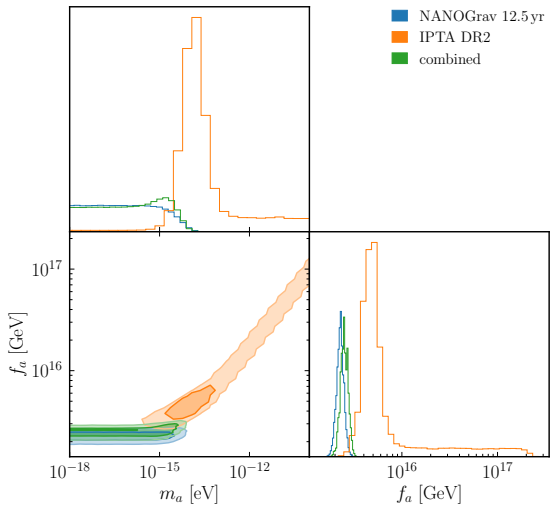

Figure VI.4: 1D and 2D posteriors for the fit to the ALP CS model of Sec. (VI.2.1.1 - VI.4.1.1). Figures were created by S.Schenk

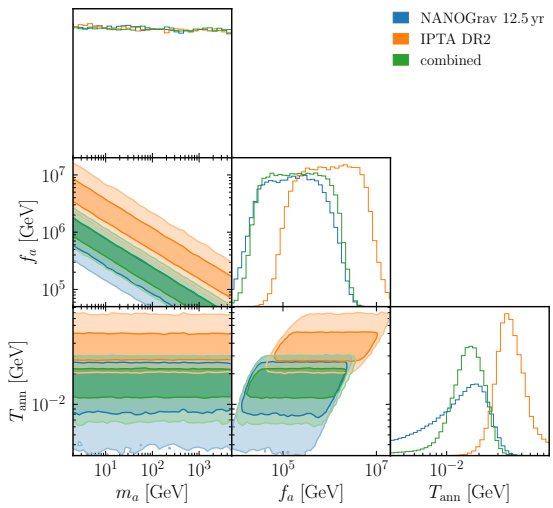

Figure VI.5: 1D and 2D posteriors for the fit to the ALP DW model of Sec. (VI.2.1.2 - VI.4.1.2). Figures were created by S.Schenk

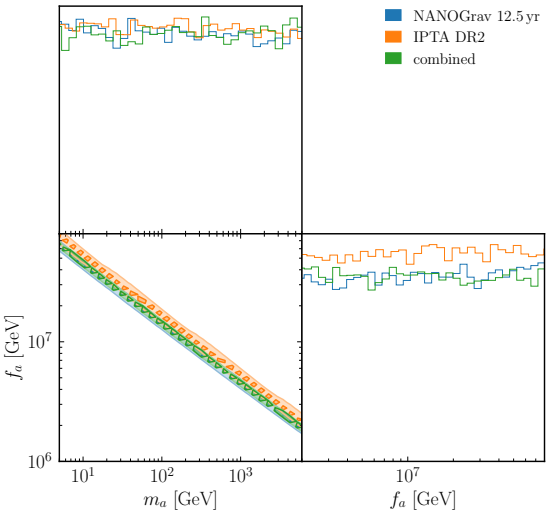

Figure VI.6: 1D and 2D posteriors for the fit to the heavy axion model generating domain walls of Sec. (VI.2.1.2 - VI.4.1.2). Figures were created by S.Schenk

CHAPTER VII

Sound Waves from Dark Sector Anisotropies

VII.1 Introduction

Dark sectors that only interact with our visible Universe gravitationally are well motivated - they often arise in string theory compactifications, or more generally appear in models with hidden sectors that address the dark matter or other puzzles of the standard model (SM). Gravitational waves have emerged as a prominent new way to probe such dark sectors. This is possible if the dark sector features large anisotropies , which then compensate the intrinsic weakness of the gravitational interactions. Sizeable anisotropies can be present in the dark sector in the form of topological strings or domain walls [350, 352, 423], or can be produced for example in first order phase transitions [88, 458, 459] or by scalar field dynamics [456, 460, 461].

Here we present a new way to detect the presence of such large anisotropies in a dark sector via their effect on the spectrum of the cosmic microwave background (CMB). The dark sector anisotropies are damped via gravitational interactions with the baryon-photon fluid, which is heated up in the process. If this happens shortly before the CMB is emitted, the photons do not have enough time to re-thermalise, and this process leads to a deviation of the CMB from a perfect black body spectrum [438, 462, 463].

These spectral distortions of the CMB are tightly constrained by existing observations, and can therefore be used to probe dark sector models that feature large anisotropies around the time of CMB emission. The constraints we obtain below are based on measurements dating back to the nineties, but already provide competitive bounds on the parameter space of some scenarios. With current technology, they could be improved by about four orders of magnitude, and we show that such measurements would dig deep into previously unconstrained parameter regions of dark sectors.

Dark sector anisotropies induce both acoustic waves in the baryon-photon fluid as well as gravitational waves (GWs). The latter also lead to spectral distortions, as was shown in Ref. [446]. We find however that there is a large class of dark sector models for which the contribution from acoustic waves dominates, and thus our mechanism often leads to significantly stronger constraints. In the case of non-decaying cosmic string and scaling seed networks the spectral distortions caused by acoustic waves were already discussed in [464, 465]. We discuss this phenomenon in general here and provide estimates applicable to a plethora of dark sectors. Besides the aforementioned cosmic strings, this includes models with domain walls, very late first order phase transitions, or scalar fields undergoing parametric resonance.

In Sec. (VII.2) we provide an overview of μ-distortions and qualitatively discuss the conditions under which dark sectors can source observable distortions. From there, the reader only interested in the reach of this new probe is advised to jump to Sec. (VII.6), where we apply our techniques to various dark sectors that are well-known GW sources. Sec. (**??**) instead provide more technical details: In Sec. (VII.3) we show that the induction of sound waves in the photon fluid through the dark sector can be decoupled from the subsequent damping, and derive an expression for the resulting μ-distortions. Analytic results for the acoustic energy caused by different types of dark sectors are obtained in Sec. (VII.4). Then in Sec. (VII.5) we put our analytical estimates to the test by comparing them to numerical results of a dark sector toy model.

VII.2 CMB spectral distortions

It is well known that the CMB spectrum is to a good approximation a black body spectrum. Any deviation of the spectrum from this shape, so called spectral distortions, however, encode valuable information about physics in the early universe. In principle any non-thermal injection or removal of energy from the photons causes such a distortion. Whether a distortion is observable depends, aside from the size of the distortion, on whether efficient processes to thermalize the spectrum again are present.

At high red-shift, and correspondingly large temperatures, processes changing the photons momentum, like Compton scattering, as well as photon number changing processes, like double Compton scattering, are present. In this regime any distortions of the CMB are therefore quickly erased. This changes for redshifts $z \lesssim 2 \times 10^6$ when photon number changing processes become ineffective. From this point onwards the photon number is a conserved quantity and one has to introduce a chemical potential μ to capture the equilibrium distribution. It becomes non-zero if energy is injected into the plasma at this point. Below red-shifts of $z \lesssim 5 \times 10^4$ Compton scattering also becomes inefficient at redistributing the momentum among the photons, such that any distortion sourced at later times is directly imprinted onto the CMB spectrum.

The source of energy injection we are interested in here is the damping of sound waves in the baryon-photon fluid. A sound wave in the plasma with momentum k is rapidly damped once its wavelength $\lambda = 2\pi/k$ falls below the diffusion scale, which is the distance a photon covers by random walking between scattering events. For modes in the range $8 \times 10^3\ \mathrm{Mpc}^{-1} \lesssim k \lesssim 2 \times 10^3\ \mathrm{Mpc}^{-1}$ this happens for redshifts $5 \times 10^4 \lesssim z \lesssim 2 \times 10^6$ leading to a μ-distortion. [1]

In the inflationary paradigm the primordial fluctuations, measured at the largest scales as CMB fluctuations and in structure formation, are predicted to be approximately flat and therefore extend to the small scales sourcing μ-distortions. In this paper we however investigate dark sectors with turbulent dynamics which, through their gravitational coupling to the photon fluid, lead to additional fluctuations at those small scales and therefore source additional μ-distortions, while leaving the scales relevant for CMB fluctuations and structure formation untouched. The details of the gravitational coupling between the different sectors are discussed below. We find that the coupling is strongest around the time a mode crosses the horizon (blue in Fig. (VII.1)). Past this point the energy of the acoustic wave in the baryon-photon fluid is approximately constant until

[1] For larger wavelength modes where the damping occurs for $z \lesssim 5 \times 10^4$ the photon momenta are not redistributed resulting in a y-distortion. This is also produced through the Sunyaev-Zeldovich effect [438, 462] limiting the sensitivity to new physics. Our results for μ-distortions can be generalized by using the respective window function (see Section VII.3 and [466]).

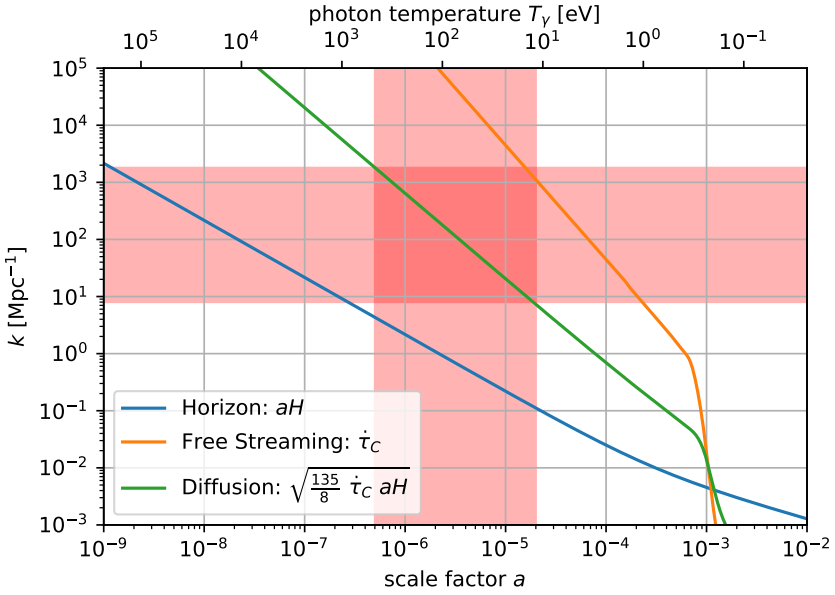

Figure VII.1: The evolution of the horizon scale (blue), the scale a photon free streams between consecutive scattering events and diffusion scale that is approximately the distance traveled by a photon in a random walk as a result of all the scattering events in one Hubble time. Once a mode passes the diffusion scale the energy stored in the acoustic oscillation is damped. If this happens during red-shifts marked in red on the x-axis a μ-distortion is sourced, singling out the modes marked in red on the y-axis as the dominant messengers of new physics. These modes enter the Horizon as early as $a \approx 10^{-9}$ allowing us to search for new physics back to when the photon temperature was $\approx 1 - 0.1$ MeV. Figure created by W.Ratzinger

the mode crosses the diffusion scale (green in Fig. (VII.1)) at which point the acoustic energy is turned into bulk energy. We have highlighted on the x-axis of Fig. (VII.1) the times at which this injection of energy leads to a μ-distortion. The modes that cross the diffusion scales during these times, highlighted on the y-axis, are therefore the dominant messengers of new physics. We can read off that these modes enter the horizon as early as $a \approx 10^{-9}$ corresponding to photon temperatures of $\approx 0.1 - 1$ MeV. Indeed we find in Sec. (VII.6) that the sensitivity of spectral distortions is diminished for scenarios in which the anisotropies appear at higher temperatures. It is conceivable that energy is injected into high k modes that are already past the damping scale or even free streaming scale and converted into bulk energy of the plasma in a fraction of a Hubble time. However we find that this process is highly inefficient due to the large separation between the damping and free streaming scale and the horizon at the times of interest.

Since the interaction between the different sectors is purely gravitationally, we find, perhaps unsurprisingly, that the induced spectral distortions are proportional to the energy comprised by the dark sector Ω_d. Furthermore the amplitude δ_d and characteristic scale k_* of the fluctuations determine the magnitude of the distortions. Larger fluctuations clearly lead to bigger distortions. On the other hand a miss-match between the characteristic scale k_*, where the fluctuations are largest, and the Horizon, where the gravitational coupling is strongest, leads to a reduction of the distortions. An example for the last factor would be a first order phase transition, where the bubble radius at collision can be much smaller than the Hubble radius.

VII.3 Source of μ-distortions through gravitational interaction

The generic setup we have in mind is a dark sector that only comprises a subdominant amount of the total energy $\Omega_d \ll 1$ but develops large anisotropies at some point $\delta\rho_d/\overline{\rho}_d = \delta_d \approx 1$. Since $\Omega_d \ll 1$, metric and density fluctuations in other sectors present in the universe remain small, which allows us to treat them perturbatively, linearizing their dynamics. It is then beneficial to work in Fourier space. We use the following definitions for the Fourier transform and the dimensionless power spectrum $\mathcal{P}$:

$$\phi(\mathbf{k}) = \int d^3x\ \phi(\mathbf{x}) \exp(-i\mathbf{k}\mathbf{x})\,; \qquad \langle \phi(\mathbf{k})\phi^*(\mathbf{k}')\rangle = \frac{2\pi^2}{k^3}\mathcal{P}_\phi(k)(2\pi)^3\delta^{(3)}(\mathbf{k}-\mathbf{k}')\,. \quad \text{(VII.1)}$$

We furthermore use the conformal Newtonian gauge for the scalar metric perturbations

$$ds^2 = a^2(\tau)\left[(1+2\Psi(\mathbf{x},\tau))d\tau^2 - (1+2\Phi(\mathbf{x},\tau))d\mathbf{x}^2\right], \quad \text{(VII.2)}$$

where the equations of motion for the potentials Φ, Ψ are given by

$$3aH\left(\dot{\Phi} - aH\Psi\right) + k^2\Phi = \frac{3a^2H^2}{2}\left(\Omega_\gamma\delta_\gamma + \Omega_n\delta_n + \Omega_d\delta_d\right), \quad \text{(VII.3)}$$

$$\Phi + \Psi = -\frac{6a^2H^2}{k^2}\left(\Omega_\gamma\sigma_\gamma + \Omega_n\sigma_n + \frac{3}{4}(1+w_d)\Omega_d\sigma_d\right). \quad \text{(VII.4)}$$

Here overdots denote derivatives w.r.t conformal time τ, and δ and σ denote the energy fluctuation and shear in the respective sectors. For times well before matter-radiation equality, $a \ll a_{\rm eq}$, the three relevant sectors are the baryon-photon fluid γ, the neutrinos n and the dark sector d. The shear is defined as the longitudinal traceless part of the

energy-momentum tensor $\sigma = -(\hat{\mathbf{k}}_i\hat{\mathbf{k}}_j - \frac{1}{3}\delta_{ij})T^i_j/(\overline{\rho}+\overline{p})$. Finally, w_d is the equation of state parameter of the dark sector.

It is clearly visible that the scalar metric perturbations induced by δ_d are suppressed by Ω_d, thus justifying the linearised treatment. More generally the linearized treatment holds as long as either Ω_d, δ_d or H^2/k^2 is small and none of them are larger than 1. Furthermore since all other sectors only couple to the dark sector via gravity, also their induced perturbations are suppressed. This also allows one to neglect the back-reaction effects of gravity onto the dark sector and one can therefore study its dynamics using an unperturbed metric. In the following, we will assume that all fluctuations in the baryon-photon fluid and the neutrinos as well as the potentials are initially zero. The effects of other uncorrelated fluctuations like e.g. inflationary ones can be studied independently, as usual in linear perturbation theory.

For modes deep inside the horizon, $k \gg aH$, one can solve for the gravitational potentials directly by neglecting the first term on the right side of Eq. (VII.3). One finds that the gravitational potentials decay as $\Phi, \Psi \propto a^2H^2/k^2$ if the fluctuations don't keep growing after their generation, which is a reasonable assumption during radiation domination. Therefore the gravitational coupling between the sectors quickly becomes negligible after horizon entry. For our specific case, it suggests that the amplitude of fluctuations in the baryon-photon fluid is set within about one Hubble time after horizon entry or after the dark sector fluctuations have been created, whichever happens later for a given mode. We can also anticipate the strength of the gravitational interaction being suppressed for modes that are deep inside the horizon when the dark sector develops its fluctuations. The details of this suppression are discussed in the next section.

For the times well before recombination, the baryon-photon fluid is well described by the tight-coupling approximation (TCA, e.g. [467, 468]) and the energy density in baryons can be neglected, leading to

$$\dot{\delta}_\gamma + \frac{4}{3}kv_\gamma = -4\dot{\Phi} \tag{VII.5}$$

$$\dot{v}_\gamma - k\left(\frac{1}{4}\delta_\gamma - \sigma_\gamma\right) = k\Psi \tag{VII.6}$$

$$\sigma_\gamma = \frac{16}{45}\frac{k}{\dot{\tau}_C}v_\gamma, \tag{VII.7}$$

where $v_\gamma = i\hat{\mathbf{k}}_i T^j_{\gamma,0}/(\overline{\rho}_\gamma + \overline{p}_\gamma)$ is the longitudinal part of the fluid velocity relative to the cosmological rest frame. The TCA takes advantage of the fact that all moments of the photon distribution past the velocity are suppressed by the high Compton scattering rate $\dot{\tau}_C = an_e\sigma_C \gg k$, where σ_C is the Compton cross-section and n_e the free electron density, which can be approximated as $\dot{\tau}_C = a^{-2}\ 4.5\times10^{-7}\ \mathrm{Mpc}^{-1}$ well before recombination. When solving these equations numerically we also take into account the free streaming neutrinos, see Sec. (VII.8.1).

The equations above can be combined to get a damped harmonic oscillator. We will first do so in the limit that the mode is already deep inside the horizon and neglect the gravitational potentials

$$\ddot{\delta}_\gamma + k^2\left(\frac{16}{45}\frac{1}{\dot{\tau}_C}\dot{\delta}_\gamma + \frac{1}{3}\delta_\gamma\right) = 0\,. \tag{VII.8}$$

In the given limit that $aH \ll k \ll \dot{\tau}_C$ the general solution to this problem is approximated

as

$$\delta_\gamma = \left[A \sin\left(\frac{k\tau}{\sqrt{3}}\right) + B\cos\left(\frac{k\tau}{\sqrt{3}}\right)\right] \exp\left(-\frac{k^2}{k_D^2(\tau)}\right). \tag{VII.9}$$

This solution is interpreted as damped acoustic waves traveling in the baryon photon fluid with the relativistic speed of sound of $c_s = 1/\sqrt{3}$. The diffusion scale k_D appearing here is determined by the equation $\frac{d}{d\tau}k_D^{-2} = \frac{8}{45}\frac{1}{\dot\tau_C}$. During radiation domination it is given as $k_D = \sqrt{\frac{135}{8}\dot\tau_C\, aH}$ as long as the free electron density is constant up to dilution by expansion. This effect is also known as Silk damping [469] and is attributed to photons performing a random walk with typical step length $\Delta x \approx 1/\dot\tau_C$ while doing $N \approx \frac{\dot\tau_C}{aH}$ steps per Hubble time. The diffusion scale is then the distance typically traversed by a photon in a Hubble time, $1/k_D \approx \Delta x\sqrt{N}$. Fluctuations on scales smaller than $1/k_D$ are therefore quickly erased. The energy of the acoustic waves is converted into photon bulk energy in this process.

From the discussion so far two important scales have emerged: the Horizon scale at which the gravitational coupling is strongest and we, therefore, expect the dark sector to efficiently source acoustic waves, and the diffusion scale. As can be seen in Fig. (VII.1), the modes of interest, marked in red on the y-axis, pass these two scales at scale factors a that are always separated by about two orders of magnitude or more. This means that we can separately discuss the generation of acoustic waves from dark sector anisotropies and the conversion of these acoustic waves into a μ distortion. After they are generated, but before the onset of damping, the amplitudes of the sound waves A, B, and therefore also the energy in acoustic waves, remains approximately constant.

In the remainder of this section we obtain an expression for the μ distortion generated by the diffusion of the acoustic waves, while the computation of the acoustic energy induced by different sources is postponed to the following sections. Relative to the total energy in the relativistic baryon-photon fluid, the acoustic energy is given as

$$\epsilon_{ac} = \frac{\rho_{ac}}{\overline{\rho}_\gamma} = \frac{1}{V}\int_V d^3x \,\left[\frac{1}{8}\delta_\gamma^2(\mathbf{x}) + \frac{2}{3}v_\gamma^2(\mathbf{x})\right] = \int d\log k\; \epsilon_{ac}(k)\,, \tag{VII.10}$$

where we defined the spectral acoustic energy in the last step which is given as

$$\epsilon_{ac}(k) = \frac{1}{8}\mathcal{P}_{\delta_\gamma}(k) + \frac{2}{3}\mathcal{P}_{v_\gamma}(k) = \frac{1}{8}\left[\mathcal{P}_A(k) + \mathcal{P}_B(k)\right] \tag{VII.11}$$

in terms of the power spectra for δ_γ, v_γ and A, B respectively.

When the acoustic waves get damped by diffusion, this energy becomes part of the photon bulk energy. If this happens between $a_{dc} = 5\times10^{-7}$, when photon number changing processes such as Double Compton scattering becomes inefficient, and $a_{\mu,y} = 2\times10^{-5}$, when Compton scattering stops redistributing the momentum between the photons, then a μ-distortion gets sourced besides an increase in the bulk temperature. The approximation commonly used to determine the μ-parameter is

$$\mu \approx 1.4\int d\log k \int_{a_{\mu,y}}^{\infty} d\log a\; \frac{d\epsilon_{ac}(k)}{d\log a}\exp\left(-\left(\frac{a_{dc}}{a}\right)^{5/2}\right), \tag{VII.12}$$

where $\frac{d\epsilon_{ac}(k)}{d\log a}$ is the acoustic "power" transmitted to the bulk energy and it is given as [467]

$$\frac{d\epsilon_{ac}(k)}{d\log a} = \frac{15}{4}\frac{\dot\tau_C}{aH}\mathcal{P}_{\sigma_\gamma} = \frac{64}{135}\frac{k^2}{\dot\tau_C aH}\mathcal{P}_{v_\gamma} = \frac{8}{3}\mathcal{P}_{v_\gamma}\frac{d}{d\log a}\left(\frac{k^2}{k_D^2}\right) \approx 2\epsilon_{ac}(k,a)\frac{d}{d\log a}\left(\frac{k^2}{k_D^2}\right), \tag{VII.13}$$

where we used in the last step that due to the oscillation time scale being much shorter than the damping time scale $1/k \ll 1/k_D$ one can approximate $\epsilon_{ac} \approx \frac{4}{3}\mathcal{P}_{v_\gamma}$ in Eq. (VII.11). In the limit that the acoustic energy takes on a constant value $\epsilon_{ac}^{\rm lim}(k)$ before damping, we have $\epsilon_{ac}(k,a) = \epsilon_{ac}^{\rm lim}(k)\exp\left(-2k^2/k_D^2(a)\right)$ during the period of damping, such that we can write the μ-parameter as

$$\mu = \int d\log k\ \epsilon_{ac}^{\rm lim}(k)\mathcal{W}(k), \tag{VII.14}$$

where we have introduced the window function [466]

$$\mathcal{W}(k) \approx 1.4\int_{a_{\mu,y}}^{\infty} d\log a\ \exp\left(-\left(\frac{a_{dc}}{a}\right)^{5/2}\right)\frac{d}{d\log a}\exp\left(-2\frac{k^2}{k_D^2(a)}\right) \tag{VII.15}$$

$$\approx 1.4\left(\exp\left[-\left(\frac{k}{1360\ \text{Mpc}^{-1}}\right)^2\left(1+\left(\frac{k}{260\ \text{Mpc}^{-1}}\right)^{0.3}+\frac{k}{340\ \text{Mpc}^{-1}}\right)^{-1}\right]\right. \tag{VII.16}$$

$$\left.-\exp\left[-\left(\frac{k}{32\ \text{Mpc}^{-1}}\right)^2\right]\right).$$

This remarkably easy expression allows one to calculate the μ-distortion a dark sector causes, given the spectral acoustic energy before damping.[2] This value can then be compared to current bounds and the detection threshold of future experiments. In Fig. VII.2 we show the numerical results of a toy model that neatly summarize this section. The dark sector is assumed to be radiation like such that $\Omega_d = $ const. while the sound waves are sourced, and the fluctuations are modeled as being zero until $a_* = 10^{-7}$ and as $\delta_d = \sin(k\tau)$ afterwards.[3] The shear in the dark sector is set to zero. We show the evolution for one mode that is still outside the horizon at $a = a_*$ and one that is already inside. Indeed it can be clearly seen that the acoustic energy is constant between generation and damping, justifying our separation approach.

VII.4 Analytic Estimate of the Induced Acoustic Energy

We now obtain an analytic estimate for the acoustic energy $\epsilon_{ac}^{\rm lim}$ caused by fluctuations in a dark sector, which together with the results from the previous section allows us to compute the μ distortions. We assume that the fluctuations are generated at a fixed time $a = a_*$. For modes that enter the horizon around or after a_* ($k \lesssim a_* H_*$), we find that the contribution of the photons and neutrinos to the gravitational potentials is of the same order as the one from the dark sector ($\Omega_d\delta_d \approx \Omega_\gamma\delta_\gamma \approx \Omega_n\delta_n$). The coupled system of equations can therefore only be solved numerically. Instead for modes that already are inside the horizon, $k > a_* H_*$, the amplitudes of δ_γ and δ_n remain suppressed by some power of $a_* H_*/k$, as discussed above. They can therefore be neglected when solving for the gravitational potentials. We therefore restrict our analytic treatment to $k > a_* H_*$.

[2] In the literature the window function is commonly defined with respect to a primordial spectrum rather than the acoustic energy spectrum and therefore represents a convolution of the dynamics of horizon entry and damping (e.g. [466]). Our definition is universally applicable, although one would have to discuss horizon entry separately.

[3] As we will argue in Sec. (VII.5.3), $\dot{\delta}_d(k\tau)$ only changes on time scales $1/k$ for sub-horizon modes making this an unphysical choice with $\dot{\delta}_d(k\tau)$ being discontinuous at a_*. We only use this ansatz here for demonstration as well as for rough estimates in the following section.

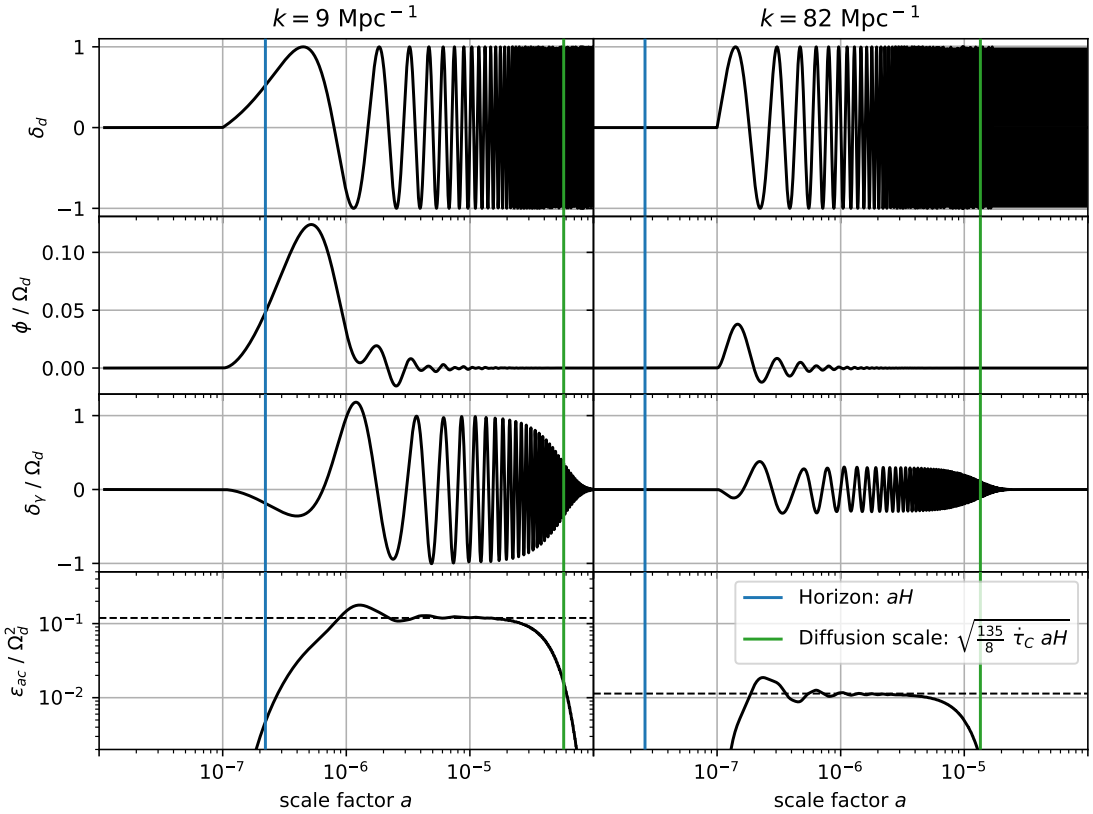

Figure VII.2: Sourcing of acoustic waves through a gravitationally coupled dark sector and subsequent damping by diffusion. The toy dark sector here is radiation like ($\Omega_d = \text{const.} \ll 1$) and its density fluctuations are zero until $a_* = 10^{-7}$ before evolving as $\delta_d = \sin(k\tau)$ (top row). The resulting gravitational potential (second row) causes acoustic oscillations in the baryon-photon fluid (third row). Since the gravitational potential rapidly decays after a mode has entered the horizon (vertical blue line) the amplitude of the acoustic oscillations quickly levels off resulting in an approximately constant acoustic energy $\epsilon_{ac}^{\text{lim}}(k)$ (bottom row, dashed line). The same effect also leads to the acoustic oscillations being suppressed for the high k mode (right side) that is already inside the horizon when the fluctuations in the dark sector develop. Finally the acoustic oscillations are damped for both modes once they cross the diffusion scale (green line). At this point the acoustic energy is injected into the bulk photon energy, leading to a sizeable μ-distortion for modes where this happens between $5 \times 10^{-7} \lesssim a \lesssim 2 \times 10^{-5}$. Figure created by W.Ratzinger

To make further progress we again combine Eq. (VII.5) and Eq. (VII.6) but this time keeping the potentials and dropping the diffusion damping, since we now want to solve for times well before the mode crosses the damping scale, to find

$$\ddot{\delta}_\gamma + \frac{1}{3}k^2\delta_\gamma = -4\ddot{\Phi} - \frac{4}{3}k^2\Psi\,. \tag{VII.17}$$

To get rid of the second time derivative of Φ, we define $\tilde{\delta}_\gamma = \delta_\gamma + 4\Phi$. As the gravitational potential decays, at late times we have $\tilde{\delta}_\gamma \approx \delta_\gamma$. Since we consider a sub-horizon mode, we can continue with only the last term on the left-hand side of Eq. (VII.3), which allows us to solve for the potentials in terms of δ_d and σ_d directly:

$$\ddot{\tilde{\delta}}_\gamma + \frac{1}{3}k^2\tilde{\delta}_\gamma = 4a^2H^2\ \Omega_d\left[\delta_d + \frac{3}{2}(1+w_d)\sigma_d\right] \equiv S(\tau). \tag{VII.18}$$

The right hand side acts as a driving force or source $S(\tau)$ for the harmonic oscillator. The Greens function for this differential equation is $G(\tau) = \sqrt{3}/k\ \sin\!\big(k\tau/\sqrt{3}\big)$, such that we can formally solve the above equation (adapted from e.g. [460, 470]) and find

$$\epsilon_{ac}^{\rm lim}(k) = \frac{1}{8}\mathcal{P}_{\delta_\gamma}(k,\tau_{\rm lim}) + \frac{2}{3}\mathcal{P}_{v_\gamma}(k,\tau_{\rm lim}) \tag{VII.19}$$

$$= \frac{3}{8}\frac{1}{k^2}\int_{\tau_*}^{\tau_{\rm lim}} d\tau' \int_{\tau_*-\tau'}^{\tau_{\rm lim}-\tau'} d\tau''\ \cos\left(\frac{k\tau''}{\sqrt{3}}\right)\mathcal{P}_S(k,\tau',\tau'+\tau'')\,. \tag{VII.20}$$

Here $\tau_{\rm lim}$ is chosen large enough such that $\epsilon_{ac}^{\rm lim}$ has approached a quasi constant value and $\tilde{\delta}_\gamma \approx \delta_\gamma$ holds, and τ_* is the time when the fluctuations in the dark sector appear. We have furthermore introduced the unequal time correlation spectrum of the source $\mathcal{P}_S(k,\tau,\tau')$, defined as

$$\langle S(\mathbf{k},\tau)S^*(\mathbf{k}',\tau')\rangle = \frac{2\pi^2}{k^3}\mathcal{P}_S(k,\tau,\tau')\ (2\pi)^3\delta^{(3)}(\mathbf{k}-\mathbf{k}')\,. \tag{VII.21}$$

To make further progress we will have to specify the characteristics of the source $S(k,\tau)$. Assuming that the equation of state of the dark sector w_d is known then so is the time dependence of $\Omega_d \propto a^{1-3w_d}$. We will hereafter assume that the dark sector behaves radiation-like such that $\Omega_d = \Omega_{d,*} = \text{const}$. The time dependence of $\delta_d(\tau)$ and $\sigma_d(\tau)$ is, however, more intricate and closely related to the spatial structure of the dark source. Since energy is a conserved quantity, the dynamics of its fluctuations $\delta_d(\tau)$ feature some universal properties as we will see shortly. We therefore drop the shear $\sigma_d(\tau)$ from the source term in order to simplify the discussion.

VII.4.1 Spatial Structure

It is reasonable to assume that the mechanism that causes the fluctuations in the dark sector has an intrinsic length scale or at least a finite range of scales over which sizeable fluctuations get produced. We assume here that there is only one characteristic scale k_* that due to causality has to lie within the horizon when the fluctuations get produced, $a_*H_* < k_*$.[4] Since there is only one characteristic scale, the fluctuations that become separated by distances greater than $1/k_*$ are uncorrelated,

$$\langle\delta_d(\mathbf{x})\delta_d(\mathbf{y})\rangle \approx 0\,; \qquad |\mathbf{x}-\mathbf{y}| > 1/k_*\,. \tag{VII.22}$$

[4] Generalisation of our results is however straight forward as long as one may consider the different length scales independently.

Distributions where there is no correlation past a certain scale are commonly referred to as "white". For concreteness we will use

$$\langle \delta_d(\mathbf{x})\delta_d(\mathbf{y})\rangle = A_{\delta_d}\exp\left(-\frac{|\mathbf{x}-\mathbf{y}|^2 k_*^2}{2}\right) \quad \Longrightarrow \quad \mathcal{P}_{\delta_d}(k) = A_{\delta_d}\sqrt{\frac{2}{\pi}}\frac{k^3}{k_*^3}\exp\left(-\frac{k^2}{2k_*^2}\right), \tag{VII.23}$$

where A_{δ_d} parameterises the amplitude of the fluctuations. The common feature of white distributions in three dimensions is that their power spectrum falls off as k^3 in the infrared, while the UV behavior depends on the exact shape. Had we chosen a distribution with compact support in position space, the power spectrum would fall off as a power-law in the UV instead of exponentially. A power-law in the UV might lead to potentially larger signals in cases where the energy injection happens shortly before CMB emission, such that only the UV tail overlaps with the window function. The exponential fall off therefore represents a conservative choice. The power spectrum gives the value of the unequal time correlation spectrum when one chooses both times to be the same $\mathcal{P}_{\delta_d}(k,\tau) = \mathcal{P}_{\delta_d}(k,\tau,\tau)$ and therefore gives the amplitude of the fluctuations at a given time. Since, the power spectrum falls for $k > k_*$ and the gravitational interaction for modes deeper inside the horizon is weaker, we can already anticipate that the acoustic energy becomes dominated by modes with $k \lesssim k_*$. For this reason, we only consider these modes in the following i.e. we only deal with length scales that are large enough such that there are no correlations past them.

VII.4.2 Time Evolution

Here we will make the Ansatz that the energy fluctuations of the dark sector can be described as a stationary statistical process past τ_*. This means that the unequal time correlation spectra can be factorized into a time autocorrelation function and a power spectrum. The power spectrum becomes constant past τ_* and the autocorrelation function $\mathcal{A}_{\delta_d}$ only depends on the difference in time

$$\mathcal{P}_{\delta_d}(k,\tau,\tau') = \mathcal{P}_{\delta_d}(k)\mathcal{A}_{\delta_d}(k,\tau-\tau')\;\theta(\tau-\tau_*)\theta(\tau'-\tau_*)\,. \tag{VII.24}$$

Let us start by considering a dark sector with relativistic dynamics. In this case, one naively expects that the only relevant time scales are $1/k_*$ and $1/k$. Because energy is a conserved quantity though, a change of δ_d on sub-horizon scales corresponds to a displacement of energy over a distance of $\approx 1/k$. This is why the only time scale for energy fluctuations to change is given by $\approx c_d/k$, where $c_d \leq 1$ is the typical velocity of energy transport in the dark sector.[5]

Since the energy fluctuations have this universal behavior, we limited the discussion to them and dropped the shear σ_d from the source S. In general we expect the shear to be of the same size as the density fluctuations δ_d and this approximation therefore introduces an $\mathcal{O}(1)$ uncertainty.

Below we calculate the acoustic energy for two examples. In the first case the energy fluctuations exhibit a stochastic behavior and the autocorrelation therefore decays as $\mathcal{A}_{\delta_d}(k,\Delta\tau) \to 0,\ |\Delta\tau| \to \infty$. For the other, we take a periodic, deterministic behavior as one expects if the dark sector comprises a fluid with waves itself.

[5] Note that since the radiation dominated FRW universe possesses no time-like Killing vector field, there is no global energy conservation. On super-horizon scales modifications of energy conservation by pressure fluctuations become relevant as e.g. observed in models of cosmic seeds [471, 472].

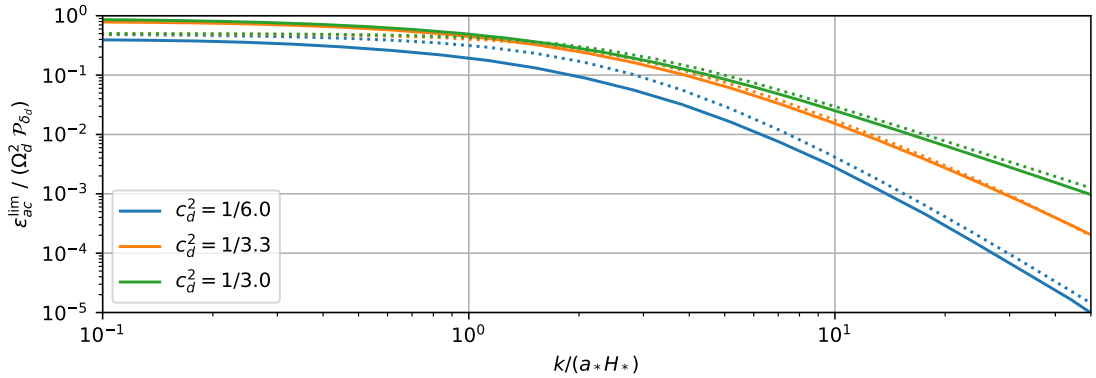

Figure VII.3: Acoustic energy $\epsilon_{ac}^{\rm lim}(k)$ induced by sound waves in a dark fluid, normalized to the magnitude of the dark fluctuations $\Omega_{d,*}^2 \mathcal{P}_{\delta_d}$. The efficiency is roughly constant for super-horizon modes $k < a_* H_*$, while it is suppressed for modes that are inside the horizon $k \gtrsim a_* H_*$ when the fluctuations develop at a_*. Solid lines show the result from a numerical simulation including the contributions of the neutrinos and baryon-photon fluid to the gravitational potentials, while the dotted lines show the estimate *Eq.* (VII.30). For $k \gg a_* H_*$ the suppression falls as $\propto (a_* H_*/k)^2$ in the resonant case $c_d = c_\gamma = 1/\sqrt{3}$ (green) and as $\propto (a_* H_*/k)^4$ in the off-resonant cases, once the discrepancy in frequency becomes relevant. Figure created by W.Ratzinger

Stochastic Source: Free Scalar Field

For a relativistic scalar field with Gaussian fluctuations, the autocorrelation function of the energy fluctuations for $k \ll k_*$ is given by

$$\mathcal{A}_{\delta_d}(k, \Delta\tau) = \mathrm{sinc}(k\,\Delta\tau)\,, \tag{VII.25}$$

as we show explicitly in Sec. (VII.8.2). Since the autocorrelation decays much faster than a Hubble time if $k \gg a_* H_*$, we approximate $\epsilon_{ac}^{\rm lim}$ as

$$\epsilon_{ac}^{\rm lim}(k) = \Omega_{d,*}^2 \mathcal{P}_{\delta_d}(k)\ \frac{6}{k^2} \int_{\tau_*}^{\infty} d\tau' a^4(\tau') H^4(\tau') \int_{-\infty}^{\infty} d\tau''\ \cos\left(\frac{k\tau''}{\sqrt{3}}\right) \mathrm{sinc}(k\tau) \tag{VII.26}$$

$$= \Omega_{d,*}^2 \mathcal{P}_{\delta_d}(k)\ 2\pi \left(\frac{a_* H_*}{k}\right)^3\,, \tag{VII.27}$$

where we used $a = \tau\ H_* a_*^2$ during radiation domination to solve the first integral. This estimate holds only for modes that are inside the horizon at a_*. The numerical results we present below suggest that for super horizon modes the efficiency of inducing acoustic waves is directly proportional to the amplitude $\mathcal{P}_{\delta_d}(k)$. We therefore use

$$\epsilon_{ac}^{\rm lim}(k) \approx \Omega_{d,*}^2 \mathcal{P}_{\delta_d}(k)\ \frac{\pi}{2\pi + (k/a_* H_*)^2} \frac{1}{1 + k/(2 a_* H_*)}\,, \tag{VII.28}$$

to estimate the acoustic energy for all regimes with $\mathcal{O}(1)$ accuracy.

Deterministic Source: Fluid

If the dark sector is comprised of a fluid itself with speed of sound c_d the autocorrelation is

$$\mathcal{A}_{\delta_d}(k, \Delta\tau) = \cos(c_d k\,\Delta\tau). \tag{VII.29}$$

In this case there is no sensible approximation that allows one to factorize the double integral in Eq. (VII.20). Therefore we directly use the results from solving the full equations of motion numerically, including backreaction from photons and neutrinos, to discuss the behaviour. To do so we model the fluctuations in the dark sector as 0 up to τ_* and as $\delta_d = \sin(c_d k(\tau - \tau_*))$ afterwards. This corresponds to $\mathcal{P}_{\delta_d}(k) = \langle \sin^2 \rangle = 1/2$. In Fig. (VII.3) we show the results for $\epsilon_{ac}^{\lim}$ normalized by $\Omega_{d,*}^2 \mathcal{P}_{\delta_d}$ for various dark speeds of sound. As one can see the efficiency of inducing acoustic waves takes on a constant $\mathcal{O}(1)$ value in all cases for modes outside the horizon at a_*. For modes inside the horizon the efficiency falls off as $(a_* H_*/k)^2$ and as $(a_* H_*/k)^4$ once the potential offset in frequency between the driving force $c_d k$ and $k/\sqrt{3}$ of the driven oscillator δ_γ becomes relevant $(\sqrt{3} - c_d)k/(a_* H_*) \gtrsim 1$. We therefore suggest using

$$\epsilon_{ac}^{\lim}(k) \approx \Omega_{d,*}^2 \mathcal{P}_{\delta_d}(k) \, \frac{\pi}{2\pi + (k/a_* H_*)^2} \frac{1}{1 + (1/3 - c_d^2)\,(k/a_* H_*)^2} \,, \tag{VII.30}$$

which matches the numerical result up to a factor of $\lesssim 2$ for the cases shown in Fig. (VII.3).

One can interpret the results Eq. (VII.28) and Eq. (VII.30) as follows: Naively one expects a suppression by $(a_* H_*/k)^4$ for modes inside the horizon, $k > a_* H_*$, that stems from the potentials decaying as $\Phi, \Psi \propto (a_* H_*/k)^2$. The potentials are however approximately constant and keep driving the acoustic oscillations in the baryon-photon fluid for a whole Hubble time after a_*, corresponding to many oscillations $N_{\rm osc} \propto k/a_* H_* \gg 1$ of the mode. The energy of a harmonic oscillator driven by a stochastic source or in resonance grows as $\propto N_{\rm osc}$ or $\propto N_{\rm osc}^2$ which leads to a milder suppression by $(a_* H_*/k)^3$ and $(a_* H_*/k)^2$ respectively.

VII.5 Detailed analysis of a simple model: $\lambda\phi^4$-Theory

To confirm the validity of our analytic estimates, we now consider a toy model for which a full numerical treatment is feasible. We have chosen a model consisting of two real scalar fields ϕ, ψ with the potential

$$V(\phi, \psi) = \frac{1}{4}\lambda\phi^4 + \frac{1}{2} g^2 \phi^2 \psi^2 \,. \tag{VII.31}$$

This model has been studied in great detail in the context of preheating e.g. [223–225, 473–475]. We consider $\langle \phi \rangle = \phi_i \ll m_{\rm Pl}$ and $\langle \psi \rangle = \langle \dot{\phi} \rangle = \langle \dot{\psi} \rangle = 0$ as the initial conditions. In this case, the energy density of the fields is always subdominant $\Omega_d \ll 1$ in contrast to the preheating scenario where the field ϕ with $\phi_i > m_{\rm Pl}$ initially drives inflation.

In addition to deriving all the parameters needed to estimate the acoustic energy analytically as described above, we solve the dynamics of the model from first principles using a lattice simulation, which allows us to extract $\delta_d(k, \tau)$ and $\sigma_d(k, \tau)$. Using these we solve for $\delta_\gamma(k, \tau)$ and arrive at the acoustic energy. We recommend the reader only interested in the application of the analytic estimates to skip forward to the next section.

We follow [474, 475] in our analysis and define the angular frequency $\omega_* = \sqrt{\lambda}\phi_i$ giving the typical curvature of the potential as well as the resonance parameter $q = g^2/\lambda$. For simplicity, we fix the latter at $q = 1$ in this work. Furthermore, we assume that both ϕ and ψ possess Gaussian fluctuations originating from inflation that are frozen before a mode enters the horizon

$$\mathcal{P}_{\phi,\psi} = \left(\frac{H_I}{2\pi}\right)^2 ; \qquad \mathcal{P}_{\dot{\phi},\dot{\psi}} \approx 0 \,, \tag{VII.32}$$

where $H_I \gg \omega_*$ denotes the Hubble parameter during inflation. We assume that after inflation the universe reheats and undergoes the same evolution as in the standard ΛCDM case, with our dark sector acting as a purely gravitationally coupled spectator. At the times relevant for generating μ-distortions the universe is still radiation dominated.

VII.5.1 Analytic Estimate

The field ϕ starts to oscillate once the Hubble rate drops to $H_{\rm osc} = \omega_*$. The energy in the field ϕ is initially $\omega_*^2\phi_i^2/4$ and dominates the dark sector such that one can estimate $\Omega_{d,osc} \propto (\phi_i/m_{\rm Pl})^2$. Past $a_{\rm osc}$ the dark sector behaves like radiation such that $\Omega_d \approx$ const. To go beyond an order of magnitude estimate, one has to solve the equation of motion for the homogeneous component of ϕ and finds

$$\Omega_{d,osc} \simeq 0.2 \left(\frac{\phi_i}{m_{\rm Pl}}\right)^2 . \tag{VII.33}$$

The oscillations of ϕ lead to a time-dependent effective mass of the field ψ, which cause its fluctuations to grow exponentially. As shown in e.g. [473] the equation of motion for the Fourier modes of the field ψ can be recast into the *Lamé* equation. From the corresponding instability chart, one can read off that the modes with $k \lesssim \omega_* a_{\rm osc}$ experience exponential growth. The mode growing the fastest is $k_* \approx \omega_* a_{\rm osc}/\sqrt{2}$ with its energy density growing as $\propto \exp(0.3\,\omega_* a_{\rm osc}\tau)$. The energy in the fluctuations is initially $\approx \omega_*^2 H_I^2/(2\pi)^2$ while the energy in the homogeneous ϕ field is $\approx \omega_*^2\phi_i^2/4$. Due to the exponential growth this difference is overcome around

$$a_* \approx a_{\rm osc}\frac{2}{0.3}\log\left(\frac{\pi\phi_i}{H_I}\right) . \tag{VII.34}$$

At this point, the energy in the fluctuations starts to dominate, causing the energy density to become fully inhomogeneous in line with the definition of a_* in the previous chapters. This allows us to calculate $a_* H_* = a_{\rm osc}\omega_* \cdot a_{\rm osc}/a_*$. For the simulations presented in the following we fixed $H_I/\phi_i = 10^{-4}$, which gives $a_* \approx 70\ a_{\rm osc}$ and $a_* H_* \approx a_{\rm osc}\omega_*/70$.

Once the fluctuations dominate, the energy gets split between the two fields and their respective kinetic and gradient contributions. If the system virializes quickly, the energy will be distributed evenly between the four, and there will be no correlations between them. If each separate contribution has $\mathcal{O}(1)$ fluctuations we find $\langle\delta_d^2\rangle = A_{\delta_d} = 1/4$, such that we can use Eq. (VII.23) to estimate $\mathcal{P}_{\delta_d}(k)$.

As a final step, we need to make an assumption about the temporal behavior of $\delta_d(k,\tau)$. Similar to the case of the free scalar field, the energy fluctuations are due to the random interference of the field modes. If anything, one expects the potentially turbulent interaction of the field modes at a_* to lead to a faster decrease in the autocorrelation function. We, therefore, use Eq. (VII.28) with the parameters derived above to analytically estimate the induced acoustic energy.

VII.5.2 Numerical Treatment

Using `CosmoLattice` [476, 477] we solve the full equations of motion of the interacting ϕ and ψ-field on a discretized space-time using a second-order Velocity Verlet algorithm (equivalent to using a leapfrog algorithm). The evolution of the background metric is set to behave like a radiation dominated universe, independently of the dark sector. We simulate a box with $N = 1024$ sites along each spatial direction with a comoving length

of $L = 2\pi a_{\rm osc}/(0.015\ \omega_*)$ and periodic boundary conditions. The fields in this box are evolved by time steps of $d\tau = 0.05\ a_{\rm osc}/\omega_*$. While this choice compromises between covering the dynamics close to the horizon at a_* and resolving the UV dynamics, once the system becomes fully non-perturbative, we ran simulations with higher spatial resolution and smaller time steps to ensure that none of our results are affected by the poor UV resolution of the run presented here.

We start the simulation at $a_i = a_{\rm osc}/10$ and use the initial conditions given above. We cut the inflationary spectrum off for $k > 1.3\ a_{\rm osc}\omega_*$ to cover the full instability band in ψ, while at the same time only including modes with $k \ll aH|_{a=a_i} = 10\ a_{\rm osc}\omega_*$ such that $\mathcal{P}_{\dot\phi,\dot\psi} \approx 0$ holds. After fixing $q = 1$ and $H_I/\phi_i = 10^{-4}$, the only remaining free parameters are ϕ_i and λ, or equivalently ϕ_i and ω_*. The dependence on these two is however fully covered by the scaling relations discussed above, with ϕ_i controlling Ω_d and ω_* the typical momentum scale k_*. We keep these relations explicit when showing our results below.

We modified `CosmoLattice` to calculate and output $\delta_d(k,\tau)$ and $\tilde\sigma_d(k,\tau)$ in time-intervals of $\Delta\tau = 0.5\ a_{\rm osc}/\omega_*$. Here we defined

$$\tilde\sigma_d(k,\tau) = (1+w)\sigma_d(k,\tau)\,. \tag{VII.35}$$

This is more convenient for numerics, since it does not require knowledge of the average pressure in the dark sector. The details of how we calculated these quantities can be found in Sec. (VII.8.3). To obtain the power spectra of these quantities, we group them in radial bins of width $k_{IR} = 0.015\ \omega_*$ and average over them. To keep the computational cost and required storage down, we limit ourselves to 70 bins that are spaced out linearly at low k and logarithmically at high k and only use up to 1000 modes per bin.[6] By interpolating between the saved values of $\delta_d(k,\tau)$ and $\tilde\sigma_d(k,\tau)$ as well as $\Omega_d(\tau)$ one can solve for the perturbations in the visible sector for each single mode(see Sec. (VII.8.1)). With this approach one doesn't have to make any assumptions about the time evolution like we did in Sec. (VII.4.2). To obtain the induced acoustic energy $\epsilon_{ac}^{\rm lim}$ or μ-distortion we then take the power spectra of $\mathcal{P}_{\delta_\gamma}(k,\tau)$ and $\mathcal{P}_{v_\gamma}(k,\tau)$ by averaging over the modes in one bin again and use Eqs. (VII.11) and (VII.13).

VII.5.3 Numerical Results

In Fig. (VII.4) we show the evolution of various energy components in the dark sector. Up to $a_{\rm osc}$ the energy is almost exclusively stored in the quartic potential while the dynamics of ϕ remains overdamped by Hubble friction. Around $a_{\rm osc}$, ϕ starts to oscillate and the energy in the dark sector red-shifts like radiation, resulting in Ω_d taking on the value given in Eq. (VII.33). The fluctuations stored in ψ are subdominant around $a_{\rm osc}$ but start growing exponentially due to the instability caused by the coupling to the oscillating ϕ-field. The black, dashed line shows the analytic estimate obtained by looking up the growth coefficient in the instability chart of the *Lamé* equation

$$\Omega_\psi(\tau) \approx \frac{1}{3}\left(\frac{H_I}{2\pi m_{\rm Pl}}\right)^2 \exp(0.3\,\omega_* a_{\rm osc}(\tau-\tau_{\rm osc}))\,. \tag{VII.36}$$

Once the energy in fluctuations of ψ catches up to the energy in the ϕ-field, there is a back-reaction that decreases the amplitude of oscillations of the homogeneous part of ϕ while

[6] Our method is equivalent to the type II, version 1 powerspectrum from the `CosmoLattice|` `technical note [478], except for limiting the number of modes per bin. CosmoLattice|` `includes modes up to` $\sqrt{3}/2\ Nk_{IR}$, `while we limited ourselfs to` $1/2\ Nk_{IR}$, `which explains why the spectra calculated by CosmoLattice| directly extend to slightly higher momenta than the once calculated by our methods in Fig. (VII.5).`

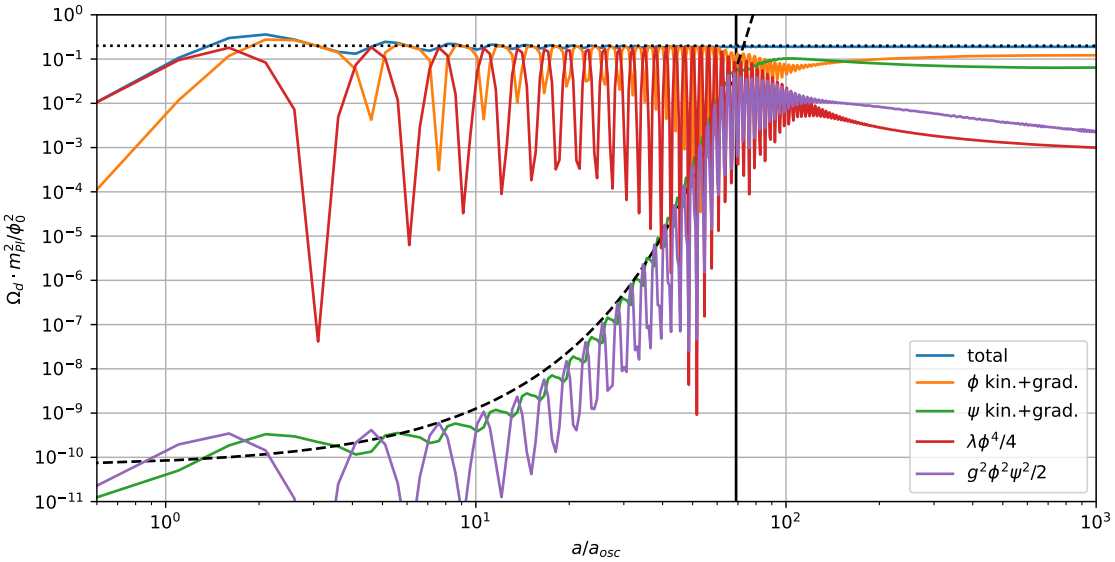

Figure VII.4: Evolution of energy components in the dark sector. Around $a_{\rm osc}$ the ϕ-field starts oscillating and the energy initially stored in the quartic potential (red) starts going back and forth between the potential and kinetic energy (orange). The dark sector transitions from vacuum to radiation like scaling and its total energy (blue) asymptotes to the value given in Eq. (VII.33) (dotted, black). The instabilities induced by the coupling (purple) in ψ lead to its energy (green) growing exponentially past $a_{\rm osc}$. The mode functions of ψ can be approximated by solutions to the *Lamé* equation, leading to the estimate given by the dashed black line. The horizontal black line marks a_*, the time when the energy in the homogeneous ϕ field equals the energy in inhomogenities of ψ as estimated in Eq. (VII.34). At this point the perturbative treatment breaks down, making the lattice analysis necessary. Past this point the majority of energy is stored in fluctuations of ϕ and ψ. Figure created by W.Ratzinger

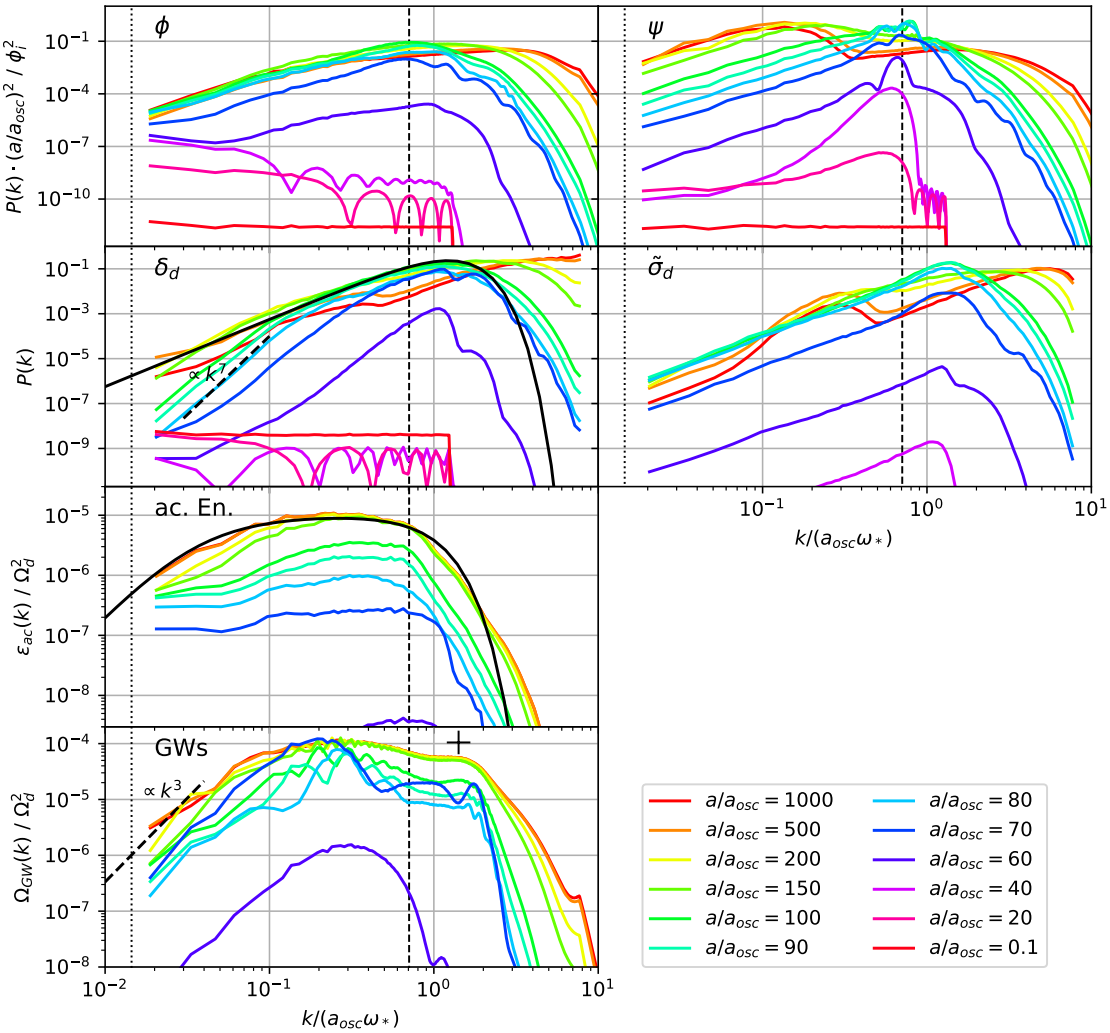

Figure VII.5: Evolution of power spectra of the ϕ and ψ-field (top row) as well as energy fluctuations δ_d and shear $\tilde{\sigma}_d$ in the dark sector (second row). In the third row we show the induced acoustic energy in the baryon-photon fluid through gravitational coupling. See Section VII.5.3 for discussion. In the bottom row we furthermore show the resulting spectrum of gravitational waves as discussed in Section VII.6.1. The vertical, black, dotted line marks the horizon scale at a_*, $k \approx a_{\rm osc}\omega_*/70$, and the dashed line gives our estimate for the fastest growing mode in ψ, $k_* \approx a_{\rm osc}\omega_*/\sqrt{2}$. The thick, black, solid and dashed lines show the analytic estimates discussed in the text. Both solid lines feature the exponential decay in the UV as a result of our conservative choice in Section VII.4.1 with the actual UV tail falling off more gradually. Figure created by W.Ratzinger

at the same time introducing sizeable inhomogeneities in ϕ. Shortly after a_* the energy becomes dominated by the gradient and kinetic terms, corresponding to fluctuations of ϕ and ψ, with the potential energy decreasing.

The evolution of the fluctuations in the fields can be seen directly from the top row of Fig. (VII.5). While the fluctuations in the ϕ field only oscillate as they enter the horizon, leading to the fringe pattern, the fluctuations in the ψ field grow exponentially in the instability band $k \lesssim a_{\rm osc}\omega_*$ with the modes around k_*, marked by the vertical dashed line, growing the fastest. At $a/a_{\rm osc} = 60$, as the system approaches a_*, we can see first signs of a back-reaction in the form of additional induced fluctuations in ϕ. Past $a_*/a_{\rm osc} = 70$ both spectra feature a primary peak that keeps moving to higher k as time progresses. This can be understood as the onset of thermalization as ϕ and ψ particles/waves scatter off one another [479–481]. Somewhat surprisingly there forms a secondary peak in the spectrum of ψ around $k \approx 0.1\ a_{\rm osc}\omega_*$. We can only speculate that this might be the result of the homogeneous part of ϕ being damped and the instability band therefore moving to lower k.

In the second row of Fig. (VII.5) we show the evolution of power spectra of the density fluctuations in the dark sector as well as the shear. Initially the spectrum of density fluctuations is due to the interference of fluctuations of ϕ with its homogeneous component that still dominates the energy. The spectrum is therefore also initially flat, as expected, and shows an oscillatory pattern similar to that of the modes entering the horizon. Around $a_* \approx 70\, a_{\rm osc}$, the fluctuations in the energy density are well described by the analytic estimate Eq. (VII.23) with the parameters derived in Sec. (VII.5.1) (straight, black line). Our estimate describes the energy fluctuations well for the Hubble time following a_*, which is when we expect most of the acoustic energy in the baryon-photon fluid to be sourced. At later times the peak moves to higher k as a result of the scattering processes discussed above. The evolution of the shear is similar although it develops a much more pronounced secondary peak at late times.

In Fig. (VII.6) we show the evolution of the energy fluctuation $\delta_d(k,\tau)$ and the shear $\tilde{\sigma}_d(k,\tau)$ for two modes in the infrared tail of the spectrum. We furthermore show the average amplitude of modes in the respective bin. As there is no clear pattern visible between the two different realisations for the same k, a stochastic description seems to be appropriate. In line with our discussion in Sec. (VII.4.2), we want to furthermore stress the difference in the evolution of $\delta_d(k,\tau)$ and $\tilde{\sigma}_d(k,\tau)$ around a_*. The shear shows $\mathcal{O}(1)$ variations on time scales $\Delta a/a_{\rm osc} \approx 1 \approx k_*\Delta\tau$ that can be related to the characteristic scale $\Delta\tau \approx 1/k_*$. The energy fluctuations on the otherhand only grow as $\propto [k(\tau-\tau_*)]^2$ and take on their late time amplitude after $\Delta\tau \approx 1/k$. This can also be seen from Fig. (VII.5) where the infrared tail of the power spectrum of the energy fluctuations is given as $\propto k^3 \cdot [k(\tau-\tau_*)]^4 \propto k^7$ at the times $a/a_{\rm osc} = 80-100$ shortly after a_* before asymptoting to the final $\propto k^3$. This behavior can be understood as the energy density is conserved on sub-horizon scales and we therefore have $\dot{\rho}(k,\tau) = ikj_\rho(k,\tau)$, which leads to $\rho(k,\tau) \propto k(\tau-\tau_*)$ assuming that the corresponding current $j_\rho(k,\tau)$ jumps to its final amplitude around a_*. Since the current $j_\rho(k,\tau)$ is however the momentum density and itself conserved, one finds $\rho(k,\tau) \propto [k(\tau-\tau_*)]^2$.

In Fig. (VII.7) we show the autocorrelation function of $\delta_d(k,\tau)$ and $\tilde{\sigma}_d(k,\tau)$ for the same values of k, calculated by averaging over the modes in the respective bin and times between $a/a_{\rm osc} = 200-1000$. For comparison we also show the analytic approximation Eq. (VII.25) for the energy fluctuations of a free scalar field (Sec. (VII.8.2)). As one can see there is good qualitative agreement in that they both have a central peak of width $\approx 1/k$. As argued in Sec. (VII.4.2) this is also expected from energy conservation. Finding these two

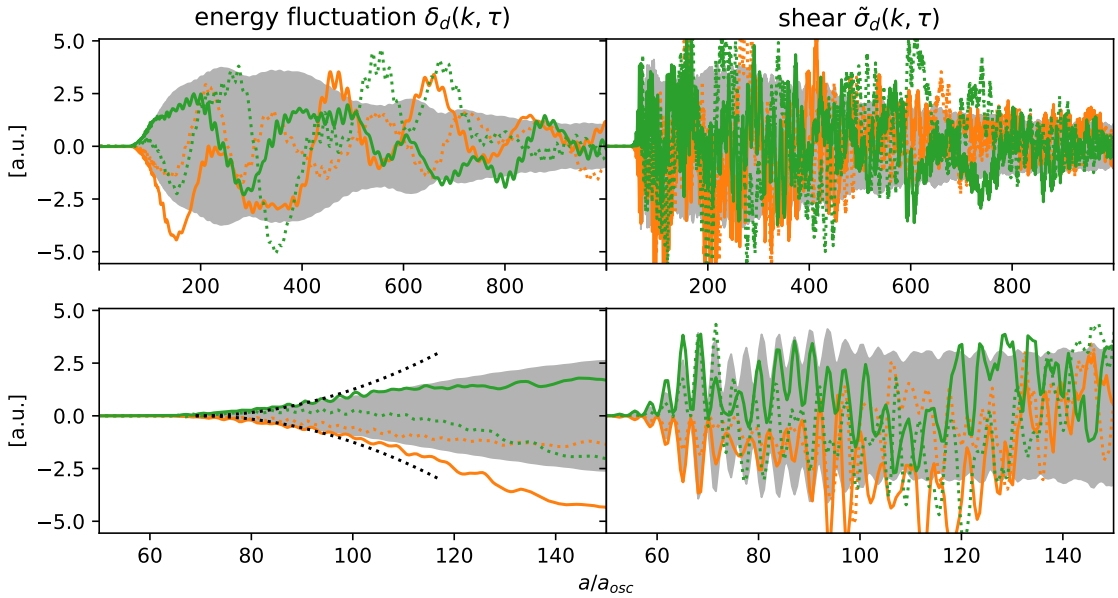

Figure VII.6: Top row: Evolution of the energy fluctuation $\delta_d(k,\tau)$ and the shear $\tilde{\sigma}_d(k,\tau)$ for two modes (orange and green) in the infrared tail of the spectrum ($k = 0.05\ a_{\rm osc}\omega_*$). The straight and dotted line give the real and imaginary part respectively. The gray envelope indicates the evolution of the power spectrum $\propto \sqrt{\mathcal{P}(k,\tau)}$ as calculated by averaging the amplitude of all mode-functions in the respective bin. Bottom row: Same as above, zoomed in on the Hubble time past $a_* \approx 70\ a_{\rm osc}$. The black dotted lines indicate the amplitude of the energy fluctuations growing $\propto [k(\tau-\tau_*)]^2$ initially. Figure created by W.Ratzinger

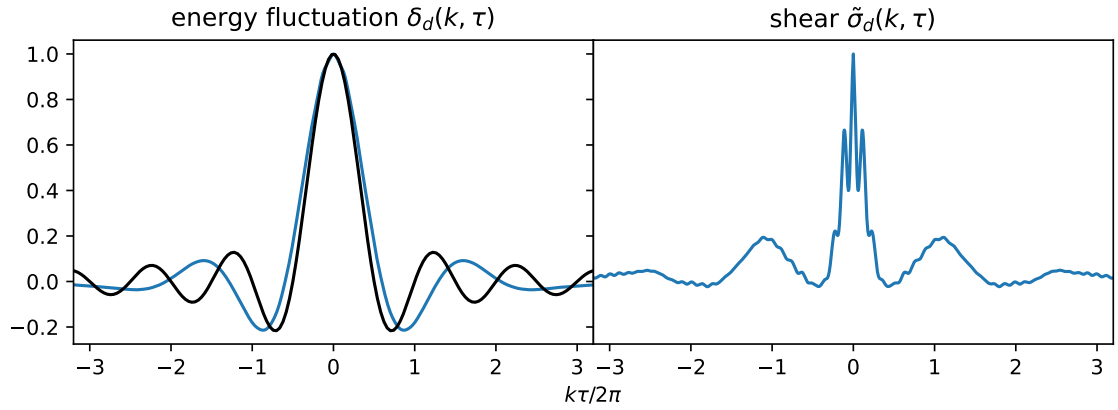

Figure VII.7: Autocorrelation of the energy fluctuation $\delta_d(k,\tau)$ and the shear $\tilde{\sigma}_d(k,\tau)$ for same momentum as in Fig. (VII.6) ($k = 0.05\ a_{\rm osc}\omega_*$). For the energy fluctuation we show for comparison the sinc that we find analytically in Sec. (VII.8.2) for a free scalar field (black). Figure created by W.Ratzinger

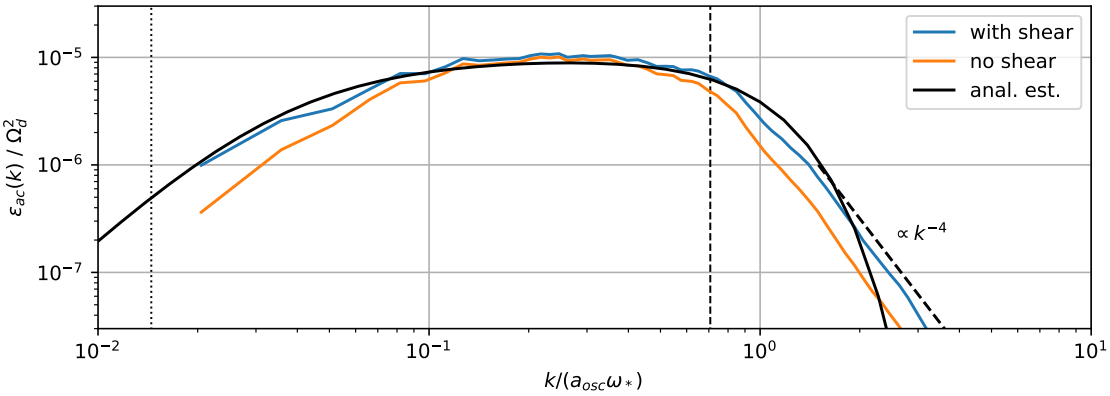

Figure VII.8: Close-up of the acoustic energy spectrum at the final time of the simulation. The blue line represents the physical result, while the orange line stems from a simulation in which the shear of the dark sector was neglected. The straight black line gives the analytical estimate, with the black dashed line indicating a k^{-4} power law that seems more appropriate to describe the UV tail than the exponential decay of the analytic estimate. The vertical, black dotted and dashed line give the horizon at a_* and the estimate of the fastest growing mode in the ψ-field, k_*. Figure created by W.Ratzinger

features makes us confident that our lattice version of the energy density indeed resembles the continuum one.[7] We also find qualitative agreement for the autocorrelation of the shear from the lattice simulation and the free scalar field. Both have features on small time scales related to the peak momentum k_* and on time scales related to k. It should however be mentioned that the autocorrelation function of the shear varies much more when varying the momentum k.

Given the evolution of fluctuations in the dark sector as shown in Fig. (VII.6), we can numerically solve the equations for fluctuations in the baryon-photon fluid on a mode-per-mode basis. This allows us to calculate the acoustic energy and the result is shown in the third row of Fig. (VII.5) and in Fig. (VII.8). From the time evolution shown in Fig. (VII.5) we see that the majority of acoustic energy is induced in the Hubble time after a_* ($a/a_{\rm osc} \approx 70 - 150$) and the energy becomes constant shortly after. Our analytic estimate in Eq. (VII.28) with the parameters derived in Sec. (VII.5.1), shown in black, accurately estimates the main features of this final spectrum: A steep fall off for modes larger than the peak momentum k_*, a flat plateau for momenta between k_* and the horizon at a_* (vertical, dotted, black line) and a k^3 infrared tail for momenta outside the horizon at a_*. Unfortunately our simulation does not properly cover super-horizon scales, but from what we can see the spectrum becomes steeper at the horizon in good agreement with our estimate.

In Fig. (VII.8) we show a close-up of the acoustic energy spectrum at the final time of the simulation. We furthermore show the result of a calculation in which we neglected the shear of the dark sector when solving for the perturbations in the baryon-photon fluid. We find that both calculations as well as the analytic estimate agree to within $\approx 20\%$ in

[7] We first tried to do this analysis for an axion coupled to a vector, using the same code as in [454]. This model and its lattice implementation are more complicated since they involve vectors. We were not able to construct an energy density on the lattice that showed these characteristics of energy conservation without decreasing the time step of the simulation by a lot, making the simulation unfeasible. We leave a systematic investigation of this issue for future work and recommend checking these features when running similar simulations.

the plateau region. Neglecting the shear, however, results in underestimating the acoustic energy by a factor of $\approx 2-3$ in the IR and UV tail of the spectrum. Furthermore we find that in the UV the spectrum falls of as k^{-4} rather than the exponential suppression suggested by the analytic estimate.

VII.6 Application to sources of GWs

Our mechanism of sourcing μ-distortions is only efficient if the dark sector features a sizeable amount of energy $\Omega_d \lesssim 0.04$ that has $\mathcal{O}(1)$ perturbations on scales close to the horizon. The upper bound on the energy here stems from the current $N_{\rm eff}$ bound discussed below. If the dynamics of the dark sector are furthermore relativistic, they efficiently produce gravitational waves. Such models have received a large amount of attention recently due to the detection by LIGO [52] and hints stemming from pulsar timing arrays (PTAs) [62, 388, 396, 397]. In the following, we want to compare the reach of searches for GWs and spectral distortions for some of these models.

Before doing so, let us clarify that the inverse statement, i.e. that all sources of primordial GWs feature large perturbations close to the horizon scale, is not necessarily true. A counter example would be strings originating from a broken local $U(1)$ gauge symmetry. In this case, GWs are mainly produced from the tiniest string loops that only populate a small fraction of the Hubble volume at a given time. Therefore the source is point-like, whereas for the dark sectors we are considering, GWs get sourced over the whole Hubble volume.

For these sectors the resulting GW spectrum is peaked around the characteristic scale k_* and the peak amplitude can schematically be parameterized as [179, 482, 483]

$$\Omega_{\rm GW,peak} \propto \Omega_d^2 \cdot \left(\frac{a_* H_*}{k_*}\right)^{\alpha} \cdot \mathcal{P}^2_{\delta_d}(k_*)\,. \tag{VII.37}$$

Just like the induced acoustic energy, the energy in GWs is suppressed by Ω_d^2. The suppression originating from the characteristic scale being inside the horizon potentially differs though from Equations Eq. (VII.28) and Eq. (VII.30), with the model dependent power α taking the values 1 and 2. If the new physics comprising the dark sector does not feature spin-2 degrees of freedom, gravitational waves can only get sourced in second-order processes resulting in the suppression by $\mathcal{P}^2_{\delta_d} \lesssim 1$. Further suppression of the GW signal occurs if the dynamics are non-relativistic, but we are not considering this case below.

Experiments and Cosmological Bounds

At the lowest frequencies and correspondingly largest scales, the amount of GWs becomes limited by the non-detection of B-modes in the CMB polarization by Planck+BICEP2+Keck [484], and we show the resulting limit in cyan in the following plots. Furthermore, the gravitationally induced scalar fluctuations would alter the resulting CMB perturbation pattern. In our age of precision cosmology, deriving such bounds is done by refitting the angular perturbations from scratch. However, such an analysis is beyond this work. Instead, we take inspiration from searches of symmetry-breaking relics carried out in e.g [485–487]. They found that the fraction in the angular power spectrum stemming from the new physics is limited to a couple of percent over a wide range of angular scales l. To visualize the remaining uncertainty, we show an aggressive bound, limiting the amount of induced fluctuations to 2% of the inflationary ones up to the CMB pivot scale, $\mathcal{P}_{\delta_\gamma} < 0.02\,\mathcal{P}^{\rm inf}_{\delta_\gamma}$ for $k < 0.05\,{\rm Mpc}^{-1}$, as well as a more conservative bound

corresponding to 10% out to scales of $k < 0.005\,\mathrm{Mpc}^{-1}$. Here $\mathcal{P}_{\delta_\gamma}^{\mathrm{inf}} \approx 16 \cdot \mathcal{P}_\xi \approx 32 \times 10^{-9}$ denotes the amount of inflationary fluctuations inferred form the Planck 2018 dataset [21]. We calculate $\mathcal{P}_{\delta_\gamma} \approx 4\epsilon_{ac}$ using the formulas given in Section VII.4. The resulting bound is shown in red.

At smaller scales, we use the results from Sec. (VII.3) and Sec. (VII.4) to calculate the μ-distortions resulting from induced acoustic waves and show the results in green. We furthermore calculate the μ-distortions stemming from the interaction of the GWs emitted by the dark sector with the baryon-photon fluid [442, 488, 489]. We show the resulting bound in pink. The actual observable distortion would perhaps be the sum of these two effects, but we show them separately to highlight the magnitude of each source of distortion. As thresholds for the detection of a μ-distortion we consider the existing bound from COBE/FIRAS $\mu < 4.7 \times 10^{-5}$ at 95% confidence level [441, 490] as well as the sensitivity of the future missions PIXIE $\mu \lesssim 3 \times 10^{-8}$ [445] and Voyage2050 $\mu \lesssim 1.9 \times 10^{-9}$ [446].

At even shorter scales, we fit the GW spectrum to the to-be-confirmed detection by pulsar timing arrays [62,388,396,397] using the first 5 frequency bins from the NANOGrav 12.5yr dataset [62] and the hierarchical method proposed in [303,491]. Direct fits including modeling of pulsar noise have been carried out for a number of the models discussed below [395, 404, 492, 493] and the results largely agree with the hierarchical method. We show the resulting 2σ region of the fit as an orange area. Furthermore, we show the reach of the planned square kilometer (SKA) array after taking data for 20 years [61, 118, 494] as an orange line.

Since we consider dark sectors with relativistic dynamics, they will inadvertently act as a form of radiation not interacting with the baryon-photon fluid and therefore contribute to the effective number of neutrinos N_{eff}. At recombination its contribution is given as

$$\Delta N_{\mathrm{eff}} = \frac{8}{7}\left(\frac{11}{4}\right)^{\frac{4}{3}} \left.\frac{\rho_d}{\rho_\gamma}\right|_{T=T_{\mathrm{rec}}} . \tag{VII.38}$$

The Planck 2018 dataset constrains $\Delta N_{\mathrm{eff}} < 0.3$ at 95% confidence level [21] and the next generation of ground-based telescopes (CMB Stage-4) is expect to achieve a sensitivity of $\Delta N_{\mathrm{eff}} < 0.03$ [443], which we show as a gray surface and line respectively.

VII.6.1 $\lambda\phi^4$-Theory

Let's start with the model we already considered in great detail in Sec. (VII.5). In Fig. (VII.5), we show in the bottom row the evolution of the energy density spectrum of gravitational waves. As one can see, similar to the acoustic energy, the energy in gravitational waves is sourced in the Hubble time following the back-reaction of the ψ-field on ϕ, $a/a_{\mathrm{osc}} \approx 70 - 150$. One might therefore try to estimate the peak amplitude with Eq. (VII.37) and $\alpha = 2$, which has been observed to give a decent estimate for similar models. Very roughly one can set $\mathcal{P}_{\delta_d}(k_*) \approx 1$. It has also been observed that the peak of the GW spectrum lies typically about a factor 2 higher than the characteristic scale of the source $k_{\mathrm{peak}} \approx 2k_*$ (see e.g. [460]). We show the resulting estimate as a black cross in Fig. (VII.5). Somewhat surprisingly, the actual peak of the GW spectrum lies a factor ≈ 4 below the characteristic scale k_*, and the estimate only corresponds to a secondary peak at higher k. The peak amplitude, however, is estimated to be within a factor of 2. In Fig. (VII.5) we have furthermore indicated the k^3 power law that one expects for $\Omega_{\mathrm{GW}}(k)$ for scales outside the horizon at a_* [416, 495] (dotted, black line).

To derive the bounds and reach of future experiments we use the spectra found in our lattice simulation and extrapolate them as $\propto k^3$ in the infrared and conservatively as 0 in the UV. The relic abundance, the energy in GWs and wave vectors k are redshifted taking into account the changing number of relativistic degrees of freedom in the SM plasma in order to compare them to the future and present bounds mentioned above. The results are shown in Fig. (VII.9). We find that at low effective masses $\omega_* \lesssim 10^{-22}$ eV the model is most stringently constrained by the non-observation of B-modes in the CMB (cyan). At intermediate values 10^{-23} eV $\lesssim \omega_* \lesssim 10^{-13}$ eV the spectral distortions induced by acoustic waves will be detectable by future missions. We find that for this model, as for all other ones that we discuss, the contribution from the GWs to the distortion is negligible. At even larger masses, the model can be tested by SKA, but in the parameter space still allowed by the $N_{\rm eff}$ constraints the signal is too weak to explain the recent findings of today's PTAs.

For this model, all bounds relying on scalar fluctuations are rather weak compared to the examples that we discuss below. The reason is that the characteristic scale lies deep inside the horizon when the perturbations arise $k_*/(a_* H_*) = \mathcal{O}(100)$ and this factor enters with a power of -3 in the estimate Eq. (VII.28). In the case of an axion coupled to a dark photon [303, 453, 457, 460, 496–506] featuring a similar instability this ratio is typically of the same order (possibly with the exception of [507]) and we expect comparable results. The situation is different for the related scenario of axion fragmentation [456,461,508–510], where this ratio can be of $\mathcal{O}(1)$ and we expect that the spectral distortions could be much larger than recently estimated in [258], where only the GWs were considered.

VII.6.2 Unstable Remnants of post-inflationary Symmetry Breaking

Symmetry breaking in the early universe is one of the most anticipated predictions for BSM physics, emerging in many extensions of the standard model e.g. [511,512]. Here we will assume that the symmetry breaking takes place after inflation resulting in a universe filled with topological defects or a network of scaling seeds. We restrict ourselves to the study of domain walls from the breaking of a discrete symmetry, as well as cosmic strings resulting from the breaking of a global $U(1)$, which appear for instance, in axion-like particle (ALP) scenarios with post-inflationary Peccei-Quinn breaking.

VII.6.2.1 Domain Walls

Domain walls (DWs) [350, 352, 423] are two dimensional topological defects that emerge from the breaking of a discrete symmetry. The parameter controlling the DWs dynamics after formation is the surface tension σ. By considering that every Hubble patch with volume $1/H^3$ contains a sheet of DW with area $1/H^2$ one can show that

$$\Omega_{DW} \simeq 0.5 \frac{\sigma}{m_{\rm Pl}^2 H}\,, \tag{VII.39}$$

where the $\mathcal{O}(1)$ prefactor is inferred from simulations during radiation domination [418]. This picture furthermore suggests that the system has $\mathcal{O}(1)$ density fluctuations at the horizon scale. As one can see the relative amount of energy in DWs grows as the universe cools down, leading to strict bounds on σ in order to not over-close the universe. Observability therefore motivates a scenario in which the degeneracy of the vacua related by the symmetry is broken by an additional term in the potential $V_{\rm bias}$. The introduction of $V_{\rm bias}$ causes the walls to experience volume pressure, that leads to the annihilation of the network once the energy in the volume becomes comparable to the energy in the surface area

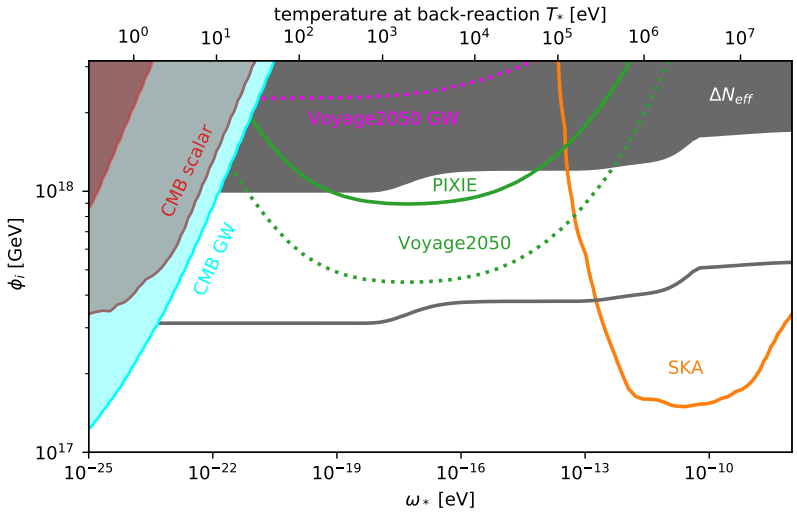

Figure VII.9: Constraints and future probes of the $\lambda\phi^4$-model introduced in Sec. (VII.5). Here ω_* determines the temperature T_* at which the fluctuations come to dominate the energy in the dark sector and the initial amplitude ϕ_i gives the energy in the dark sector Ω_d. The gray area and line give the current and future bounds resulting from Ω_d increasing N_{eff} at recombination. For T_* below $\mathcal{O}(10^2\,\text{eV})$ the scenario is constrained by fits to CMB fluctuations (red) as well as the non-observation of B-polarization modes (cyan). For the wide range of annihilation temperatures of $(10^2 - 10^7)\,\text{eV}$ spectral distortions are able to probe this scenario with the future missions PIXIE (straight) and Voyage2050 (dotted). We show the bound including only the contribution from scalar acoustic waves in green and the one from only considering GWs in pink. At temperatures above $10^5\,\text{eV}$ the model becomes testable by the future pulsar timing array SKA (orange line). Figure created by W.Ratzinger

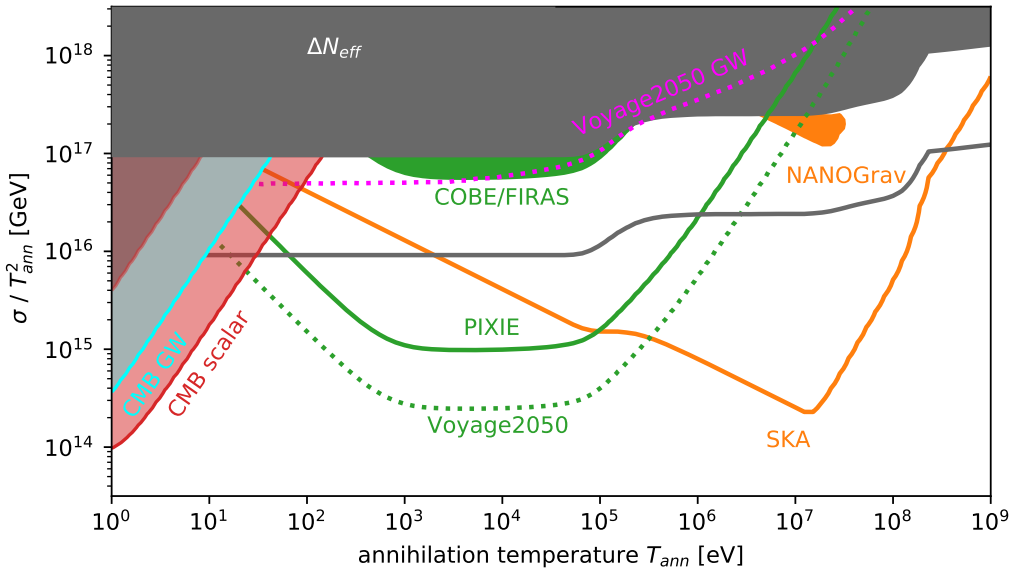

Figure VII.10: Left: Constraints and future probes of domain walls in terms of the annihilation temperature of the network $T_{\rm ann}$ and the surface tension σ. See the text and Fig. (VII.9) for discussion. We have picked two benchmarks A and B. Right: On the top we show the GW signal for the benchmarks in relation to the power law integrated noise of SKA. While SKA can not distinguish the two scenarios, the induced spectral distortion is drastically different as can be seen from the bottom panel. Figure created by W.Ratzinger

of the DWs. In a radiation dominated universe the time of DW annihilation corresponds to the following temperature [418]

$$T_{\rm ann} \approx 10\ {\rm MeV} \left(\frac{\sigma}{{\rm TeV}^3}\right)^{-\frac{1}{2}} \left(\frac{{\rm V}_{\rm bias}}{{\rm MeV}^4}\right)^{\frac{1}{2}} . \tag{VII.40}$$

The GWs from annihilating DWs were first studied analytically [513, 514] and later on quantitatively using lattice simulations [418, 430, 515–517]. On the lattice one finds that the GW spectrum is peaked at $k_{peak} = 2\pi a_{\rm ann} H_{\rm ann}$ and the peak amplitude at emission is given as [430]

$$\Omega_{GW,{\rm peak,ann}} \simeq 0.02\ \Omega^2_{DW,{\rm ann}} . \tag{VII.41}$$

This is exactly what one expects from Eq. (VII.37) for a source with dynamics on the horizon scale and $\mathcal{O}(1)$ density fluctuations. The shape of the spectrum is $\propto k^3$ for $k < k_{peak}$ and $\propto k^{-1}$ for $k > k_{peak}$.

To estimate the acoustic energy induced by the DWs we use the spectrum given in Eq. (VII.23) and set the normalisation to $A_{\delta_d} = 1$. Since the spectrum peaks at $\approx 2k_*$ we set $k_* = k_{peak}/2$. We have no reason to expect that the energy fluctuations $\delta_d(k,\tau)$ show a deterministic behavior and therefore use Eq. (VII.28). The DWs are expect to source acoustic energy for the whole time that the network exists with the biggest contribution stemming from the time of annihilation when the relative energy in the network is largest. As a conservative estimate we only take this contribution into account and set $a_* H_* = a_{\rm ann} H_{\rm ann}$ and $\Omega_{d,*} = \Omega_{DW,{\rm ann}}$ in Eq. (VII.28).

In order to not over-close the Universe, we assume that the remnants of the DW network rapidly decay into dark, massless or light particles that consequently contribute to $N_{\rm eff}$. We

take into account the appropriate redshift to arrive at the results shown in Fig. (VII.10). We again find that the spectral distortions are dominantly produced through the damping of acoustic waves as can be seen by comparing the green and pink dotted line. The amount of acoustic energy and gravity waves is approximately the same $\epsilon_{\rm ac} \sim \Omega_{\rm GW} \propto \Omega_d^2$, but only a small fraction of the energy in gravity waves is injected into the photons, while all of the acoustic energy is converted when the modes cross the diffusion scale.

Since the fluctuations are horizon sized, there is no suppression of the acoustic energy, resulting in stronger signals when compared to the model considered above, while still being compatible with the $N_{\rm eff}$-bound. As can be seen from Fig. (VII.10), in parts of the parameter space $T_{\rm ann} = 10^3 - 10^5\,{\rm eV}$ the existing COBE/FIRAs data already constrains the distortions induced through acoustic waves (green area), slightly improving upon the bound from $N_{\rm eff}$.

On the right side of Fig. (VII.10) we sketch the GW spectrum for two benchmark points together with the expected sensitivity of SKA.[8] Since PTAs are only sensitive to the UV tail of the spectrum, if the annihilation temperature is below $T_{\rm ann} \lesssim 10^7\,{\rm eV}$, SKA is not able to distinguish between the two benchmarks. On the bottom we show the acoustic energy density spectra in relation to $\mu_{\rm thr,PIXIE}/\mathcal{W}(k)$, where $\mu_{\rm thr,PIXIE} = 3 \times 10^{-8}$ is the threshold for detection by PIXIE and $\mathcal{W}(k)$ is the window function given in Eq. (VII.15). Broadly speaking the overlap of the acoustic spectra with $\mu_{\rm thr,PIXIE}/\mathcal{W}(k)$ gives the size of the signal compared to the threshold in accordance with Eq. (VII.14). It becomes clear that the benchmarks, although indistinguishable by the SKA measurement, lead to drastically different μ-distortions. This goes to demonstrate the role spectral distortions might have in the upcoming age of multi-messenger cosmology. The future missions PIXIE and Voyage2050 will go far beyond all other probes in this range.

VII.6.2.2 Global Strings

Cosmic Strings (CSs) [350, 423], one dimensional topological defects, are remnants of a spontaneous $U(1)$ symmetry breaking. The essential parameter controlling the dynamics of the strings is the symmetry breaking scale f_ϕ that determines the string tension. We will base our analysis in the following on the findings of [383]. There it is found that the energy density in the string network is given as

$$\Omega_s(a) \simeq 1.0 \cdot \log^2\left(\frac{f_\phi}{H(a)}\right)\left(\frac{f_\phi}{m_{\rm Pl}}\right)^2 , \tag{VII.42}$$

during radiation domination once the system has entered the scaling regime. The time-dependent logarithmic factor $\log(f_\phi/H) = \mathcal{O}(100)$ enters here, since parameters like the string tension and the number of strings per Hubble patch show this scaling in case of the breaking of a global $U(1)$ symmetry. The existence and extent of this logarithmic dependence still remains debated for observables like the emitted GWs [383, 425, 429, 487] though. According to [383] the energy of emitted GWs is given as

$$\Omega_{GW}(k) \simeq 0.2 \cdot \Omega_s^2|_{aH=k} \, . \tag{VII.43}$$

Similar to the example of domain walls, we will again consider the possibility that an explicit breaking of the $U(1)$ symmetry enforces the annihilation of the network. This breaking is parameterized by the mass m_ϕ of the pseudo Nambu-Goldstone boson. Once

[8] While for our parameter scan we use the exponential suppression in the UV from Eq. (VII.23), for this sketch we show a power law that we think is more realistic. The majority of the signal is due to the peak such that this introduces only a small uncertainty in the parameter scan.

Hubble drops to $H_* = m_\phi$, the field settles in its true minimum resulting in the formation of domain walls that collapse the network. Ref. [383] finds that the GW spectrum features a peak at $k_{\rm peak} = 2\pi a_* H_*$ with the amplitude at the peak and higher frequencies given by the formula above and falls off as k^3 for lower frequencies.

To determine the $N_{\rm eff}$ bound we use that the energy in relativistic Nambu-Goldstone bosons at emission is [383]

$$\Omega_\phi \approx 0.3 \cdot \log^2\left(\frac{f_\phi}{H(a_*)}\right)\left(\frac{f_\phi}{m_{\rm Pl}}\right)^2 . \tag{VII.44}$$

Part of these bosons will become non-relativistic and contribute to the DM density. We refer the reader to [383] for the derivation of the DM abundance as well as other bounds arising from structure formation (see also [518, 519]).

To estimate the acoustic energy induced by strings, we employ largely the same arguments and procedures as shown for the DWs: As a conservative estimate, we limit ourselves to the contribution of the strings leaving aside the bosons. We therefore plug $k_* = k_{peak}/2$, $A_{\delta_d} = 1$ and Eq. (VII.42) into Eq. (VII.28) to get the estimate. To account for the continuous induction of acoustic energy during the scaling regime, we replace the exponential suppression for $k > k_{peak}$ by only a logarithmic dependence $\propto \log^4(k/k_{peak})$, in which we assumed that this is only due to the time dependence of $\Omega_s(a)$. The results are shown in Fig. (VII.11). We are additionally showing the reach of the future space-based interferometer LISA adopted from [383] as an orange line. The region in which the resulting DM overcloses the universe is shown in blue and the bounds arising from structure formation in purple. It should be mentioned that if our assumption of the density fluctuations being of horizon size at annihilation $k_* = \pi a_* H_*$ also holds true at late times, the stronger (purple shaded) bound is applicable. Interactions among the bosons could possibly relax this assumption though leading to a less stringent bound (solid purple).

In the parameter space in which the pseudo Nambu-Goldstone bosons contribution to DM is not overclosing the universe, SKA and LISA only probe the UV tail of the GW spectrum, which renders them insensitive to the decay of the network and therefore m_ϕ. Since for $m_\phi \gtrsim 10^{-22}$eV the period in which acoustic waves are sourced is shortened, spectral distortions offer an opportunity to estimate or at least constrain m_ϕ in most of the parameter space with detectable GWs.

Before moving on, let us compare our results to the ones obtained in [464, 465] for non-decaying networks of scaling seeds. Both papers consider the spectral distortions due to gravitationally induced acoustic waves in the baryon-photon fluid, just as we do in this paper. Ref. [464] considers the case of cosmic strings and found that only $\mu \approx 10^{-13}$ can be reached without being in tension with CMB observations, while our analysis suggests that distortions as large as $\mu \approx 10^{-9} - 10^{-10}$ are possible.[9] In [465] the breaking of an $\mathcal{O}(N)$ symmetry with $N \geq 4$ was studied that features no topological artefacts but a network of scaling seeds with quasi constant Ω_d and dynamics of horizon size. This system

[9] It should be mentioned that [464] concerns the case of local strings. Global strings effectively radiate off their energy as Goldstone bosons preventing the formation of small loops, while local strings predominantly decay into gravitational waves and therefore form small loops. This makes the two scenarios drastically different when it comes to the emission of gravitational waves. We seem to agree with [464] that the gravitational drag from a surrounding fluid only concerns the largest scales of the respective network, as can be seen from our estimate Eq. (VII.28) decaying as k^{-3} and the integration over the loop-length in [464] being dominated by the largest loops. Therefore, in this regard the two scenarios should be similar and this does not necessarily explain the tension between our results. Ref. [464] introduces a wiggliness parameter that potentially enhances the distortion. If this parameter is proportional to $\log(f_\phi/H)$ the two estimates can be reconciled.

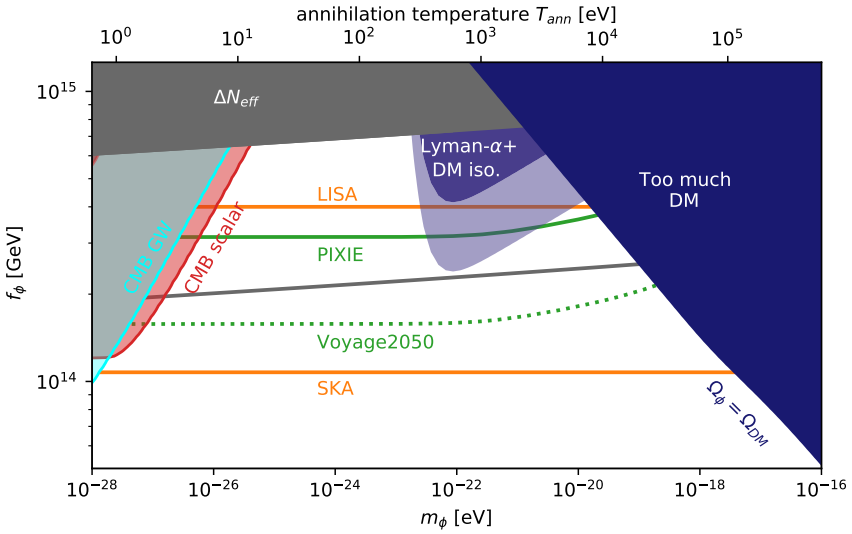

Figure VII.11: Present and future constraints on cosmic string networks resulting from the breaking of a global $U(1)$ at the scale f_ϕ. We assume that the network annihilates at a temperature T_{ann} due to an explicit breaking of the symmetry parameterized by the mass of the resulting pseudo Nambu-Goldstone boson m_ϕ. Additionally to the bounds shown in Fig. (**??**), we also show the reach of the interferometer LISA searching for GWs. Further constraints on this parameter region arise due to the emitted axions making up a fraction of DM and featuring large isocurvature perturbations in conflict with Lyman-α observations (purple). For annihilation temperatures $T_{ann} \geq 10^5$eV the most severe constraint comes from overproducing axion DM. Again the great complementarity between GWs and spectral distortion experiments shall be emphasized, with the later being sensitive to the mass (at least for $m_\phi > 10^{-22}$ eV). Figure created by W.Ratzinger

is therefore very similar to cosmic strings. They find that present CMB bounds allow for $\mu \approx 10^{-9}$ for non-decaying networks in good agreement with our result.

VII.6.3 Phase transitions

Many theories of BSM physics predict a first-order phase transition (FOPT) in the post-inflationary universe (see e.g. [88, 458, 459]). These FOPT proceed through bubble nucleation and bubble collisions at relativistic speeds and are therefore a great source of GWs [520, 521]. We consider the case in which the FOPT takes place in a purely gravitationally coupled sector as in [118, 119, 435] and only consider the sound wave contribution to the GW spectrum [91, 178]. While this is often the dominant source of GWs from thermal FOPTs, this is a conservative estimate of the GW spectrum since it neglects contributions from bubble collisions and turbulence.

The parameters describing such a system are the energy density in the dark sector Ω_d that can readily be exchanged for the contribution to N_{eff} using Eq. (VII.38), the amount of energy freed in the phase transition relative to the one in the dark fluid α_d, [10] the time

[10] The situation commonly discussed only concerns the case where the universe is filled with one fluid. When dealing with multiple fluids the introduction of α_d and Ω_d is necessary as opposed to only using $\alpha = \Omega_d \alpha_d/(1+\alpha_d)$. Since the bubble walls only couple to the fluid in the dark sector, the matching conditions are only imposed on the dark sector and as a result the efficiency of generating sound waves depends on α_d as opposed to α [119].

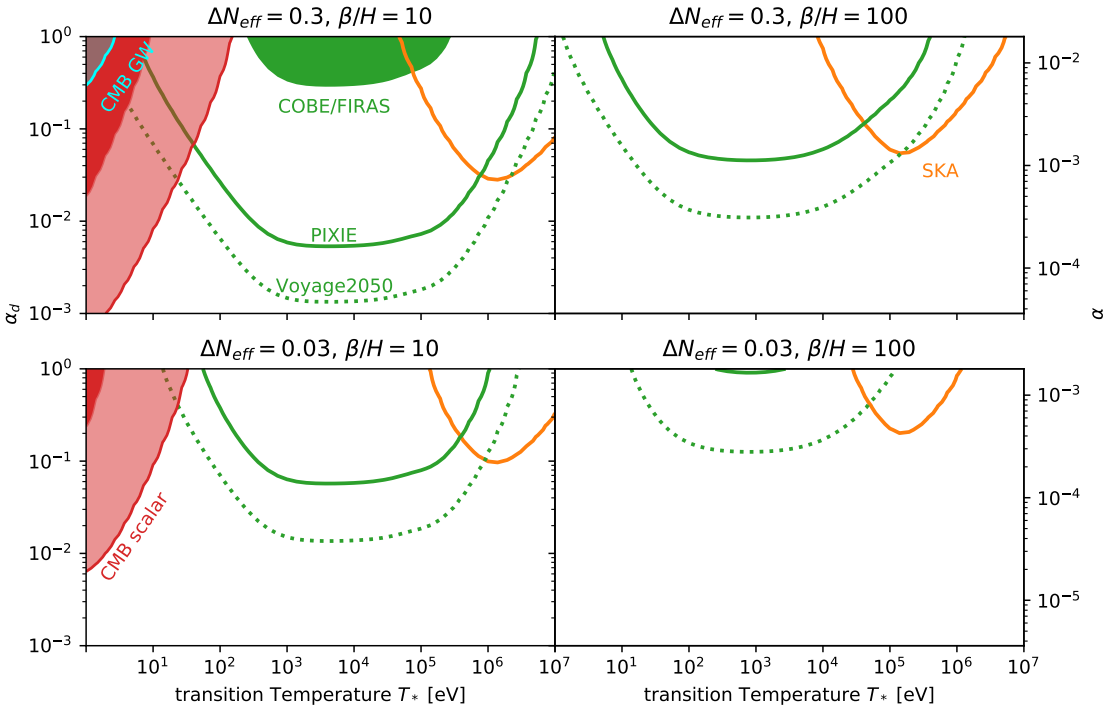

Figure VII.12: Current and future constraints on a phase transition in a dark sector, in terms of the SM plasma temperature at the time of the transition and the released energy relative to the energy in the dark fluid α_d, for different values of ΔN_{eff} and the inverse duration of the phase transition $\frac{\beta}{H}$. We only take into account the effects of the sound waves in the dark fluid caused by the transition. At temperatures $T_* = 1 - 10\,\text{eV}$ the scenario is constrained by CMB fluctuations in (red) and the non-observation of B-mode polarization in the CMB in (cyan). In the temperature range of $T_* = 10 - 10^6\,\text{eV}$ spectral distortions from acoustic waves (green) can probe the scenario. Strong phase transitions in a dark sector saturating the N_{eff} bound can already be constrained by the COBE/FIRAS results. At temperatures $T_* = 10^5 - 10^7\,\text{eV}$ the scenario can in the future be detected by SKA, while the present N_{eff} bound (top row) rules out the NANOGrav signal being generated this way. For convenience we have converted α_d to $\alpha = \Omega_d \alpha_d/(1+\alpha_d)$ on the left y-axis. Figure created by W.Ratzinger

of the transition which we will give as the temperature T_* of the SM plasma at the time,[11] as well as the inverse time scale of the transition β. To keep our discussion simple we further set the wall velocity $v_w \simeq 1$ and restrict us to a speed of sound $c_d = 1/\sqrt{3}$ in the dark sector, [12] which allows us to estimate its acoustic energy relative to its total energy as

$$\epsilon_{\mathrm{ac},d} = \frac{\rho_{\mathrm{ac},d}}{\rho_d} = \frac{\kappa(\alpha_d)\alpha_d}{1+\alpha_d}\,; \qquad \kappa(\alpha_d) = \frac{\alpha_d}{0.73 + 0.083\sqrt{\alpha_d} + \alpha_d}\,, \tag{VII.45}$$

where κ gives the efficiency factor for converting the released energy into sound waves as found in [85].

The energy density of GWs coming from the sound waves which are emitted from a dark sector with nucleated bubbles of sub-horizon size is [179]

$$\Omega_{GW}(k) \simeq 0.16 \left(\frac{k}{k_{\mathrm{peak}}}\right)^3 \left(\frac{7}{4+3(k/k_{\mathrm{peak}})}\right)^{7/2} \cdot \Omega_{d*}^2 \cdot \frac{H_*}{\beta} \cdot \left(\frac{\kappa(\alpha_d)\alpha_d}{1+\alpha_d}\right)^2 . \tag{VII.46}$$

The first term is again an $\mathcal{O}(1)$ prefactor for $k = k_{\mathrm{peak}} = 2a_*\beta/\sqrt{3}$ and determines the shape of the spectrum, while we can identify the other terms with the factors in the rough estimate of Eq. (VII.37).

The density fluctuations in the relativistic dark sector, just as in the baryon-photon fluid, are related to the acoustic energy via $A_{\delta_d} = \langle \delta_d^2 \rangle = 4\epsilon_{\mathrm{ac},d}$ in the virial limit. Again we set $k_* = k_{\mathrm{peak}}/2$, but in this case we use Eq. (VII.30) to determine the gravitationally induced acoustic waves. This is justified, since one expects that δ_d only shows a stochastic behavior for a time $\approx 1/\beta$ while the walls are present and proceeds with the deterministic propagation of sound waves for the remaining Hubble time following the transition.

The ratio β/H_* determines if the PT completes mainly driven by the expansion of a few nucleated bubbles or by the nucleation of new bubbles everywhere in space. Large values of β/H_* correspond to faster nucleation rates which means that more bubbles will nucleate inside the Hubble horizon until the PT has completed, and hence their bubble radii get smaller. One expects an inverse relation between β/H_* and the amplitude of the GW spectrum. Since β/H_* determines the average bubble radius at the time of collision, it also controls the peak frequency of the GW spectrum. For very strong FOPTs one might have to reformulate the definition of β/H_* as it may become inappropriate and was emphasized in [522, 523].

In Fig. (VII.12) we show our results. Similar to the previous examples we find that spectral distortions bridge the gap between phase transitions detectable by CMB fluctuations ($T_* = 1 - 10\,\mathrm{eV}$) and by PTAs such as SKA ($T_* = 10^5 - 10^7\,\mathrm{eV}$). The probes relying on scalar mediation are however particularly strong for $\alpha_d \ll 1$. In this case the fluctuations in the dark sector are small $\mathcal{P}_{\delta_d} \ll 1$, which suppresses the GWs relative to the sourced acoustic waves, as one can see by comparing Eq. (VII.37) with Eqs. (VII.28) and (VII.30).

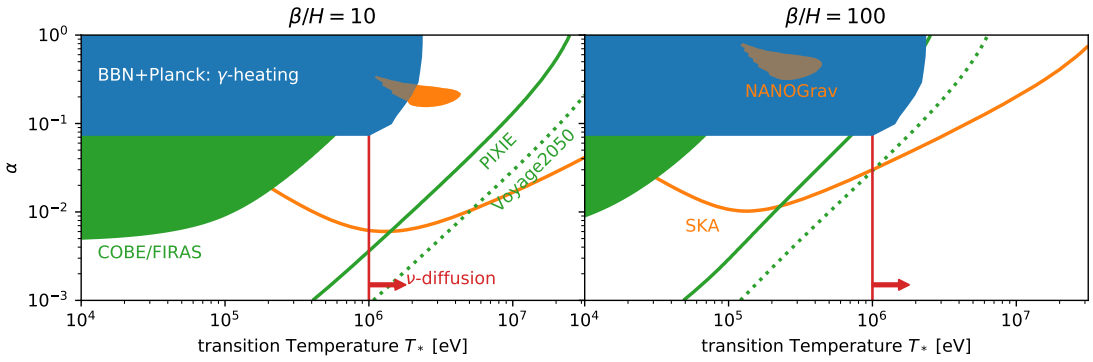

Figure VII.13: Current and future constraints on a first order phase transition at temperature T_* releasing a relative energy α into the SM-plasma. For temperatures below $\approx 2\,\mathrm{MeV}$ the released energy α leads to tensions in BBN and CMB measurements of the baryon to photon ratio (blue). The sound waves caused by the phase transition source GWs that can explain the NANOGrav hint (orange, filled) and in the future can be detected over a wide range of parameter space (orange line). The green area and lines show the current and future sensitivity to spectral distortions caused by the sound waves. At temperatures above $\approx 1\,\mathrm{MeV}$ the sound waves and therefore spectral distortions are expected to be reduced due to damping by neutrino diffusion. Figure created by W.Ratzinger

VII.6.4 Comment on Directly Coupled Sectors

Clearly, one can obtain stronger bounds from spectral distortions if there are additional interactions between the new physics sector and the SM plasma besides gravity. In this sense, the bounds presented above can be interpreted as lower limits since gravity is always present. Studies of such scenarios will need to make specific assumptions about the nature of the coupling and can therefore not be carried out in a model-independent way as we did in Sec. (VII.3 and Section VII.4), but case by case as was done e.g. for cosmic strings [524, 525].

In light of the recent findings by PTAs, we here want to briefly comment on the case in which a phase transition directly causes sound waves in the SM plasma and subsequently emits GWs. From the previous section, we saw that GWs from PTs in decoupled sectors can not explain the NANOGrav data due to the N_{eff} bound. If the energy released in the PT is instead directly deposited into SM degrees of freedom, the N_{eff} constraint does not apply. One can therefore consider the case where the PT sources sound waves in the SM plasma directly, which then produce the GWs.

Since the walls now directly source the acoustic energy in the baryon-photon fluid, we no longer rely on the gravitational coupling. Instead the acoustic energy spectrum can be constructed from the total acoustic energy given in [85] and assuming a white noise spectrum

$$\epsilon_{\mathrm{ac}}(k) = \frac{\kappa(\alpha)\alpha}{1+\alpha}\sqrt{\frac{2}{\pi}}\frac{k^3}{k_*^3}\exp\left(-\frac{k^2}{2k_*^2}\right), \tag{VII.47}$$

[11] The dark sector, if it is thermal, must not have the same temperature as the SM plasma. If it posses one relativistic degree of freedom its temperature is necessarily smaller. See [118, 119] for further details.

[12] In figure VII.3 we show the effect of varying the sound velocity and find that the suppression in the amount of acoustic energy is small as long as the changes don't exceed $\approx k_*/(a_*H_*) \approx \beta/H_*$. It has been found though that even small changes in both the sound velocity and the wall velocity can have an significant impact on the efficiency factor κ, entering both the GW and acoustic energy estimate. [85]

with $k_* = a_*\beta/\sqrt{3}$. To estimate the GW signal strength, we use the formulas from the previous section, setting $\Omega_d \to 1$ and replacing $\alpha_d \to \alpha$. With these changes we arrive back at the expression for the case where there is only one fluid present [179].[13]

The results are shown in Fig. (VII.13). An energy injection around or after BBN at $T \approx 1$ MeV leads to a possible tension between the baryon to photon ratio obtained from BBN and CMB measurements. The resulting current bound on α and its temperature dependence has been investigated in [436], and we show it in blue. As can be seen, this bound already excludes a decent chunk of the 2σ-region of the NANOGrav fit (orange, filled). However we find that the remaining region can be probed by future distortion experiments, provided that our above estimate holds. Furthermore we obtain a significant overlap of the parameter space testable by SKA and spectral distortions.

The previously mentioned conclusions come, however, with the following caveat: At the beginning of BBN around $T \approx 1$ MeV, the neutrinos decoupled from the rest of the SM plasma. Similar to the decoupling of photons, one has to expect that all perturbations on sub-horizon scales might be significantly damped due to the diffusion of neutrinos. We anticipate that this effect would reduce the reach of distortion searches for PT temperatures above 1 MeV. The previously mentioned effect covers a significant region of the viable parameter space shown by the red line in Fig. (VII.13). For transition temperatures close to 1 MeV, in that region, a reduction of the GW amplitude is plausible as well as their emission and the damping by ν-diffusion are taking place simultaneously. We leave a detailed study of these effects to future work.

VII.7 Conclusion

Spectral distortions caused by gravitationally induced acoustic waves in the baryon-photon fluid provide a powerful probe of new physics. We showed that the induction of the acoustic waves via the gravitational coupling and the subsequent damping due to diffusion can be separated. Since the latter is completely determined by SM physics, the μ-distortions can be calculated solely from the amplitude or equivalently the energy of the waves (Eq. (VII.12)).

We here for the first time presented a general, analytic estimate of this acoustic energy caused by a purely gravitationally coupled sector (Eqs. (VII.28) and (VII.30)). This estimate only relies on a few parameters describing the dynamics of the dark sector. The most important amongst them are the amount of energy constituted by the dark sector, the amplitude of its energy fluctuations as well as the ratio between the typical length scale of the fluctuations and the horizon when the fluctuations are generated. While we restricted ourselves to studying sectors with relativistic dynamics, we expect that the results from Sec. (VII.4) can be generalized to non-relativistic dynamics easily.

We continued by studying a particularly easy model consisting of two scalars in all detail. Solving for the dynamics in the dark sector using a lattice simulation and afterwards calculating the acoustic waves numerically allowed us to get the acoustic energy from first principles. We compared the result obtained in this way to our analytic estimate and found agreement to within $\mathcal{O}(1)$ factors, in the peak region even to within 20%.

Finally our analytic estimate allowed us to evaluate the spectral distortion signal for several dark sector scenarios. We were able to demonstrate that dark sectors with energy fluctuations present at temperatures between $\approx 10 - 10^6$ eV are either already constrained

[13] For transition temperatures below ≈ 1 MeV the neutrinos are decoupled and there are technically two sectors. Since the energy in the baryon-photon fluid is still $\Omega_\gamma \approx 1$, we make this simplifying assumption.

by the non-observation of spectral distortions or can be probed in the future. These regions of parameter space are not constrained by other probes relying only on gravitational coupling like $N_{\rm eff}$, CMB fluctuations and GWs. A particular interesting opportunity lies in the possible interplay with GW observations by PTAs. Here spectral distortions might be key in lifting observational degeneracies on the parameter space of various models.

VII.8 Appendix

VII.8.1 Numerics of Fluctuation Dynamics

To find the μ-distortion and/or acoustic energy $\epsilon_{\rm ac}^{\rm lim}$ we solve Eqs. (VII.3) to (VII.6) numerically, supplemented with the free streaming neutrinos. To describe the neutrinos we have to go past the first three moments of the phase-space distribution δ, v and σ. We adopt the conventions used in [526] and write density fluctuations as deviations in temperature $\Theta(\mathbf{x}, \hat{\mathbf{p}}, \tau) = \frac{\delta T}{T}(\mathbf{x}, \hat{\mathbf{p}}, \tau)$. After Fourier transforming $\mathbf{x} \to \mathbf{k}$ the momenta of the distribution are defined as

$$\theta_l = i^l \int_{-1}^{1} \frac{d\eta}{2} P_l(\eta)\theta(\eta)\,, \tag{VII.48}$$

where P_l is the lth Legendre polynomial and $\eta = \hat{\mathbf{k}} \cdot \hat{\mathbf{p}}$. The first three moments can be related via $\delta = 4\theta_0$, $v = 3\theta_1$ and $\sigma = 2\theta_2$ to the definitions used in the main text. For free streaming neutrinos the dynamics of $\Theta_n(\mathbf{x}, \hat{\mathbf{p}}, \tau)$ are described by the Boltzmann equation without a scattering term, which in the expansion introduced above becomes [468, 526]

$$\dot{\theta}_{n,0} + k\theta_{n,1} = -\dot{\phi} \tag{VII.49}$$

$$\dot{\theta}_{n,1} - k\left(\frac{1}{3}\theta_{n,0} - \frac{2}{3}\theta_{n,2}\right) = \frac{k}{3}\psi \tag{VII.50}$$

$$\dot{\theta}_{n,l} - k\left(\frac{l}{2l+1}\theta_{n,l-1} - \frac{l+1}{2l+1}\theta_{n,l+1}\right) = 0\,; \qquad l \geq 2\,. \tag{VII.51}$$

We truncate this hierarchy by neglecting moments $l > l_{\rm max} = 4$ and follow [468] to close the system of equations using

$$\theta_{n,l_{\rm max}+1} = \frac{2l_{\rm max}+1}{k\tau}\theta_{n,l_{\rm max}} - \theta_{n,l_{\rm max}-1}\,. \tag{VII.52}$$

As initial conditions we consider the gravitational potentials as well as all the fluctuations in the SM sector to be zero and supply the fluctuations of the dark sector either as an analytic Ansatz or as an interpolation of the values we get from the lattice simulation. To calculate $\epsilon_{\rm ac}^{\rm lim}$ we set $\dot{\tau}_C^{-1} = 0$ to decouple the generation of the acoustic energy completely from the damping. When calculating the μ-distortion directly without the separation approximation derived in Section VII.3, one needs to include $\dot{\tau}_C$ when solving the differential equations and calculate the time integral in Eq. (VII.12) numerically using the solutions.

VII.8.2 Free Scalar Field

Below we calculate the energy fluctuations and their autocorrelation functions for a single relativistic scalar field ϕ with Gaussian fluctuations

$$\mathcal{P}_\phi(k) = A_\phi \sqrt{\frac{2}{\pi}} \frac{k^3}{\tilde{k}_*^3} \exp\left(-\frac{k^2}{2\tilde{k}_*^2}\right), \tag{VII.53}$$

where $1/\tilde{k}_*$ is the characteristic length scale of fluctuations in the field as opposed to the energy density. We assume that the modes of the field are virialized such that $\mathcal{P}_{\dot{\phi}}(k) = \omega_k^2 \mathcal{P}_\phi(k)$, where $\omega_k^2 = k^2 + m^2$ is the frequency of the respective mode. For a free scalar field the mode functions follow the equation of motion of an unperturbed harmonic oscillator, which is why the autocorrelation of both ϕ and $\dot{\phi}$ is given as $\cos(\omega_k t)$, while the cross-correlation is given as

$$\langle \phi(\mathbf{k}, t) \dot{\phi}^*(\mathbf{k}', t') \rangle = \frac{2\pi^2}{k^3} \mathcal{P}_\phi(k)\, \omega_k \sin\left(\omega_k (t - t')\right)\, (2\pi)^3 \delta^{(3)}(\mathbf{k} - \mathbf{k}')\,. \tag{VII.54}$$

Energy Fluctuations

The energy density of the field is

$$\rho_\phi = \frac{1}{2}\left(\dot{\phi}^2 + \nabla\phi^2 + m^2\phi^2\right) \tag{VII.55}$$

and its Fourier coefficients are given as

$$\rho_\phi(\mathbf{k}) = \frac{1}{2}\int \frac{d^3p}{(2\pi)^3}\, \dot{\phi}(\mathbf{p})\dot{\phi}(\mathbf{k}-\mathbf{p}) + \left[m^2 - \mathbf{p}\cdot(\mathbf{k}-\mathbf{p})\right] \phi(\mathbf{p})\phi(\mathbf{k}-\mathbf{p})\,. \tag{VII.56}$$

The mean energy density can be calculated as

$$\overline{\rho}_\phi = \frac{1}{V}\langle \rho_\phi(\mathbf{k}=0)\rangle = \begin{cases} 3A_\phi \tilde{k}_*^2 & \omega_k \approx k \\ A_\phi m^2 & \omega_k \approx m \end{cases} \tag{VII.57}$$

for the relativistic and non-relativistic case, respectively, and V denotes the volume one is averaging over. When calculating the correlation of energy fluctuations $\langle \rho_\phi(\mathbf{k}) \rho_\phi^*(\mathbf{k}')\rangle$ we encounter the following kinds of correlators between Gaussian variables:

$$\langle \phi(\mathbf{p})\phi(\mathbf{k}-\mathbf{p})\phi^*(\mathbf{p}')\phi^*(\mathbf{k}'-\mathbf{p}')\rangle \tag{VII.58}$$

$$= \langle \phi(\mathbf{p})\phi^*(\mathbf{p}')\rangle\langle \phi(\mathbf{k}-\mathbf{p})\phi^*(\mathbf{k}'-\mathbf{p}')\rangle + \langle \phi(\mathbf{p})\phi^*(\mathbf{k}'-\mathbf{p}')\rangle\langle \phi(\mathbf{k}-\mathbf{p})\phi^*(\mathbf{p}')\rangle \tag{VII.59}$$

$$= (2\pi)^3\delta^3(\mathbf{k}-\mathbf{k}')\left[(2\pi)^3\delta^3(\mathbf{p}-\mathbf{p}') + (2\pi)^3\delta^3(\mathbf{p}-(\mathbf{k}'-\mathbf{p}'))\right] \frac{2\pi^2}{p^3}\mathcal{P}_\phi(\mathbf{p}) \frac{2\pi^2}{|\mathbf{k}-\mathbf{p}|^3}\mathcal{P}_\phi(\mathbf{k}-\mathbf{p})\,, \tag{VII.60}$$

where we assumed $\mathbf{k} \neq 0$ and therefore $\langle \phi(\mathbf{p})\phi(\mathbf{k}-\mathbf{p})\rangle = 0$. Putting it all together we arrive at

$$\begin{aligned} \mathcal{P}_{\rho_\phi}(k, t, t+\Delta t) = \frac{k^3}{2\pi^2}\frac{1}{2}\int \frac{d^3p}{(2\pi)^3}\frac{2\pi^2}{p^3}\mathcal{P}_\phi(p)\frac{2\pi^2}{|\mathbf{k}-\mathbf{p}|^3}\mathcal{P}_\phi(k-p)\cdot \\ \Big[\left(\omega_p^2\omega_{k-p}^2 + (m^2 - \mathbf{p}\cdot(\mathbf{k}-\mathbf{p}))^2\right)\cos(\omega_p\Delta t)\cos(\omega_{k-p}\Delta t) + \\ 2\omega_p\omega_{k-p}(m^2 - \mathbf{p}\cdot(\mathbf{k}-\mathbf{p}))\sin(\omega_p\Delta t)\sin(\omega_{k-p}\Delta t)\Big]. \end{aligned} \tag{VII.61}$$

We can further evaluate this expression for $k \ll \tilde{k}^*$. In this case we approximate $\mathbf{p} = \mathbf{p} - \mathbf{k}$ except when evaluating ω_p and ω_{k-p} in the sine and cosine, since we want to keep track of the time evolution. The p-integral is dominated by modes with $p \approx \tilde{k}^*$ and we therefore approximate

$$\Delta\omega = \omega_p - \omega_{k-p} \approx \begin{cases} \mathbf{k}\cdot\mathbf{p}/|\mathbf{p}| & \omega_{\tilde{k}_*} \approx \tilde{k}_* \\ \mathbf{k}\cdot\mathbf{p}/m & \omega_{\tilde{k}_*} \approx m\,. \end{cases} \tag{VII.62}$$

We then find by using trigonometric identities

$$\mathcal{P}_{\rho_\phi}(k,t,t+\Delta t) \approx \frac{k^3}{2\pi^2}\int_0^\infty d\log p\ \frac{2\pi^2}{p^3}\mathcal{P}_\phi^2(p)\,\omega_p^4\int_{S^2}\frac{d\Omega_p}{4\pi}\cos(\Delta\omega\Delta t)\,. \tag{VII.63}$$

The last integral in this expression is the autocorrelation function of the energy fluctuations. In the relativistic case it does not depend on $|\mathbf{p}|$, while in the non-relativistic we can approximate $|\mathbf{p}| \approx \tilde{k}_*$ and introduce the typical velocity of energy transport in the dark sector as $c_d = \tilde{k}_*/m$ to find

$$\mathcal{A}_{\delta_\phi}(k,\Delta t) = \begin{cases}\mathrm{sinc}(kt) & \omega_{\tilde{k}_*} \approx \tilde{k}_* \\ \mathrm{sinc}(c_d k t) & \omega_{\tilde{k}_*} \approx m\,.\end{cases} \tag{VII.64}$$

We argued in the main text that the only relevant time scale for the autocorrelation of the energy density is c_d/k, with c_d the typical velocity of energy transport. Here we showed this explicitly.

Shear

The space-space part of the energy momentum tensor of a scalar field is given by

$$T_{ij} \approx \nabla_i\phi\nabla_j\phi\,, \tag{VII.65}$$

where we neglected contributions proportional to g_{ij} that exclusively contribute to the trace. We find the shear by going to Fourier space and projecting out the longitudinal traceless component

$$\sigma_\phi(\mathbf{k}) = \frac{1}{\overline{\rho}_\phi+\overline{p}_\phi}\left[\frac{1}{k^2}k_iT_{ij}(\mathbf{k})k_j - \frac{1}{3}T_{ii}(\mathbf{k})\right]. \tag{VII.66}$$

From there the steps are the same as for the energy density and we arrive at

$$\mathcal{P}_{\sigma_\phi}(k,t,t+\Delta t) = \frac{1}{(\overline{\rho}_\phi+\overline{p}_\phi)^2}\frac{k^3}{2\pi^2}2\int\frac{d^3p}{(2\pi)^3}\frac{2\pi^2}{p^3}\mathcal{P}_\phi(p)\frac{2\pi^2}{|\mathbf{k}-\mathbf{p}|^3}\mathcal{P}_\phi(k-p)\cdot \tag{VII.67}$$
$$\left[\left(\hat{\mathbf{k}}\mathbf{p}\right)\left(\hat{\mathbf{k}}(\mathbf{p}-\mathbf{k})\right) - \frac{1}{3}\mathbf{p}(\mathbf{p}-\mathbf{k})\right]^2\cos(\omega_p\Delta t)\cos(\omega_{k-p}\Delta t)\,.$$

When we expand the cosines again for $k \ll \tilde{k}_*$, we find

$$\cos(\omega_p\Delta t)\cos(\omega_{k-p}\Delta t) = \frac{1}{2}\left(\cos\left(2\omega_{\tilde{k}_*}t\right) + \cos(\Delta\omega t)\right)\,. \tag{VII.68}$$

To arrive at the autocorrelation function one would need to carry out the integration. But we are content here with only showing that for a non-conserved quantity like the shear indeed both time scales $1/\tilde{k}_*$ and $1/k$ enter. This can already be seen from the above expression with the $\cos\left(2\omega_{\tilde{k}_*}t\right)$ term not canceling.

VII.8.3 Simulation of the $\lambda\phi^4$-Theory

Energy Density

When working with a Velocity Verlet (VV) or Runge Kuta type integrator both the fields and their time derivatives or equivalently momenta are given at the same point in time.

This is not the case for a leapfrog integration scheme, but can easily be achieved by introducing a half time step for the momenta, to recover the Velocity Verlet procedure. From these one can calculate the total energy as discussed in e.g. [476]. In principle a generalization to an energy density is straight forward. The only term one has to treat carefully is the gradient energy

$$E_{\text{grad}} = \frac{1}{2}\sum_{\mathbf{x}}\sum_{i=1}^{3}\Delta_i^+\phi\Delta_i^+\phi\,, \tag{VII.69}$$

where $\Delta_i^{\pm}\phi$ denote the components of the forward and backward gradient

$$\Delta_i^{\pm}\phi(\mathbf{x}) = \pm\frac{\phi(\mathbf{x}\pm dx\ \hat{\mathbf{e}}_i)-\phi(\mathbf{x})}{dx}\,, \tag{VII.70}$$

where dx is the spacial lattice spacing and $\hat{\mathbf{e}}_i$ the unit vector in direction i. These reproduce $\nabla_i\phi(\mathbf{x})$ only up to $\mathcal{O}(dx)$ but $\nabla_i\phi(\mathbf{x}\pm dx/2\ \hat{\mathbf{e}}_i)$ to $\mathcal{O}(dx^2)$. We therefore employ the following averaging scheme to get an energy density that is correct up to $\mathcal{O}(dx^2)$

$$\rho_{\text{tot}}(\mathbf{x}) = \frac{1}{2}\sum_{\Phi\in\{\phi,\psi\}}\left[\dot{\Phi}\dot{\Phi}+\frac{1}{2}\sum_{i=1}^{3}(\Delta_i^+\Phi\Delta_i^+\Phi+\Delta_i^-\Phi\Delta_i^-\Phi)\right]+V(\phi,\psi)\,. \tag{VII.71}$$

This scheme has the added benefit of reproducing the energy that is used in `CosmoLattice` when consistently evolving the scale factor or checking energy conservation

$$E_{\text{tot}} = \sum_{\mathbf{x}}\rho_{\text{tot}}(\mathbf{x})\,. \tag{VII.72}$$

The expressions given here and below only hold in a flat space-time but can easily be generalized to expanding backgrounds using the α-time concept of `CosmoLattice` [476, 477].

Shear

The shear is the longitudinal-traceless component of the anisotropic stress. For a scalar field it is given as the outer product of the gradient Eq. (VII.65) and we have to find an averaging scheme again to achieve $\mathcal{O}(dx^2)$ accuracy, since $\nabla_i\phi$ and $\nabla_j\phi$ are positioned on different sites of the lattice for $i\neq j$. In principle a scheme where one averages after taking the product is possible but we choose to go with a scheme using

$$\Delta_i^{\text{sym}}\phi(\mathbf{x}) = \frac{1}{2}\frac{\phi(\mathbf{x}+dx\ \hat{\mathbf{e}}_i)-\phi(\mathbf{x}-dx\ \hat{\mathbf{e}}_i)}{dx}\,, \tag{VII.73}$$

since this is used for the simulation of gravitational waves in `CosmoLattice` and the involved transverse-traceless projections [527]. We then have

$$T_{ij}\approx\sum_{\Phi\in\{\phi,\psi\}}\Delta_i^{\text{sym}}\Phi\Delta_j^{\text{sym}}\Phi\,. \tag{VII.74}$$

After going to Fourier space $T_{ij}(\mathbf{k})$ with $\mathbf{k}=dk\ \mathbf{n}$ with dk the infrared cut-off of the lattice and $\mathbf{n}\in\mathbb{Z}^3$, we apply the following projector to find the shear

$$\tilde{\sigma}(\mathbf{k}) = \frac{1}{\rho}\sum_{i,j=0}^{3}\left(\hat{\mathbf{p}}_i^{\text{sym}}(\mathbf{k})\hat{\mathbf{p}}_j^{\text{sym}}(\mathbf{k})-\frac{1}{3}\delta_{ij}\right)T_{ij}(\mathbf{k})\,, \tag{VII.75}$$

where multiplying by $-i\mathbf{p}_i^{\text{sym}}(\mathbf{k})$ in Fourier space corresponds to applying Δ_i^{sym} in position space

$$\mathbf{p}_i^{\text{sym}}(\mathbf{k}) = \frac{1}{dx}\sin\left(dx\,k_i\right)\,. \tag{VII.76}$$

Part IV

Aftermath

CHAPTER VIII

Summary and Conclusions

In this thesis, our objective has been to explore the following question:

> "To what extent can gravitational waves contribute to our understanding of the particle physics of the very early universe?"

We have tackled this question by investigating various models and scenarios, which are well motivated by the limitations of the Standard Model of particle physics and the ΛCDM model of cosmology. Each part, along with its chapters and contents, is discussed in chronological order.

In Part. (I) of this thesis, we delve into the possibility of an observable SGWB from the confinement FOPT in SU(N_c) pYM dark sector. We considered the dark sector to interact very weakly with the SM and merely through gravitational interactions. Such a scenario is well-motivated and realistic in the context of CDM. Given the strong coupling nature of the theory, we needed techniques capable of addressing such challenges, leading us to resort to the AdS/CFT correspondence. Specifically, we employed the IhQCD model to characterize SU(N_c) pYM theories for $N_c \geq 3$, by initially conducting a fitting procedure with the model to lattice equilibrium thermodynamics.

Subsequently, we constructed both an effective potential and an effective action to facilitate the calculation of the thermal tunneling rate and obtain the relevant parameters for estimating the GW spectra. For the effective potential, we utilized the free energy landscape approach, while for the kinetic term, we initially relied on an ansatz inspired by previous phenomenological studies. Later, we refined this approach through adequate calculations.

The results of these endeavors [5, 6] were remarkable. Initially, we observed an $\mathcal{O}(1)$ agreement with previous work when employing the ansatz from phenomenology. However, upon performing a more comprehensive calculation, we discovered a suppression of roughly three orders of magnitude in the peak amplitude of the GW spectra in SU(3) YM theory. Finally we emphasize that these theories possess a finite amount of supercooling through their holographic construction. This also provides the conclusion that there may be an universal upper bound on the GW spectra emitted from these theories.

In Part. (II) of this thesis, the objective was to investigate the detectability of different configurations and initial conditions for the QCD axion, either through GWs or via its gravitational clumping of substructures. In Chap. (IV), we examined the effects of the KM mechanism on axion mini clusters and minihalos to identify potential distinctive features from the standard scenario.

Our findings revealed that in the KM scenario, the mass range of AMCs is broader compared to the standard case, as the axion starts oscillating later than in the conventional

scenario. This leads to the primary conclusion that in the KM scenario, AMCs are heavier, and the clumping of such AMCs could result in halos that are orders of magnitude heavier. This, in turn, would directly impact microlensing events arising from minicluster halos.

We investigated a recent microlensing event observed by the Hyper Suprime-Cam (HSC) to assess whether an AMC formed in the KM regime could account for the event. While axion stars formed in the standard case could only be explained by the lightest viable QCD axion, we discovered that although AMCs in the KM regime are significantly heavier, the mass dependence from axion stars to AMCs is too weak to viably describe the event.

In Chap. (V), we delved into an investigation to determine whether the GW signal from a network of QCD axion strings, subjected to modified cosmological histories, could potentially explain the then-current data from the NANOGrav 12.5-year dataset. Despite exhibiting a GW signal of sufficient strength within the PTA band to reconcile with the data, this exploration also provides valuable insights into the nature of the CDM candidate and sheds light on the reheating phase of the universe.
Part. (III) of this thesis was devoted to understanding if new physics sources like metastable topological defects from approximate global U(1) symmetries could generate GWs large enough to explain the recent PTA datasets without being ruled out by other cosmological constraints. Furthermore we also explored the possibility of a new type of constraints stemming from μ-distortions due to damping of acoustic sound waves in the photon baryon fluid. From Chap. (VI) we find that alp strings are most likely ruled out by constraints stemming from ΔN_{eff} and that the PTA data may serve as an independent constraint on meta-stable global strings.
However we also find that DWs have regions of viable parameter space both in the cases where the excess energy density is hidden in dark radiation or if there are decays into the SM plasma present. For the case in which the energy density of DWs are within a Dark Sector μ-distortions will prove to be a strong constraint and may alleviate the underlying nature of the PTA source in this case. For the case in which the DWs are connected to QCD through a clockwork mechanism, the ALPs in this framework may be searched for with future colliders primarily through ALP decays into gluons.
In Chap. (VII) we found that μ-distortions through the damping of dark sector density fluctuations into the photon baryon fluid from only gravitational interactions is a far stronger probe for new physics than what was presented in [442] by making use of GWs. As also found and emphasized in [442] that μ-distortions allows us to bridge the gap between existing constraints from CMB and PTAs. The great complementarity between sources emitting μ-distortions thorugh DS density fluctuations and gravitational waves allows for a present multimessenger probe of GWs in the PTA range.
In the following paragraphs, I present my overarching conclusions drawn from this thesis. This work has explored the possibility of utilizing different sources of GWs to understand the particle physics of the early universe, yielding many exciting findings. These are indeed thrilling times, with PTA and LVK collaborations already collecting data, where a potential source of a SGWB may be identified in the coming years. Furthermore, the construction of LISA and ET will allow us to probe the physics of the early universe and improve our understanding of the dynamical evolution of binary mergers.

With these significant ongoing and future experimental endeavors in mind, my final conclusion is that theoretical predictions and frameworks for consistent and accurate predictions are now more timely than ever. The necessity for tools beyond perturbation theory, especially in the context of strongly coupled theories and dynamics involving non-perturbative phenomena, is essential for our community to progress. Part 1 of this thesis represents an attempt in this direction. Part II-III of this thesis allure the possibility that

we may already have seen or will see signals of new physics in the coming years from PTAs or through μ-distortions.

Acknowledgements

All names and personal references were removed from the acknowledgements in the electronic publication of this dissertation

I sincerely thank you all who have aided me along this bumpy road these past couple of years. First, I would like to express gratitude to my supervisor who offered me the opportunity to work on exciting topics with a constant effort to maintain an office atmosphere filled with inspiration and humbleness. His patience and support towards me as a scientist and friend over the years when confronted with my frequent mistakes and misunderstandings. Furthermore, his ability to listen to my "wild" ideas with patience and humbleness, and offer his advice to me as a scientist and as a friend. Meanwhile writing this made me also realize he had to endure my bull-headedness, for instance at Blockwerk for trying to get me to take on his advice on bouldering routes. Jeez, he has had to endure quite a bit for having me as his student. A special thanks to my academic references for their great efforts alongside my advisor in endorsing me for future employment. They have been pivotal in my ongoing progress of conducting physics through numerous discussions about physics, life, and everything in between. I am excited to see what the future physics and life output of these collaborations will generate in the future.

I would also like to express my gratitude towards my second advisor and committee members for taking the time to evaluate my thesis. Given my time here in Mainz over the past years, I have had the great fortune to have worked with a great set of collaborators with whom my research would not been where it is today without them. The discussions always led to new insights and were a stimulating environment for developing new ideas either in physics and also outside the realms of physics. My gratitude goes towards my past and present group members, office mates, and the whole THEP department for contributing to a great environment both within the actual working hours and beyond them with coffee break discussions, evening parties, and whisky tastings. I want to express my gratitude towards the administration department for handling my lacking-sense of documents the correct way and being accessible even on short notice at times. I also want to thank the Mainz Physics Academy graduate school for their nice retreats, financial support, and soft skill training courses.

Last but certainly not least I am very grateful to my family, friends, and loved ones for keeping me sane at times. May it be during the pandemic periods with online evening chats, corona walks, skateboarding sessions, or just being there to listen at times. My family, I am very fortunate for all the love and support you have provided me with throughout my life. Your unconditional belief in me that I would find my way in life as a person I cherish endlessly. Your constant interest in what's up in the world of physics while trying to reduce intricate concepts to a common tongue has been a fun challenge over the years.

List of Figures

Chapter IV

Chapter V

Chapter VI

Chapter VII

List of Tables

Chapter VII

Bibliography

[1] N. Ramberg and L. Visinelli, *QCD axion and gravitational waves in light of NANOGrav results*, *Phys. Rev. D* **103** (2021) 063031 [2012.06882].

[2] N. Ramberg and L. Visinelli, *Probing the Early Universe with Axion Physics and Gravitational Waves*, *Phys. Rev. D* **99** (2019) 123513 [1904.05707].

[3] B. Barman, N. Bernal, N. Ramberg and L. Visinelli, *QCD Axion Kinetic Misalignment without Prejudice*, *Universe* **8** (2022) 634 [2111.03677].

[4] N. Ramberg, W. Ratzinger and P. Schwaller, *One μ to rule them all: CMB spectral distortions can probe domain walls, cosmic strings and low scale phase transitions*, *JCAP* **02** (2023) 039 [2209.14313].

[5] E. Morgante, N. Ramberg and P. Schwaller, *Gravitational waves from dark SU(3) Yang-Mills theory*, *Phys. Rev. D* **107** (2023) 036010 [2210.11821].

[6] N. R. Enrico Morgante and P. Schwaller, *The Dark Kaleidioscope: Holograms & Gravitational Waves from the dark*. In Preparation, 2024.

[7] E. Madge, E. Morgante, C. Puchades-Ibáñez, N. Ramberg, W. Ratzinger, S. Schenk et al., *Primordial gravitational waves in the nano-Hertz regime and PTA data — towards solving the GW inverse problem*, *JHEP* **10** (2023) 171 [2306.14856].

[8] S. L. Glashow, J. Iliopoulos and L. Maiani, *Weak Interactions with Lepton-Hadron Symmetry*, *Phys. Rev. D* **2** (1970) 1285.

[9] S. Weinberg, *A Model of Leptons*, *Phys. Rev. Lett.* **19** (1967) 1264.

[10] A. Salam, *Weak and Electromagnetic Interactions*, *Conf. Proc. C* **680519** (1968) 367.

[11] G. 't Hooft and M. J. G. Veltman, *Regularization and Renormalization of Gauge Fields*, *Nucl. Phys. B* **44** (1972) 189.

[12] D. J. Gross and F. Wilczek, *Ultraviolet Behavior of Nonabelian Gauge Theories*, *Phys. Rev. Lett.* **30** (1973) 1343.

[13] H. D. Politzer, *Reliable Perturbative Results for Strong Interactions?*, *Phys. Rev. Lett.* **30** (1973) 1346.

[14] H. Fritzsch, M. Gell-Mann and H. Leutwyler, *Advantages of the Color Octet Gluon Picture*, *Phys. Lett. B* **47** (1973) 365.

[15] G. Zweig, *An SU(3) model for strong interaction symmetry and its breaking. Version 1*, .

[16] M. Gell-Mann, *A Schematic Model of Baryons and Mesons*, *Phys. Lett.* **8** (1964) 214.

[17] C.-N. Yang and R. L. Mills, *Conservation of Isotopic Spin and Isotopic Gauge Invariance*, *Phys. Rev.* **96** (1954) 191.

[18] A. Riotto, *Particle cosmology*, tech. rep., CERN, 2010.

[19] Supernova Search Team collaboration, *Observational evidence from supernovae for an accelerating universe and a cosmological constant*, *Astron. J.* **116** (1998) 1009 [astro-ph/9805201].
[20] SDSS collaboration, *Cosmological parameters from SDSS and WMAP*, *Phys. Rev. D* **69** (2004) 103501 [astro-ph/0310723].
[21] Planck collaboration, *Planck 2018 results. VI. Cosmological parameters*, *Astron. Astrophys.* **641** (2020) A6 [1807.06209].
[22] Planck collaboration, *Planck 2018 results. X. Constraints on inflation*, *Astron. Astrophys.* **641** (2020) A10 [1807.06211].
[23] A. G. Riess et al., *A 2.4% Determination of the Local Value of the Hubble Constant*, *Astrophys. J.* **826** (2016) 56 [1604.01424].
[24] E. Di Valentino, O. Mena, S. Pan, L. Visinelli, W. Yang, A. Melchiorri et al., *In the realm of the Hubble tension—a review of solutions*, *Class. Quant. Grav.* **38** (2021) 153001 [2103.01183].
[25] A. E. Nelson, *Naturally Weak CP Violation*, *Phys. Lett. B* **136** (1984) 387.
[26] S. M. Barr, *A Natural Class of Nonpeccei-quinn Models*, *Phys. Rev. D* **30** (1984) 1805.
[27] R. D. Peccei and H. R. Quinn, *CP Conservation in the Presence of Instantons*, *Phys. Rev. Lett.* **38** (1977) 1440.
[28] R. D. Peccei and H. R. Quinn, *Constraints Imposed by CP Conservation in the Presence of Instantons*, *Phys. Rev. D* **16** (1977) 1791.
[29] E. Berkowitz, M. I. Buchoff and E. Rinaldi, *Lattice QCD input for axion cosmology*, *Phys. Rev. D* **92** (2015) 034507 [1505.07455].
[30] S. Borsanyi, M. Dierigl, Z. Fodor, S. D. Katz, S. W. Mages, D. Nogradi et al., *Axion cosmology, lattice QCD and the dilute instanton gas*, *Phys. Lett. B* **752** (2016) 175 [1508.06917].
[31] C. Bonati, M. D'Elia, M. Mariti, G. Martinelli, M. Mesiti, F. Negro et al., *Axion phenomenology and θ-dependence from $N_f = 2 + 1$ lattice QCD*, *JHEP* **03** (2016) 155 [1512.06746].
[32] P. Petreczky, H.-P. Schadler and S. Sharma, *The topological susceptibility in finite temperature QCD and axion cosmology*, *Phys. Lett. B* **762** (2016) 498 [1606.03145].
[33] S. Borsanyi et al., *Calculation of the axion mass based on high-temperature lattice quantum chromodynamics*, *Nature* **539** (2016) 69 [1606.07494].
[34] F. Burger, E.-M. Ilgenfritz, M. P. Lombardo and A. Trunin, *Chiral observables and topology in hot QCD with two families of quarks*, *Phys. Rev. D* **98** (2018) 094501 [1805.06001].
[35] C. Bonati, M. D'Elia, G. Martinelli, F. Negro, F. Sanfilippo and A. Todaro, *Topology in full QCD at high temperature: a multicanonical approach*, *JHEP* **11** (2018) 170 [1807.07954].
[36] S. Bottaro and E. Meggiolaro, *QCD axion and topological susceptibility in chiral effective Lagrangian models at finite temperature*, *Phys. Rev. D* **102** (2020) 014048 [2004.11901].
[37] M. P. Lombardo and A. Trunin, *Topology and axions in QCD*, *Int. J. Mod. Phys. A* **35** (2020) 2030010 [2005.06547].
[38] D. J. E. Marsh, *Axion Cosmology*, *Phys. Rept.* **643** (2016) 1 [1510.07633].
[39] R. L. Davis, *Cosmic Axions from Cosmic Strings*, *Phys. Lett. B* **180** (1986) 225.
[40] V. B. Klaer and G. D. Moore, *The dark-matter axion mass*, *JCAP* **11** (2017) 049 [1708.07521].

[41] M. Gorghetto, E. Hardy and G. Villadoro, *Axions from Strings: the Attractive Solution*, *JHEP* **07** (2018) 151 [1806.04677].
[42] M. Kawasaki, T. Sekiguchi, M. Yamaguchi and J. Yokoyama, *Long-term dynamics of cosmological axion strings*, *PTEP* **2018** (2018) 091E01 [1806.05566].
[43] A. Vaquero, J. Redondo and J. Stadler, *Early seeds of axion miniclusters*, *JCAP* **04** (2019) 012 [1809.09241].
[44] M. Buschmann, J. W. Foster and B. R. Safdi, *Early-Universe Simulations of the Cosmological Axion*, *Phys. Rev. Lett.* **124** (2020) 161103 [1906.00967].
[45] M. Gorghetto, E. Hardy and G. Villadoro, *More axions from strings*, *SciPost Phys.* **10** (2021) 050 [2007.04990].
[46] M. S. Turner, *Coherent Scalar Field Oscillations in an Expanding Universe*, *Phys. Rev. D* **28** (1983) 1243.
[47] S. Weinberg, *A New Light Boson?*, *Phys. Rev. Lett.* **40** (1978) 223.
[48] M. Drees, F. Hajkarim and E. R. Schmitz, *The Effects of QCD Equation of State on the Relic Density of WIMP Dark Matter*, *JCAP* **06** (2015) 025 [1503.03513].
[49] L. Visinelli and P. Gondolo, *Axion cold dark matter in non-standard cosmologies*, *Phys. Rev. D* **81** (2010) 063508 [0912.0015].
[50] G. G. Raffelt, *Astrophysical axion bounds*, *Lect. Notes Phys.* **741** (2008) 51 [hep-ph/0611350].
[51] R. T. Co, L. J. Hall, K. Harigaya, K. A. Olive and S. Verner, *Axion Kinetic Misalignment and Parametric Resonance from Inflation*, *JCAP* **08** (2020) 036 [2004.00629].
[52] LIGO Scientific, Virgo collaboration, *Observation of Gravitational Waves from a Binary Black Hole Merger*, *Phys. Rev. Lett.* **116** (2016) 061102 [1602.03837].
[53] LIGO Scientific collaboration, *Exploring the Sensitivity of Next Generation Gravitational Wave Detectors*, *Class. Quant. Grav.* **34** (2017) 044001 [1607.08697].
[54] A. Dirkes, *Gravitational waves — A review on the theoretical foundations of gravitational radiation*, *Int. J. Mod. Phys. A* **33** (2018) 1830013 [1802.05958].
[55] M. Punturo et al., *The Einstein Telescope: A third-generation gravitational wave observatory*, *Class. Quant. Grav.* **27** (2010) 194002.
[56] TianQin collaboration, *TianQin: a space-borne gravitational wave detector*, *Class. Quant. Grav.* **33** (2016) 035010 [1512.02076].
[57] LISA collaboration, *Laser Interferometer Space Antenna*, 1702.00786.
[58] L. Badurina, O. Buchmueller, J. Ellis, M. Lewicki, C. McCabe and V. Vaskonen, *Prospective sensitivities of atom interferometers to gravitational waves and ultralight dark matter*, *Phil. Trans. A. Math. Phys. Eng. Sci.* **380** (2021) 20210060 [2108.02468].
[59] A. Sesana et al., *Unveiling the gravitational universe at μ-Hz frequencies*, *Exper. Astron.* **51** (2021) 1333 [1908.11391].
[60] EPTA, InPTA: collaboration, *The second data release from the European Pulsar Timing Array - III. Search for gravitational wave signals*, *Astron. Astrophys.* **678** (2023) A50 [2306.16214].
[61] G. Janssen et al., *Gravitational wave astronomy with the SKA*, *PoS* **AASKA14** (2015) 037 [1501.00127].
[62] NANOGrav collaboration, *The NANOGrav 12.5 yr Data Set: Search for an Isotropic Stochastic Gravitational-wave Background*, *Astrophys. J. Lett.* **905** (2020) L34 [2009.04496].

[63] L. Giombi and M. Hindmarsh, *General relativistic bubble growth in cosmological phase transitions*, *JCAP* **03** (2024) 059 [2307.12080].
[64] D. Croon, *TASI lectures on Phase Transitions, Baryogenesis, and Gravitational Waves*, *PoS* **TASI2022** (2024) 003 [2307.00068].
[65] M. B. Hindmarsh, M. Lüben, J. Lumma and M. Pauly, *Phase transitions in the early universe*, *SciPost Phys. Lect. Notes* **24** (2021) 1 [2008.09136].
[66] D. Bodeker and G. D. Moore, *Can electroweak bubble walls run away?*, *JCAP* **05** (2009) 009 [0903.4099].
[67] D. Bodeker and G. D. Moore, *Electroweak Bubble Wall Speed Limit*, *JCAP* **05** (2017) 025 [1703.08215].
[68] T. Konstandin, G. Nardini and I. Rues, *From Boltzmann equations to steady wall velocities*, *JCAP* **09** (2014) 028 [1407.3132].
[69] A. Megevand and A. D. Sanchez, *Velocity of electroweak bubble walls*, *Nucl. Phys. B* **825** (2010) 151 [0908.3663].
[70] S. Höche, J. Kozaczuk, A. J. Long, J. Turner and Y. Wang, *Towards an all-orders calculation of the electroweak bubble wall velocity*, *JCAP* **03** (2021) 009 [2007.10343].
[71] X. Wang, F. P. Huang and X. Zhang, *Bubble wall velocity beyond leading-log approximation in electroweak phase transition*, 2011.12903.
[72] A. Azatov and M. Vanvlasselaer, *Bubble wall velocity: heavy physics effects*, *JCAP* **01** (2021) 058 [2010.02590].
[73] G. C. Dorsch, S. J. Huber and T. Konstandin, *On the wall velocity dependence of electroweak baryogenesis*, *JCAP* **08** (2021) 020 [2106.06547].
[74] Y. Gouttenoire, R. Jinno and F. Sala, *Friction pressure on relativistic bubble walls*, *JHEP* **05** (2022) 004 [2112.07686].
[75] W.-Y. Ai, B. Garbrecht and C. Tamarit, *Bubble wall velocities in local equilibrium*, *JCAP* **03** (2022) 015 [2109.13710].
[76] S. Balaji, M. Spannowsky and C. Tamarit, *Cosmological bubble friction in local equilibrium*, *JCAP* **03** (2021) 051 [2010.08013].
[77] W.-Y. Ai, B. Laurent and J. van de Vis, *Model-independent bubble wall velocities in local thermal equilibrium*, *JCAP* **07** (2023) 002 [2303.10171].
[78] T. Krajewski, M. Lewicki and M. Zych, *Bubble-wall velocity in local thermal equilibrium: hydrodynamical simulations vs analytical treatment*, *JHEP* **05** (2024) 011 [2402.15408].
[79] I. Baldes, Y. Gouttenoire and F. Sala, *String Fragmentation in Supercooled Confinement and Implications for Dark Matter*, *JHEP* **04** (2021) 278 [2007.08440].
[80] F. Bigazzi, A. Caddeo, T. Canneti and A. L. Cotrone, *Bubble wall velocity at strong coupling*, *JHEP* **08** (2021) 090 [2104.12817].
[81] Y. Bea, J. Casalderrey-Solana, T. Giannakopoulos, D. Mateos, M. Sanchez-Garitaonandia and M. Zilhão, *Bubble wall velocity from holography*, *Phys. Rev. D* **104** (2021) L121903 [2104.05708].
[82] Y. Bea, J. Casalderrey-Solana, T. Giannakopoulos, A. Jansen, D. Mateos, M. Sanchez-Garitaonandia et al., *Holographic bubbles with Jecco: expanding, collapsing and critical*, *JHEP* **09** (2022) 008 [2202.10503].
[83] R. A. Janik, M. Jarvinen, H. Soltanpanahi and J. Sonnenschein, *Perfect Fluid Hydrodynamic Picture of Domain Wall Velocities at Strong Coupling*, *Phys. Rev. Lett.* **129** (2022) 081601 [2205.06274].
[84] M. Sanchez-Garitaonandia and J. van de Vis, *Prediction of the bubble wall velocity*

for a large jump in degrees of freedom, 2312.09964.
[85] J. R. Espinosa, T. Konstandin, J. M. No and G. Servant, *Energy Budget of Cosmological First-order Phase Transitions*, *JCAP* **06** (2010) 028 [1004.4187].
[86] I. Baldes, S. Blasi, A. Mariotti, A. Sevrin and K. Turbang, *Baryogenesis via relativistic bubble expansion*, *Phys. Rev. D* **104** (2021) 115029 [2106.15602].
[87] A. Azatov, M. Vanvlasselaer and W. Yin, *Baryogenesis via relativistic bubble walls*, *JHEP* **10** (2021) 043 [2106.14913].
[88] E. Witten, *Cosmic Separation of Phases*, *Phys. Rev. D* **30** (1984) 272.
[89] C. J. Hogan and M. J. Rees, *Axion Miniclusters*, *Phys. Lett. B* **205** (1988) 228.
[90] LISA Cosmology Working Group collaboration, *Gravitational waves from first-order phase transitions in LISA: reconstruction pipeline and physics interpretation*, 2403.03723.
[91] C. Caprini et al., *Detecting gravitational waves from cosmological phase transitions with LISA: an update*, *JCAP* **03** (2020) 024 [1910.13125].
[92] M. Lewicki and V. Vaskonen, *Gravitational waves from bubble collisions and fluid motion in strongly supercooled phase transitions*, *Eur. Phys. J. C* **83** (2023) 109 [2208.11697].
[93] J. M. Maldacena, *The Large N limit of superconformal field theories and supergravity*, *Adv. Theor. Math. Phys.* **2** (1998) 231 [hep-th/9711200].
[94] G. 't Hooft, *Dimensional reduction in quantum gravity*, *Conf. Proc. C* **930308** (1993) 284 [gr-qc/9310026].
[95] L. Susskind, *The World as a hologram*, *J. Math. Phys.* **36** (1995) 6377 [hep-th/9409089].
[96] E. Witten, *Anti-de Sitter space and holography*, *Adv. Theor. Math. Phys.* **2** (1998) 253 [hep-th/9802150].
[97] E. Witten, *Anti-de Sitter space, thermal phase transition, and confinement in gauge theories*, *Adv. Theor. Math. Phys.* **2** (1998) 505 [hep-th/9803131].
[98] S. S. Gubser, I. R. Klebanov and A. M. Polyakov, *Gauge theory correlators from noncritical string theory*, *Phys. Lett. B* **428** (1998) 105 [hep-th/9802109].
[99] J. Polchinski, *Dirichlet Branes and Ramond-Ramond charges*, *Phys. Rev. Lett.* **75** (1995) 4724 [hep-th/9510017].
[100] J. L. Petersen, *Introduction to the Maldacena conjecture on AdS / CFT*, *Int. J. Mod. Phys. A* **14** (1999) 3597 [hep-th/9902131].
[101] M. Krssak, *Energy Momentum Tensor Correlators in Improved Holographic QCD*, Ph.D. thesis, Bielefeld U., 2013.
1310.0222.
[102] F. R. Ares, *First order phase transitions beyond the Standard Model*, Ph.D. thesis, University of Sussex, Sussex U., 2023.
[103] J. M. Bardeen, B. Carter and S. W. Hawking, *The Four laws of black hole mechanics*, *Commun. Math. Phys.* **31** (1973) 161.
[104] S. W. Hawking, *Particle Creation by Black Holes*, *Commun. Math. Phys.* **43** (1975) 199.
[105] G. W. Gibbons and S. W. Hawking, *Cosmological Event Horizons, Thermodynamics, and Particle Creation*, *Phys. Rev. D* **15** (1977) 2738.
[106] S. S. Gubser, I. R. Klebanov and A. A. Tseytlin, *Coupling constant dependence in the thermodynamics of N=4 supersymmetric Yang-Mills theory*, *Nucl. Phys. B* **534** (1998) 202 [hep-th/9805156].
[107] A. Bazavov et al., *Equation of state and QCD transition at finite temperature*, *Phys. Rev. D* **80** (2009) 014504 [0903.4379].

[108] S. Catterall and T. Wiseman, *Black hole thermodynamics from simulations of lattice Yang-Mills theory*, *Phys. Rev. D* **78** (2008) 041502 [0803.4273].
[109] S. Catterall, R. G. Jha, D. Schaich and T. Wiseman, *Testing holography using lattice super-Yang-Mills theory on a 2-torus*, *Phys. Rev. D* **97** (2018) 086020 [1709.07025].
[110] D. T. Son and A. O. Starinets, *Minkowski space correlators in AdS / CFT correspondence: Recipe and applications*, *JHEP* **09** (2002) 042 [hep-th/0205051].
[111] C. P. Herzog and D. T. Son, *Schwinger-Keldysh propagators from AdS/CFT correspondence*, *JHEP* **03** (2003) 046 [hep-th/0212072].
[112] G. Policastro, D. T. Son and A. O. Starinets, *The Shear viscosity of strongly coupled N=4 supersymmetric Yang-Mills plasma*, *Phys. Rev. Lett.* **87** (2001) 081601 [hep-th/0104066].
[113] G. Policastro, D. T. Son and A. O. Starinets, *From AdS / CFT correspondence to hydrodynamics*, *JHEP* **09** (2002) 043 [hep-th/0205052].
[114] D. T. Son and A. O. Starinets, *Viscosity, Black Holes, and Quantum Field Theory*, *Ann. Rev. Nucl. Part. Sci.* **57** (2007) 95 [0704.0240].
[115] P. Kovtun, D. T. Son and A. O. Starinets, *Viscosity in strongly interacting quantum field theories from black hole physics*, *Phys. Rev. Lett.* **94** (2005) 111601 [hep-th/0405231].
[116] K. Yagi and N. Seto, *Detector configuration of DECIGO/BBO and identification of cosmological neutron-star binaries*, *Phys. Rev. D* **83** (2011) 044011 [1101.3940].
[117] P. Schwaller, D. Stolarski and A. Weiler, *Emerging Jets*, *JHEP* **05** (2015) 059 [1502.05409].
[118] M. Breitbach, J. Kopp, E. Madge, T. Opferkuch and P. Schwaller, *Dark, Cold, and Noisy: Constraining Secluded Hidden Sectors with Gravitational Waves*, *JCAP* **07** (2019) 007 [1811.11175].
[119] M. Fairbairn, E. Hardy and A. Wickens, *Hearing without seeing: gravitational waves from hot and cold hidden sectors*, *JHEP* **07** (2019) 044 [1901.11038].
[120] R. Garani, M. Redi and A. Tesi, *Dark QCD matters*, *JHEP* **12** (2021) 139 [2105.03429].
[121] M. Redi, A. Tesi and H. Tillim, *Gravitational Production of a Conformal Dark Sector*, *JHEP* **05** (2021) 010 [2011.10565].
[122] R. Contino, A. Mitridate, A. Podo and M. Redi, *Gluequark Dark Matter*, *JHEP* **02** (2019) 187 [1811.06975].
[123] A. Mitridate, M. Redi, J. Smirnov and A. Strumia, *Dark Matter as a weakly coupled Dark Baryon*, *JHEP* **10** (2017) 210 [1707.05380].
[124] A. Mitridate, M. Redi, J. Smirnov and A. Strumia, *Cosmological Implications of Dark Matter Bound States*, *JCAP* **05** (2017) 006 [1702.01141].
[125] P. Asadi, E. D. Kramer, E. Kuflik, T. R. Slatyer and J. Smirnov, *Glueballs in a thermal squeezeout model*, *JHEP* **07** (2022) 006 [2203.15813].
[126] P. Asadi, E. D. Kramer, E. Kuflik, G. W. Ridgway, T. R. Slatyer and J. Smirnov, *Accidentally Asymmetric Dark Matter*, *Phys. Rev. Lett.* **127** (2021) 211101 [2103.09822].
[127] J. Smirnov and J. F. Beacom, *New Freezeout Mechanism for Strongly Interacting Dark Matter*, *Phys. Rev. Lett.* **125** (2020) 131301 [2002.04038].
[128] V. De Luca, A. Mitridate, M. Redi, J. Smirnov and A. Strumia, *Colored Dark Matter*, *Phys. Rev. D* **97** (2018) 115024 [1801.01135].
[129] D. J. Gross, J. A. Harvey, E. J. Martinec and R. Rohm, *The Heterotic String*,

Phys. Rev. Lett. **54** (1985) 502.
[130] L. J. Dixon, J. A. Harvey, C. Vafa and E. Witten, *Strings on Orbifolds*, *Nucl. Phys. B* **261** (1985) 678.
[131] L. J. Dixon, J. A. Harvey, C. Vafa and E. Witten, *Strings on Orbifolds. 2.*, *Nucl. Phys. B* **274** (1986) 285.
[132] B. S. Acharya, *M theory, Joyce orbifolds and superYang-Mills*, *Adv. Theor. Math. Phys.* **3** (1999) 227 [hep-th/9812205].
[133] J. Halverson and D. R. Morrison, *On gauge enhancement and singular limits in G_2 compactifications of M-theory*, *JHEP* **04** (2016) 100 [1507.05965].
[134] N. Craig, A. Katz, M. Strassler and R. Sundrum, *Naturalness in the Dark at the LHC*, *JHEP* **07** (2015) 105 [1501.05310].
[135] R. Barbieri, D. Greco, R. Rattazzi and A. Wulzer, *The Composite Twin Higgs scenario*, *JHEP* **08** (2015) 161 [1501.07803].
[136] M. Low, A. Tesi and L.-T. Wang, *Twin Higgs mechanism and a composite Higgs boson*, *Phys. Rev. D* **91** (2015) 095012 [1501.07890].
[137] P. Asadi, E. D. Kramer, E. Kuflik, G. W. Ridgway, T. R. Slatyer and J. Smirnov, *Thermal squeezeout of dark matter*, *Phys. Rev. D* **104** (2021) 095013 [2103.09827].
[138] Y. Bai and P. Schwaller, *Scale of dark QCD*, *Phys. Rev. D* **89** (2014) 063522 [1306.4676].
[139] P. Carenza, R. Pasechnik, G. Salinas and Z.-W. Wang, *Glueball Dark Matter Revisited*, *Phys. Rev. Lett.* **129** (2022) 261302 [2207.13716].
[140] P. Baratella, A. Pomarol and F. Rompineve, *The Supercooled Universe*, *JHEP* **03** (2019) 100 [1812.06996].
[141] P. Creminelli, A. Nicolis and R. Rattazzi, *Holography and the electroweak phase transition*, *JHEP* **03** (2002) 051 [hep-th/0107141].
[142] B. von Harling and G. Servant, *QCD-induced Electroweak Phase Transition*, *JHEP* **01** (2018) 159 [1711.11554].
[143] F. Bigazzi, A. Caddeo, A. L. Cotrone and A. Paredes, *Dark Holograms and Gravitational Waves*, *JHEP* **04** (2021) 094 [2011.08757].
[144] F. Bigazzi, A. Caddeo, A. L. Cotrone and A. Paredes, *Fate of false vacua in holographic first-order phase transitions*, *JHEP* **12** (2020) 200 [2008.02579].
[145] STAR collaboration, *Experimental and theoretical challenges in the search for the quark gluon plasma: The STAR Collaboration's critical assessment of the evidence from RHIC collisions*, *Nucl. Phys. A* **757** (2005) 102 [nucl-ex/0501009].
[146] J. Casalderrey-Solana, H. Liu, D. Mateos, K. Rajagopal and U. A. Wiedemann, *Gauge/String Duality, Hot QCD and Heavy Ion Collisions*. Cambridge University Press, 2014, 10.1017/9781009403504, [1101.0618].
[147] U. Gursoy and E. Kiritsis, *Exploring improved holographic theories for QCD: Part I*, *JHEP* **02** (2008) 032 [0707.1324].
[148] U. Gursoy, E. Kiritsis, L. Mazzanti and F. Nitti, *Holography and Thermodynamics of 5D Dilaton-gravity*, *JHEP* **05** (2009) 033 [0812.0792].
[149] U. Gursoy, E. Kiritsis and F. Nitti, *Exploring improved holographic theories for QCD: Part II*, *JHEP* **02** (2008) 019 [0707.1349].
[150] U. Gursoy, E. Kiritsis, L. Mazzanti and F. Nitti, *Improved Holographic Yang-Mills at Finite Temperature: Comparison with Data*, *Nucl. Phys. B* **820** (2009) 148 [0903.2859].
[151] S. W. Hawking and D. N. Page, *Thermodynamics of Black Holes in anti-De Sitter*

Space, *Commun. Math. Phys.* **87** (1983) 577.
[152] S. W. Hawking, I. G. Moss and J. M. Stewart, *Bubble Collisions in the Very Early Universe*, *Phys. Rev. D* **26** (1982) 2681.
[153] S. S. Gubser and A. Nellore, *Mimicking the QCD equation of state with a dual black hole*, *Phys. Rev. D* **78** (2008) 086007 [0804.0434].
[154] J. Greensite, *The Confinement problem in lattice gauge theory*, *Prog. Part. Nucl. Phys.* **51** (2003) 1 [hep-lat/0301023].
[155] N. Brambilla et al., *QCD and Strongly Coupled Gauge Theories: Challenges and Perspectives*, *Eur. Phys. J. C* **74** (2014) 2981 [1404.3723].
[156] J. B. Kogut, *A Review of the Lattice Gauge Theory Approach to Quantum Chromodynamics*, *Rev. Mod. Phys.* **55** (1983) 775.
[157] E. Shuryak, *Lectures on nonperturbative QCD (Nonperturbative Topological Phenomena in QCD and Related Theories)*, 1812.01509.
[158] L. G. Yaffe, *Large N phase transitions and the fate of small Schwarzschild-AdS black holes*, *Phys. Rev. D* **97** (2018) 026010 [1710.06455].
[159] Y. Bea, J. Casalderrey-Solana, T. Giannakopoulos, A. Jansen, S. Krippendorf, D. Mateos et al., *Spinodal Gravitational Waves*, 2112.15478.
[160] M. Attems, Y. Bea, J. Casalderrey-Solana, D. Mateos and M. Zilhão, *Dynamics of Phase Separation from Holography*, *JHEP* **01** (2020) 106 [1905.12544].
[161] M. Attems, *Holographic approach of the spinodal instability to criticality*, *JHEP* **08** (2021) 155 [2012.15687].
[162] B. Lucini and M. Panero, *SU(N) gauge theories at large N*, *Phys. Rept.* **526** (2013) 93 [1210.4997].
[163] A. Dumitru, Y. Hatta, J. Lenaghan, K. Orginos and R. D. Pisarski, *Deconfining phase transition as a matrix model of renormalized Polyakov loops*, *Phys. Rev. D* **70** (2004) 034511 [hep-th/0311223].
[164] M. Panero, *Thermodynamics of the QCD plasma and the large-N limit*, *Phys. Rev. Lett.* **103** (2009) 232001 [0907.3719].
[165] N. Jokela, M. Järvinen and A. Piispa, *Refining holographic models of the quark-gluon plasma*, 2405.02394.
[166] M. Caselle, A. Nada and M. Panero, *QCD thermodynamics from lattice calculations with nonequilibrium methods: The SU(3) equation of state*, *Phys. Rev. D* **98** (2018) 054513 [1801.03110].
[167] R. Li and J. Wang, *Thermodynamics and kinetics of Hawking-Page phase transition*, *Phys. Rev. D* **102** (2020) 024085.
[168] S. W. Hawking and G. T. Horowitz, *The Gravitational Hamiltonian, action, entropy and surface terms*, *Class. Quant. Grav.* **13** (1996) 1487 [gr-qc/9501014].
[169] S. R. Coleman and E. J. Weinberg, *Radiative Corrections as the Origin of Spontaneous Symmetry Breaking*, *Phys. Rev. D* **7** (1973) 1888.
[170] A. D. Linde, *Decay of the False Vacuum at Finite Temperature*, *Nucl. Phys. B* **216** (1983) 421.
[171] M. Matteini, M. Nemevšek, Y. Shoji and L. Ubaldi, *False Vacuum Decay Rate From Thin To Thick Walls*, 2404.17632.
[172] A. Ekstedt, O. Gould and J. Hirvonen, *BubbleDet: a Python package to compute functional determinants for bubble nucleation*, *JHEP* **12** (2023) 056 [2308.15652].
[173] O. Gould, A. Kormu and D. J. Weir, *A nonperturbative test of nucleation calculations for strong phase transitions*, 2404.01876.

[174] F. R. Ares, O. Henriksson, M. Hindmarsh, C. Hoyos and N. Jokela, *Gravitational Waves at Strong Coupling from an Effective Action*, *Phys. Rev. Lett.* **128** (2022) 131101 [2110.14442].
[175] J. Ellis, M. Lewicki and J. M. No, *On the Maximal Strength of a First-Order Electroweak Phase Transition and its Gravitational Wave Signal*, *JCAP* **04** (2019) 003 [1809.08242].
[176] D. Croon, O. Gould, P. Schicho, T. V. I. Tenkanen and G. White, *Theoretical uncertainties for cosmological first-order phase transitions*, *JHEP* **04** (2021) 055 [2009.10080].
[177] K. Enqvist, J. Ignatius, K. Kajantie and K. Rummukainen, *Nucleation and bubble growth in a first order cosmological electroweak phase transition*, *Phys. Rev. D* **45** (1992) 3415.
[178] C. Caprini et al., *Science with the space-based interferometer eLISA. II: Gravitational waves from cosmological phase transitions*, *JCAP* **04** (2016) 001 [1512.06239].
[179] M. Hindmarsh, S. J. Huber, K. Rummukainen and D. J. Weir, *Numerical simulations of acoustically generated gravitational waves at a first order phase transition*, *Phys. Rev. D* **92** (2015) 123009 [1504.03291].
[180] M. Hindmarsh and M. Hijazi, *Gravitational waves from first order cosmological phase transitions in the Sound Shell Model*, *JCAP* **12** (2019) 062 [1909.10040].
[181] H.-K. Guo, K. Sinha, D. Vagie and G. White, *Phase Transitions in an Expanding Universe: Stochastic Gravitational Waves in Standard and Non-Standard Histories*, *JCAP* **01** (2021) 001 [2007.08537].
[182] J. Ellis, M. Lewicki and J. M. No, *Gravitational waves from first-order cosmological phase transitions: lifetime of the sound wave source*, *JCAP* **07** (2020) 050 [2003.07360].
[183] J. Ellis, M. Lewicki, J. M. No and V. Vaskonen, *Gravitational wave energy budget in strongly supercooled phase transitions*, *JCAP* **06** (2019) 024 [1903.09642].
[184] C. Gowling and M. Hindmarsh, *Observational prospects for phase transitions at LISA: Fisher matrix analysis*, *JCAP* **10** (2021) 039 [2106.05984].
[185] B. Lucini, M. Teper and U. Wenger, *The High temperature phase transition in SU(N) gauge theories*, *JHEP* **01** (2004) 061 [hep-lat/0307017].
[186] F. R. Ares, O. Henriksson, M. Hindmarsh, C. Hoyos and N. Jokela, *Effective actions and bubble nucleation from holography*, *Phys. Rev. D* **105** (2022) 066020 [2109.13784].
[187] J. Halverson, C. Long, A. Maiti, B. Nelson and G. Salinas, *Gravitational waves from dark Yang-Mills sectors*, *JHEP* **05** (2021) 154 [2012.04071].
[188] R. Pasechnik, M. Reichert, F. Sannino and Z.-W. Wang, *Gravitational waves from composite dark sectors*, *JHEP* **02** (2024) 159 [2309.16755].
[189] M. Reichert, F. Sannino, Z.-W. Wang and C. Zhang, *Dark confinement and chiral phase transitions: gravitational waves vs matter representations*, *JHEP* **01** (2022) 003 [2109.11552].
[190] W.-C. Huang, M. Reichert, F. Sannino and Z.-W. Wang, *Testing the dark SU(N) Yang-Mills theory confined landscape: From the lattice to gravitational waves*, *Phys. Rev. D* **104** (2021) 035005 [2012.11614].
[191] V. Guada, M. Nemevšek and M. Pintar, *FindBounce: Package for multi-field bounce actions*, *Comput. Phys. Commun.* **256** (2020) 107480 [2002.00881].
[192] I. Garcia Garcia, R. Lasenby and J. March-Russell, *Twin Higgs WIMP Dark Matter*, *Phys. Rev. D* **92** (2015) 055034 [1505.07109].

[193] M. Hindmarsh, S. J. Huber, K. Rummukainen and D. J. Weir, *Shape of the acoustic gravitational wave power spectrum from a first order phase transition*, *Phys. Rev. D* **96** (2017) 103520 [1704.05871].
[194] D. Cutting, M. Hindmarsh and D. J. Weir, *Vorticity, kinetic energy, and suppressed gravitational wave production in strong first order phase transitions*, *Phys. Rev. Lett.* **125** (2020) 021302 [1906.00480].
[195] F. Wilczek, *Problem of Strong P and T Invariance in the Presence of Instantons*, *Phys. Rev. Lett.* **40** (1978) 279.
[196] R. D. Peccei and H. R. Quinn, *Some Aspects of Instantons*, *Nuovo Cim. A* **41** (1977) 309.
[197] P. Arias, D. Cadamuro, M. Goodsell, J. Jaeckel, J. Redondo and A. Ringwald, *WISPy Cold Dark Matter*, *JCAP* **06** (2012) 013 [1201.5902].
[198] A. Arvanitaki, S. Dimopoulos, S. Dubovsky, N. Kaloper and J. March-Russell, *String Axiverse*, *Phys. Rev. D* **81** (2010) 123530 [0905.4720].
[199] J. Preskill, M. B. Wise and F. Wilczek, *Cosmology of the Invisible Axion*, *Phys. Lett. B* **120** (1983) 127.
[200] F. W. Stecker and Q. Shafi, *The Evolution of Structure in the Universe From Axions*, *Phys. Rev. Lett.* **50** (1983) 928.
[201] M. Dine and W. Fischler, *The Not So Harmless Axion*, *Phys. Lett. B* **120** (1983) 137.
[202] L. F. Abbott and P. Sikivie, *A Cosmological Bound on the Invisible Axion*, *Phys. Lett. B* **120** (1983) 133.
[203] R. T. Co, L. J. Hall and K. Harigaya, *Axion Kinetic Misalignment Mechanism*, *Phys. Rev. Lett.* **124** (2020) 251802 [1910.14152].
[204] C.-F. Chang and Y. Cui, *New Perspectives on Axion Misalignment Mechanism*, *Phys. Rev. D* **102** (2020) 015003 [1911.11885].
[205] H. M. Georgi, L. J. Hall and M. B. Wise, *Grand Unified Models With an Automatic Peccei-Quinn Symmetry*, *Nucl. Phys. B* **192** (1981) 409.
[206] M. Dine and N. Seiberg, *String Theory and the Strong CP Problem*, *Nucl. Phys. B* **273** (1986) 109.
[207] S. B. Giddings and A. Strominger, *String Wormholes*, *Phys. Lett. B* **230** (1989) 46.
[208] R. Holman, S. D. H. Hsu, T. W. Kephart, E. W. Kolb, R. Watkins and L. M. Widrow, *Solutions to the strong CP problem in a world with gravity*, *Phys. Lett. B* **282** (1992) 132 [hep-ph/9203206].
[209] M. Kamionkowski and J. March-Russell, *Planck scale physics and the Peccei-Quinn mechanism*, *Phys. Lett. B* **282** (1992) 137 [hep-th/9202003].
[210] S. Ghigna, M. Lusignoli and M. Roncadelli, *Instability of the invisible axion*, *Phys. Lett. B* **283** (1992) 278.
[211] S. M. Barr and D. Seckel, *Planck scale corrections to axion models*, *Phys. Rev. D* **46** (1992) 539.
[212] M. Dine, *Problems of naturalness: Some lessons from string theory*, in *Conference on Topics in Quantum Gravity*, 7, 1992, hep-th/9207045.
[213] E. Hardy, *Miniclusters in the Axiverse*, *JHEP* **02** (2017) 046 [1609.00208].
[214] Z. Yin and L. Visinelli, *Axion star condensation around primordial black holes and microlensing limits*, 2404.10340.
[215] J. Lee, K. Murai, F. Takahashi and W. Yin, *Bubble Misalignment Mechanism for Axions*, 2402.09501.
[216] B. Eggemeier, J. Redondo, K. Dolag, J. C. Niemeyer and A. Vaquero, *First Simulations of Axion Minicluster Halos*, *Phys. Rev. Lett.* **125** (2020) 041301

[1911.09417].
[217] K. M. Zurek, C. J. Hogan and T. R. Quinn, *Astrophysical Effects of Scalar Dark Matter Miniclusters*, *Phys. Rev. D* **75** (2007) 043511 [astro-ph/0607341].
[218] M. Fairbairn, D. J. E. Marsh, J. Quevillon and S. Rozier, *Structure formation and microlensing with axion miniclusters*, *Phys. Rev. D* **97** (2018) 083502 [1707.03310].
[219] D. J. Gross, R. D. Pisarski and L. G. Yaffe, *QCD and Instantons at Finite Temperature*, *Rev. Mod. Phys.* **53** (1981) 43.
[220] P. Di Vecchia and G. Veneziano, *Chiral Dynamics in the Large N Limit*, *Nucl. Phys. B* **171** (1980) 253.
[221] G. Grilli di Cortona, E. Hardy, J. Pardo Vega and G. Villadoro, *The QCD axion, precisely*, *JHEP* **01** (2016) 034 [1511.02867].
[222] M. Gorghetto and G. Villadoro, *Topological Susceptibility and QCD Axion Mass: QED and NNLO corrections*, *JHEP* **03** (2019) 033 [1812.01008].
[223] Y. Shtanov, J. H. Traschen and R. H. Brandenberger, *Universe reheating after inflation*, *Phys. Rev. D* **51** (1995) 5438 [hep-ph/9407247].
[224] L. Kofman, A. D. Linde and A. A. Starobinsky, *Reheating after inflation*, *Phys. Rev. Lett.* **73** (1994) 3195 [hep-th/9405187].
[225] L. Kofman, A. D. Linde and A. A. Starobinsky, *Towards the theory of reheating after inflation*, *Phys. Rev. D* **56** (1997) 3258 [hep-ph/9704452].
[226] R. T. Co, L. J. Hall and K. Harigaya, *QCD Axion Dark Matter with a Small Decay Constant*, *Phys. Rev. Lett.* **120** (2018) 211602 [1711.10486].
[227] D. H. Lyth, *Axions and inflation: Sitting in the vacuum*, *Phys. Rev. D* **45** (1992) 3394.
[228] K. J. Bae, J.-H. Huh and J. E. Kim, *Update of axion CDM energy*, *JCAP* **09** (2008) 005 [0806.0497].
[229] P. Arias, N. Bernal, D. Karamitros, C. Maldonado, L. Roszkowski and M. Venegas, *New opportunities for axion dark matter searches in nonstandard cosmological models*, *JCAP* **11** (2021) 003 [2107.13588].
[230] I. Affleck and M. Dine, *A New Mechanism for Baryogenesis*, *Nucl. Phys. B* **249** (1985) 361.
[231] R. T. Co and K. Harigaya, *Axiogenesis*, *Phys. Rev. Lett.* **124** (2020) 111602 [1910.02080].
[232] R. T. Co, L. J. Hall and K. Harigaya, *Predictions for Axion Couplings from ALP Cogenesis*, *JHEP* **01** (2021) 172 [2006.04809].
[233] R. T. Co, N. Fernandez, A. Ghalsasi, L. J. Hall and K. Harigaya, *Lepto-Axiogenesis*, *JHEP* **21** (2020) 017 [2006.05687].
[234] K. Harigaya and I. R. Wang, *Axiogenesis from $SU(2)_R$ phase transition*, *JHEP* **10** (2021) 022 [2107.09679].
[235] R. T. Co, D. Dunsky, N. Fernandez, A. Ghalsasi, L. J. Hall, K. Harigaya et al., *Gravitational wave and CMB probes of axion kination*, *JHEP* **09** (2022) 116 [2108.09299].
[236] R. T. Co, K. Harigaya and A. Pierce, *Cosmic perturbations from a rotating field*, *JCAP* **10** (2022) 037 [2202.01785].
[237] P. Barnes, R. T. Co, K. Harigaya and A. Pierce, *Lepto-axiogenesis and the scale of supersymmetry*, 2208.07878.
[238] J. D. Barrow, *Massive Particles as a Probe of the Early Universe*, *Nucl. Phys. B* **208** (1982) 501.
[239] A. Ayala, I. Domínguez, M. Giannotti, A. Mirizzi and O. Straniero, *Revisiting the*

bound on axion-photon coupling from Globular Clusters, *Phys. Rev. Lett.* **113** (2014) 191302 [1406.6053].

[240] S. Nakagawa, F. Takahashi and M. Yamada, *Trapping Effect for QCD Axion Dark Matter*, *JCAP* **05** (2021) 062 [2012.13592].

[241] L. Di Luzio, B. Gavela, P. Quilez and A. Ringwald, *Dark matter from an even lighter QCD axion: trapped misalignment*, *JCAP* **10** (2021) 001 [2102.01082].

[242] M. P. Hertzberg, E. D. Schiappacasse and T. T. Yanagida, *Axion Star Nucleation in Dark Minihalos around Primordial Black Holes*, *Phys. Rev. D* **102** (2020) 023013 [2001.07476].

[243] E. D. Schiappacasse and T. T. Yanagida, *Can QCD axion stars explain Subaru HSC microlensing?*, *Phys. Rev. D* **104** (2021) 103020 [2109.13153].

[244] H. Fukunaga, N. Kitajima and Y. Urakawa, *Can axion clumps be formed in a pre-inflationary scenario?*, *JCAP* **02** (2021) 015 [2004.08929].

[245] N. Kitajima, K. Kogai and Y. Urakawa, *New scenario of QCD axion clump formation. Part I. Linear analysis*, *JCAP* **03** (2022) 039 [2111.05785].

[246] A. Arvanitaki, S. Dimopoulos, M. Galanis, L. Lehner, J. O. Thompson and K. Van Tilburg, *Large-misalignment mechanism for the formation of compact axion structures: Signatures from the QCD axion to fuzzy dark matter*, *Phys. Rev. D* **101** (2020) 083014 [1909.11665].

[247] A. D. Linde and D. H. Lyth, *Axionic domain wall production during inflation*, *Phys. Lett. B* **246** (1990) 353.

[248] E. W. Kolb and I. I. Tkachev, *Large amplitude isothermal fluctuations and high density dark matter clumps*, *Phys. Rev. D* **50** (1994) 769 [astro-ph/9403011].

[249] E. W. Kolb and I. I. Tkachev, *Axion miniclusters and Bose stars*, *Phys. Rev. Lett.* **71** (1993) 3051 [hep-ph/9303313].

[250] E. W. Kolb and I. I. Tkachev, *Nonlinear axion dynamics and formation of cosmological pseudosolitons*, *Phys. Rev. D* **49** (1994) 5040 [astro-ph/9311037].

[251] L. Visinelli and J. Redondo, *Axion Miniclusters in Modified Cosmological Histories*, *Phys. Rev. D* **101** (2020) 023008 [1808.01879].

[252] L. Di Luzio, M. Giannotti, E. Nardi and L. Visinelli, *The landscape of QCD axion models*, *Phys. Rept.* **870** (2020) 1 [2003.01100].

[253] M. Khlopov, B. A. Malomed and I. B. Zeldovich, *Gravitational instability of scalar fields and formation of primordial black holes*, *Mon. Not. Roy. Astron. Soc.* **215** (1985) 575.

[254] W. Hu, R. Barkana and A. Gruzinov, *Cold and fuzzy dark matter*, *Phys. Rev. Lett.* **85** (2000) 1158 [astro-ph/0003365].

[255] S. Folkerts, C. Germani and J. Redondo, *Axion Dark Matter and Planck favor non-minimal couplings to gravity*, *Phys. Lett. B* **728** (2014) 532 [1304.7270].

[256] G. Ballesteros, J. Redondo, A. Ringwald and C. Tamarit, *Standard Model—axion—seesaw—Higgs portal inflation. Five problems of particle physics and cosmology solved in one stroke*, *JCAP* **08** (2017) 001 [1610.01639].

[257] K. Hamaguchi, Y. Kanazawa and N. Nagata, *Axion quality problem alleviated by nonminimal coupling to gravity*, *Phys. Rev. D* **105** (2022) 076008 [2108.13245].

[258] C. Eröncel, R. Sato, G. Servant and P. Sørensen, *ALP dark matter from kinetic fragmentation: opening up the parameter window*, *JCAP* **10** (2022) 053 [2206.14259].

[259] C. Eröncel and G. Servant, *ALP Dark Matter Mini-Clusters from Kinetic Fragmentation*, 2207.10111.

[260] H. Xiao, I. Williams and M. McQuinn, *Simulations of axion minihalos*, *Phys. Rev.*

D **104** (2021) 023515 [2101.04177].
[261] J. Enander, A. Pargner and T. Schwetz, *Axion minicluster power spectrum and mass function*, *JCAP* **12** (2017) 038 [1708.04466].
[262] D. Ellis, D. J. E. Marsh and C. Behrens, *Axion Miniclusters Made Easy*, *Phys. Rev. D* **103** (2021) 083525 [2006.08637].
[263] W. H. Press and P. Schechter, *Formation of galaxies and clusters of galaxies by selfsimilar gravitational condensation*, *Astrophys. J.* **187** (1974) 425.
[264] J. A. Peacock, *Cosmological physics*. Cambridge University Press, 1999, https://doi.org/10.1017/CBO9780511804533.
[265] P. Tinyakov, I. Tkachev and K. Zioutas, *Tidal streams from axion miniclusters and direct axion searches*, *JCAP* **01** (2016) 035 [1512.02884].
[266] B. J. Kavanagh, T. D. P. Edwards, L. Visinelli and C. Weniger, *Stellar Disruption of Axion Miniclusters in the Milky Way*, *Phys. Rev. D* **104** (2021) 063038 [2011.05377].
[267] T. D. P. Edwards, B. J. Kavanagh, L. Visinelli and C. Weniger, *Transient Radio Signatures from Neutron Star Encounters with QCD Axion Miniclusters*, *Phys. Rev. Lett.* **127** (2021) 131103 [2011.05378].
[268] V. Berezinsky, V. Dokuchaev and Y. Eroshenko, *Small - scale clumps in the galactic halo and dark matter annihilation*, *Phys. Rev. D* **68** (2003) 103003 [astro-ph/0301551].
[269] V. S. Berezinsky, V. I. Dokuchaev and Y. N. Eroshenko, *Small-scale clumps of dark matter*, *Phys. Usp.* **57** (2014) 1 [1405.2204].
[270] T. Goerdt, O. Y. Gnedin, B. Moore, J. Diemand and J. Stadel, *The survival and disruption of CDM micro-haloes: Implications for direct and indirect detection experiments*, *Mon. Not. Roy. Astron. Soc.* **375** (2007) 191 [astro-ph/0608495].
[271] A. Schneider, L. Krauss and B. Moore, *Impact of Dark Matter Microhalos on Signatures for Direct and Indirect Detection*, *Phys. Rev. D* **82** (2010) 063525 [1004.5432].
[272] B. Paczynski, *Gravitational microlensing by the galactic halo*, *Astrophys. J.* **304** (1986) 1.
[273] K. Griest, *Galactic Microlensing as a Method of Detecting Massive Compact Halo Objects*, *Astrophys. J.* **366** (1991) 412.
[274] E. W. Kolb and I. I. Tkachev, *Femtolensing and picolensing by axion miniclusters*, *Astrophys. J. Lett.* **460** (1996) L25 [astro-ph/9510043].
[275] M. Fairbairn, D. J. E. Marsh and J. Quevillon, *Searching for the QCD Axion with Gravitational Microlensing*, *Phys. Rev. Lett.* **119** (2017) 021101 [1701.04787].
[276] D. Croon, D. McKeen, N. Raj and Z. Wang, *Subaru-HSC through a different lens: Microlensing by extended dark matter structures*, *Phys. Rev. D* **102** (2020) 083021 [2007.12697].
[277] D. Croon, D. McKeen and N. Raj, *Gravitational microlensing by dark matter in extended structures*, *Phys. Rev. D* **101** (2020) 083013 [2002.08962].
[278] J. Barranco and A. Bernal, *Self-gravitating system made of axions*, *Phys. Rev. D* **83** (2011) 043525 [1001.1769].
[279] P.-H. Chavanis, *Mass-radius relation of Newtonian self-gravitating Bose-Einstein condensates with short-range interactions: I. Analytical results*, *Phys. Rev. D* **84** (2011) 043531 [1103.2050].
[280] J. Eby, P. Suranyi, C. Vaz and L. C. R. Wijewardhana, *Axion Stars in the Infrared Limit*, *JHEP* **03** (2015) 080 [1412.3430].
[281] L. Visinelli, S. Baum, J. Redondo, K. Freese and F. Wilczek, *Dilute and dense*

axion stars, *Phys. Lett. B* **777** (2018) 64 [1710.08910].
[282] E. D. Schiappacasse and M. P. Hertzberg, *Analysis of Dark Matter Axion Clumps with Spherical Symmetry*, *JCAP* **01** (2018) 037 [1710.04729].
[283] E. Seidel and W. M. Suen, *Oscillating soliton stars*, *Phys. Rev. Lett.* **66** (1991) 1659.
[284] E. J. Copeland, M. Gleiser and H. R. Muller, *Oscillons: Resonant configurations during bubble collapse*, *Phys. Rev. D* **52** (1995) 1920 [hep-ph/9503217].
[285] L. A. Urena-Lopez, *Oscillatons revisited*, *Class. Quant. Grav.* **19** (2002) 2617 [gr-qc/0104093].
[286] L. Visinelli, *Boson Stars and Oscillatons: A Review*, *Int. J. Mod. Phys. D* (2021) [2109.05481].
[287] E. Seidel and W.-M. Suen, *Formation of solitonic stars through gravitational cooling*, *Phys. Rev. Lett.* **72** (1994) 2516 [gr-qc/9309015].
[288] D. G. Levkov, A. G. Panin and I. I. Tkachev, *Gravitational Bose-Einstein condensation in the kinetic regime*, *Phys. Rev. Lett.* **121** (2018) 151301 [1804.05857].
[289] J. Eby, P. Suranyi and L. C. R. Wijewardhana, *The Lifetime of Axion Stars*, *Mod. Phys. Lett. A* **31** (2016) 1650090 [1512.01709].
[290] H. Niikura et al., *Microlensing constraints on primordial black holes with Subaru/HSC Andromeda observations*, *Nature Astron.* **3** (2019) 524 [1701.02151].
[291] S. Sugiyama, M. Takada and A. Kusenko, *Possible evidence of QCD axion stars in HSC and OGLE microlensing events*, 2108.03063.
[292] H.-Y. Schive, M.-H. Liao, T.-P. Woo, S.-K. Wong, T. Chiueh, T. Broadhurst et al., *Understanding the Core-Halo Relation of Quantum Wave Dark Matter from 3D Simulations*, *Phys. Rev. Lett.* **113** (2014) 261302 [1407.7762].
[293] D. Karamitros, *MiMeS: Misalignment mechanism solver*, *Comput. Phys. Commun.* **275** (2022) 108311 [2110.12253].
[294] L. Lentati et al., *European Pulsar Timing Array Limits On An Isotropic Stochastic Gravitational-Wave Background*, *Mon. Not. Roy. Astron. Soc.* **453** (2015) 2576 [1504.03692].
[295] R. M. Shannon et al., *Gravitational waves from binary supermassive black holes missing in pulsar observations*, *Science* **349** (2015) 1522 [1509.07320].
[296] M. A. McLaughlin, *The North American Nanohertz Observatory for Gravitational Waves*, *Class. Quant. Grav.* **30** (2013) 224008 [1310.0758].
[297] A. Brazier et al., *The NANOGrav Program for Gravitational Waves and Fundamental Physics*, 1908.05356.
[298] NANOGrav collaboration, *The NANOGrav 12.5 yr Data Set: Search for an Isotropic Stochastic Gravitational-wave Background*, *Astrophys. J. Lett.* **905** (2020) L34 [2009.04496].
[299] R. w. Hellings and G. s. Downs, *UPPER LIMITS ON THE ISOTROPIC GRAVITATIONAL RADIATION BACKGROUND FROM PULSAR TIMING ANALYSIS*, *Astrophys. J. Lett.* **265** (1983) L39.
[300] V. Vaskonen and H. Veermäe, *Did NANOGrav see a signal from primordial black hole formation?*, *Phys. Rev. Lett.* **126** (2021) 051303 [2009.07832].
[301] V. De Luca, G. Franciolini and A. Riotto, *NANOGrav Data Hints at Primordial Black Holes as Dark Matter*, *Phys. Rev. Lett.* **126** (2021) 041303 [2009.08268].
[302] Y. Nakai, M. Suzuki, F. Takahashi and M. Yamada, *Gravitational Waves and Dark Radiation from Dark Phase Transition: Connecting NANOGrav Pulsar Timing*

Data and Hubble Tension, 2009.09754.
[303] W. Ratzinger and P. Schwaller, *Whispers from the dark side: Confronting light new physics with NANOGrav data*, 2009.11875.
[304] S. Vagnozzi, *Implications of the NANOGrav results for inflation*, *Mon. Not. Roy. Astron. Soc.* **502** (2021) L11 [2009.13432].
[305] G. Domènech and S. Pi, *NANOGrav Hints on Planet-Mass Primordial Black Holes*, 2010.03976.
[306] J. Ellis and M. Lewicki, *Cosmic String Interpretation of NANOGrav Pulsar Timing Data*, *Phys. Rev. Lett.* **126** (2021) 041304 [2009.06555].
[307] S. Blasi, V. Brdar and K. Schmitz, *Has NANOGrav found first evidence for cosmic strings?*, *Phys. Rev. Lett.* **126** (2021) 041305 [2009.06607].
[308] R. Samanta and S. Datta, *Gravitational wave complementarity and impact of NANOGrav data on gravitational leptogenesis: cosmic strings*, 2009.13452.
[309] M. Kawasaki, K. Kohri and N. Sugiyama, *Cosmological constraints on late time entropy production*, *Phys. Rev. Lett.* **82** (1999) 4168 [astro-ph/9811437].
[310] M. Kawasaki, K. Kohri and N. Sugiyama, *MeV scale reheating temperature and thermalization of neutrino background*, *Phys. Rev. D* **62** (2000) 023506 [astro-ph/0002127].
[311] S. Hannestad, *What is the lowest possible reheating temperature?*, *Phys. Rev. D* **70** (2004) 043506 [astro-ph/0403291].
[312] K. Ichikawa, M. Kawasaki and F. Takahashi, *The Oscillation effects on thermalization of the neutrinos in the Universe with low reheating temperature*, *Phys. Rev. D* **72** (2005) 043522 [astro-ph/0505395].
[313] F. De Bernardis, L. Pagano and A. Melchiorri, *New constraints on the reheating temperature of the universe after WMAP-5*, *Astropart. Phys.* **30** (2008) 192.
[314] M. Gerbino, K. Freese, S. Vagnozzi, M. Lattanzi, O. Mena, E. Giusarma et al., *Impact of neutrino properties on the estimation of inflationary parameters from current and future observations*, *Phys. Rev. D* **95** (2017) 043512 [1610.08830].
[315] G. B. Gelmini, P. Gondolo, A. Soldatenko and C. E. Yaguna, *Direct detection of neutralino dark mattter in non-standard cosmologies*, *Phys. Rev. D* **76** (2007) 015010 [hep-ph/0610379].
[316] G. B. Gelmini and P. Gondolo, *Ultra-cold WIMPs: relics of non-standard pre-BBN cosmologies*, *JCAP* **10** (2008) 002 [0803.2349].
[317] A. L. Erickcek and K. Sigurdson, *Reheating Effects in the Matter Power Spectrum and Implications for Substructure*, *Phys. Rev. D* **84** (2011) 083503 [1106.0536].
[318] I. R. Waldstein, A. L. Erickcek and C. Ilie, *Quasidecoupled state for dark matter in nonstandard thermal histories*, *Phys. Rev. D* **95** (2017) 123531 [1609.05927].
[319] L. Visinelli, *(Non-)thermal production of WIMPs during kination*, *Symmetry* **10** (2018) 546 [1710.11006].
[320] L. Visinelli and P. Gondolo, *Kinetic decoupling of WIMPs: analytic expressions*, *Phys. Rev. D* **91** (2015) 083526 [1501.02233].
[321] D. Grin, T. L. Smith and M. Kamionkowski, *Axion constraints in non-standard thermal histories*, *Phys. Rev. D* **77** (2008) 085020 [0711.1352].
[322] M. Giovannini, *Gravitational waves constraints on postinflationary phases stiffer than radiation*, *Phys. Rev. D* **58** (1998) 083504 [hep-ph/9806329].
[323] A. Riazuelo and J.-P. Uzan, *Quintessence and gravitational waves*, *Phys. Rev. D* **62** (2000) 083506 [astro-ph/0004156].
[324] P. J. Steinhardt and M. S. Turner, *Saving the Invisible Axion*, *Phys. Lett. B* **129** (1983) 51.

[325] R. J. Scherrer and M. S. Turner, *Decaying Particles Do Not Heat Up the Universe*, *Phys. Rev. D* **31** (1985) 681.
[326] L. H. Ford, *Gravitational Particle Creation and Inflation*, *Phys. Rev. D* **35** (1987) 2955.
[327] B. Spokoiny, *Deflationary universe scenario*, *Phys. Lett. B* **315** (1993) 40 [gr-qc/9306008].
[328] M. Joyce, *Electroweak Baryogenesis and the Expansion Rate of the Universe*, *Phys. Rev. D* **55** (1997) 1875 [hep-ph/9606223].
[329] P. Salati, *Quintessence and the relic density of neutralinos*, *Phys. Lett. B* **571** (2003) 121 [astro-ph/0207396].
[330] S. Profumo and P. Ullio, *SUSY dark matter and quintessence*, *JCAP* **11** (2003) 006 [hep-ph/0309220].
[331] C. Wetterich, *Cosmology and the Fate of Dilatation Symmetry*, *Nucl. Phys. B* **302** (1988) 668 [1711.03844].
[332] A. B. Burd and J. D. Barrow, *Inflationary Models with Exponential Potentials*, *Nucl. Phys. B* **308** (1988) 929.
[333] E. J. Copeland, A. R. Liddle and D. Wands, *Exponential potentials and cosmological scaling solutions*, *Phys. Rev. D* **57** (1998) 4686 [gr-qc/9711068].
[334] P. G. Ferreira and M. Joyce, *Cosmology with a primordial scaling field*, *Phys. Rev. D* **58** (1998) 023503 [astro-ph/9711102].
[335] B. Whitt, *Fourth Order Gravity as General Relativity Plus Matter*, *Phys. Lett. B* **145** (1984) 176.
[336] J. D. Barrow and S. Cotsakis, *Inflation and the Conformal Structure of Higher Order Gravity Theories*, *Phys. Lett. B* **214** (1988) 515.
[337] D. Wands, *Extended gravity theories and the Einstein-Hilbert action*, *Class. Quant. Grav.* **11** (1994) 269 [gr-qc/9307034].
[338] J. P. Derendinger, L. E. Ibanez and H. P. Nilles, *On the Low-Energy d = 4, N=1 Supergravity Theory Extracted from the d = 10, N=1 Superstring*, *Phys. Lett. B* **155** (1985) 65.
[339] M. Dine, R. Rohm, N. Seiberg and E. Witten, *Gluino Condensation in Superstring Models*, *Phys. Lett. B* **156** (1985) 55.
[340] B. de Carlos, J. A. Casas and C. Munoz, *Supersymmetry breaking and determination of the unification gauge coupling constant in string theories*, *Nucl. Phys. B* **399** (1993) 623 [hep-th/9204012].
[341] B. Ratra and P. J. E. Peebles, *Cosmological Consequences of a Rolling Homogeneous Scalar Field*, *Phys. Rev. D* **37** (1988) 3406.
[342] G. F. Giudice, E. W. Kolb, A. Riotto, D. V. Semikoz and I. I. Tkachev, *Standard model neutrinos as warm dark matter*, *Phys. Rev. D* **64** (2001) 043512 [hep-ph/0012317].
[343] G. F. Giudice, E. W. Kolb and A. Riotto, *Largest temperature of the radiation era and its cosmological implications*, *Phys. Rev. D* **64** (2001) 023508 [hep-ph/0005123].
[344] G. F. Giudice, A. Riotto and I. I. Tkachev, *The Cosmological moduli problem and preheating*, *JHEP* **06** (2001) 020 [hep-ph/0103248].
[345] L. Visinelli, *Cosmological perturbations for an inflaton field coupled to radiation*, *JCAP* **01** (2015) 005 [1410.1187].
[346] L. Visinelli, *Observational Constraints on Monomial Warm Inflation*, *JCAP* **07** (2016) 054 [1605.06449].
[347] K. Freese, E. I. Sfakianakis, P. Stengel and L. Visinelli, *The Higgs Boson can delay*

Reheating after Inflation, *JCAP* **05** (2018) 067 [1712.03791].
[348] Z. G. Berezhiani, A. S. Sakharov and M. Y. Khlopov, *Primordial background of cosmological axions*, *Sov. J. Nucl. Phys.* **55** (1992) 1063.
[349] R. L. Davis, *Goldstone Bosons in String Models of Galaxy Formation*, *Phys. Rev. D* **32** (1985) 3172.
[350] A. Vilenkin and A. E. Everett, *Cosmic Strings and Domain Walls in Models with Goldstone and PseudoGoldstone Bosons*, *Phys. Rev. Lett.* **48** (1982) 1867.
[351] A. Vilenkin, *Cosmic Strings*, *Phys. Rev. D* **24** (1981) 2082.
[352] A. Vilenkin, *Cosmic Strings and Domain Walls*, *Phys. Rept.* **121** (1985) 263.
[353] A. Vilenkin and T. Vachaspati, *Radiation of Goldstone Bosons From Cosmic Strings*, *Phys. Rev. D* **35** (1987) 1138.
[354] D. Harari and P. Sikivie, *On the Evolution of Global Strings in the Early Universe*, *Phys. Lett. B* **195** (1987) 361.
[355] R. L. Davis and E. P. S. Shellard, *DO AXIONS NEED INFLATION?*, *Nucl. Phys. B* **324** (1989) 167.
[356] R. A. Battye and E. P. S. Shellard, *Global string radiation*, *Nucl. Phys. B* **423** (1994) 260 [astro-ph/9311017].
[357] R. A. Battye and E. P. S. Shellard, *String radiative back reaction*, *Phys. Rev. Lett.* **75** (1995) 4354 [astro-ph/9408078].
[358] R. A. Battye and E. P. S. Shellard, *Axion string constraints*, *Phys. Rev. Lett.* **73** (1994) 2954 [astro-ph/9403018].
[359] C. J. A. P. Martins and E. P. S. Shellard, *String evolution with friction*, *Phys. Rev. D* **53** (1996) 575 [hep-ph/9507335].
[360] M. Yamaguchi, M. Kawasaki and J. Yokoyama, *Evolution of axionic strings and spectrum of axions radiated from them*, *Phys. Rev. Lett.* **82** (1999) 4578 [hep-ph/9811311].
[361] M. Yamaguchi, J. Yokoyama and M. Kawasaki, *Evolution of a global string network in a matter dominated universe*, *Phys. Rev. D* **61** (2000) 061301 [hep-ph/9910352].
[362] A. Vilenkin and E. P. S. Shellard, *Cosmic Strings and Other Topological Defects*. Cambridge University Press, 7, 2000.
[363] T. Hiramatsu, M. Kawasaki and K. Saikawa, *Evolution of String-Wall Networks and Axionic Domain Wall Problem*, *JCAP* **08** (2011) 030 [1012.4558].
[364] T. Hiramatsu, M. Kawasaki, T. Sekiguchi, M. Yamaguchi and J. Yokoyama, *Improved estimation of radiated axions from cosmological axionic strings*, *Phys. Rev. D* **83** (2011) 123531 [1012.5502].
[365] T. Hiramatsu, M. Kawasaki, K. Saikawa and T. Sekiguchi, *Axion cosmology with long-lived domain walls*, *JCAP* **01** (2013) 001 [1207.3166].
[366] T. Hiramatsu, M. Kawasaki, K. Saikawa and T. Sekiguchi, *Production of dark matter axions from collapse of string-wall systems*, *Phys. Rev. D* **85** (2012) 105020 [1202.5851].
[367] V. B. Klaer and G. D. Moore, *How to simulate global cosmic strings with large string tension*, *JCAP* **10** (2017) 043 [1707.05566].
[368] T. Vachaspati and A. Vilenkin, *Evolution of cosmic networks*, *Phys. Rev. D* **35** (1987) 1131.
[369] M. Sakellariadou, *Gravitational waves emitted from infinite strings*, *Phys. Rev. D* **42** (1990) 354.
[370] M. Sakellariadou, *Radiation of Nambu-Goldstone bosons from infinitely long cosmic strings*, *Phys. Rev. D* **44** (1991) 3767.

[371] J. J. Blanco-Pillado, K. D. Olum and B. Shlaer, *Large parallel cosmic string simulations: New results on loop production*, *Phys. Rev. D* **83** (2011) 083514 [1101.5173].
[372] J. J. Blanco-Pillado and K. D. Olum, *Stochastic gravitational wave background from smoothed cosmic string loops*, *Phys. Rev. D* **96** (2017) 104046 [1709.02693].
[373] C. Hagmann and P. Sikivie, *Computer simulations of the motion and decay of global strings*, *Nucl. Phys. B* **363** (1991) 247.
[374] S. Chang, C. Hagmann and P. Sikivie, *Studies of the motion and decay of axion walls bounded by strings*, *Phys. Rev. D* **59** (1999) 023505 [hep-ph/9807374].
[375] J. J. Blanco-Pillado, K. D. Olum and B. Shlaer, *The number of cosmic string loops*, *Phys. Rev. D* **89** (2014) 023512 [1309.6637].
[376] Y. Cui, M. Lewicki, D. E. Morrissey and J. D. Wells, *Probing the pre-BBN universe with gravitational waves from cosmic strings*, *JHEP* **01** (2019) 081 [1808.08968].
[377] L. Visinelli and P. Gondolo, *Dark Matter Axions Revisited*, *Phys. Rev.* **D80** (2009) 035024 [0903.4377].
[378] L. Visinelli and P. Gondolo, *Axion cold dark matter in view of BICEP2 results*, *Phys. Rev. Lett.* **113** (2014) 011802 [1403.4594].
[379] Y. Kahn, B. R. Safdi and J. Thaler, *Broadband and Resonant Approaches to Axion Dark Matter Detection*, *Phys. Rev. Lett.* **117** (2016) 141801 [1602.01086].
[380] J. L. Ouellet et al., *First Results from ABRACADABRA-10 cm: A Search for Sub-μeV Axion Dark Matter*, *Phys. Rev. Lett.* **122** (2019) 121802 [1810.12257].
[381] M. E. Tobar, B. T. McAllister and M. Goryachev, *The Electrodynamics of Free and Bound Charge Electricity Generators using Impressed Sources and the Modification to Maxwell's Equations*, *arXiv e-prints* (2019) arXiv:1904.05774 [1904.05774].
[382] C. A. Thomson, B. T. McAllister, M. Goryachev, E. N. Ivanov and M. E. Tobar, *UPconversion Loop Oscillator Axion Detection experiment: A precision frequency interferometric axion dark matter search with a Cylindrical Microwave Cavity*, 1912.07751.
[383] M. Gorghetto, E. Hardy and H. Nicolaescu, *Observing invisible axions with gravitational waves*, *JCAP* **06** (2021) 034 [2101.11007].
[384] NANOGrav collaboration, *The NANOGrav 12.5 yr Data Set: Observations and Narrowband Timing of 47 Millisecond Pulsars*, *Astrophys. J. Suppl.* **252** (2021) 4 [2005.06490].
[385] NANOGrav collaboration, *The NANOGrav 15 yr Data Set: Detector Characterization and Noise Budget*, *Astrophys. J. Lett.* **951** (2023) L10 [2306.16218].
[386] NANOGrav collaboration, *The NANOGrav 15 yr Data Set: Evidence for a Gravitational-wave Background*, *Astrophys. J. Lett.* **951** (2023) L8 [2306.16213].
[387] NANOGrav collaboration, *The NANOGrav 15 yr Data Set: Observations and Timing of 68 Millisecond Pulsars*, *Astrophys. J. Lett.* **951** (2023) L9 [2306.16217].
[388] J. Antoniadis et al., *The International Pulsar Timing Array second data release: Search for an isotropic gravitational wave background*, *Mon. Not. Roy. Astron. Soc.* **510** (2022) 4873 [2201.03980].
[389] M. Kramer and D. J. Champion, *The European Pulsar Timing Array and the Large European Array for Pulsars*, *Class. Quant. Grav.* **30** (2013) 224009.

[390] G. Desvignes et al., *High-precision timing of 42 millisecond pulsars with the European Pulsar Timing Array*, *Mon. Not. Roy. Astron. Soc.* **458** (2016) 3341 [1602.08511].
[391] G. Hobbs, *The Parkes Pulsar Timing Array*, *Class. Quant. Grav.* **30** (2013) 224007 [1307.2629].
[392] M. Kerr et al., *The Parkes Pulsar Timing Array project: second data release*, *Publ. Astron. Soc. Austral.* **37** (2020) e020 [2003.09780].
[393] R. N. Manchester, *The International Pulsar Timing Array*, *Class. Quant. Grav.* **30** (2013) 224010 [1309.7392].
[394] B. B. P. Perera et al., *The International Pulsar Timing Array: Second data release*, *Mon. Not. Roy. Astron. Soc.* **490** (2019) 4666 [1909.04534].
[395] NANOGrav collaboration, *Searching for Gravitational Waves from Cosmological Phase Transitions with the NANOGrav 12.5-Year Dataset*, *Phys. Rev. Lett.* **127** (2021) 251302 [2104.13930].
[396] B. Goncharov et al., *On the evidence for a common-spectrum process in the search for the nanohertz gravitational-wave background with the Parkes Pulsar Timing Array*, 2107.12112.
[397] S. Chen et al., *Common-red-signal analysis with 24-yr high-precision timing of the European Pulsar Timing Array: Inferences in the stochastic gravitational-wave background search*, *Mon. Not. Roy. Astron. Soc.* **508** (2021) 4970 [2110.13184].
[398] B. Bécsy, N. J. Cornish and L. Z. Kelley, *Exploring Realistic Nanohertz Gravitational-wave Backgrounds*, *Astrophys. J.* **941** (2022) 119 [2207.01607].
[399] J. Ellis, M. Fairbairn, G. Hütsi, M. Raidal, J. Urrutia, V. Vaskonen et al., *Prospects for Future Binary Black Hole GW Studies in Light of PTA Measurements*, 2301.13854.
[400] W. DeRocco and J. A. Dror, *Searching For Stochastic Gravitational Waves Below a Nanohertz*, 2304.13042.
[401] A. Ashoorioon, K. Rezazadeh and A. Rostami, *NANOGrav signal from the end of inflation and the LIGO mass and heavier primordial black holes*, *Phys. Lett. B* **835** (2022) 137542 [2202.01131].
[402] K. Freese and M. W. Winkler, *Have pulsar timing arrays detected the hot big bang: Gravitational waves from strong first order phase transitions in the early Universe*, *Phys. Rev. D* **106** (2022) 103523 [2208.03330].
[403] T. Bringmann, P. F. Depta, T. Konstandin, K. Schmidt-Hoberg and C. Tasillo, *Does NANOGrav observe a dark sector phase transition?*, 2306.09411.
[404] R. Z. Ferreira, A. Notari, O. Pujolas and F. Rompineve, *Gravitational Waves from Domain Walls in Pulsar Timing Array Datasets*, 2204.04228.
[405] W. Buchmuller, V. Domcke and K. Schmitz, *From NANOGrav to LIGO with metastable cosmic strings*, *Phys. Lett. B* **811** (2020) 135914 [2009.10649].
[406] G. Lazarides, R. Maji and Q. Shafi, *Cosmic strings, inflation, and gravity waves*, *Phys. Rev. D* **104** (2021) 095004 [2104.02016].
[407] G. Lazarides, R. Maji and Q. Shafi, *Gravitational waves from quasi-stable strings*, *JCAP* **08** (2022) 042 [2203.11204].
[408] D. Wang, *Novel Physics with International Pulsar Timing Array: Axionlike Particles, Domain Walls and Cosmic Strings*, 2203.10959.
[409] K. Kohri and T. Terada, *Solar-Mass Primordial Black Holes Explain NANOGrav Hint of Gravitational Waves*, *Phys. Lett. B* **813** (2021) 136040 [2009.11853].
[410] Z.-C. Zhao and S. Wang, *Bayesian Implications for the Primordial Black Holes from NANOGrav's Pulsar-Timing Data Using the Scalar-Induced Gravitational*

Waves, *Universe* **9** (2023) 157 [2211.09450].
[411] V. Dandoy, V. Domcke and F. Rompineve, *Search for scalar induced gravitational waves in the International Pulsar Timing Array Data Release 2 and NANOgrav 12.5 years dataset*, 2302.07901.
[412] J. A. Ellis, M. Vallisneri, S. R. Taylor and P. T. Baker. *ENTERPRISE: Enhanced Numerical Toolbox Enabling a Robust PulsaR Inference SuitE (v3.0.0)*, *Zenodo* (2020), doi:10.5281/zenodo.4059815.
[413] S. R. Taylor, P. T. Baker, J. S. Hazboun, J. Simon and S. J. Vigeland. *enterprise_extensions (v2.3.3)*, (2021) https://github.com/nanograv/enterprise_extensions.
[414] W. G. Lamb, S. R. Taylor and R. van Haasteren, *The Need For Speed: Rapid Refitting Techniques for Bayesian Spectral Characterization of the Gravitational Wave Background Using PTAs*, 2303.15442.
[415] L. S. Friedrich, M. J. Ramsey-Musolf, T. V. I. Tenkanen and V. Q. Tran, *Addressing the Gravitational Wave - Collider Inverse Problem*, 2203.05889.
[416] C. Caprini and D. G. Figueroa, *Cosmological Backgrounds of Gravitational Waves*, *Class. Quant. Grav.* **35** (2018) 163001 [1801.04268].
[417] C. W. Bauer, Z. Ligeti, M. Schmaltz, J. Thaler and D. G. E. Walker, *Supermodels for early LHC*, *Phys. Lett. B* **690** (2010) 280 [0909.5213].
[418] K. Saikawa, *A review of gravitational waves from cosmic domain walls*, *Universe* **3** (2017) 40 [1703.02576].
[419] T. Higaki, K. S. Jeong, N. Kitajima, T. Sekiguchi and F. Takahashi, *Topological Defects and nano-Hz Gravitational Waves in Aligned Axion Models*, *JHEP* **08** (2016) 044 [1606.05552].
[420] C.-W. Chiang and B.-Q. Lu, *Testing clockwork axion with gravitational waves*, *JCAP* **05** (2021) 049 [2012.14071].
[421] S. Blasi, A. Mariotti, A. Rase, A. Sevrin and K. Turbang, *Friction on ALP domain walls and gravitational waves*, *JCAP* **04** (2023) 008 [2210.14246].
[422] E. Babichev, D. Gorbunov, S. Ramazanov and A. Vikman, *Gravitational shine of dark domain walls*, *JCAP* **04** (2022) 028 [2112.12608].
[423] T. W. B. Kibble, *Topology of Cosmic Domains and Strings*, *J. Phys. A* **9** (1976) 1387.
[424] M. Buschmann, J. W. Foster, A. Hook, A. Peterson, D. E. Willcox, W. Zhang et al., *Dark matter from axion strings with adaptive mesh refinement*, *Nature Commun.* **13** (2022) 1049 [2108.05368].
[425] D. G. Figueroa, M. Hindmarsh, J. Lizarraga and J. Urrestilla, *Irreducible background of gravitational waves from a cosmic defect network: update and comparison of numerical techniques*, *Phys. Rev. D* **102** (2020) 103516 [2007.03337].
[426] M. Hindmarsh, J. Lizarraga, A. Lopez-Eiguren and J. Urrestilla, *Approach to scaling in axion string networks*, *Phys. Rev. D* **103** (2021) 103534 [2102.07723].
[427] Y. Gouttenoire, G. Servant and P. Simakachorn, *Kination cosmology from scalar fields and gravitational-wave signatures*, 2111.01150.
[428] Y. Gouttenoire, G. Servant and P. Simakachorn, *Beyond the Standard Models with Cosmic Strings*, *JCAP* **07** (2020) 032 [1912.02569].
[429] C.-F. Chang and Y. Cui, *Gravitational waves from global cosmic strings and cosmic archaeology*, *JHEP* **03** (2022) 114 [2106.09746].
[430] T. Hiramatsu, M. Kawasaki and K. Saikawa, *On the estimation of gravitational wave spectrum from cosmic domain walls*, *JCAP* **02** (2014) 031 [1309.5001].

[431] M. Kawasaki, K. Saikawa and T. Sekiguchi, *Axion dark matter from topological defects*, *Phys. Rev. D* **91** (2015) 065014 [1412.0789].
[432] T. Higaki, K. S. Jeong, N. Kitajima and F. Takahashi, *The QCD Axion from Aligned Axions and Diphoton Excess*, *Phys. Lett. B* **755** (2016) 13 [1512.05295].
[433] https://nanograv.org/science/data/nanograv-125y-kde-representation-ceffyl.
[434] J. Ellis and R. van Haasteren. *jellis18/PTMCMCSampler: Official Release*, *Zenodo* (2017), doi:10.5281/zenodo.1037579.
[435] P. Schwaller, *Gravitational Waves from a Dark Phase Transition*, *Phys. Rev. Lett.* **115** (2015) 181101 [1504.07263].
[436] Y. Bai and M. Korwar, *Cosmological constraints on first-order phase transitions*, *Phys. Rev. D* **105** (2022) 095015 [2109.14765].
[437] P. F. de Salas, M. Lattanzi, G. Mangano, G. Miele, S. Pastor and O. Pisanti, *Bounds on very low reheating scenarios after Planck*, *Phys. Rev. D* **92** (2015) 123534 [1511.00672].
[438] J. Chluba and R. A. Sunyaev, *The evolution of CMB spectral distortions in the early Universe*, *Mon. Not. Roy. Astron. Soc.* **419** (2012) 1294 [1109.6552].
[439] J. Chluba and D. Jeong, *Teasing bits of information out of the CMB energy spectrum*, *Mon. Not. Roy. Astron. Soc.* **438** (2014) 2065 [1306.5751].
[440] J. Chluba et al., *Spectral Distortions of the CMB as a Probe of Inflation, Recombination, Structure Formation and Particle Physics: Astro2020 Science White Paper*, *Bull. Am. Astron. Soc.* **51** (2019) 184 [1903.04218].
[441] F. Bianchini and G. Fabbian, *CMB spectral distortions revisited: A new take on <math display="inline"><mi>μ</mi></math> distortions and primordial non-Gaussianities from FIRAS data*, *Phys. Rev. D* **106** (2022) 063527 [2206.02762].
[442] T. Kite, A. Ravenni, S. P. Patil and J. Chluba, *Bridging the gap: spectral distortions meet gravitational waves*, *Mon. Not. Roy. Astron. Soc.* **505** (2021) 4396 [2010.00040].
[443] CMB-S4 collaboration, *CMB-S4 Science Book, First Edition*, 1610.02743.
[444] Simons Observatory collaboration, *The Simons Observatory: Science goals and forecasts*, *JCAP* **02** (2019) 056 [1808.07445].
[445] A. Kogut et al., *The Primordial Inflation Explorer (PIXIE): A Nulling Polarimeter for Cosmic Microwave Background Observations*, *JCAP* **07** (2011) 025 [1105.2044].
[446] J. Chluba et al., *New horizons in cosmology with spectral distortions of the cosmic microwave background*, *Exper. Astron.* **51** (2021) 1515 [1909.01593].
[447] A. Ghoshal, Y. Gouttenoire, L. Heurtier and P. Simakachorn, *Primordial Black Hole Archaeology with Gravitational Waves from Cosmic Strings*, 2304.04793.
[448] M. Bauer, M. Neubert and A. Thamm, *Collider Probes of Axion-Like Particles*, *JHEP* **12** (2017) 044 [1708.00443].
[449] M. Bauer, M. Heiles, M. Neubert and A. Thamm, *Axion-Like Particles at Future Colliders*, *Eur. Phys. J. C* **79** (2019) 74 [1808.10323].
[450] F. Ferrer, E. Masso, G. Panico, O. Pujolas and F. Rompineve, *Primordial Black Holes from the QCD axion*, *Phys. Rev. Lett.* **122** (2019) 101301 [1807.01707].
[451] G. B. Gelmini, J. Hyman, A. Simpson and E. Vitagliano, *Primordial black hole dark matter from catastrogenesis with unstable pseudo-Goldstone bosons*, *JCAP* **06** (2023) 055 [2303.14107].

[452] Y. Gouttenoire and E. Vitagliano, *Domain wall interpretation of the PTA signal confronting black hole overproduction*, 2306.17841.
[453] N. Kitajima, T. Sekiguchi and F. Takahashi, *Cosmological abundance of the QCD axion coupled to hidden photons*, *Phys. Lett. B* **781** (2018) 684 [1711.06590].
[454] W. Ratzinger, P. Schwaller and B. A. Stefanek, *Gravitational Waves from an Axion-Dark Photon System: A Lattice Study*, *SciPost Phys.* **11** (2021) 001 [2012.11584].
[455] R. Namba and M. Suzuki, *Implications of Gravitational-wave Production from Dark Photon Resonance to Pulsar-timing Observations and Effective Number of Relativistic Species*, *Phys. Rev. D* **102** (2020) 123527 [2009.13909].
[456] A. Chatrchyan and J. Jaeckel, *Gravitational waves from the fragmentation of axion-like particle dark matter*, *JCAP* **02** (2021) 003 [2004.07844].
[457] E. Madge, W. Ratzinger, D. Schmitt and P. Schwaller, *Audible axions with a booster: Stochastic gravitational waves from rotating ALPs*, *SciPost Phys.* **12** (2022) 171 [2111.12730].
[458] C. J. Hogan, *NUCLEATION OF COSMOLOGICAL PHASE TRANSITIONS*, *Phys. Lett. B* **133** (1983) 172.
[459] V. A. Kuzmin, V. A. Rubakov and M. E. Shaposhnikov, *On the Anomalous Electroweak Baryon Number Nonconservation in the Early Universe*, *Phys. Lett. B* **155** (1985) 36.
[460] C. S. Machado, W. Ratzinger, P. Schwaller and B. A. Stefanek, *Audible Axions*, *JHEP* **01** (2019) 053 [1811.01950].
[461] N. Fonseca, E. Morgante, R. Sato and G. Servant, *Axion fragmentation*, *JHEP* **04** (2020) 010 [1911.08472].
[462] Y. B. Zeldovich and R. A. Sunyaev, *The Interaction of Matter and Radiation in a Hot-Model Universe*, *Astrophys. Space Sci.* **4** (1969) 301.
[463] A. Kogut, M. H. Abitbol, J. Chluba, J. Delabrouille, D. Fixsen, J. C. Hill et al., *CMB Spectral Distortions: Status and Prospects*, 1907.13195.
[464] H. Tashiro, E. Sabancilar and T. Vachaspati, *CMB Distortions from Damping of Acoustic Waves Produced by Cosmic Strings*, *JCAP* **08** (2013) 035 [1212.3283].
[465] M. A. Amin and D. Grin, *Probing early-universe phase transitions with CMB spectral distortions*, *Phys. Rev. D* **90** (2014) 083529 [1405.1039].
[466] J. Chluba and D. Grin, *CMB spectral distortions from small-scale isocurvature fluctuations*, *Mon. Not. Roy. Astron. Soc.* **434** (2013) 1619 [1304.4596].
[467] W. Hu and N. Sugiyama, *Small scale cosmological perturbations: An Analytic approach*, *Astrophys. J.* **471** (1996) 542 [astro-ph/9510117].
[468] C.-P. Ma and E. Bertschinger, *Cosmological perturbation theory in the synchronous and conformal Newtonian gauges*, *Astrophys. J.* **455** (1995) 7 [astro-ph/9506072].
[469] W. Hu, N. Sugiyama and J. Silk, *The Physics of microwave background anisotropies*, *Nature* **386** (1997) 37 [astro-ph/9604166].
[470] D. G. Figueroa, M. Hindmarsh and J. Urrestilla, *Exact Scale-Invariant Background of Gravitational Waves from Cosmic Defects*, *Phys. Rev. Lett.* **110** (2013) 101302 [1212.5458].
[471] R. Durrer, M. Kunz and A. Melchiorri, *Cosmic structure formation with topological defects*, *Phys. Rept.* **364** (2002) 1 [astro-ph/0110348].
[472] R. Durrer, M. Kunz, C. Lineweaver and M. Sakellariadou, *Cosmic microwave background anisotropies from scaling seeds: Fit to observational data*, *Phys. Rev. Lett.* **79** (1997) 5198 [astro-ph/9706215].

[473] P. B. Greene, L. Kofman, A. D. Linde and A. A. Starobinsky, *Structure of resonance in preheating after inflation*, *Phys. Rev. D* **56** (1997) 6175 [hep-ph/9705347].
[474] D. G. Figueroa and F. Torrenti, *Parametric resonance in the early Universe—a fitting analysis*, *JCAP* **02** (2017) 001 [1609.05197].
[475] D. G. Figueroa and F. Torrenti, *Gravitational wave production from preheating: parameter dependence*, *JCAP* **10** (2017) 057 [1707.04533].
[476] D. G. Figueroa, A. Florio, F. Torrenti and W. Valkenburg, *The art of simulating the early Universe – Part I*, *JCAP* **04** (2021) 035 [2006.15122].
[477] D. G. Figueroa, A. Florio, F. Torrenti and W. Valkenburg, *CosmoLattice*, 2102.01031.
[478] D. G. Figueroa and A. Florio, "Technical note 1: Power spectra." https://cosmolattice.net/assets/technical_notes/CosmoLattice_TechnicalNote_PowerSpectrum.pdf, 06, 2022.
[479] D. Boyanovsky, C. Destri and H. J. de Vega, *The Approach to thermalization in the classical phi**4 theory in (1+1)-dimensions: Energy cascades and universal scaling*, *Phys. Rev. D* **69** (2004) 045003 [hep-ph/0306124].
[480] R. Micha and I. I. Tkachev, *Turbulent thermalization*, *Phys. Rev. D* **70** (2004) 043538 [hep-ph/0403101].
[481] C. Destri and H. J. de Vega, *Ultraviolet cascade in the thermalization of the classical phi**4 theory in 3+1 dimensions*, *Phys. Rev. D* **73** (2006) 025014 [hep-ph/0410280].
[482] J. T. Giblin and E. Thrane, *Estimates of maximum energy density of cosmological gravitational-wave backgrounds*, *Phys. Rev. D* **90** (2014) 107502 [1410.4779].
[483] W. Buchmüller, V. Domcke, K. Kamada and K. Schmitz, *The Gravitational Wave Spectrum from Cosmological $B-L$ Breaking*, *JCAP* **10** (2013) 003 [1305.3392].
[484] T. J. Clarke, E. J. Copeland and A. Moss, *Constraints on primordial gravitational waves from the Cosmic Microwave Background*, *JCAP* **10** (2020) 002 [2004.11396].
[485] Planck collaboration, *Planck 2013 results. XXV. Searches for cosmic strings and other topological defects*, *Astron. Astrophys.* **571** (2014) A25 [1303.5085].
[486] T. Charnock, A. Avgoustidis, E. J. Copeland and A. Moss, *CMB constraints on cosmic strings and superstrings*, *Phys. Rev. D* **93** (2016) 123503 [1603.01275].
[487] A. Lopez-Eiguren, J. Lizarraga, M. Hindmarsh and J. Urrestilla, *Cosmic Microwave Background constraints for global strings and global monopoles*, *JCAP* **07** (2017) 026 [1705.04154].
[488] A. Ota, T. Takahashi, H. Tashiro and M. Yamaguchi, *CMB μ distortion from primordial gravitational waves*, *JCAP* **10** (2014) 029 [1406.0451].
[489] J. Chluba, L. Dai, D. Grin, M. Amin and M. Kamionkowski, *Spectral distortions from the dissipation of tensor perturbations*, *Mon. Not. Roy. Astron. Soc.* **446** (2015) 2871 [1407.3653].
[490] D. J. Fixsen, E. S. Cheng, J. M. Gales, J. C. Mather, R. A. Shafer and E. L. Wright, *The Cosmic Microwave Background spectrum from the full COBE FIRAS data set*, *Astrophys. J.* **473** (1996) 576 [astro-ph/9605054].
[491] C. J. Moore and A. Vecchio, *Ultra-low-frequency gravitational waves from cosmological and astrophysical processes*, *Nature Astron.* **5** (2021) 1268 [2104.15130].
[492] Z.-C. Chen, Y.-M. Wu and Q.-G. Huang, *Search for the Gravitational-wave Background from Cosmic Strings with the Parkes Pulsar Timing Array Second*

Data Release, *Astrophys. J.* **936** (2022) 20 [2205.07194].
[493] X. Xue et al., *Constraining Cosmological Phase Transitions with the Parkes Pulsar Timing Array*, *Phys. Rev. Lett.* **127** (2021) 251303 [2110.03096].
[494] A. Weltman et al., *Fundamental physics with the Square Kilometre Array*, *Publ. Astron. Soc. Austral.* **37** (2020) e002 [1810.02680].
[495] C. Caprini, R. Durrer, T. Konstandin and G. Servant, *General Properties of the Gravitational Wave Spectrum from Phase Transitions*, *Phys. Rev. D* **79** (2009) 083519 [0901.1661].
[496] P. Agrawal, G. Marques-Tavares and W. Xue, *Opening up the QCD axion window*, *JHEP* **03** (2018) 049 [1708.05008].
[497] J. A. Dror, K. Harigaya and V. Narayan, *Parametric Resonance Production of Ultralight Vector Dark Matter*, *Phys. Rev. D* **99** (2019) 035036 [1810.07195].
[498] R. T. Co, A. Pierce, Z. Zhang and Y. Zhao, *Dark Photon Dark Matter Produced by Axion Oscillations*, *Phys. Rev. D* **99** (2019) 075002 [1810.07196].
[499] M. Bastero-Gil, J. Santiago, L. Ubaldi and R. Vega-Morales, *Vector dark matter production at the end of inflation*, *JCAP* **04** (2019) 015 [1810.07208].
[500] P. Agrawal, N. Kitajima, M. Reece, T. Sekiguchi and F. Takahashi, *Relic Abundance of Dark Photon Dark Matter*, *Phys. Lett. B* **801** (2020) 135136 [1810.07188].
[501] C. S. Machado, W. Ratzinger, P. Schwaller and B. A. Stefanek, *Gravitational wave probes of axionlike particles*, *Phys. Rev. D* **102** (2020) 075033 [1912.01007].
[502] Z. J. Weiner, P. Adshead and J. T. Giblin, *Constraining early dark energy with gravitational waves before recombination*, *Phys. Rev. D* **103** (2021) L021301 [2008.01732].
[503] P. Adshead, J. T. Giblin and Z. J. Weiner, *Gravitational waves from gauge preheating*, *Phys. Rev. D* **98** (2018) 043525 [1805.04550].
[504] J. R. C. Cuissa and D. G. Figueroa, *Lattice formulation of axion inflation. Application to preheating*, *JCAP* **06** (2019) 002 [1812.03132].
[505] N. Kitajima, J. Soda and Y. Urakawa, *Nano-Hz Gravitational-Wave Signature from Axion Dark Matter*, *Phys. Rev. Lett.* **126** (2021) 121301 [2010.10990].
[506] R. T. Co, K. Harigaya and A. Pierce, *Gravitational Waves and Dark Photon Dark Matter from Axion Rotations*, 2104.02077.
[507] A. Banerjee, E. Madge, G. Perez, W. Ratzinger and P. Schwaller, *Gravitational wave echo of relaxion trapping*, *Phys. Rev. D* **104** (2021) 055026 [2105.12135].
[508] J. Jaeckel, V. M. Mehta and L. T. Witkowski, *Monodromy Dark Matter*, *JCAP* **01** (2017) 036 [1605.01367].
[509] J. Berges, A. Chatrchyan and J. Jaeckel, *Foamy Dark Matter from Monodromies*, *JCAP* **08** (2019) 020 [1903.03116].
[510] E. Morgante, W. Ratzinger, R. Sato and B. A. Stefanek, *Axion fragmentation on the lattice*, *JHEP* **12** (2021) 037 [2109.13823].
[511] M. Dine, L. Randall and S. D. Thomas, *Supersymmetry breaking in the early universe*, *Phys. Rev. Lett.* **75** (1995) 398 [hep-ph/9503303].
[512] D. Kazanas, *Dynamics of the Universe and Spontaneous Symmetry Breaking*, *Astrophys. J. Lett.* **241** (1980) L59.
[513] A. Vilenkin, *Gravitational Field of Vacuum Domain Walls and Strings*, *Phys. Rev. D* **23** (1981) 852.
[514] J. Preskill, S. P. Trivedi, F. Wilczek and M. B. Wise, *Cosmology and broken discrete symmetry*, *Nucl. Phys. B* **363** (1991) 207.
[515] T. Hiramatsu, M. Kawasaki and K. Saikawa, *Gravitational Waves from Collapsing*

Domain Walls, *JCAP* **05** (2010) 032 [1002.1555].
[516] M. Kawasaki and K. Saikawa, *Study of gravitational radiation from cosmic domain walls*, *JCAP* **09** (2011) 008 [1102.5628].
[517] K. Saikawa, *Gravitational waves from cosmic domain walls: a mini-review*, *J. Phys. Conf. Ser.* **1586** (2020) 012039.
[518] R. Murgia, G. Scelfo, M. Viel and A. Raccanelli, *Lyman-α Forest Constraints on Primordial Black Holes as Dark Matter*, *Phys. Rev. Lett.* **123** (2019) 071102 [1903.10509].
[519] K. K. Rogers and H. V. Peiris, *Strong Bound on Canonical Ultralight Axion Dark Matter from the Lyman-Alpha Forest*, *Phys. Rev. Lett.* **126** (2021) 071302 [2007.12705].
[520] C. J. Hogan, *Gravitational radiation from cosmological phase transitions*, *Mon. Not. Roy. Astron. Soc.* **218** (1986) 629.
[521] M. Kamionkowski, A. Kosowsky and M. S. Turner, *Gravitational radiation from first order phase transitions*, *Phys. Rev. D* **49** (1994) 2837 [astro-ph/9310044].
[522] S. J. Huber and T. Konstandin, *Production of gravitational waves in the nMSSM*, *JCAP* **05** (2008) 017 [0709.2091].
[523] R. Jinno, S. Lee, H. Seong and M. Takimoto, *Gravitational waves from first-order phase transitions: Towards model separation by bubble nucleation rate*, *JCAP* **11** (2017) 050 [1708.01253].
[524] H. Tashiro, E. Sabancilar and T. Vachaspati, *CMB Distortions from Superconducting Cosmic Strings*, *Phys. Rev. D* **85** (2012) 103522 [1202.2474].
[525] M. Anthonisen, R. Brandenberger, A. Laguë, I. A. Morrison and D. Xia, *Cosmic Microwave Background Spectral Distortions from Cosmic String Loops*, *JCAP* **02** (2016) 047 [1509.07998].
[526] S. Dodelson, *Modern Cosmology*. Academic Press, Amsterdam, 2003.
[527] D. G. Figueroa, J. Garcia-Bellido and A. Rajantie, *On the Transverse-Traceless Projection in Lattice Simulations of Gravitational Wave Production*, *JCAP* **11** (2011) 015 [1110.0337].